GaN/AlGaN nanowires for quantum devices

Akhil Ajay

Communauté
UNIVERSITÉ Grenoble Alpes

THÈSE

Pour obtenir le grade de

DOCTEUR DE LA COMMUNAUTE UNIVERSITE GRENOBLE ALPES

Spécialité : NANOPHYSIQUE

Arrêté ministériel : 25 mai 2016

Présentée par

Akhil AJAY

Thèse dirigée par **Eva MONROY** et codirgée par **Martien DEN HERTOG**

préparée au sein du **Laboratoire PHotonique, ELectronique et Ingéniérie QuantiqueS (PHELIQS)**
dans **l'École Doctorale Physique**

Nanofils de GaN/AlGaN pour les composants quantiques

GaN/AlGaN nanowires for quantum devices

Thèse soutenue publiquement le **25 septembre 2018**
devant le jury composé de :

M Philippe BOUCAUD
Rapporteur
Mme Maria TCHERNYCHEVA
Rapporteur
M Regis ANDRE
President
M Jordi ARBIOL
Membre
M Gregor KOBLMÜLLER
Membre
M Jonas LÄHNEMANN
Membre

Acknowledgements

This manuscript is a result of my research in the group of “Nanophysique et Semiconducteurs (NPSC)” at the “Institut Nanosciences et Cryogénie (INAC)” at “Commissariat à l’énergie atomique et aux énergies alternatives (CEA)” in Grenoble, France. Starting from my master internships in the same group, for almost five years, I had the opportunity to live and work here in Grenoble and be with many amazing people.

First, I would like to express, from the bottom of my heart, deep appreciations and gratitude towards my supervisor, Eva Monroy. You were a constant source of guidance and support. I would like to thank you for guiding me right from my master internship days and finally leading to the thesis. Throughout my stay in the lab, you have been both a source of limitless inspiration and energy. I have learned many valuable lessions to be a good scientist and to be a good human being from you.

I would also like to thank Martien den Hertog, my cosupervisor. You have been a source of unparallel support, cheerfulness and guidance. Your curious questions during our discussions have helped me a lot to improve my understanding and knowledge and that would surely be missed.

For me, the quote *“If I have seen further, it is by standing on the shoulders of giants”,* refers mostly to these two amazing supervisors I had. I hope we cross paths again and again in the future. It was a great honor to have worked with you two and to have contributed to our multidisciplanry research.

I would like to thank Henri Mariette (former director of NPSC), Régis André and Bruno Gayral (directors of NPSC), and Jean-Michel Gerard (director of PHELIQS) for welcoming me into the group. My research was possible thanks to the European project TeraGaN (ERC-StG #278428) and French national research agency via GANEX program ANR-11-LABX-0014) and ANR-COSMOS (ANR-12-JS10-0002). I would also like to thank the other administrative staff, Carmelo Castagna and Céline Conche for all their help in navigating the administration of CEA.

I would like to extend my thanks to all the members of the jury for their time and effort to evaluate and for coming all this way to attend the thesis defense in Grenoble. Heartfull thanks to Philippe Boucaud and Maria Tchernycheva, the reporters for this manuscript, for their valuable comments and discussions. Also thanks to Regis Andre, Jordi Arbiol, Gregor Koblmüller and Jonas Lähnemann for their interesting questions and discussion regarding the research. Also, I would like to thank Bruno Gayral, Catherine Bougerol and Joël Bleuse use for their help in making my presentation the best it could possibly be.

I would like to thank our fruitful collaborators from the University of Giessen, namely Jörg Schörmann, Pascal Hille and Martin Eickhoff for their valuable contributions in studying Ge doping. Special thanks to our collaborators and short term colleagues from the University of Alcala, in particular Rodrigo Blasco, Marco Jiménez Rodriguez and Sirona Valdueza-Felip. It

was a great plesure to work with you. I would also like thank our collaborators from Lisbon, Katharina Lorentz and Lorentz Alves for their ongoing support in studing Ge doping in AlGaN.

I am very thankful for all my colleagues here at CEA: Yoann Curé, Yann Genuist, Jean Dussaud, and Didier Boilot for their help in always making sure that our MBEs and necessary equipements are functioning and taking care of logistics, Edith Bellet-Amalric for her help with the XRD machines, Catherine Bougerol for her beautiful TEM images, Joël Bleuse for the TRPL training and discussion, Lucien Notin for the AFM training, and Nicolas Mollard for the SEM training.

I am extremely thankful to my collegues Caroline Lim, Maria Spies, Jonas Lähnemann, David Browne, Luca Redaelli, Mark Beeler, Sirona Valdueza-Felip. The research is a fruit of the combined effort of each and everyone of you. Your support to my life in the lab and in Grenoble is immeasurable. I wish you all the best in your endevours and hope we meet again!

The lab also housed many wonderful souls who made Grenoble a real home for me and made many sweet memories. I was so lucky to have these people around. Thank you Madalina, Marion, Mathieu, Nathaniel, Saptarshi, Romain, Lynda, Buk, Martin, Akanksha, Farsane, Guilherme, Daria, Anna, Amine, Tobias, Thibault, Matthias, Zhihua, Agnès, Joanna, Saransh, Balakumar, Saranath and Alexandre.

Special thanks to my friends Jennifer, Nimisha, Shanti, Safeer, Meera, Anas, Shivani, Cindy, Elisa, Fadoua, Thauana, Ahlem, Dani, Kautar, Aurélien, Deba, Max, Dhruv, Rahul, Titiksha, Amit, Morgane, Sinara, Krishna, Bichu, Namanu, Nicolas, Manon, Aparna, Hamza for their constant support and adventures that we shared.

A big thanks to my family for being there always

Akhil

Résumé

Ce manuscrit étant complètement écrit en anglais, ces quelques pages résument en français les problématiques et les expériences menées ainsi que leurs résultats.

Les nouvelles propriétés des nanofils semi-conducteurs ont conduit à son émergence en tant qu'éléments prometteurs pour les composants avancés. Ce travail porte sur l'ingénierie inter-sous-bande (ISB) des nanofils de GaN où nous insérons des hétérostructures GaN/(Al,Ga)N pour les rendre optiquement actives dans la région spectrale infrarouge (IR). Les transitions ISB sont des transitions d'énergie entre les niveaux confinés quantiques dans la bande de conduction des nanostructures. Toutes les structures analysées dans cette thèse ont été synthétisées par épitaxie par jets moléculaires assisté par plasma.

Le **chapitre 1** décrit la motivation et les objectifs, ainsi que l'organisation du manuscrit. L'objectif de ce travail était d'explorer la possibilité de développer une technologie inter-sous-bande basée sur des nanofils de GaN. Dans ce but, d'une part, nous étudions des dopants alternatifs pour un meilleur contrôle de la morphologie des fils et de la distribution des porteurs, et d'autre part, nous essayons de décaler l'absorption inter-sous-bande des nanofils vers des longueurs d'ondes plus longues. Nous comparons systématiquement les structures à base de nanofils avec des structures planaires bien établies. Nous explorons également la fabrication de nanofils en utilisant une approche « top-down », c'est-à-dire par gravure.

Le **chapitre 2** commence par un bref résumé des propriétés générales des semi-conducteurs à base de nitrure III, décrivant leur structure cristalline et leurs caractéristiques électroniques, mécaniques et optiques les plus pertinentes. Nous présentons ensuite diverses nanostructures de semi-conducteurs et leur structure de bande. Enfin, nous passons en revue la physique des transitions inter-sous-bandes et soulignons les règles de sélection qui régissent ces transitions et les effets à plusieurs corps à prendre en compte.

Le **chapitre 3** contient une description des méthodes expérimentales et des outils utilisés dans ce travail. Une attention particulière est accordée à la description de l'épitaxie par jets moléculaires assisté par plasma (PAMBE), la méthode de croissance utilisée pour synthétiser tous les échantillons décrits dans cette thèse.

Un contrôle précis des niveaux élevés de dopage est crucial pour les composants inter-sous-bande. Par conséquent, au **chapitre 4**, nous présentons une étude du Ge en tant que dopant alternatif de type N, à la place de Si, pour les films minces de GaN et d'AlGaN développés par PAMBE. Le silicium, le dopant de type n préféré pour GaN, contribue à générer des dislocations de type bord et à une augmentation de la contrainte. Le dopage avec Si à des niveaux supérieurs à 10^{19} cm^{-3} est connu pour provoquer une rugosité importante de la surface et éventuellement une propagation des fissures. Le germanium, comme le silicium,

est un donneur peu profond dans GaN, avec une énergie d'activation théorique de 31,1 meV. Le rayon ionique d'un atome de Ge est similaire à celui du Ga et la longueur de la liaison métal-azote ne diminue que de 1,4% avec le Ge, contre 5,5% avec le Si. Par conséquent, Ge peut occuper le site du réseau Ga causant beaucoup moins de distorsion du réseau que les autres dopants. Tout comme Si, l'état DX de Ge est instable et n'affecte pas l'efficacité du dopage. Compte tenu des perspectives fondamentales et appliquées, il est important de mener des études approfondies sur le Ge en tant que dopant dans le GaN. Dans ce travail, nous montrons que l'utilisation de Ge comme dopant dans GaN pendant la croissance de PAMBE n'affecte pas la cinétique de croissance de GaN. Des couches minces de GaN dopées au Ge ont été développées avec des concentrations maximales de porteurs allant jusqu'à $6,7 \times 10^{20}$ cm^{-3} à 300 K, bien au-dessus de la densité de Mott. La concentration de Ge et la densité de porteurs libres varient linéairement avec le flux de Ge dans la gamme étudiée. Toutes les couches de GaN dopées au Ge ont une morphologie de surface lisse avec des terrasses atomiques, sans aucune preuve de fissuration, et la mosaïque des échantillons ne dépend pas de manière significative de la concentration de Ge. La variation de la bande interdite de GaN dopée au Ge avec la concentration de porteurs est compatible avec les calculs théoriques de la renormalisation de la bande interdite dus à l'interaction électron-électron-électron et à l'effet Burstein-Moss. Ces résultats valident l'utilisation de Ge dans GaN pour des applications nécessitant des niveaux de dopage élevés.

Il y a aussi un intérêt à étudier Ge en tant que dopant dans l'AlGaN. Il y a des prédictions théoriques que le début de la transition DX pour Ge dans AlGaN à une teneur en Al de 52%. Cependant, pour le Si, les mesures de conductivité suggèrent une conductivité réduite à une teneur en Al aussi basse que 50%. In this work, nous avons réussi à développer des films minces $Al_xGa_{1-x}N$ dopés au Ge avec $x \leq 0,66$. Nous avons montré que Ge n'induit aucune dégradation structurelle ou optique dans les échantillons d'AlGaN avec $x < 0,4$. Pour des compositions plus élevées en Al, des clusters riches en Ge ont été observés. En maintenant la concentration de constante de Ge à 1×10^{21} cm^{-3}, les mesures à effet Hall à température ambiante ont montré une diminution progressive de la concentration de porteurs lors de l'augmentation de la fraction molaire Al, la diminution étant déjà visible dans x = 0,24. Les échantillons avec x = 0,64-0,66 restent conducteurs (σ = 0,8-0,3 $\Omega^{-1}cm^{-1}$), mais la concentration des porteurs chute à 1×10^{18} cm^{-3}, ce qui implique une activation du donneur de 0,1%. Du point de vue optique, la photoluminescence (PL) à basse température était dominée par des transitions bande à bande. En augmentant la concentration de dopage, la PL se déplace à une énergie plus élevée en raison du remplissage de la bande de conduction. De plus, à partir de l'évolution de la position du pic de PL avec la température, on observe l'écrantage de la localisation induite par les fluctuations de la composition de l'alliage.

Dans la gamme des concentrations d'Al que nous avons abordées, le comportement du dopant Ge ne représente pas une amélioration drastique par rapport au Si dans les propriétés de transport. Cependant, nous devons garder à l'esprit que nous présentons le premier rapport sur l'AlGaN dopé au Ge, à notre connaissance, et qu'il existe une grande dispersion dans les données sur l'AlGaN dopé au Si. Les valeurs de conductivité varient considérablement

d'un rapport à l'autre, ce qui suggère une dépendance aux conditions de croissance. Par conséquent, il est difficile de comparer nos données sur l'AlGaN dopé au Ge avec la littérature sur l'AlGaN dopé au Si, mais notre observation de la conductivité jusqu'à 66% de la teneur en Al est extrêmement prometteuse.

Le **chapitre 5** décrit le développement des nanofils de GaN par PAMBE. L'insertion d'une couche tampon en AlN est nécessaire pour améliorer l'alignement vertical des fils. Cependant, la présence d'AlN se traduit par une énorme croissance bidimensionnelle. Pour résoudre ce problème, nous avons développé un procédé de croissance d'AlN à basse température. Nous avons également effectué une analyse de l'impact du flux de gallium et de la température du substrat sur la coalescence et le taux de croissance des nanofils.

Le chapitre 6 présente une étude des hétérostructures GaN / AlN conçues pour absorber la gamme spectrale de l'infrarouge à courte longueur d'onde (SWIR). Nous évaluons à la fois l'effet de la nature du dopant de type n, soit Ge ou Si, ainsi que la concentration en dopants sur les propriétés optiques. Nous comparons les nanofils auto-assemblés et les couches planaires, et nous introduisons également une approche de fabrication « top-down ».

Bien que des composants ISB à base de GaN aient été démontrés, ils reposent principalement sur une géométrie plane et utilisent Si comme dopant. Sur la base des progrès du dopage Ge dans les couches minces de GaN, il est devenu intéressant d'évaluer les performances des structures ISB en fonction de la nature du dopant, soit Ge ou Si. Pour évaluer le potentiel d'utilisation de Ge en tant que dopant dans des composants ISB, nous avons réalisé une étude comparative d'hétérostructures GaN/AlN planes dopées Si et absorbant dans le SWIR. Les études de diffraction des rayons X ont montré que dans ces hétérostructures, avec un fort désaccord de maille, les échantillons fortement dopés au Si présentent un élargissement des diffractogrammes de rayons x (balayage en ω) plus important par rapport aux échantillons dopés au Ge, ce qui indique une meilleure qualité structurelle des échantillons dopés au Ge. Les échantillons dopés au Ge et au Si ont tous présenté une absorption ISB dans la plage de 1,45 à 1,75 µm. L'élargissement de la transition est plus important dans le cas des échantillons dopés au Si, ce qui indique une rugosité de l'hétérointerface plus élevée dans ce cas. À notre connaissance, ces résultats constituent la première étude systématique des transitions ISB dans des structures à base de GaN planaires dopées au Ge.

D'autre part, la première étude systématique de l'absorption d'ISB dans des nanofils avec des puits quantiques dopés utilisait Ge comme dopant de type n. Dans ce cas, les hétérostructures GaN/AlN (4–8 nm / 4 nm) dopées au Ge sur des nanofils de GaN présentaient une absorption ISB dans le domaine SWIR, dans la plage 1,3-1,95 µm avec des transitions larges (FWHM ≈ 400 meV). Au début de ce travail de thèse, il n'y avait aucun information sur l'absorption d'ISB dans les nanofils contenant des hétérostructures GaN/AlN avec des puits quantiques GaN dopés au Si. Nous avons donc réalisé une étude comparative des hétérostructures GaN/AlN à nanofils dopés au Si et au Ge absorbant dans le SWIR. Dans le cadre de ces travaux, nous avons publié la première observation de l'absorption ISB dans des

hétérostructures de nanofils GaN/AlN dopées au Si avec des niveaux de dopage différents, avec des performances comparables à celles de leurs homologues dopés au Ge. Sur la base de cette étude, nous concluons que les nanofils dopés au Si et au Ge conviennent potentiellement à la fabrication d'hétérostructures de nanofils GaN/AlN pour l'optoélectronique ISB. Dans les deux cas, nous avons obtenu une largeur de raie amélioré de 200 meV pour l'absorption ISB à 1,55 µm, par rapport aux rapports précédents. Cependant, la largeur de raie de l'absorption ISB reste nettement supérieure à celle observée dans les structures planaires, en raison des inhomogénéités associées au processus de croissance auto-assemblé. Cela signifie que l'homogénéité entre les nanofils individuels à travers la tranche d'échantillons est le facteur limitant plutôt que le dopant.

Une autre approche pour surmonter les inhomogénéités dans les dimensions des puits quantiques dans les fils consiste à effectuer une gravure des hétérostructures planaires afin de créer des réseaux tridimensionnelles de micro- ou nano-piliers. Dans le cas des hétérostructures III-As, les réseaux de nano- et micro-piliers pour l'émission de THz ont été démontrés par une méthode « top-down » définie par lithographie. Un tel processus utilisant des hétérostructures GaN/AlN n'avait pas été tenté au début de ce travail de thèse. Nous avons présenté une analyse systématique de l'absorption ISB dans les micro- et nano-piliers contenant des hétérostructures GaN / AlN absorbant dans le domaine SWIR. Nous montrons que lorsque l'espacement du réseau de piliers est comparable aux longueurs d'ondes sondées, les résonances à cristaux photoniques dominent les spectres d'absorption. Cependant, lorsque ces résonances sont à des longueurs d'onde beaucoup plus courtes que l'absorption ISB, l'absorption est clairement observée, sans aucune dégradation de leur amplitude ou de leur largeur de raie.

Le **chapitre 7** décrit les hétérostructures GaN/(Al,Ga)N dans des nanofils de GaN structurellement conçus pour absorber dans la région infrarouge de moyenne longueur d'onde (MWIR). Au début de mon travail de thèse, les transitions ISB dans les nanofils de GaN/AlN n'avaient été observées que dans la gamme 1,3-1,95 µm, malgré l'utilisation de puits GaN aussi grands que 8 nm. Cela a été expliqué par la dispersion introduite par des irrégularités dans l'épaisseur et le diamètre du puits le long de l'axe de croissance. Ainsi, l'absorption s'élargit, ce qui réduit son intensité maximale. Dans une telle situation, des niveaux de dopage plus élevés sont nécessaires pour identifier l'absorption de l'ISB, ce qui entraîne un décalage de la transition dû aux effets à plusieurs corps. Il est donc important de s'efforcer d'améliorer l'homogénéité du nanofil dans le sens de la croissance en termes de diamètre. L'uniformité d'un nanofil à un autre le long du substrat est également importante. Cela garantirait des pics d'absorption plus nets et un contrôle des dimensions de l'hétérostructure. Ensuite, la transition ISB peut être déplacée vers des longueurs d'ondes plus longues, soit en utilisant des puits quantiques plus grands, soit en utilisant des alliages ternaires AlGaN comme barrières de puits quantiques, réduisant ainsi le champ électrique interne dans les puits. À cette fin, nous avons synthétisé des hétérostructures de nanofils auto-assemblées GaN/AlN et GaN/$Al_{0.4}Ga_{0.6}N$. Dans le cas des hétérostructures GaN/AlN dans les nanofils de GaN, nous avons fait varier la largeur des puits GaN de 1,5 à 5,7 nm. Les

hétérostructures avec des puits de 1,5 à 4 nm présentent des interfaces GaN/AlN nettes. Cependant, dans les puits plus grands (5,7 nm), l'un des hétérointerfaces GaN / AlN était plutôt un alliage gradué, qui s'étend d'environ 1,5 à 2 nm et a une forte influence sur les fonctions d'onde électronique dans le puits. En augmentant la largeur du puits GaN dans les hétérostructures, on observe un décalage vers le rouge de l'absorption ISB de 1,4 à 3,4 µm à température ambiante. Les résultats correspondent bien aux modèles théoriques, en tenant compte des caractéristiques structurelles (y compris la netteté ou le mélange des interfaces) et des effets à plusieurs corps associés au niveau de dopage. Pour les hétérostructures GaN/$Al_{0.4}Ga_{0.6}N$, l'alliage ternaire représente une réduction de la polarisation, ce qui conduit au décalage vers le bleu des transitions bande à bande et au décalage vers le rouge des transitions ISB. En conséquence, nous avons obtenu une absorption ISB dans les longueurs d'onde de 4,5 à 6,4 µm.

Dans le **chapitre 8**, nous évaluons la possibilité d'observer les transitions ISB dans la gamme de fréquences 1,5–9 THz dans les puits quantiques GaN/AlGaN non-polaires déposées sur le plan m. Nous étudions l'effet de la variation de la concentration en dopage de Si et nous explorons l'utilisation de Ge en tant que dopant. Pour étendre la technologie ISB basée sur GaN à l'infrarouge lointain (FIR), nous avons conçu une série de puits quantiques GaN/AlGaN plan m dont on fait varier les dimensions et les compositions Al pour séparer les deux niveaux électroniques confinés de 20–33 meV (correspondant à 4,8-8 THz), et découpler les transitions des puits voisins. Ces puits quantiques à faible composition d'Al (composition en Al dans l'alliage AlGaN inférieure à 10% et concentration moyenne en Al dans l'hétérostructure inférieure à 6%) présentent des couches plates et régulières dans les deux directions perpendiculaires *a* et *c*, et une très bonne qualité cristalline. Ces structures ont montré une absorption ISB à basse température dans la gamme de 6,3 à 37,4 meV (1,5 à 9 THz), fournissant une démonstration expérimentale de la possibilité pour GaN de couvrir une grande partie de la bande 7-10 THz interdite aux technologies à base de GaAs. Cependant, l'absorption ISB démontrée est spectralement large, avec une largeur de bande normalisée proche de 1, qui est attribuée à la densité élevée de dopage de Si ($n_s = 3\times10^{12}$ cm^{-2}). Sur la base de ce résultat, nous étudions plus avant l'effet de la densité de dopage sur ces structures FIR. Sur la base de ce résultat, nous avons étudié l'effet de la densité de dopage sur de telles structures FIR. L'augmentation du niveau de dopage entraîne une augmentation et un décalage vers le bleu du pic d'absorption, ainsi qu'une augmentation de la largeur de raie. Pour des niveaux de dopage élevés, il y a une amélioration systématique en utilisant Ge comme dopant, qui se manifeste dans des bandes d'absorption plus étroites.

Au **chapitre 9**, nous présentons le premier photo-détecteur ISB dans un nanofil unique (NW-QWIP), utilisant des hétérostructures GaN/AlN présentant des transitions ISB autour de 1,55 µm. L'observation de l'absorption de l'ISB dans des ensembles de nanofils nous a motivé pour le développement de QWIPs à base de nanofils. La première démonstration d'un tel dispositif est présentée dans ce manuscrit. En utilisant les dimensions extraites des mesures microscopie électronique en transmission, des simulations tridimensionnelles ont été effectuées pour expliquer l'absorption observée. Contrairement au photo-courant bande à

bande (dans le ultraviolet), le photo-courant infrarouge évolue linéairement avec la puissance d'éclairage incidente. Cette linéarité confirme que les photo-courants ultraviolet et infrarouge sont générés par différents mécanismes, les derniers étant moins sensibles aux phénomènes liés à la surface, comme prévu pour les transitions ISB dans une hétérostructure à nanofils. En conclusion, ce travail est une étude de preuve de principe des photo-détecteurs à nanofils ISB.

D'autre part, nous avons fabriqué des photo-détecteurs UV à nanofil unique constitués d'un nanofil de GaN avec une hétérostructure AlN/GaN/AlN intégrée. L'influence de l'hétérostructure est confirmée par le comportement asymétrique des caractéristiques courant-tension dans l'obscurité et sur illumination. En polarisation inverse (tension négative sur le segment supérieur du fil), les détecteurs se comportent linéairement avec la puissance optique incidente lorsque le diamètre du nanofil reste inférieur à un certain seuil (autour de 80 nm). Ceci s'explique par la linéarité du processus de photo-génération, la séparation des porteurs photo-générés induite par le champ électrique axial et le fait que l'illumination n'a pas d'effet significatif sur le champ électrique radial dans un nanofil déplété de porteurs de charge. Dans le cas de nanofils qui ne sont pas complètement déplétés (diamètre > 80 nm), le changement du niveau de Fermi au niveau des parois induit par la lumière entraîne une variation du diamètre du canal conducteur central dans le fils, ce qui conduit à une photo-réponse non linéaire.

Le **chapitre 10** résume le travail accompli et les principales réalisations et présente certaines perspectives de ce travail.

La technologie ISB des nanofils à base de GaN en est à ses débuts. Avec la démonstration de la détection ISB dans un nanofil unique, nous avons défini une orientation pour les dispositifs à nanofil unique en général. L'avenir devrait voir de nombreuses applications des nanofils dans l'électronique flexible, les dispositifs optoélectroniques à haut rendement, les dispositifs implantables, etc. La reproductibilité, le contrôle et le traitement des nanofils se sont considérablement développés au cours de la dernière décennie. Cependant, il est encore loin de la production industrielle de masse nécessaire à la majorité des applications. Des techniques de manipulation avancées pour des nano-objets uniques sont en cours de développement, ce qui contribuera au traitement et à la création de nouveaux périphériques plus performants.

Contents

1. Context and motivation

1.1 A brief history of infrared technology

The study of the distribution of radiant heat "across and outside" the visible solar spectrum with a set of thermometers by William Herschel almost 200 years ago resulted in the realization that there are rays invisible to the naked eye [1]. Since these rays were positioned outside the red part of the visible spectrum they were named infrared (IR) rays. The discovery of IR thermal emission at room temperature fueled the first applications as thermal imagers for the military. Night vision sensors, tank sight systems, heat seeking missiles were the immediate application of IR technology. At present, IR technology is widely used in many civil fields, such as remote temperature sensing, remote control, or short-range wireless communication. IR satellite images can now solve natural and economic problems. They can be used to understand the location of mineral deposits or the contents of forest or the state of a crop. IR imaging in medical diagnostics have also gained popularity recently.

Particularly interesting IR regions from the application viewpoint include the 1.3-1.55 µm wavelength window which is used for fiber optic communications [2], and the two atmospheric windows at 3-5 µm, for sensing hot objects (e.g. a flame or a jet engine), and at 8-14 µm, for high-performance thermal imaging around ambient temperature. There is an interest in even longer wavelengths for space applications [3]. The Terahertz range which roughly corresponds to the spectral region from 30 to 1000 µm (0.3 THz to 10 THz) is a non-ionizing radiation that appears as a harmless alternative to x-rays in medical, biological and security screening, and finds additional applications in high-speed wireless communication, industrial quality control, and spectroscopic imaging. There are various divisions for the IR spectrum depending upon applications. One of the most common is presented in Table 1.1.

Classification	Wavelength range
Near IR	0.75 µm – 1.4 µm
Short-wavelength IR	1.4 µm - 3 µm
Mid-wavelength IR	3 µm - 8 µm
Long-wavelength IR	8 µm -15 µm
Far IR	15 µm – 1000 µm

Table. 1.1: Classification of IR wavelength spectrum

The most widely used IR device is the IR detector [4]. There are two classes of IR detectors, namely thermal detectors and photon detectors. In a thermal detector the incident radiation changes the temperature of the system, which results in a change in some measurable physical property. Examples of such detectors include the bolometer and the pyrometer. They have modest sensitivity and slow response. They are commercially successful because they are relatively cheap [3].

The second class of detectors, namely photon detectors, is largely related to the progress in the semiconductor industry. They rely normally on band-to-band transitions in semiconducting materials. Narrow bandgap materials like InSb, PbTe and PbS were initially used to make IR detectors. Later ternary alloys like III−V ($InAs_{1-x}Sb_x$), IV−VI ($Pb_{1-x}Sn_xTe$), and II−VI ($Hg_{1-x}Cd_xTe$) were also introduced with the purpose of tuning the bandgap to improve the spectral response [4]. The $Hg_{1-x}Cd_xTe$ (HgCdTe) alloys might be the most successful materials for commercial IR photon detectors. The technology of HgCdTe has matured and produced a wide variety of detectors in different ranges over fifty years since the early sixties [5]. Later InGaAs alloys were attempted, like the $In_{0.53}Ga_{0.47}As$ (E_g = 0.73 eV), lattice-matched to InP, is an excellent detector material for the near−IR (1.0–1.7−µm) spectral range. However, the performance of InGaAs devices decreases rapidly if the alloy composition is varied due to lattice-mismatch-induced defects [4].

The introduction of quantum systems like quantum wells, quantum dots and nanowires provided an alternative solution to these problems. Esaki and Sakaki suggested that quantum confinement in GaAs/$Al_xGa_{1-x}As$ quantum wells (QWs) can be tuned to obtain intersubband (ISB) transitions [6]. The first experimental evidence of ISB absorption in a multi-QW (MQW) system was reported in 1985 by West and Eglash [7] followed by the fabrication of the first quantum well infrared photodetector (QWIP) in 1987 by Levine *et al.* [8]. In a QWIP, the quantum barrier height and quantum well width are crucial factors that decide the detectable wavelength band. In the last decade, QWIP cameras have undergone rapid development thanks to the standard manufacturing technology of GaAs, and they challenge HgCdTe alloy in the commercial scenario. QWIPs are characterized by fast response time and low power consumption. Current challenges in the QWIP technology include bringing up the operating temperature and extending their operation to shorter wavelength (less than 3 µm), which has been limited by material transparency and the available conduction band offset [2].

1.2 III-Nitride semiconductors

III-Nitride semiconductors (GaN, AlN, InN) are key materials for the development of optoelectronics and electronic devices in the 21st century thanks to their direct bandgap and doping capabilities. They are now extensively used in light emitting diodes (LEDs), which have revolutionized solid-state lightning. Nitride-based light emitters have also found applications in data storage, traffic lights, indoor agriculture etc. On the other hand, their high breakdown field and high electron mobility, combined with their mechanical and thermal robustness, makes them suitable candidates for high power electronics. AlGaN-based UV emitters for disinfection and water purification, and InGaN-based solar cells are currently under development.

III-Nitrides have also become interesting materials for infrared optoelectronics using intersubband transitions. In the late 90s, Suzuki *et al.* studied about the feasibility of the application of GaN based ISB technology for the telecommunication spectral range [9]. But real experimental work in ISB technology with III-nitrides began with C F Gmachl at Bell

laboratories only in 1999 [10], where she demonstrated ISB transitions in the wavelength range 1.75 µm to 4.5 µm. She also made estimates of the ultrafast excited electron lifetime of GaN/AlN QWs [11]. It was not until 2003 that the first ISB photodetector based on III-nitrides was developed. Hofstetter *et al.* had fabricated a QWIP using GaN/AlN wells and they were able to measure the emission from a 1.55 µm superluminescent LED [12]. However, such a photoconductive QWIP displayed large dark current, originating from structural defects in the highly-mismatched GaN/AlN structures. The device was only able to operate up to 170 K.

An alternative to circumvent the leakage problem was found exploiting the device photovoltaic response, associated to the intrinsic asymmetry of the potential profile in polar GaN wells. The photovoltaic operation of GaN/AlN QWIPs at telecommunication wavelengths and at room temperature was first studied in detail by Hofstetter *et al.* [13–17]. These photovoltaic ISB detectors were based on resonant optical rectification processes [15,18]. In a GaN/AlN superlattice, due to the asymmetry of the potential in the QWs, the excitation of an electron into the upper quantized level is accompanied by a charge displacement in the growth direction, so that an electrical dipole moment is created. For a high electron density and a large number of QWs, these microscopic dipole moments can be detected as an external photovoltage. A strong enhancement of the responsivity has been achieved by using quantum dots (QDs) instead of QWs in the active region [19].

Another approach to reduce leakage is the quantum cascade detector (QCD), which consists of several periods of an active QW coupled to a short-period superlattice, which serves as extractor [20,21]. In contrast to QWIPs, they operate at zero bias. Under illumination, electrons from the ground state of the active QW, e_1, are excited to the upper state, e_2, and then transferred to the extractor region where they experience multiple relaxations towards the next active QW. Operated as photovoltaic detectors, their dark current is extremely low and the capacitance can be reduced by increasing the number of periods, which enables high frequency response.

The polarization induced electric fields of III-nitrides were put to use to develop efficient GaN/AlGaN QCDs in the near-IR region. For example, Vardi *et al*. in 2008 [22] demonstrated devices that operated in the near IR spectral range with a room temperature zero-bias responsivity of 10 mA/W at 1.7 µm. More recently, in 2013, Sakr *et al.* demonstrated a GaN/AlGaN waveguide QCD at λ = 1.55 µm with 40 GHz frequency bandwidth for 10×10 μm^2 devices. They could obtain a peak response of 9.5±2 mA/W [23].

1.3 Semiconducting nanowires

In the last two decades, semiconducting nanowires have been widely studied due to the novel properties stemming from their low dimensionality. The first nanowire laser was demonstrated using ZnO [24] in 2001 and since then we have optically pumped coherent laser emission in nanowires who act as both waveguides for optical cavities and gain media for light amplification. Combining direct-gap III-V and II-VI nanowires with silicon nanowires and planar

silicon structures have produced multicolor electrically driven nanophotonic and integrated nanoelectronic-photonic systems [25]. Similar results were achieved using multi-quantum well (MQW) nanowire heterostructures, consisting of a GaN nanowire core that functions as the primary part of the optical cavity, and epitaxial InGaN/ GaN MQW shells that serve as the composition tunable gain medium [26].

In terms of photodetectors, the low electrical cross-section of nanowires implies low electrical capacitance, thus a larger operation bandwidth than planar devices. Owing to antenna effects, this comes without degradation of light absorption. Indeed, nanowire arrays can exhibit higher absorption than a thin film of the equivalent thickness [27]. The large surface-to-volume ratio allows misfit strain to be elastically released, which expands the possibilities for the active region design in terms of both size and composition. Also, the three-dimensional (3D) confinement of carriers in nanowire heterostructures might open new possibilities to control the carrier relaxation time [28,29].

The feasibility of electron transport via quantized levels in the conduction band of GaN/AlN heterostructured nanowires has been demonstrated by the fabrication of resonant tunneling diodes [30,31]. However, the field of nanowire ISB transitions is still in the nascent phase. Tanaka et al. [32] reported ISB absorption centered at 1.77 µm (= 0.7 eV) with a full width at half maximum (FWHM) of about 230 meV in a GaN/AlN (1 nm/2.7 nm) periodic heterostructure in GaN nanowires with the AlN barriers doped with Si at 2×10^{19} cm^{-3}. In this configuration, it is assumed that the electrons from the donor levels in the AlN barriers should be transferred to the GaN nanodisks. Studies in GaN/AlN planar heterostructures indicate an improvement of the ISB absorption linewidth if the doping is performed directly in the GaN wells [33]. However, at the beginning of this PhD work, there was no report on ISB absorption in GaN/AlN nanowire heterostructures with Si-doped GaN nanodisks. Difficulties were attributed to the fact that Si dopants tend to degrade nanowire morphology and migrate towards the nanowire sidewalls, resulting in inefficient doping [34]. Replacing Si by Ge, Beeler *et al.* [35] observed ISB absorption in GaN:Ge/AlN (4-8 nm /4 nm) heterostructures on GaN nanowires, in the short-wavelength infrared region. The transitions were broad though, with a FWHM of ≈ 400 meV.

1.4 Motivation and targets

Using nanowires instead of planar heterostructures in ISB devices can lead to better performance due to lower electrical cross-sections. Also nanowires have generally diameters smaller than the wavelengths associated to their ISB transitions, and exhibit a large dielectric mismatch with the environment. The target of this work was to explore the possibilities of intersubband engineering GaN nanowires. With this purpose, on the one hand, we study **alternative dopants** for better control of the morphology and carrier distribution, and on the other hand, we try to **extend this technology towards longer wavelengths**. We systematically compare well-established planar designs with nanowire structures. We also explore the

alternative top-down approach for nanowire fabrication. The following is a summary of our motivation for the various topics that are presented in this manuscript.

a) Alternative dopants

Silicon, the preferred n-type dopant for wurtzite GaN, contributes to edge type dislocation climb, leading to an increase in tensile stress [36–38]. Doping with Si in excess of 10^{19} cm^{-3} is reported to cause surface roughening and eventually crack propagation [37]. Ge, like Si, is a shallow donor in GaN, with a theoretical activation energy of 31.1 meV [39]. The ionic radius of a Ge atom is similar to that of Ga and the metal-nitrogen bond length changes by only 1.4% with Ge, compared to 5.5% with Si [40]. Hence Ge can occupy the Ga lattice site causing far less lattice distortion than other dopants. Also like Si, the DX- state of Ge is unstable and does not affect doping efficiency [40]. From both perspectives, fundamental and applied, it is important to perform extensive studies on Ge as a dopant in GaN.

There is also an interest to study Ge as a dopant in AlGaN. Gordon et al. [41] predicted that the onset of DX transition for Ge in AlGaN is at an Al content of 52%. They theoretically predicted that the DX configuration of Ge is more stable than that of Si (≈ 1 eV deeper into the bandgap), which is predicted to occur at 94% of Al content. However for Si, conductivity measurements suggest decreased conductivity at an Al content as low as 50% [42], which was attributed to shallow hydrogen like donor states. Experimental data was non-existent to verify theoretical predictions for Ge doped AlGaN.

To assess the interest of using Ge as a dopant in GaN intersubband devices, it is important to compare its performance in GaN/AlN heterostructures, both in the planar and in the nanowire geometry. While GaN based ISB devices have been demonstrated, they are primarily based on a planar geometry and utilize Si as a dopant. So based on the advancements in Ge doping in GaN thin films, it has become interesting to assess the performance of ISB structures as a function of the nature of the dopant, either Ge or Si. On the other hand, the first systematic study of ISB absorption in nanowires with doped quantum wells used Ge as n-type dopant in the already mentioned study by Beeler *et al* [35]. In that case, Ge-doped GaN/AlN (4–8 nm / 4 nm) heterostructures on GaN nanowires displayed ISB absorption in the short-wavelength infrared (SWIR) domain in the 1.3-1.95 µm range with broad transitions (FWHM of ≈ 400 meV). At the start of my PhD, there was no report on ISB absorption in GaN/AlN nanowire heterostructures with Si-doped GaN quantum wells.

b) Extension of the ISB transition in GaN/AlN nanowires towards longer wavelengths

At the beginning of my thesis work, ISB transitions in GaN/AlN nanowires had only been observed in the 1.3-1.95 µm range, in spite of using GaN wells as large as 8 nm [35]. This is explained by the dispersion introduced by irregularities in the well thickness and diameter along the growth axis. Thus, the absorption broadens, which reduces its peak intensity. In such a situation, higher doping levels are required to identify the ISB absorption, which leads to a blueshift of the transition due to many-body effects. It is therefore important to make an effort to improve the homogeneity of the nanowire along the growth direction in terms of diameter. Also important is uniformity from one nanowire to another along the substrate. This would ensure sharper absorption peaks and control of the heterostructure dimensions. Then,

the ISB transition can be shifted to longer wavelengths either by using larger quantum wells or by using AlGaN ternary alloys as quantum well barriers, thus reducing the internal electric field in the wells.

c) Top-down nanowires

Another approach to overcome inhomogeneities in the heterostructure dimensions consists in carefully performing top-down etching on planar heterostructures to create 3D arrays of micro/nano pillars. With III-As heterostructures, nano- and micropillar arrays for THz emission were demonstrated by lithographically defined top-down etching [43–45]. Such a process using GaN/AlN heterostructures had not been attempted at the beginning of this work.

d) Nonpolar orientations for far-infrared

The extension of the study of ISB transitions in nanowires towards the far-IR (FIR) was not possible due to time constraints. However, I have participated in the evaluation of nonpolar crystallographic orientations, particularly the m-plane, as an alternative to obtain GaN/AlGaN QWs without internal electric field [46–48]. We have shown that such structures can cover most of the 7–10 THz band inaccessible to GaAs based technologies.

e) Single nanowire photodetectors

The observation of ISB absorption in nanowire ensembles motivated us for the development of nanowire-based QWIPs. The first demonstration of such a device is presented in this manuscript.

1.5 Organization of the manuscript

Following these introductory pages, Chapter 2 starts with a brief summary of the general properties of III-nitride semiconductors, describing their crystal structure and their most relevant electronic, mechanical and optical features. Then, we present various semiconductor nanostructures and the appearance of subbands. Finally, we review the physics of ISB transitions and highlight the selection rules that govern these transitions and many-body effects that are to be considered.

Chapter 3 contains a description of the experimental methods and tools used in this work. Particular attention is paid to the description of plasma-assisted molecular beam epitaxy (PAMBE), the growth method used to synthesize all the samples described in this thesis.

In chapter 4, we present a study of Ge as an alternate n-type dopant, in place of Si, for wurtzite GaN and AlGaN thin films grown by PAMBE. We first prove that Ge does not introduce any perturbation in the GaN growth. We then analyze the effect of doping on the structural quality and estimate the Ge incorporation. We systematically assess the effect of Ge in electrical properties complemented by observing optical properties for various Ge doping concentrations and Al content in AlGaN.

Chapter 5 describes the development of GaN nanowires grown by PAMBE. The insertion of a thin AlN buffer layer is necessary to improve the vertical alignment of the wires. However, the presence of AlN results in huge two-dimensional (2D) undergrowth. To solve this problem, we develop a low-temperature AlN growth process. We then make an analysis of the impact of the gallium flux and substrate temperature on the coalescence and growth rate of the nanowires.

In chapter 6, we present a study of GaN/AlN heterostructures designed to absorb in the SWIR spectral range. We assess both the effect of the nature of the n-type dopant, either Ge or Si, as well as the dopant concentration on the optical properties. We compare self-assembled nanowires and planar layers, and we also introduce heterostructures contained in top-down nano/micropillar arrays, and we study the effect of patterning on their ISB absorption.

Chapter 7 describes the GaN/(Al,Ga)N heterostructures in GaN nanowires structurally designed to absorb in the mid-wavelength infrared (MWIR) region. To shift the absorption to longer wavelengths, we follow two approaches, the first one increasing the GaN well width in GaN/AlN heterostructures from 1.5 to 5.7 nm, which leads to a redshift of the intersubband absorption from 1.4 to 3.4 µm. Through the second approach, we demonstrate intersubband absorption in GaN/$Al_{0.4}Ga_{0.6}N$ heterostructures, thereby reducing the effects of polarization, which redshifts the intersubband transitions to cover the spectral range from 4.5 to 6.4 µm.

In chapter 8, we assess the possibility to observe ISB transitions in the 1.5–9 THz frequency range in nonpolar m-plane GaN/AlGaN MQWs, covering most of the 7–10 THz band inaccessible to GaAs based technologies. Such nonpolar structures present inhomogeneities of the Al composition in the barriers along the growth axis, however we did not identify any extended structural defects introduced by the epitaxial process. We study the effect of varying the Si doping concentration and we explore the use of Ge as a dopant.

In chapter 9, we present the first single-nanowire ISB photodetector (NW-QWIP), using GaN/AlN nanowire heterostructures that exhibit ISB transitions around 1.55 µm. In parallel, using band-to-band transitions, we report a single-nanowire UV photodetector incorporating an AlN/GaN/AlN heterostructure. Such a device presents a UV response that is linear with the optical power when the nanowire diameter is small enough to ensure a complete depletion of the wire.

Chapter 10 summarizes the accomplished work and main achievements, and considers its relevance and impact for future developments.

2. Introduction

2.1 Introduction to III-nitrides

2.1.1 Crystal structure

III-Nitride semiconductors like AlN, InN and GaN can appear in three crystalline configurations, namely wurtzite (α-phase), zinc blende (β-phase) and rock salt (γ-phase) structures. The wurtzite structure shows hexagonal symmetry with two hexagonal sublattices of metal (Al, Ga, In) and nitrogen (N) atoms which are shifted with respect to each other ideally by 3/8 [0001] (figure 2.1 (a)). The zinc-blende structure, also called sphalerite, shows a cubic symmetry, consisting of two interpenetrating face-centered cubic sublattices. One sublattice is shifted with respect to the other by ¼ [111] (figure 3.1 (b)). The rock salt structure, with a cubic symmetry where the two atom types form two interpenetrating face-centered cubic lattices, is the rarest configuration, appearing when crystals are synthesized under high pressure.

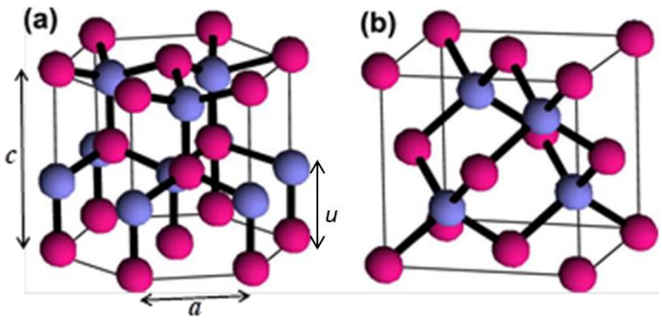

Figure 2.1: Schematic representation of (a) the wurtzite and (b) zinc-blende structures. The pink and violet spheres indicate metal and N atoms, respectively.

In this work, we focus on III-nitrides with wurtzite structure, which is the thermodynamically more stable configuration. I have used GaN as a reference for the discussion, unless described otherwise. Figure 2.1 (a) shows the *a* and *c* parameters of the hexagonal crystal structure of III-nitrides, and the anion-cation bond length *u* along the [0001] axis. A four index *(h k i l)* notation is used to refer to crystallographic planes or axis, which are described as a function of three base vectors a_1, a_2, a_3 and the out-of-plane vector *c*, as presented in Figure 2.2. Note that *i = -h-k*, since the three base vectors are separated by an angle of 120°.

The family of basal planes is termed as {0001} *c*-plane. The *c*-plane orientation is the most commonly used in opto- and microelectronics. There are two other families of planes which are of high importance, namely the {1-100} *m*-plane and {11-20} *a*-plane, both perpendicular to the *c*-plane and containing an equal number of Ga and N atoms. These main crystal plane orientations in GaN are illustrated in figure 2.2.

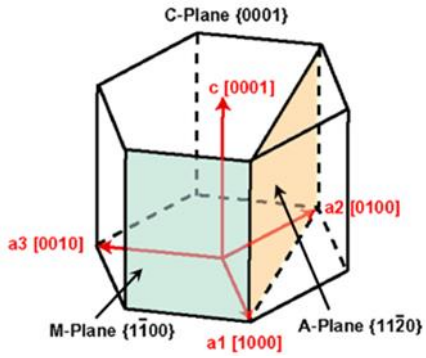

Figure 2.2: Hexagonal structure of GaN with representations of the base vectors and main crystallographic planes.

Since the hexagonal lattice is not centrosymmetric, the [0001] and [000-1] directions are not equal. In the GaN bond perpendicular to the {0001} plane, the vector pointing from Ga to N is identified arbitrarily as the [0001] direction. If the material is grown along this direction then it is called Ga-polar if it is grown in the opposite direction then it is called N-polar.

In an ideal wurtzite crystal, the *c/a* and *u/c* ratios are 1.633 and 0.375, respectively. However, due to the difference in metal ions, the bond lengths and the resultant *c/a* ratios of AlN, GaN, and InN are different. Table 2.1 describes the lattice parameters of wurtzite III-nitrides at 300 K.

	InN	**GaN**	**AlN**
c (Å)	5.703	5.185	4.982
a (Å)	3.545	3.189	3.112
c/a	1.608	1.626	1.6
u/c	0.377	0.377	0.382
References	[49]	[49,50]	[49,50]

Table 2.1: Lattice parameters of bulk InN, GaN and AlN.

The knowledge of heteroepitaxy along the *c*-plane is well established. However, the growth in *m*- and *a*-plane orientations was not considered until recently due to the unavailability of suitable substrates. During the last decade, the realization of the importance of non-polar III-nitrides have first led to the fabrication of non-polar films/templates on foreign substrates. Few examples include *a*-plane GaN on *r*-plane sapphire substrates [51], or *m*-plane GaN on *m*-plane SiC [52]. However, the heteroepitaxial growth on a and m-plane layers is prone to high defect densities. More recently, halide vapor phase epitaxy (HVPE) has developed to the point of producing relatively thick (< 1 µm) GaN crystals along the [0001] direction [53], which can be diced into high-quality *a*- and *m*- plane platelets for epitaxy of nonpolar structures. The main drawback of this method, as of now, is the high cost involved and the limited surface area available for growth.

2.1.2 Band structure

The band structure of a semiconductor emerges as a solution of the Schrödinger equation of non-interacting electrons in the periodic lattice. Visualization of the bandgap requires a plot of energy vs. wavevector $k = (k_x, k_y, k_z)$. It is common to plot band structures as curves of $E_n(k)$ for values of k along straight lines connecting symmetry points in the k-space. These points of symmetry occur in the first Brillouin zone and are labelled as Γ, Δ, Λ, Σ. The bandgap is described as the energy difference between the bottom of the conduction band and the top of the valence band. If the bottom of the conduction band and top of the valence band occur at the same symmetry point, then the material is said to have a direct bandgap. In the case of wurtzite III-nitrides, the bandgap is direct, with the conduction band minimum and the valence band maximum located at the Γ point. Due to the asymmetric nature of the wurtzite structure the valence band degeneracy is lifted. Thus the heavy hole (HH), light hole (LH) and spin-orbit, crystal field splitting (CH) subbands are separated as shown in the figure 2.3. The top of HH and LH subbands are higher than CH subband in energy for GaN. However, in the case of AlN the top of the CH subband is at higher energy than the HH or LH subbands.

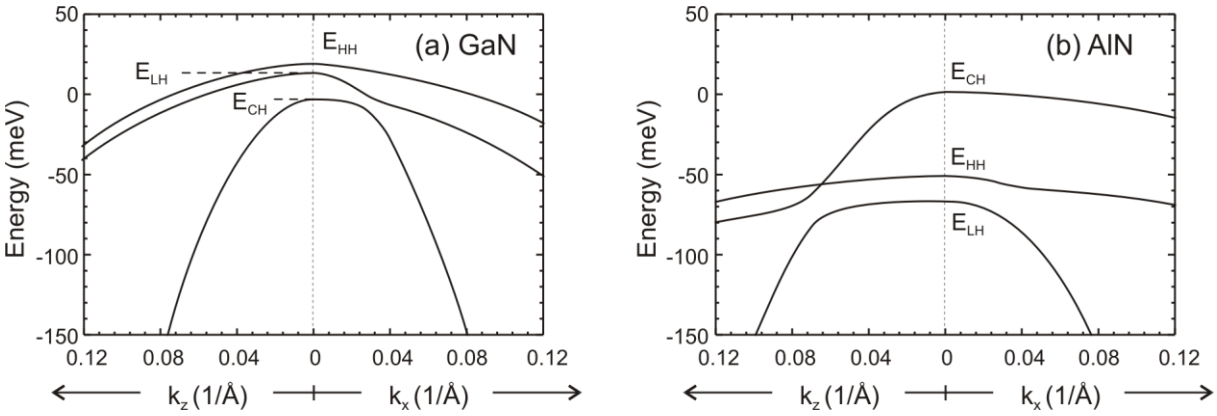

Figure 2.3: Electronic structure of the valance band of (a) GaN and (b) AlN near the Brillouin zone centre point Γ for unstrained wurtzite material. For simplicity, zero energy is assigned to the top of the valence band.

The values of the bandgap of GaN, AlN and InN are summarized in table 2.2. An effective mass approximation can be utilized to describe the band structure at Γ(k=0) by assuming a parabolic band structure at this point. This means that the electron or hole behavior can be modelled as a free particle with an effective mass m* experiencing a fixed potential. Typical values of the effective masses for electrons and holes in III-nitrides are recorded in table 2.2.

For ternary compounds like AlGaN or InGaN the bandgap is approximated by a quadratic equation:

$$E_g(AB) = xE_g(A) + (1-x)E_g(B) - x(1-x)b \qquad \text{(equation 2.1)}$$

where b is the bowing parameter, which accounts for the deviation from a linear interpolation between the two binaries A and B. The bowing parameter has a value of 0.8-1.3 eV in the case

of AlGaN [54]. By changing the Al or In content in GaN it is hence possible to obtain alloys with desirable bandgap.

	GaN	AlN
E_g (T = 0 K) (eV)	3.507 [55]	6.23 [55]
α_V (meV/K)	0.909 [55]	1.999 [55]
β_D (K)	830 [55]	1429 [55]
m^*_e	0.2 m_0 [56]	(0.32-0.40) m_0 [55,57]
m^*_h	1.25 m_0 [58]	1.44 m_0 [59]

Table 2.2: Band parameters of GaN and AlN: bandgap energy at T = 0 K; Varshni parameters; electron and hole effective masses (m_0 being the nominal mass in vacuum).

The bandgap of these materials is temperature dependent due to electron-lattice interactions and temperature dependence of the lattice parameters [60,61]. The temperature variation of the bandgap can be estimated by using the Varshni equation:

$$E_g(T) = E_g(T = 0\ K) - \frac{\alpha_V T^2}{\beta_D + T} \qquad \text{(equation 2.2)}$$

where α_V and β_D are the Varshni and Debye coefficients respectively, whose values for GaN and AlN are listed in Table 2.2.

2.1.3 Elastic properties

Strain is introduced during the epitaxial growth because of the mismatch of lattice constants and thermal expansion coefficients with the substrate. Strain affects the optical, electrical and bandgap properties of the III-nitrides.

In the framework of linear elasticity, Hooke's law describes the relation between the stress (σ_{ij}) applied to a material and the strain (ε_{kl}):

$$\sigma_{ij} = \sum C_{ijkl}\ \varepsilon_{kl} \qquad \text{(equation 2.3)}$$

where (C_{ijkl}) is the fourth-order elastic tensor. For simplification, we introduce the indices {1,2,3,4,5,6}, which replace the pairs of indices {xx,yy,zz,yz,zx,xy}:

$$\varepsilon_1 = \varepsilon_{xx}\ ;\ \ \varepsilon_2 = \varepsilon_{yy}\ ;\ \ \varepsilon_3 = \varepsilon_{zz}$$

$$\varepsilon_4 = \varepsilon_{yz}\ ,\ \varepsilon_{zy}\ ;\ \ \varepsilon_5 = \varepsilon_{zx}\ ,\ \varepsilon_{xz}\ ;\ \ \varepsilon_6 = \varepsilon_{xy}\ ,\ \varepsilon_{yx}$$

The elastic module can be represented by a matrix (a second-order tensor). For a crystal of hexagonal symmetry, this matrix contains six elastic modules, of which five are independent, as given in equation (2.4):

$$C_{ij} = \begin{pmatrix} C_{11} & C_{12} & C_{13} & 0 & 0 & 0 \\ C_{12} & C_{11} & C_{13} & 0 & 0 & 0 \\ C_{13} & C_{13} & C_{33} & 0 & 0 & 0 \\ 0 & 0 & 0 & C_{44} & 0 & 0 \\ 0 & 0 & 0 & 0 & C_{44} & 0 \\ 0 & 0 & 0 & 0 & 0 & \frac{1}{2}(C_{11} - C_{12}) \end{pmatrix} \quad \text{(equation 2.4)}$$

Calculated and experimental values of the parameters C_{ij} for InN, GaN and AlN are summarized in table 2.3.

	C_{11}	C_{12}	C_{13}	C_{33}	C_{44}	References
InN	271	124	94	200	46	[62] theory
	223	115	92	224	48	[63] theory
GaN	374	106	70	379	101	[64] exp.
	390	145	106	398	105	[65] exp.
	365	135	114	381	109	[66] exp.
	370	145	110	390	90	[67] exp.
	396	144	100	392	91	[62] theory
	367	135	103	405	95	[63] theory
AlN	411	149	99	389	125	[68] exp.
	410	140	100	390	120	[67] exp.
	398	140	127	382	96	[62] theory
	396	137	108	373	116	[63] theory

Table 2.3: Experimental and theoretical stiffness constants of InN, GaN and AlN in GPa.

During heteroepitaxy of thin films of III-nitrides on the (0001) plane, the in-plane stress is uniform ($\sigma_{11} = \sigma_{22} = \sigma$) and there is no stress along the *c* axis or shear stress (biaxial stress configuration). In this case, the Hooke law is simplified as in equation (2.5).

$$\begin{pmatrix} \sigma \\ \sigma \\ 0 \end{pmatrix} = \begin{pmatrix} C_{11} & C_{12} & C_{13} \\ C_{12} & C_{11} & C_{13} \\ C_{13} & C_{13} & C_{33} \end{pmatrix} \cdot \begin{pmatrix} \varepsilon_1 \\ \varepsilon_2 \\ \varepsilon_3 \end{pmatrix} \quad \text{(equation 2.5)}$$

Therefore, in such a situation, the strain components ε_1 and ε_2 are equal and their value is given by:

$$\varepsilon_1 = \varepsilon_2 = \varepsilon_{xx} = -(a_{epi} - a_{sub})/a_{sub} \quad \text{(equation 2.6)}$$

where a_{epi} and a_{sub} are the lattice constants of the epilayer and the substrate, respectively. The biaxial strain induces a strain ε_3 of opposite sign along the [0001] axis perpendicular to the surface given by:

$$\varepsilon_3 = \varepsilon_{zz} = -2(C_{13}/C_{33})\,\varepsilon_{xx} \qquad \text{(equation 2.7)}$$

2.1.4 Polarization effects in III-nitrides

A prominent feature among III-nitrides is the presence of strong polarization in the crystal. Since nitrogen atoms are more electronegative than metal atoms, the cation-N bonds can be considered as an electrostatic dipole. Due to the lack of symmetry of the wurtzite structure, this charge distribution is not fully compensated along the [0001] direction, which leads to spontaneous polarization $P_{sp.}$. The values of spontaneous polarization for III-nitride materials are described in table 2.4.

	GaN	AlN	InN	Ref.
P_{sp} (C/m²)	-0.029	-0.081	-0.032	[69]
P_{sp} (C/m²)	-0.032	-0.100	-0.041	[70]

Table 2.4: Calculated spontaneous polarization for wurtzite type GaN, AlN and InN.

If stress is applied to the III-nitride lattice, the lattice parameters *c* and *a* of the crystal structure will be changed to accommodate the stress. Thus, the polarization strength will be changed. This additional polarization in strained crystals is called piezoelectric polarization. The piezoelectric polarization in wurtzite III-nitrides can be calculated with the following equation:

$$\vec{P}_{PZ} = \begin{pmatrix} 0 & 0 & 0 & 0 & e_{15} & 0 \\ 0 & 0 & 0 & e_{15} & 0 & 0 \\ e_{31} & e_{31} & e_{33} & 0 & 0 & 0 \end{pmatrix} \times \begin{pmatrix} \varepsilon_{xx} \\ \varepsilon_{yy} \\ \varepsilon_{zz} \\ \varepsilon_{yz} \\ \varepsilon_{xz} \\ \varepsilon_{xy} \end{pmatrix} \qquad \text{(equation 2.8)}$$

where e_{ij} are the piezoelectric coefficient of the material and ε_j is the stress tensor. The piezoelectric polarization constants for InN, GaN and AlN are indicated in table 2.5.

	e_{33} (C/m²)	e_{31} (C/m²)	e_{15} (C/m²)
InN	0.97	-0.57	-
GaN	0.73	-0.49	-0.30
AlN	1.46	-0.60	-0.48
Ref.	[69]	[69]	[71]

Table 2.5: Calculated piezoelectric constants for InN, GaN and AlN.

2.2 Introduction to semiconductor nanostructures

The advancement in epitaxial deposition techniques allowed the fabrication of heterostructures. Figure 2.4 shows the three possibilities of alignment of bandgap minima along the growth direction depending on the band offsets, known as type I, II and III. The idea can be taken further to produce heterostructures like QWs (figure 2.5), where quantified electron levels appear as a result of the quantum confinement.

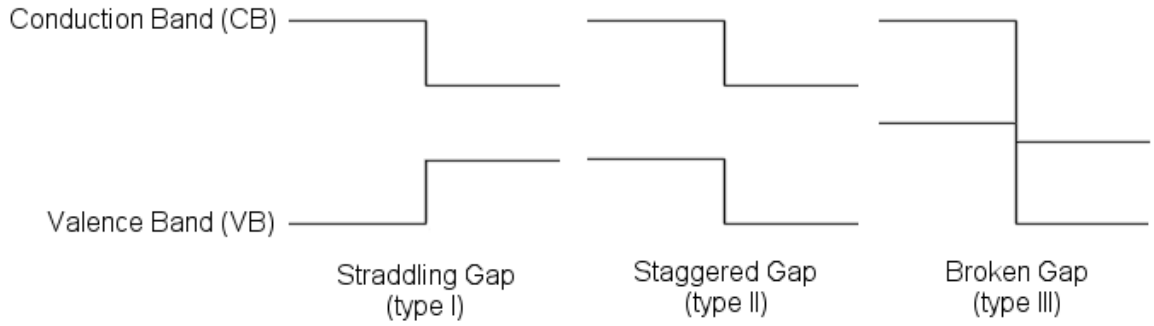

Figure 2.4: Description of the band edge profile at heterojunctions.

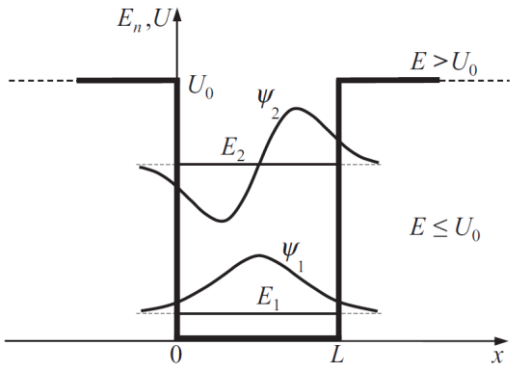

Figure 2.5: Simplified model of quantization of energy levels of a particle in a QW with finite barriers (modified from ref. [72]).

In III-nitrides, heterostructures are always type I. The conduction band offset in the GaN/AlN system is around 1.8 eV [73]. The discontinuity of the polarization vector at a heterointerface results in a fixed charge sheet at the interface, which can induce accumulation or depletion of free carriers. This fixed charge sheet generates an internal electric field in nanostructures, which is maximum for growth along the <0001> axis, where it can reach several MV/cm. In (0001)-oriented QWs, the internal electric field generates a band bending as seen in figure 2.6 (a). This leads to a spatial separation of electron and hole wave functions along the growth axis, which results in the so-called quantum confined Stark effect (QCSE). This means that the band-to-band transition is shifted to lower energy and the radiative lifetime increases due to the reduced electron-hole wave function overlap.

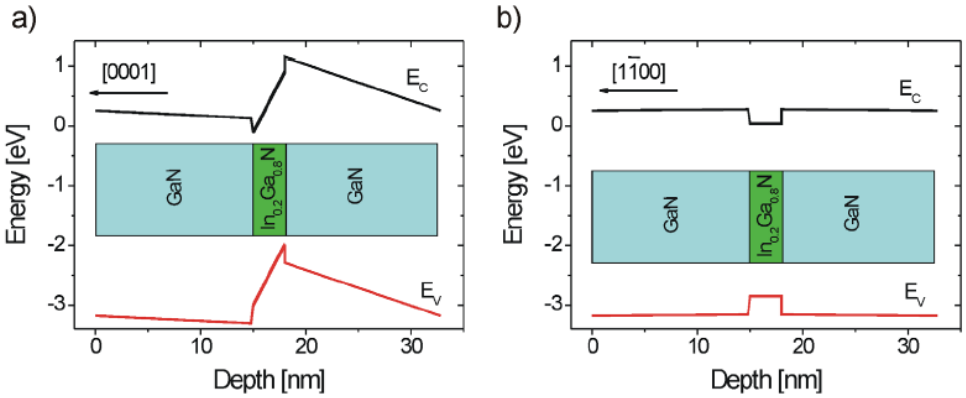

Figure 2.6: Band edge profile for an InGaN QW with GaN barrier interface in (a) *c*-plane growth (b) *m*-plane growth.

In the case of heterostructures grown on the *m*-plane or on the *a*-plane, the polarization dipoles are perpendicular to the direction of growth. Therefore, there is no polarization discontinuity at the heterostructure interfaces along the growth direction. Hence these are called non-polar orientations or non-polar directions [74]. The band structure of a QW presents a square profile, as described in figure 2.6 (b).

Various nanostructures like QWs, nanowires, or QDs have been widely studied. These are basically differentiated based on the number of dimensions in the volume of the object with nanoscale size. A detailed description of the calculation of their band structure can be found in ref. [75]. A simple description of the results is mentioned here to guide the reader to the difference between QW structures and nanowire-based QWs, which are essentially quantum dots if the nanowire radius is small enough to provide 3D confinement. Nevertheless, exact calculation of states needs the contribution of all 3 degrees of confinement even at large radius (typically 40-80 nm in our case).

The energy of an electron in a QW with confinement in *x*-direction can be written as

$$E_{2D} = E_{nx} + \frac{p_y^2 + p_z^2}{2m^*} \qquad \text{(equation 2.9)}$$

where E_{nx} is the energy of the nth level of quantized motion in the *x*-direction. The electrons in such nth state can have total energy $E_n \leq E < \infty$. This set of quantum states for the given *n* is usually called the subband of dimensional quantization.

In the case of the nanowire grown along the *z*-direction, with confinement in *x*- and *y*-direction, the energy of the electron can be written similarly as,

$$E_{1D} = E_{nx,ny} + \frac{p_z^2}{2m^*} \qquad \text{(equation 2.10)}$$

The nanowires also form similar subband quantization. The momentum dependence on the total energy of the electron is described in figure 2.7 (a, b) for 2D and 1D confinement.

In the case of a cubic quantum dot with confinement in *x*-, *y*- and *z*- directions, the total energy is a constant depending on the quantum numbers nx, ny and nz.

$$E_{0D} = E_{nx,ny,nz} \qquad \text{(equation 2.11)}$$

Note that for the case of quantum dots E_{111} is the ground state $E^{(1)}$ and $E_{112} = E_{121} = E_{211}$ is the first excited state $E^{(2)}$. The energy levels in a quantum dot are shown in figure 2.7 (c).

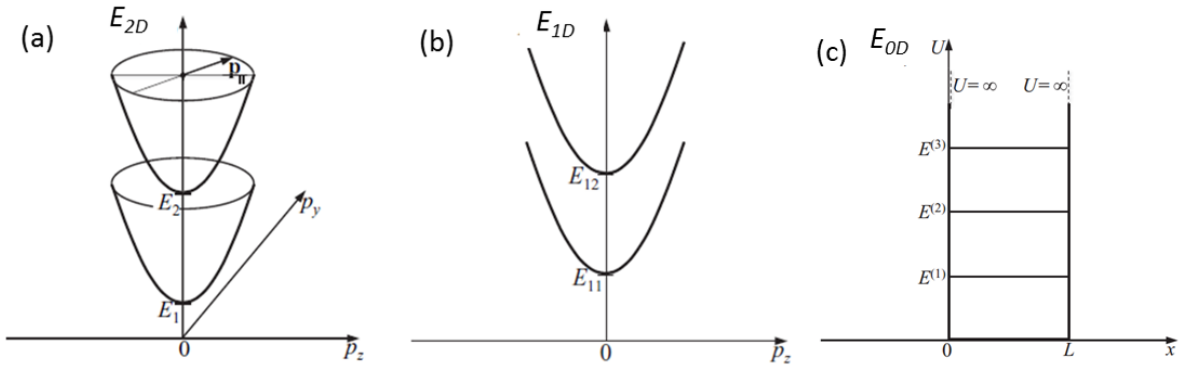

Figure 2.7: (a) Quantized energy levels, E_1 and E_2 *for* n_x =1 and 2 in a QW, and the dependences of the electron energy, E_{2D}, on the momentum. (b) Quantized energy levels, E_{11} and E_{12} *for* $n_x n_y$ =11 and 12 in a nanowire, and the dependences of the electron energy, E_{1D}, on the momentum. (c) Energy levels in a quantum dot (modified from ref. [72]).

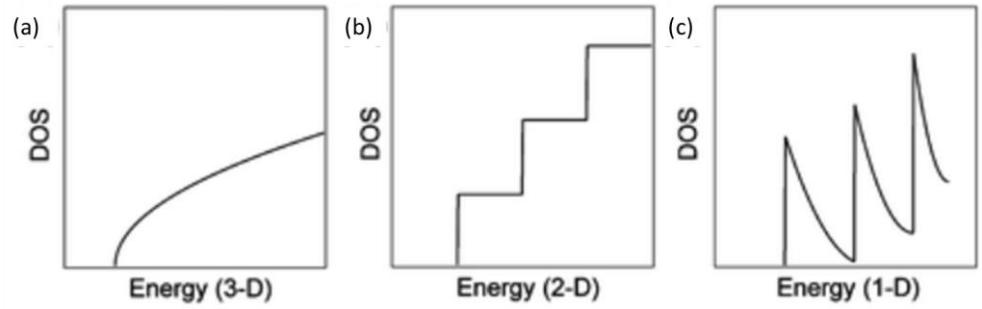

Figure 2.8: Schematic illustration of the density of states (DOS) as a function of energy for (a) a 3D material, (b) a QW (2D), (c) a nanowire (1D) (modified from ref. [76]).

Close to a band minimum, E_{min}, the electrons in a 3D semiconductor can be described as having a constant effective mass, m^*. Then the 3D density of states can be described as,

$$g_{c,3D} = \frac{dN_{3D}}{dE} = \frac{8\pi\sqrt{2}}{h^3} m^{*3/2} \sqrt{E - E_{min}} \; for \; E \geq E_{min} \qquad \text{(equation 2.12)}$$

In contrast, for a 2D semiconductor such as a QW, where the electrons are confined to a 2D plane, the 2D density of states can be described as,

$$g_{c,2D} = \frac{dN_{2D}}{dE} = \frac{4\pi m^*}{h^2} \; for \; E \geq E_{min} \qquad \text{(equation 2.13)}$$

And for a 1D semiconductor such as a nanowire, where the electrons have only 1 degree of freedom, the 1D density of states can be described as,

$$g_{c,1D} = \frac{dN_{1D}}{dE} = \sqrt{\frac{2\pi m^*}{h^2}} \frac{1}{\sqrt{E - E_{min}}} \text{ for } E \geq E_{min} \qquad \text{(equation 2.14)}$$

Finally, for a 0D semiconductor such as quantum dot with confinement in all directions, the 0D density of state can be described as

$$g_{c,0D} = 2\delta(E - E_{min}) \qquad \text{(equation 2.15)}$$

A schematic illustration of the density of states as a function of energy in the above mentioned cases is shown in figure 2.8.

2.3 ISB transitions

The terms "intersubband" (ISB) or "intraband" refer to electronic transitions between confined states in either the conduction band or the valence band of semiconductor heterostructures. Typically such transitions occur in the IR spectral range. As early as 1974, Kamgar recorded the first optical transitions between bound electronic levels [77] within the conduction band, which were associated to the surface band bending. ISB transitions between confined states within the conduction band or the valence band are possible in the engineered band structure of QWs. The first measurement of ISB absorption in GaAs QWs was performed by West and Eglash [78]. For an absorption from e_1 to e_2, the ground state and first excited state of the conduction band in a QW, it is necessary to have a large population of electrons available in e_1 (figure 2.9 (a)). For emission of light, we need to have a transition from a higher energy state to a lower energy state. This could be possible if there are at least two confined states in the QW (figure 2.9 (b)).

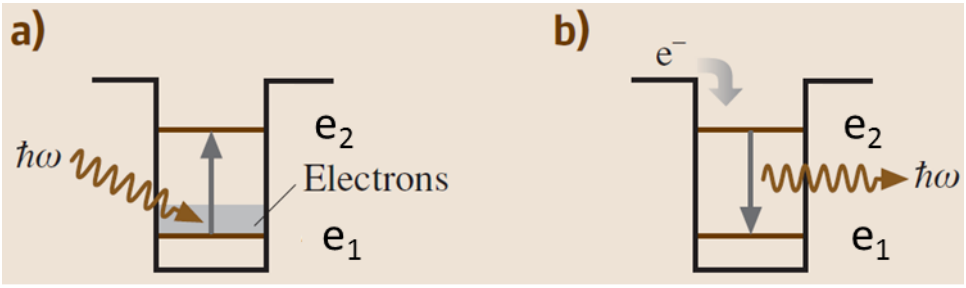

Figure 2.9: (a) ISB absorption resulting in transition from e_1 to e_2 (b) ISB emission due to electron transition from e_2 to e_1 (modified from ref. [79])

2.3.1 Review of the physics of ISB transitions in a QW

For an extensive study of the physics of ISB transitions, we refer to the work of Liu and Capasso [80]. A QW can be treated as an approximation of the particle in a box problem. This leads to solutions containing subbands. Here electronic states are confined in the *z*-direction but free in the *x-y* plane. Optical transitions happen between such subband states. The

probability of an optical transition from an initial state $|\psi_i\rangle$ at energy E_i to another state $|\psi_f\rangle$ at energy E_f is given by Fermi's golden rule:

$$W_{if} = \frac{2\pi}{\hbar}\left|\langle\psi_i|H'|\psi_f\rangle\right|^2\delta(E_f - E_i - \hbar\omega) \qquad \text{(equation 2.16)}$$

where H' is the interaction Hamiltonian, $\hbar\omega$ is the radiation energy with $\hbar$ being the reduced Planck's constant ($\frac{h}{2\pi}$). Since the radiation wavelength is much larger than lattice periodicity for ISB transitions, we can apply the dipolar approximation to explain H':

$$H' = \frac{iqF_0}{2m^*\omega}(\boldsymbol{e}.\boldsymbol{p}) \qquad \text{(equation 2.17)}$$

where q is the elementary charge, m^* is the effective mass of the electron, F_0 is the amplitude of the electric field, $\boldsymbol{e}$ is the polarization operator and $\boldsymbol{p}$ is the momentum operator. The Bloch theorem states that the total electron wave function $\psi(\boldsymbol{r},t)$ is the product of the Bloch function and the envelope wave function, where $\boldsymbol{r}$ is the position and t is the time. The Bloch function ($u(\boldsymbol{r})$) depends on the material periodicity, while the envelop function is a slowly varying plane wave ($f(\boldsymbol{r})$). The total wave function, hence takes the form

$$\psi(\boldsymbol{r},t) = u(\boldsymbol{r})f(\boldsymbol{r})e^{-iE_nt/h} \qquad \text{(equation 2.18)}$$

where E_n is the energy of the nth quantized level. Substituting 2.17 and 2.18 in equation 2.16 we obtain the transition rate as

$$W_{if} = \frac{\pi q^2 {F_0}^2}{2\hbar {m^*}^2\omega^2}|\langle u_b f_s|\boldsymbol{e}.\boldsymbol{p}|u_{b'}f_{s'}\rangle|^2\delta(E_f - E_i - \hbar\omega) \qquad \text{(equation 2.19)}$$

where *b* and *b'* are the band indices, *s* and *s'* are the subband indices of the initial and final states, respectively. Following Liu and Capasso [80], the matrix elements can be written as

$$\langle u_b f_s|\boldsymbol{e}.\boldsymbol{p}|u_{b'}f_{s'}\rangle = \boldsymbol{e}.\langle u_b|p|u_{b'}\rangle\langle f_s|f_{s'}\rangle + e.\langle u_b|u_{b'}\rangle\langle f_s|\boldsymbol{p}|f_{s'}\rangle$$

(equation 2.20)

If $b \neq b'$ then $\langle u_b|u_{b'}\rangle = 0$, leaving only the first term which corresponds to interband transitions between b and b'. If $b = b'$, then the first term vanishes leaving only the ISB terms behind. Since $\langle u_b|u_{b'}\rangle = 1$, the ISB transition can be described by the matrix element $\langle f_s|\boldsymbol{p}|f_{s'}\rangle$.

Now we separate the envelope function from the wave function as the Hamiltonian is considered time-invariant. The potential variation in the QW can be assumed to be in the *z*-direction and the wave function is assumed to be free in the x and y directions. The normalized envelop function can be written of the form,

$$f_s(r) = \frac{1}{\sqrt{A}}e^{i\boldsymbol{k}_{2d}\boldsymbol{r}}\chi_s(z) \qquad \text{(equation 2.21)}$$

where $\boldsymbol{k}_{2d}$ is the two-dimensional (2d) wave vector, $\boldsymbol{r}$ is the position vector, *A* is the area of the QW in *x*-*y* and χ_s is the component of the envelop function along z axis. Now we can use equation 2.18 to expand the ISB matrix element. $\langle f_s|\boldsymbol{e}.\boldsymbol{p}|f_{s'}\rangle$

$$\langle f_{s,\boldsymbol{k}_{2d}}|\boldsymbol{e}.\boldsymbol{p}|f_{s',\boldsymbol{k'}_{2d}}\rangle = \frac{1}{A}\int e^{-i\boldsymbol{k}_{2d}\boldsymbol{r}}\chi^*{}_s(z)[e_x p_x + e_y p_y + e_z p_z]e^{i\boldsymbol{k'}_{2d}\boldsymbol{r}}\chi_{s'}(z)d^3r$$

(equation 2.22)

The terms containing e_x and e_y vanishes unless the initial and final states are identical. Hence, the new matrix element describes ISB absorption in a one band model. It is now clear that the electric field of the radiation must have a *z* component to be absorbed as an ISB transition. This accounts for the famous polarization selection rule in ISB transitions. The dipole matrix elements describing the ISB transitions could now be written as

$$\langle s|p_z|s'\rangle = \int \chi^*{}_s(z)p_z\chi_{s'}(z)dz \qquad \text{(equation 2.23)}$$

The transition rate from equation 2.16 can be now written as,

$$W = \frac{\pi q^2 {F_0}^2}{2\hbar}\Delta|e_z|^2|\langle\chi_s|z|\chi_{s'}\rangle|^2\delta(E_f - E_i - \hbar\omega) \qquad \text{(equation 2.24)}$$

where Δ is the Kronecker delta function to account for momentum conservation. **Due to the presence of e_z, only the electric fields in z direction (direction of confinement in the QW) couple to the energy levels of QWs.** In a symmetric potential well, the wave functions are symmetric and exhibit such parity selection rules. The dipole matrix will become zero for wave functions with same parity. Due to the presence of the QCSE in polar III-nitride heterostructures, which forms a triangular asymmetric potential, the parity selection rules are relaxed.

Note that $\hbar\omega W$ is the energy absorbed per unit volume per unit time. Dividing this by the energy flux, we would obtain the absorption coefficient α.

2.3.2 Doping and many-body effects

For the characterization of the ISB absorption or the fabrication of photodetectors, *n*-doping is an important parameter as the ground state of the conduction band needs to be populated with electrons. High doping density leads to the formation of a dense electron plasma and hence the effects of electron-electron interactions have to be considered to calculate ISB transition energy and broadening. Such many-body effects can be classified as:

i) effects on the energy levels (namely the exchange interaction and direct Coulomb interaction), and
ii) effects on the transition energy (namely the depolarization shift and exciton shift).

Exchange interaction. It stems from the Pauli principle and accounts for the repulsion between electrons with parallel spin. It mainly affects the highly-populated ground state by lowering its energy, which ultimately results in a total blueshift of the ISB transition energy (and a redshift of the band-to-band transition). When the excited states can be considered unpopulated (at typical doping densities < 10^{19} cm^{-3}), the exchange interaction effect is negligible. However at high doping levels, the exchange interaction between the ground state subband and the excited state subbands must be accounted for. According to [81,82], this exchange interaction in a QW can be approximated as

$$\Delta E_{exch} \cong -\frac{q\sqrt{2\pi n_s}}{4\pi\epsilon_R\epsilon_0}\, 0.18\sqrt{\frac{2n_s}{\pi}} \qquad \text{(equation 2.25)}$$

where n_s is the 2D density of charge, q is the electron charge, ϵ_0 is the electric permittivity, ϵ_R is the dielectric constant in GaN.

Direct Coulomb interaction. It accounts for electrostatic potential resulting from the difference between the spatial distribution of the charges and the spatial distribution of the ionized donors. It is relatively weak in our case, when doping the QWs but quite large when doping the barriers. Hence, the effect of direct Coulomb interactions are not taken into account in this work.

Depolarization shift. As an external radiation excites the electron from the ground state to the excited state, the radiation interacts with the electron plasma. Each single electron feels an effective electric field that is thus different from the external electric field. The electron plasma literally screens the external electric field, resulting in a modulation of the carrier density and in the increase of the transition energy. This is also called plasmon shift [83]. The correction of the transition energy in a model with two electronic levels is described by the equation

$$E_{12}^{depol} = E_{12}\sqrt{1+\alpha} \qquad \text{(equation 2.26)}$$

where the parameter α can be estimated (according to [84]) as

$$\alpha = \frac{2q^2 n_s}{\epsilon_R\epsilon_0 E_{12}} \int_{-\infty}^{+\infty} \left[\int_{-\infty}^{z} \phi_2(z')\phi_1(z')\, dz'\right]^2 dz \qquad \text{(equation 2.27)}$$

where ϕ_i is the wave function of the state $|i\rangle$.

The exciton shift. It accounts for the Coulomb interaction between the excited electron and the quasi-hole left in the ground state [85]. The exciton shift reduces the transition energy, which can be expressed (according to [86,87]) as

$$E_{12}^{excit} = E_{12}\sqrt{1-\beta} \qquad \text{(equation 2.28)}$$

with

$$\beta = -\frac{2n_s}{E_{12}} \int_{-\infty}^{+\infty} |\phi_1(z)|^2 |\phi_2(z)|^2 dz\, \frac{\partial U_{xc}[n(z)]}{\partial n(z)} \qquad \text{(equation 2.29)}$$

where U_{xc} is the exchange-correlation potential:

$$U_{xc} = -\left(\frac{9\pi}{4}\right)^{\frac{1}{3}} \frac{2}{\pi r_s} \frac{e^2}{8\pi\epsilon_R\epsilon_0 a^*}\left[1 + \frac{B}{A} r_s \ln\left(1 + \frac{A}{r_s}\right)\right] \qquad \text{(equation 2.30)}$$

where $a^* = \frac{\epsilon_R a_B m_0}{m^*}$ is the exciton Bohr radius, $r_s = \left[\frac{4\pi}{3} a^{*3} n(z)\right]^{-1/3}$ is dimensionless and characterizes the electron gas, a_B is the Bohr radius, $A = 21$, $B = 0.7734$.

3. Methods

In this chapter, we describe the simulation methodology and experimental techniques used in this work. We start with the simulation software and techniques used to model our samples. We then introduce the epitaxial growth process using PAMBE having a real-time in-situ characterization technique namely reflection high-energy electron diffraction. We also present a summary of the different substrates used. We then make a short description of the various characterization techniques used in this work. In particular, we study the morphology and structure of our samples using x-ray diffraction, atomic force microscopy, scanning electron microscopy and transmission electron microscopy. The optical properties are assessed by photoluminescence techniques and Fourier transform IR spectroscopy.

3.1 Simulations

During this thesis, simulations of the strain distribution, band diagram, and electronic structure of various III-nitride nanostructures were performed using the nextnano^3 software [88]. It is a versatile tool allowing users to define a material system with an arbitrary geometry having specified physical parameters. The software takes into account the presence of spontaneous and piezoelectric polarization. It calculates the strain distribution in the structure by minimizing the elastic energy. It does quantum mechanical and semi-classical treatments on the system and solves the Schrödinger and Poisson equations. The detailed description of the models used for calculations is beyond the scope of this manuscript, but can be found in the PhD thesis of Stefan Birner [89] at the Technische Universität München.

The software allows the user to redefine the material parameters assigned to each binary semiconductor, as well as the bowing parameters that are applied for the second order extrapolation for ternary compounds. The set of material parameters used in this work were selected from the literature by a previous PhD student, Prem Kumar Kandaswamy, as those that provided a better description of our experimental results [33]. The values for GaN and AlN are recorded in table 3.1, and all the bowing parameters for AlGaN are set to zero for simplicity.

During this work, we used a 1D approximation for modelling planar heterostructures both in *c*-plane (section 6.1) and *m*-plane (chapter 8). We generally model 3 QW/barrier periods in the middle of the heterostructure, and impose periodic boundary conditions at the edges of the simulation region. The simulation of three QWs instead of just one is useful to detect geometrical errors in the definition of the structure and to visualize the coupling of the QWs as the extension of the electron and hole wave functions into the neighboring wells.

For nanowires, we generally used a 3D input model. For 3D calculations, all the nanowires discussed in this manuscript were defined as a hexagonal prism consisting of a long GaN section followed by a sequence of GaN/Al(Ga)N stacks and capped with GaN. The growth

axis was [000−1]. The structure was defined on a GaN substrate, to provide a reference in-plane lattice parameter. The nanowire GaN base and the AlN/Al(Ga)N heterostructures were laterally enclosed by an AlN shell and the whole structure was embedded in a rectangular prism of air, which permits elastic deformation. The effect of surface states was modelled either by introducing a 2D charge density at the air/nanowire interface of value $\sigma = -2\times10^{12}$ cm^{-2} (which is a lower estimation for a chemically clean GaN m-surface according to ref. [90]) or by pinning the Fermi level 0.6 eV below the conduction band edge at the m-plane GaN/air interfaces [91,92], and 2.1 eV below the conduction band edge at the m-plane AlN/air interfaces [93].

In a first stage, the 3D strain distribution is calculated by minimization of the elastic energy assuming zero stress at the nanowire surface. Then, for the calculation of the band profiles, the piezoelectric fields resulting from the strain distribution are taken into account. nextnano^3 calculates the band structure using the 8×8 **k.p** model. This model overcomes the limitations of the effective-mass approximation, where the assumption of parabolic bands leads to major deviations in the calculation of ISB transition energies, reported upto 25% [73]. Then the Poisson and Schrödinger equations are solved self-consistently.

Parameters (units)	**[ref.]**		**GaN**	**AlN**
Lattice constants (nm)	[94]	*a*	0.3189	0.3112
		c	0.5185	0.4982
Spontaneous polarization (C.m^{-2})	[95]		-0.029	-0.081
Piezoelectric constants (C.m^{-2})	[95]	e_{13}	-0.49	-0.60
		e_{33}	0.73	1.46
Elastic constants (GPa)	[96,97]	C_{11}	390	396
		C_{12}	145	140
		C_{13}	106	108
		C_{33}	398	373
Dielectric constants	[98]		10	8.5
Luttinger parameters	[99]	A_1	-5.947	-3.991
		A_2	-0.528	-0.311
		A_3	5.414	3.671
		A_4	-2.512	-1.147
		A_5	-2.510	-1.329
		A_6	-3.202	-1.952
		A_7	0	0
		$E_P^{\parallel}$ (eV)	14	17.3
		$E_P^{\perp}$ (eV)	14	16.3
Deformation potentials (eV)	[98]	a_{c1}	-4.6	-4.5
		a_{c2}	-4.6	-4.5
		D_1	-1.70	-2.89
		D_2	6.30	4.89
		D_3	8.00	7.78
		D_4	-4.00	-3.89
		D_5	-4.00	-3.34
		D_6	-5.66	-3.94

Band offset (eV)	[73]	1.8

Table 3.1: Material parameters used in nextnano^3.

nextnano^3 does not completely incorporate many-body effects. It only takes into account the screening of the internal electric fields for increasing dopant densities. In order to estimate the correct ISB transitions, we first calculate ISB transitions in low doped structures using 1D simulations with nextnano^3. We then numerically estimate the shift introduced by many-body effects namely depolarization shifts and exchange interactions.

The magnitude of the exchange interaction ΔE_{exch} was calculated using equation 2.25 with $\epsilon_R = 10$ as the dielectric constant in GaN [100]. The shift of the ISB energy induced by depolarization was calculated using equations 2.26 and 2.27 with the electron wave functions obtained from nextnano^3 simulations of the structures with low doping levels. Note that the complexity of the problem does not allow 3D calculations of the many-body effects. Hence all related calculations are studied in 1D in this manuscript.

3.2 Epitaxial growth

Epitaxy at its simplest definition refers to the deposition or growth of a crystalline overlayer (called epitaxial film/layer) over a crystalline substrate, where the orientation of the epitaxial layer is influenced by the substrate. Its etymological origin from Greek can be translated as “arranged upon”. The epitaxy is defined as homoepitaxy if the substrate and the epitaxial layer are essentially the same material. It is defined as heteroepitaxy if they are different.

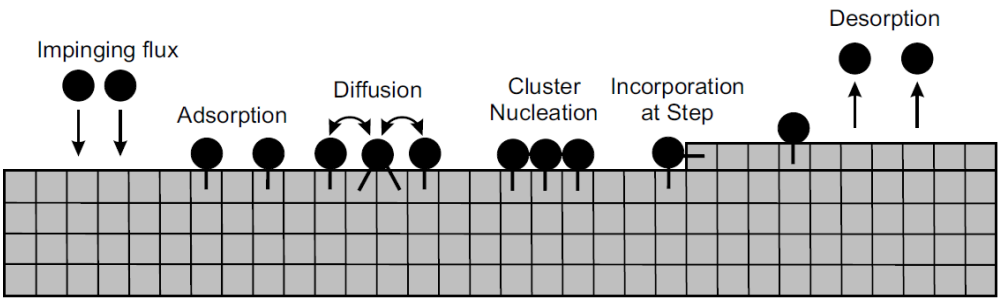

Figure 3.1: Atomistic processes that can occur at the surface during the epitaxy (after ref. [101]).

The process of growth also depends on the thermodynamic properties of the surface of epitaxy and kinetic parameters of the adatoms such as diffusion length and adsorption lifetime. The various atomistic processes that can occur on a growing surface are described in figure 3.1, namely adsorption, nucleation, diffusion, desorption, step incorporation etc. The resulting growth modes are described in figure 3.2, including

(a) Multi-layer growth: When the adatom diffusion length is short, it results in the nucleation of multi-layer-thick clusters, ultimately forming a rough surface.

(b, c) Layer-by-layer growth: When the diffusion length is longer, the increased diffusion length results in the nucleation of monolayer (ML) clusters, with the atomic layers completed one by one.

(d) Step-flow growth: When diffusion length is even longer, the longer diffusion length gives the adatoms enough mobility to reach the step edges, which are often energetically favorable incorporation sites.

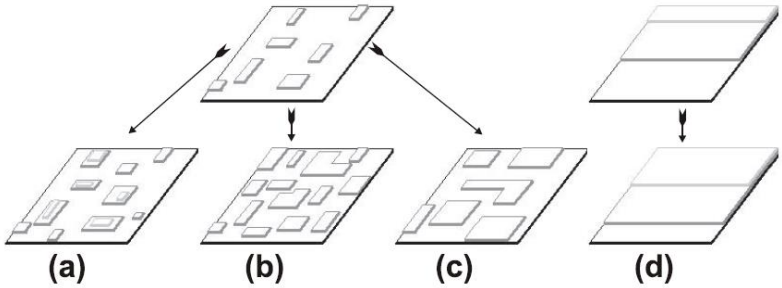

Figure 3.2: Growth modes as a function of the adatom diffusion length: (a) multi-layer growth, (b) and (c) layer-by-layer growth, (d) step-flow growth (after ref. [101]).

In the case of heteroepitaxy the atomistic processes described in figure 3.1 still hold, however the epitaxy is also largely influenced by other factors such as the lattice mismatch of the two materials, surface free energy, and dislocations formation energy. This results in the growth modes described in figure 3.3, which are:

a) Volmer-Weber: For materials with a large lattice mismatch, the material tries to keep much of the surface uncovered without wetting.
b) Franck van der Merwe: It is 2D growth. The misfit strain during the growth can be released by the formation of dislocations.
c) Stranski-Krastanov: The material initially wets the surface, but eventually forms 3D islands over the 2D wetting layer after a critical height.

Figure 3.3: Various heteroepitaxy growth modes: (a) Volmer-Weber (b) Franck van der Merwe (c) Stranski-Krastanov.

3.2.2 Plasma-assisted molecular beam epitaxy

Molecular beam epitaxy (MBE) was invented in the late 1960s at the Bell Telephone Laboratories by A. Y. Cho and J. R. Arthur [102]. During the growth, constituent adatoms or molecules to be deposited are thermally evaporated or sublimated from effusion cells that contain Knudsen-type crucibles. MBE requires high vacuum or ultra-high vacuum (UHV) (10^{-8}–10^{-12} mbar) to ensure the beam nature of the evaporated materials and prevent their

scattering in their path towards the substrate. The vacuum also ensures that the contamination of the growth surface remains as low as possible.

A functional schematics of the MBE used in this study is displayed in figure 3.4. All samples in this work were grown using this technique. Active nitrogen free radicals are obtained by cracking high-purity molecular nitrogen (6N5) with a radio frequency plasma source. This technique is known as **plasma-assisted MBE** (PAMBE) to differentiate between other sources of nitrogen like ammonia-based sources. Our MBE system was equipped with an automatic N plasma source HD25 supplied by Oxford Applied Research. The output power was varied to modify the flux of active nitrogen.

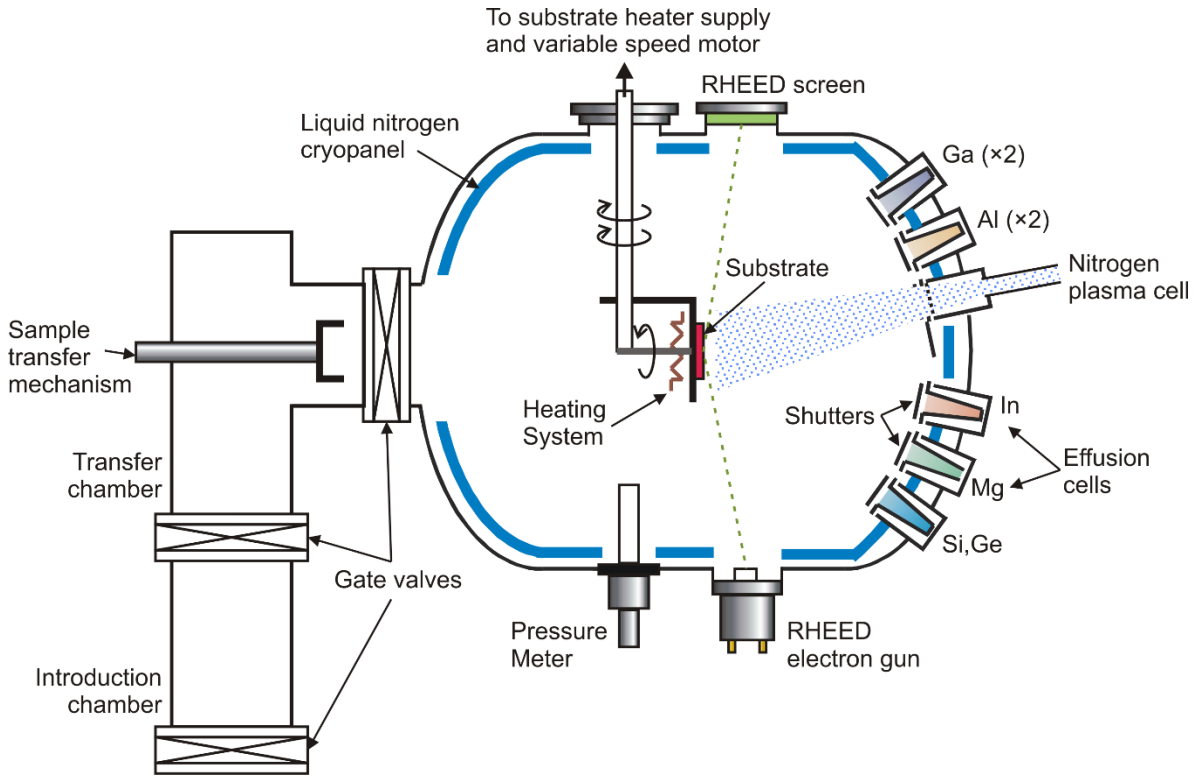

Figure 3.4: Schematics of the PAMBE used in this study (modified from ref. [101]).

The scheme also displays the various effusion cells used, including Ga, Al, Si and Ge. Accurate regulation of the cell temperatures is achieved through proportional-integral-derivative controllers. A mechanical shutter in front of each cell is used to interrupt the atom beam. The Knudsen-type crucibles are made of pyrolytic boron nitride.

The substrate is glued or fixed onto a molybdenum sample holder (molyblock). The molyblock is fixed on an axis manipulator which allows to automatically rotate and heat the substrate. The entire section with cells and substrate, where the growth happens is called the growth chamber, which is cooled down with liquid nitrogen to get a base pressure in the 10^{-11} mbar range. The molyblock is loaded into the growth chamber through a load lock system consisting of an introduction chamber (base pressure in the 10^{-9} mbar range) and transfer

chamber (base pressure in the 10^{-10} mbar range). The introduction chamber is opened under nitrogen flux to exchange the molyblock.

The rather low growth temperature in MBE (compared to hydride vapour phase epitaxy (HVPE) or metal organic vapour phase epitaxy (MOVPE)) and relatively low growth rate (less than 1 ML/s) results in a good control over layer thickness and reduced inter-diffusion effects. This leads to excellent interface and surface morphology, from which we profit to grow our heterostructures. The UHV environment in the MBE also offers the possibility to have in-situ control of the growth, with techniques like reflection high-energy electron diffraction (RHEED) and quadrupole mass spectrometry.

3.2.3 Reflection high-energy electron diffraction

Reflection high-energy electron diffraction (RHEED) is an in-situ and real-time characterization technique to study the morphology and crystal structure of the growing surface. Electrons are emitted from a hot filament, which is excited by a 1.5 A current, and accelerated under high-voltage of 32 kV (values from our setup). The electron beam strikes the sample at a grazing angle, and the diffracted beam then impinges on a fluorescent phosphor screen mounted in the direction opposite to the electron gun.

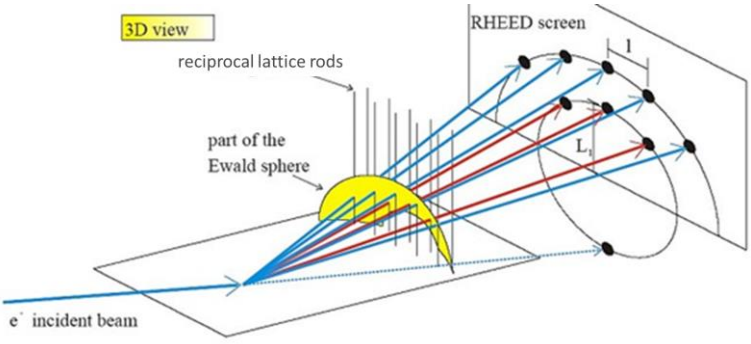

Figure 3.5: Working principle of RHEED used in this study.

A schematic description of the RHEED measurement principle is shown in figure 3.5. The obtained image displayed on the screen is the Fourier transform of the lattice interacting with the beam. It corresponds to the intersection of the reciprocal lattice with the Ewald Sphere of radius $k_i = (2\pi)/\lambda$ where λ is the wavelength of the electron. In an atomically smooth and single crystalline sample the crystal lattice would actually correspond to perpendicular rods as shown. That would lead to spots, but due to the Ewald sphere being larger, instrumental divergence and crystal imperfections a streaky pattern is usually observed. Analysing the pattern one can obtain, the 2D or 3D nature of the growth front and a qualitative estimation of the crystal quality.

By studying the RHEED intensity we can measure the growth rate under layer-by-layer growth conditions. The time-dependent change in the density of atoms at the growth front during the growth process results in an oscillatory variation of the RHEED intensity with time. If we consider a flat surface, the coverage of atoms on the surface is defined as θ. When the layer is complete, the coverage can be minimum (n^{th} layer, θ is 0) or maximum ($n+1^{th}$ layer, θ is 1) leading to a smooth surface. In both the cases the RHEED intensity is maximum. Starting with a minimum coverage of θ = 0, we can describe the procedure to determine the growth rate, as illustrated in figure 3.6. For intermediate coverage, the intensity decreases with increase in coverage upto θ = 0.5. Here the roughness is maximum and the intensity is at its lowest. Further growth would increase the coverage but decrease the roughness as shown in figure 3.6. At θ = 0.75, the intensity recovers as the roughness is reduced as the growth front picks up more adatoms. The surface flattens at θ = 1, reaching again a maximum RHEED intensity and the process continues in a cyclic manner as the growth continues. A single RHEED intensity oscillation period corresponds to the growth of a single layer. During the operation of our PAMBE system, the calibration of the growth rate and the control of the alloy composition and thickness of the 2D layers were done observing such RHEED oscillatory behavior.

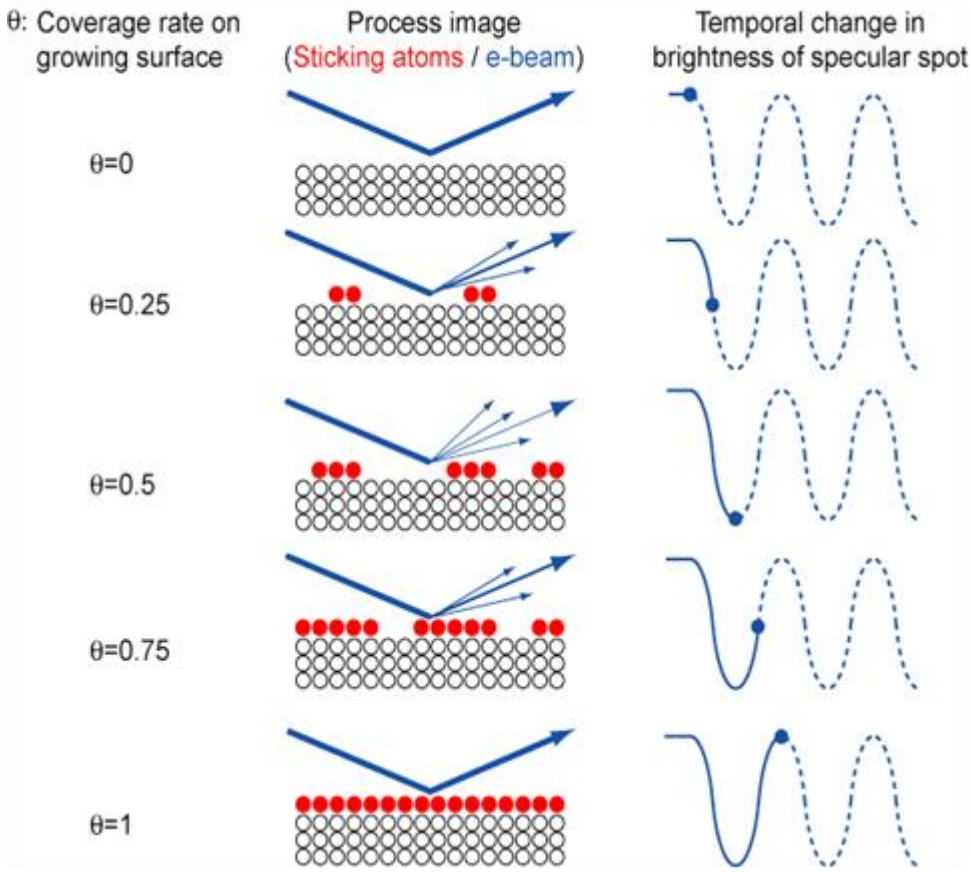

Figure 3.6: Schematic description of the procedure to determine the growth rate from the variation of the RHEED intensity (modified from ref. [103]).

3.2.4 Growth of polar GaN, AlN and AlGaN

At the beginning of my PhD thesis, the PAMBE growth of 2D GaN structures was well developed, in particular for the *c*-plane growth front [104–106]. A well accepted model for explaining the GaN layer formation occurring during growth [107] is displayed as a schematic representation in figure 3.7. The impinging atomic nitrogen adheres to the growing surface and this is called adsorption. The impinging Ga atoms are also adsorbed but in a weakly bound physisorbed state. It could easily be desorbed from this surface. Some of the Ga adatoms can be moved from this state to a chemisorbed state through the formations of new chemical bonds at the surface. The reverse process can also occur: chemisorbed Ga atoms can be transferred back to a physisorbed state. In the chemisorbed state, when the Ga atom meets a N atom, a GaN layer is formed.

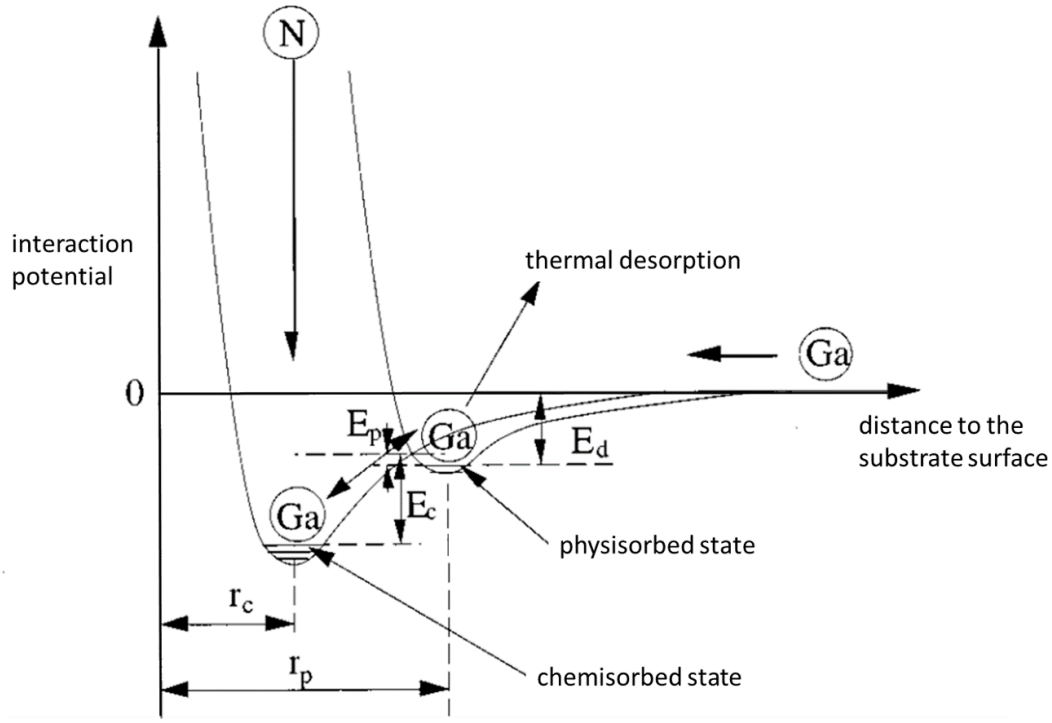

Figure 3.7: Schematic representation of the process occurring during a GaN layer growth (modified from ref. [108]).

The deposition of 2D GaN layers is performed under slight-Ga rich conditions. However, an excessive Ga flux would lead to the formation of metal droplets on the surface, which degrades the surface morphology. In order to obtain smooth GaN layers, the growth was shown to proceed with a Ga bilayer at the growth front as illustrated in figure 3.8. This slightly excess Ga adlayer minimizes the (0001) surface energy and delays potential plastic and elastic relaxations and hence allows obtaining smooth 2D GaN layer growth [106,109].

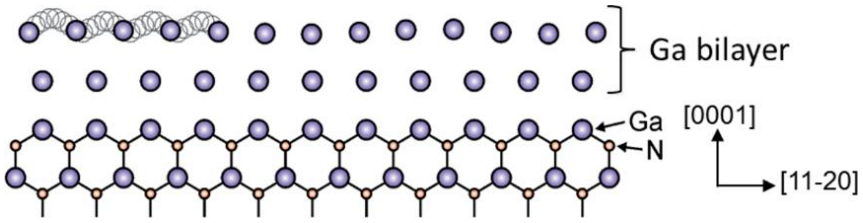

Figure 3.8: Schematic representation of the laterally-contracted Ga bilayer model (modified from ref. [110]). The first Ga layer is aligned with the underlying substrate while the second layer is liquid.

To obtain such a bilayer, it is important to notice the correlation between the Ga flux and the Ga coverage on the c-plane surface at a fixed substrate temperature [104]. The amount of Ga adsorbed on the surface can be quantified using RHEED by looking at the desorption transients. The GaN surface is first exposed for a few seconds to a Ga and N flux simultaneously. Then both fluxes are stopped (shuttering the effusion cells) and the RHEED intensity is recorded during the Ga desorption from this GaN surface. The experiment is repeated for a constant temperature (780°C) a fixed N flux (0.28 ML/s) and different Ga fluxes. Four regimes can be identified, as shown in figure 3.9:

- Regime A: GaN growth rate $\Phi < 0.3$ ML/s. A small quantity of Ga is present.
- Regime B: 0.3 ML/s $< \Phi < 0.5$ ML/s. Less than 1 ML of Ga at the growth front.
- Regime C: 0.5 ML/s $< \Phi < 1$ ML/s. A bilayer of Ga (≈2.4 ML) at the growth front.
- Regime D: Ga flux > 1 ML/s. The Ga accumulation regime (much Ga excess), leading to the formation of metal droplets.

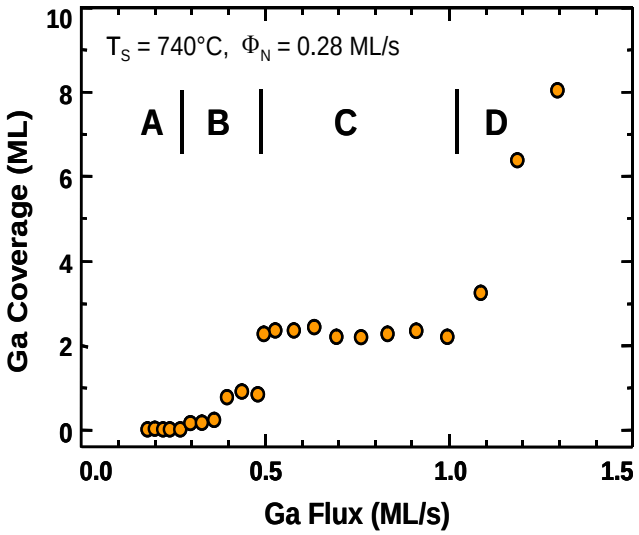

Figure 3.9: Ga coverage on top of the GaN(0001) surface as a function of the Ga flux (modified from ref. [111]).

Similarly, the Ga coverage as a function of Ga flux over various substrate temperatures was also studied, as illustrated in figure 3.10. The AFM images shown in figure 3.10 also show that the bilayer growth process results in smooth GaN layers; corresponding to the regime C.

In the case of 2D growth of smooth *c*-plane AlN layers, we also require metal-rich conditions. However, Al cannot be desorbed at the standard GaN growth temperatures (substrate temperature ≈700°C) and hence a growth interruption under N flux is needed to remove any accumulated Al. Smooth AlN can also be deposited under stoichiometric growth conditions with excess of Ga on the growing interface in order to minimize the surface energy. The Ga – N bond is weaker than the Al – N bond and hence Al is preferentially incorporated.

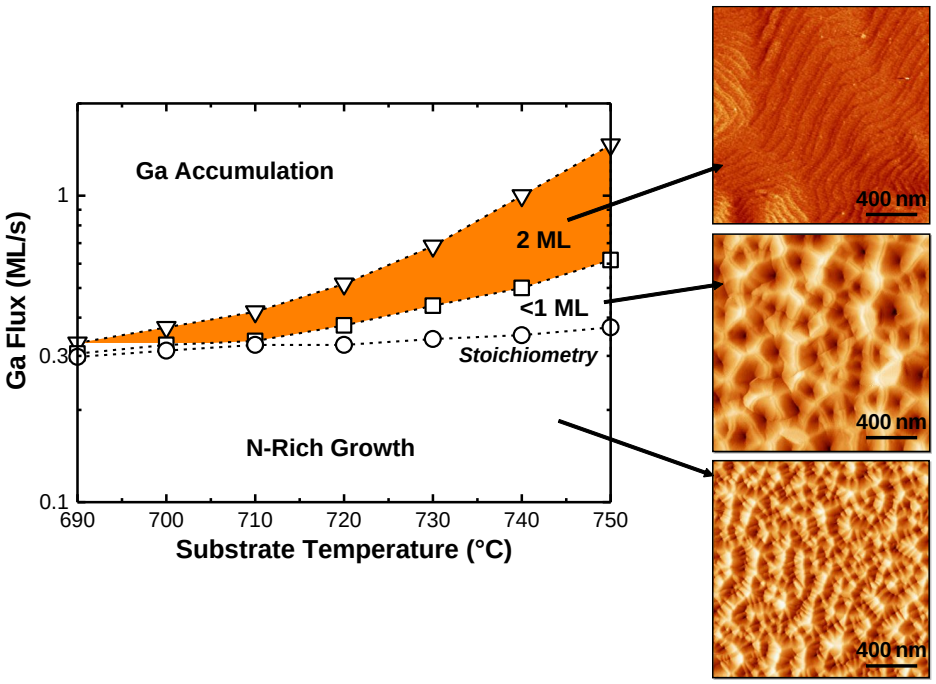

Figure 3.10: Ga coverage regimes as a function of both substrate temperature and impinging Ga flux. Insets show AFM images obtained in the different growth regimes. z-scales are 5nm, 150 nm and 100 nm (top to bottom) (modified from ref. [112]).

To grow smooth 2D *c*-plane AlGaN layers, we require similar Ga-rich conditions [113,114]. All the Al atoms impinging on the surface should adsorb onto the surface (sticking coefficient =1). We fixed the Al/N ratio at the required Al content and Ga is used in excess, just as it is used in GaN 2D layers. But for Al contents > 40%, we have to decrease the substrate temperature to maintain a 2D growth. Reducing the growth temperature also allows balancing the different diffusion barriers of Al, Ga and N.

3.2.5 Growth of nanowires

The growth of semiconductor nanowires in a controllable fashion has been challenging, yet many methodologies and techniques are being investigated. In general, all the growth or fabrication approaches can be classified as “bottom-up” or “top-down”. As the name suggests, a top-down approach focuses on simply carving out a structure from a large piece of material by means of various lithographic techniques and etching methods etc. On the contrary, the bottom-up approach constructs nanowires by simply combining constituent adatoms.

In this work, we deal with bottom-up nanowires unless explicitly mentioned otherwise. The bottom-up approach itself has many subtypes: catalyst-assisted growth, self-catalyzed growth, catalyst free growth, oxide-assisted growth, selective area growth and template-assisted growth. The catalyst-free growth technique utilized here has the advantage of not having to use any foreign material or impurity, hence producing nanowires of high quality from the chemical point of view. Regarding the growth mechanism, one widely accepted explanation is worth discussing, called the diffusion model, first postulated by Sears [115] and further developed by others [116,117]. The axial growth rate V can be given by,

$$V = \frac{dL}{dt} = \Phi_i + \frac{2\Phi_i \lambda_s}{r} tanh \frac{L}{\lambda_s} \qquad \text{(equation 3.1)}$$

where L is the wire length, r is the wire radius, Φ_i is the impinging atom flux, $\lambda_s$is the diffusion length of the adatoms. The first term describes the growth by direct impingement of atoms and the second term describes the diffusion on the substrate and side facets. Note that the model takes into account only one atomic species and does not take into account factors like the sticking coefficient or the decomposition rate.

Such catalyst free, self-assembled nanowires of GaN have already been demonstrated in PAMBE, and when grown, they generally occur as a forest of highly dense nanowires [118–122]. Various crystalline and amorphous substrates have been attempted, and in our study we will focus on the widely studied Si (111). Growth of such nanowires proceeds via a more nitrogen-rich environment than that required for planar growth. Figure 3.11 illustrates a growth diagram for various Ga impinging fluxes and substrate temperatures. The dotted line indicates the N flux, which is kept constant. The “no growth” regime is dominated by thermal decomposition and desorption of Ga from the surface. The regime (b) is where nanowire nucleation and growth occurs which is indeed a narrow window. Within such a narrow window, the growth of nanowires, in terms of the size of the nanowire, degree of coalescence, speed of the growth, have to be optimized to grow nanowires according to the design requirement. At lower temperature and higher Ga fluxes (regime (a)), the growth becomes highly planar with heavily coalesced nanowires at the boundary of the two regimes. The scanning electron microscopy (SEM) images in figure 3.10 are representatives of the regimes.

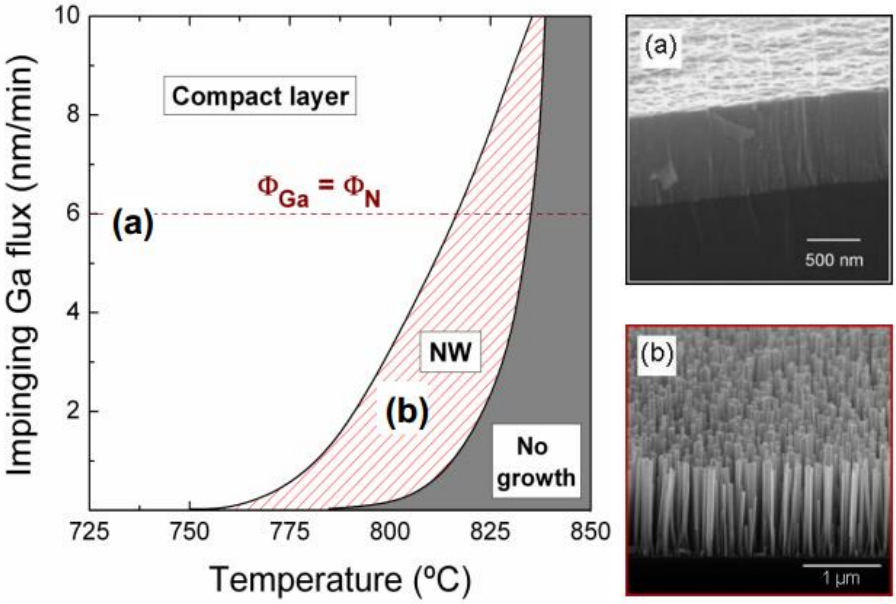

Figure 3.11: Nanowire growth window with substrate temperature and Ga flux (after ref. [123]).

The nanowires hence grown with PAMBE on Si (111) have been found to have the wurtzite crystal structure with N-polarity in the nanowire growth direction [124]. Knowing the polarity of nanowires is important, just like in the case of planar layers, since it influences various physiochemical properties, like incorporation of dopants, polarization fields and formation of defects [95,125]. Furthermore, it determines the direction of the polarization-related internal electric field when heterostructures are implemented within the nanowire.

3.2.6 Substrates

For the experiments described in this thesis, we used various substrates, which we classify here as sapphire-based, silicon-based and GaN-based substrates due to their different IR transmission properties.

Sapphire-based substrates. Sapphire-based templates are transparent in the SWIR but have a cut-off at ≈ 6 µm, as shown in figure 3.12. In this work, planar samples for SWIR studies were grown on AlN-on-sapphire templates. These templates were deposited by MOVPE at Dowa Electronics Materials Co., Ltd. They consist of 1.0±0.1 µm-thick AlN(0001) on *c*-plane sapphire. The FWHM of the ω-scan measured by x-ray diffraction around the (0002) reflection is smaller than 150 arcsec, and the dislocation density is ≈ 10^9 cm^{-2}.

Silicon-based substrates. To ensure transparency in the IR spectral range, we used floating-zone Si(111) substrates with a thickness of 500±25 µm and a resistivity >20 kΩ/cm. The substrates were provided by BT Electronics. In this work we used these substrates for growing the nanowire samples.

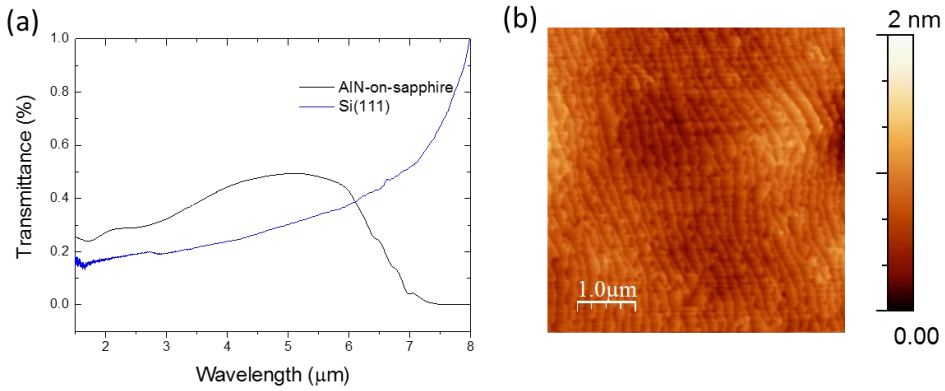

Figure 3.12: (a) Transmittance spectra of Al-on-sapphire and Si(111) substrate measured by Fourier transform IR spectroscopy and (b) AFM image of the AlN-on-sapphire substrate used in this study.

GaN-based substrates. These substrates were free-standing, semi-insulating (s.i.), Fe-doped *m*-GaN platelets sliced from (0001)-oriented GaN boules synthesized by HVPE (resistivity > 10^6 Ωcm, dislocation density < 5×10^6 cm^{-2}) by Nanowin (Suzhou Nanowin Science and Technology Co. Ltd). We use s.i. substrates instead of non-intentionally doped (n.i.d.) GaN (*n*-type) due to their transparency in the FIR range. The transmission spectra of the substrates are shown in figure 3.13 (a) compared with n.i.d. substrates. AFM images of the *m*-plane substrates are shown in figure 3.13 (b), with root mean square (rms) surface roughness of 0.18 nm, respectively.

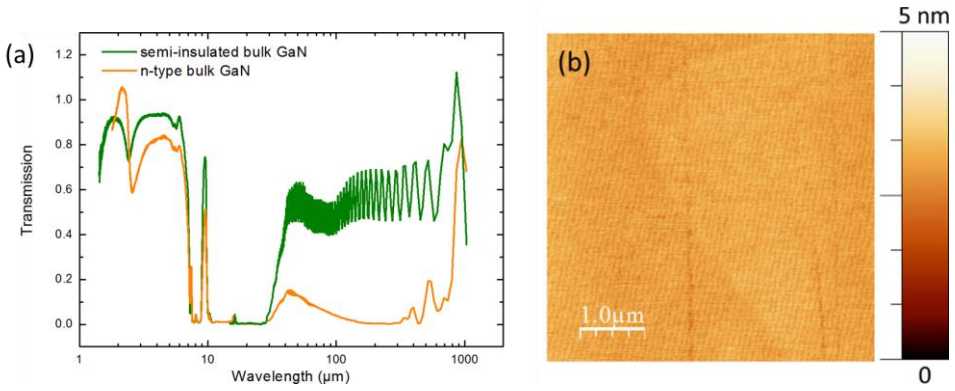

Figure 3.13: (a) Transmission spectra of semi-insulated and *n*-type n.i.d free-standing GaN substrates. (b) Typical AFM images of the *m*-plane free-standing substrates used in this work.

3.3 Characterization

In this section, all the characterization techniques that I have used for the thesis are described. Those techniques where I have not performed the characterization but only the data analysis (e.g. high angle annular dark field scanning transmission electron microscopy (HAADF STEM)) are also mentioned for clarity.

3.3.1 Atomic force microscopy

Atomic Force Microscopy (AFM) is a characterization technique that allows us to examine the surface morphology of the samples. We used a Veeco Dimension 3100 system for all the samples studied with AFM in this manuscript and the images were processed using WSXM free software.

AFM belongs to the class of scanning probe microscopies (SPM), where a physical probe is used to scan the surface of the sample. The schematics of a typical AFM setup is described in figure 3.14. The probe of the AFM is a sharp tip on the end of a cantilever arrangement. It is usually made of silicon nitride or silicon. In contact mode, the tip is made to scan across the sample in all three directions by using piezoelectric actuators. A laser beam reflected from the top of the cantilever is analyzed with a set of photo detectors.

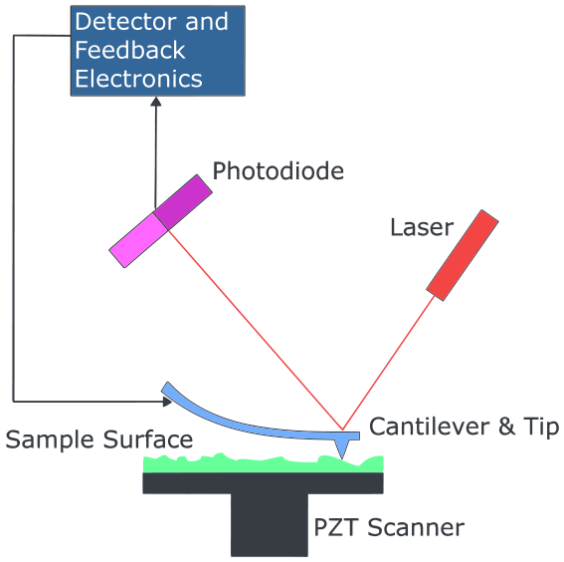

Figure 3.14: Schematic diagram of a typical AFM setup.

When the tip is brought close to the sample, the tip experiences various kinds of forces like electrostatic, capillary, van der Waals etc. The forces can be attractive and repulsive. The nature of the forces and tip sample distance can be understood from figure 3.15. Variations in the tip-sample distance change the force between them. This causes deflections in the cantilever and hence in the laser spot on the photo detectors. In short, the deflection in the laser spot is a function of the change in tip-sample distance.

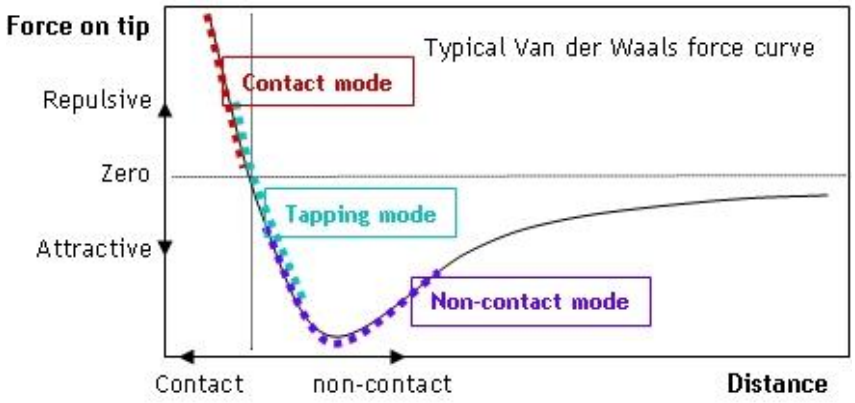

Figure 3.15: Variation of force with tip-sample distance (modified from ref. [126]).

In non-contact mode, the cantilever is kept a few tens or hundreds of angstroms away from the sample. The tip is made to oscillate at a large amplitude and frequency near or at the resonant frequency. The changes in the amplitude of the oscillation give information about the topography of the sample. The tapping mode is a combination of both the contact and non-contact mode. In this mode, the probe is made to oscillate at the resonant frequency or near resonant frequency. As the tip is brought closer to the sample, the interaction between the tip and the sample causes the frequency to change. The feedback system is employed to maintain the frequency constant working in a similar way to that of the contact mode. For our studies I used the AFM in the tapping mode.

3.3.2 X-ray diffraction

We used X-ray diffraction (XRD) to characterize the period of our MQWs in 2D layers and nanowires, to estimate the strain state of the layers, as well as to assess the crystalline quality of our samples from the broadening of the reflections. As x-ray excitation, we used the $k_{\alpha 1}$ emission line of Cu ($\lambda_{XRD} = 0.154056$ nm). In this work, we measured ω-2θ scans, ω-scans and reciprocal space maps.

Primarily we used two XRD systems:

a) PANalytical X'Pert PRO MRD system (samples of sections 4.1), operated in collaboration with J. Schörmann (Justus-Liebig-Universität Giessen, Germany), and
b) Rigaku Smartlab x-ray diffractometer (CEA-INAC, Grenoble).

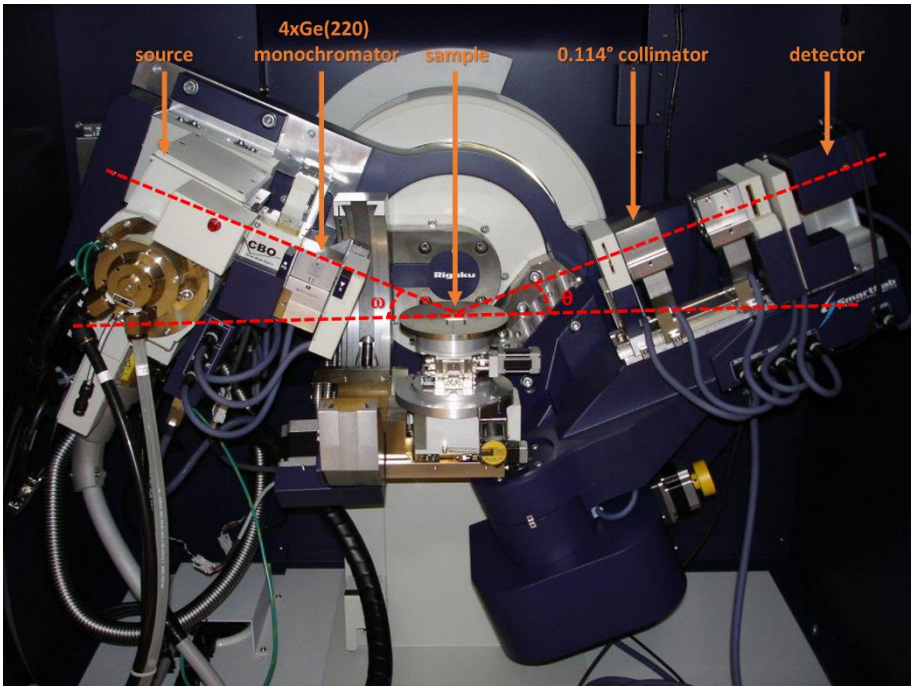

Figure 3.16: The Rigaku Smartlab system in the used configuration.

The Rigaku Smartlab system which I used, is explained further (figure 3.16). The x-ray source is an evacuated tube in which electrons are emitted from a heated tungsten filament and accelerated by an electric potential (≈40 kV) to finally impinge on a Cu target. The x-ray beam coming out from the source is reflected and converted into a parallel beam by a parabolic mirror. A beam of parallel (0.01° divergence) and monochromatic x-rays is incident on a crystal at the angle ω_i, which is the angle between the sample plane and the incident beam. A highly parallel and monochromatic incident x-ray beam is achieved by using one or two monochromators each consisting of two Ge (220) monocrystals. This results in an x-ray beam with a wavelength spread $\Delta\lambda_{XRD}/\lambda_{XRD} = 2.2 \times 10^{-5}$ and divergence, $\Delta\Theta = 0.0033°$.

The sample is placed on a monocrystalline Si plate to minimize the background noise. However, the sample surface may not correspond to the epitaxial planes due to the substrate miscut and hence we need to align the epitaxial plane with the optical axis of the setup by using possible angular rotation mechanisms of the sample stage and detectors available in the instrument.

To obtain high-resolution XRD (HR-XRD), a 0.114° collimator or a Ge(220)x2 analyzer is placed between the sample and the detector. It improves the angular precision of the diffracted beam (<0.001°) and is used to measure all the planar samples. In this configuration, the direct beam intensity is higher than 10^6 counts per second (cps) and the noise is about 1 cps. However for the nanowires, measurements were made with an open detector configuration; which means that the detectors were directly exposed. This was done because of the scattering induced by the nanowires leading to broadening of the beams, leaving the high resolution redundant.

The MQW period P_{MQW} can be extracted from the angular separation of two MQW satellites in the ω-2θ scans:

$$P_{MQW} = \frac{\pm n\lambda_{XRD}}{2(\sin\theta_{\pm n} - \sin\theta_0)} \qquad \text{(equation 3.2)}$$

where θ_0 and $\theta_{\pm n}$ are the zero-order and ±n-order MQW satellites. Information on the mosaicity and crystalline quality of planar structures were extracted from the ω-scans (also called "rocking curves"), measured at a fixed value of θ. Finally, evaluation of the strain state of the layers required a combination of ω-2θ scans of symmetric reflections and reciprocal space maps of asymmetric reflections, to extract the various lattice parameters using Bragg's law.

3.3.3 Photoluminescence

Photoluminescence (PL) is the light emission that occurs in a material due to absorption of photons. We have used this characterization technique for our samples to study band-to-band transitions. Furthermore, the technique also lets us assess the elemental composition, the presence of impurities and the material quality. PL has been found to be very sensitive to defects [127].

In a typical PL setup the sample is illuminated by a laser light having energy higher than that of the bandgap. Using this energy, electrons are excited from the valence band to the conduction band. This generates electron-hole pairs. The electron hole pair can recombine through a radiative process, non-radiative process or a combination of the two. For PL studies, only radiative recombinations are directly detected. The figure 3.17 shows the possible radiative recombination paths. For each path, depending on the energy level difference between the electron and hole, the photon emitted (or observed) will have a different energy.

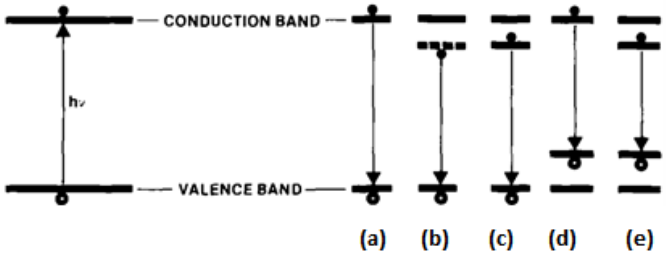

Figure 3.17: Radiative recombination mechanisms occur between (a) free electron-free hole (b) excitonic recombination (c) donor electron-free hole (d) free electron-hole acceptor level (e) donor electron-acceptor hole (modified from ref. [128]).

As represented in figure 3.17, the electron-hole pair can have a band-to-band recombination (a), which is rare at low temperatures, where the most common type of recombination is excitonic recombination (b), where the emission energy is reduced by the

the exciton binding energy. Such excitons can be free or bound to a donor or acceptor, which modify their energy. It is also possible to have recombination between an electron in a donor level and a free hole (c), a free electron and a hole in an acceptor level (d), or an electron in a donor level and a hole in an acceptor level, also called donor-acceptor recombination (e).

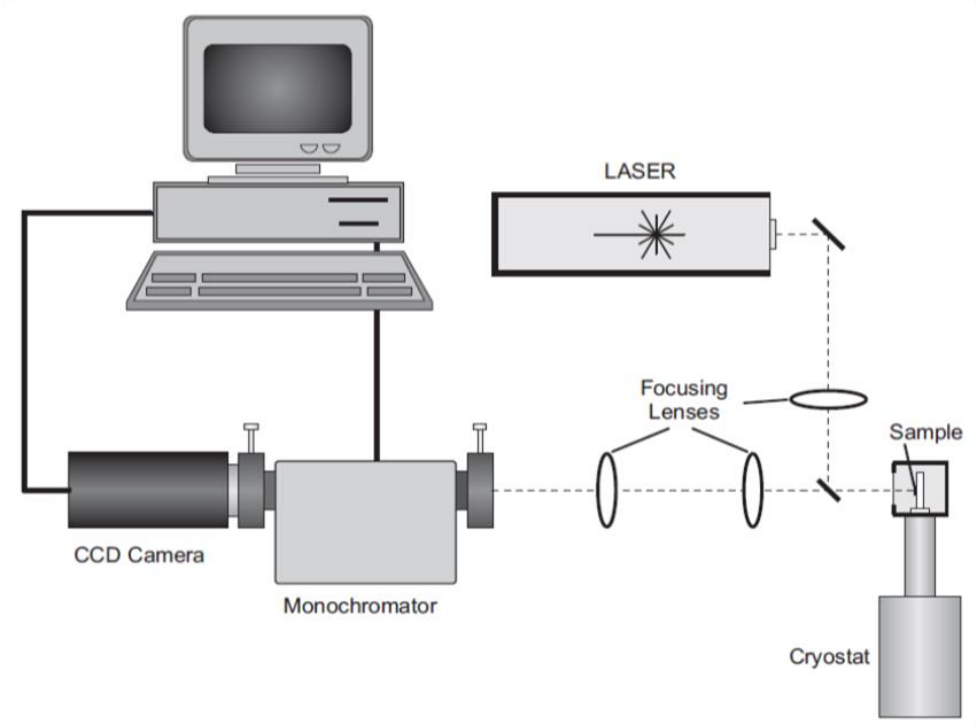

Figure. 3.18. Schematics of the PL setup.

Figure 3.18 shows the setup used to study PL. The light source was either a continuous-wave frequency-doubled Ar^+ laser ($\lambda = 488/2 = 244$ nm) or a pulsed Nd-YAG laser ($\lambda = 266$ nm, pulse width = 0.5 ns, repetition rate = 8 kHz). For the nanowires under study an excitation power of 5 µW was used unless mentioned otherwise. Typically, the planar samples were studied at higher power of 100 µW. The spot diameter was maintained approximately at 100 µm. The photons emitted by the sample are studied using a Jobin Yvon HR460 monochromator coupled with a liquid nitrogen cooled UV-enhanced charge-coupled device (CCD) camera. This lets us understand the number of photons emitted for various frequencies of light. We will find a peak in intensity of light at the frequency corresponding to the energy of the recombination processes that occur.

The samples were mounted on a cold finger of a He cryostat. Very low temperature (5K) was employed to minimize thermally activated non-radiative recombination processes and thermal line broadening. Temperature dependent PL measurements were taken by heating the sample in the same setup to the required temperature at reduced liquid He flow. The particular volume of the sample where PL can be studied depends upon the absorption depth of the exciting laser and diffusion length of the minority carriers.

Time-resolved PL (TRPL) was used to study carrier relaxation dynamics in nanowire and planar samples of chapter 6. The samples were excited by a laser pulse and we analyzed the evolution of the PL emission intensity as a function of time. The excitation source was a frequency-tripled Ti:sapphire laser (excitation λ = 270 nm) with a pulse width of 200 fs. The laser was augmented with a cavity damper section with a base pulse repetition rate of 54 MHz. This allowed the period between pulses to be varied from 20 ns to 500 ns. The excitation power was about 250 µW. The luminescence was dispersed by a Jobin Yvon Triax320 monochromator and was detected by a Hamamatsu C−10910 streak camera.

3.3.4 Fourier transform IR spectroscopy

Fourier Transform IR (FTIR) spectroscopy was used to study transmitted or reflected IR light when incident on a sample. I have used a Bruker Vertex 70v FTIR interferometer for the measurements in this manuscript. All samples were studied in transmission mode unless mentioned otherwise.

Traditionally IR spectroscopy instruments were dispersive. This means that they used a prism or grating to separate out an individual frequency from the IR source of the instrument. A detector then measures the amount of energy at each frequency. The data is compiled together to form a spectrum. The instrument has to scan through the entire range of frequencies to obtain the desired spectral range, thus making measurements highly time consuming. FTIR, on the contrary, uses an interferometer. The interferometer employs a beam splitter which splits an incoming IR beam (from a continuous IR source) into two beams of which one is reflected off a flat mirror and the other is reflected off a flat mirror which is moving. The optical path of the two beams are different as one of the mirrors is moving and when they recombine back at the beam splitter they produce an interference. The resulting signal is termed as an interferogram. The interferogram has information of all the frequencies emitted from the source. The interferogram is now the new source signal which goes into the sample and is detected after transmission. Fourier transformation is then employed by a computer to convert the detected interferogram into the spectrum. Hence the name Fourier transform IR spectroscopy.

The schematics of the Bruker Vertex 70v FTIR spectrometer is displayed in figure 3.19. It has inbuilt sources, optics and detectors for SWIR, and for MWIR and long-wavelength IR (LWIR) wavelengths. For FIR measurements, we used an Hg-arc external source and He-cooled bolometer in addition to the inbuilt components, details of which are given in table 3.2. We also used polarizers to obtain TM and TE polarized light.

The fact that only electric fields in the direction of confinement give rise to ISB absorption leads to the use of non-standard sample geometries. In normal transition experiments, the light is incident perpendicular to the sample. In the situation of quantum wells growth by epitaxy, this means that the electric field of the perpendicularly incident light will always be in the plane of the QW and not along the direction of confinement. We use an oblique angle of incidence to solve this problem.

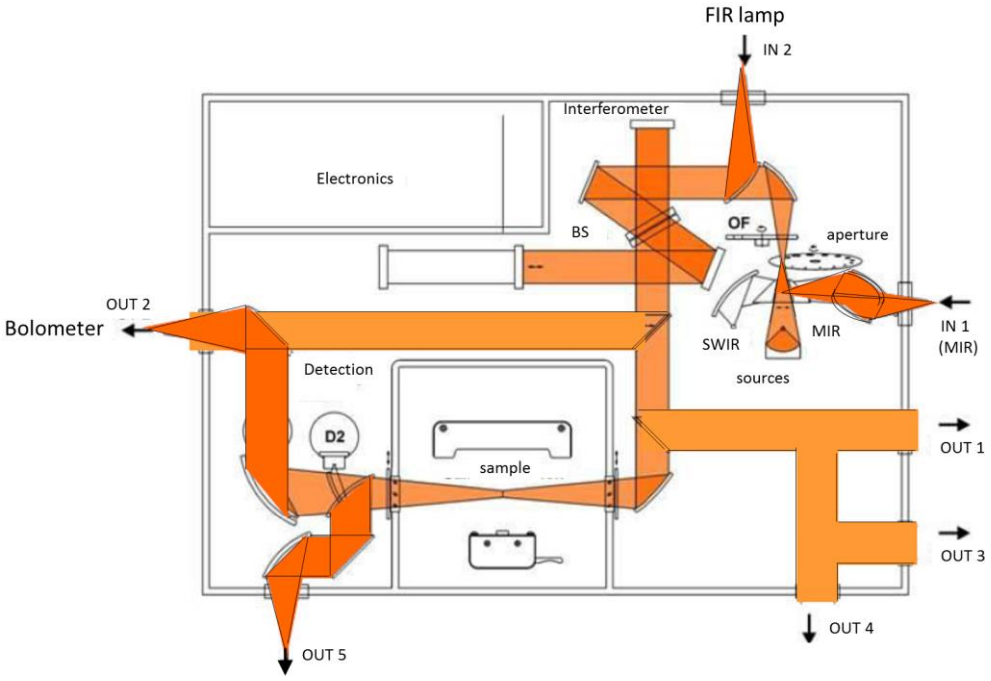

Figure 3.19: Description of the FTIR spectrometer (modified from Bruker manual).

	SWIR	MWIR-LWIR	FIR
Source	Tungsten	Globar (SiC)	Hg-arc
Beam-splitter	CaF_2	KBr	Si
Detector	HgCdTe	HgCdTe	Bolometer
Temperature of detector	77 K (Liquid Ni)	77 K (Liquid Ni)	5 K (Liquid He)

Table 3.2: Description of experimental set up for various spectral ranges associated with the FTIR spectrometer.

Therefore, planar samples were made into a multi-pass waveguide geometry by polishing them against a diamond surface. The angle of the facets depends on the refractive index of the material and is designed to allow maximum absorption from the sample. Samples were polished at 45° when using bulk GaN or sapphire based substrates. This multi-pass waveguide configuration allows 4-5 interactions of the incident light with the active region. For characterization in the FIR range, two pieces of each sample were polished and placed face-to-face to increase the signal-to-noise ratio. In the case of SWIR-MWIR characterization, only one piece of each sample was polished and simply placed on the sample holder of the FTIR sample compartment. These configurations are described in figure 3.20 (a), (b).

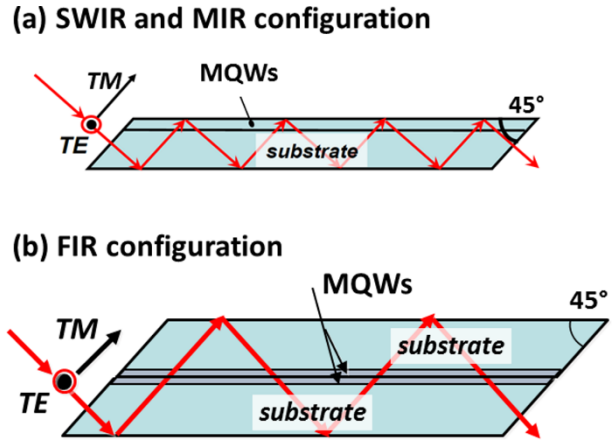

Figure 3.20: Multipass waveguide configurations in the case of 45° polishing for measurements (a) in the SWIR-MWIR and (b) in the FIR (modified from ref. [101]).

For the nanowire samples under study, a grazing angle of incidence is used as shown in figure 3.21.

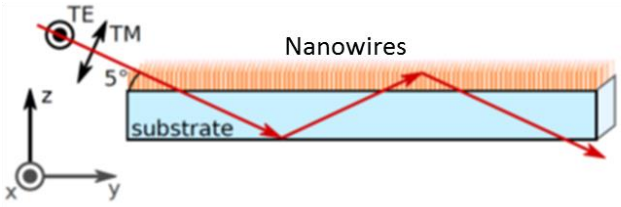

Figure 3.21: Sample configuration for the measurement of nanowire samples.

3.3.5 Hall effect

Hall effect is an efficient characterization technique to measure the concentration of free charge carriers, mobility and resistivity. Temperature dependent measurements were used to measure the activation energy of the carriers. It describes the production of a voltage difference in an electrical conductor when an electric current is passed through it in presence of a transverse magnetic field. The voltage will be developed transverse to both the magnetic field and electric current.

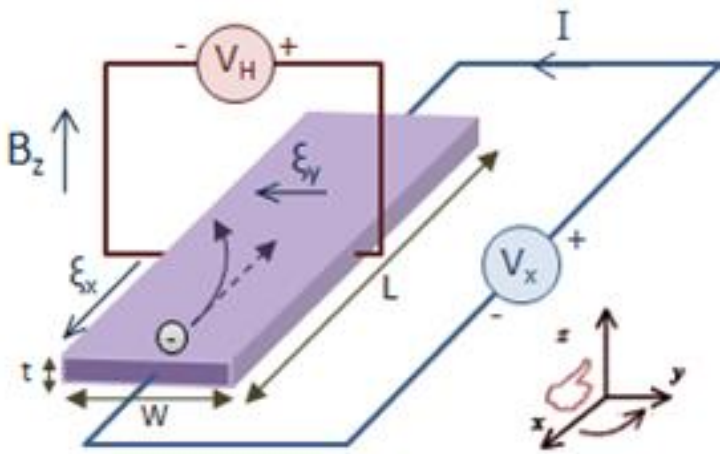

Figure 3.22: Illustration of Hall effect.

Consider a semiconductor sample of thickness *t*, width W and length L as shown in figure 3.22. An electric field is applied via current I_x along x-direction and a magnetic field B_z is applied along the z-direction. The charge carriers with density n and charge q in the sample would experience a Lorentz force. Due to the Lorentz force, a transverse voltage called the Hall voltage V_H is developed in the semiconductor material, and this voltage is perpendicular to both the magnetic field and the current. V_H is given by,

$$V_H = \frac{I_x B_z}{ntq} \qquad \text{(equation 3.5)}$$

The samples were prepared in the van der Pauw method. We made Ohmic contacts with Indium on the four corners of our samples which were in the shape of a square. The accuracy of the measurements is enhanced by using reversed polarity and reciprocal measurements with the four contacts. The resistivity of the samples can hence be obtained and as a result we would also obtain the mobility of the free carriers. Hall measurements were performed at various values of the magnetic field between -1 and 1 T. The value of the magnetic field was measured by a probe located next to the sample. The carrier activation energy could be estimated by performing temperature dependent measurements by using a closed-cycle He cryostat.

3.3.6 Scanning electron microscopy

Scanning electron microscopy (SEM) is a microscopy technique based on the interaction of a scanning electron beam and the surface of a sample. In this work, a Zeiss Ultra 55 or a Zeiss 55 microscope was utilized to study the samples. Contrary to conventional optical microscopy, a much higher resolution is obtained due to the smaller effective wavelength of electrons. We utilized a high energy electron beam with an acceleration potential of 3-5 keV during the operation.

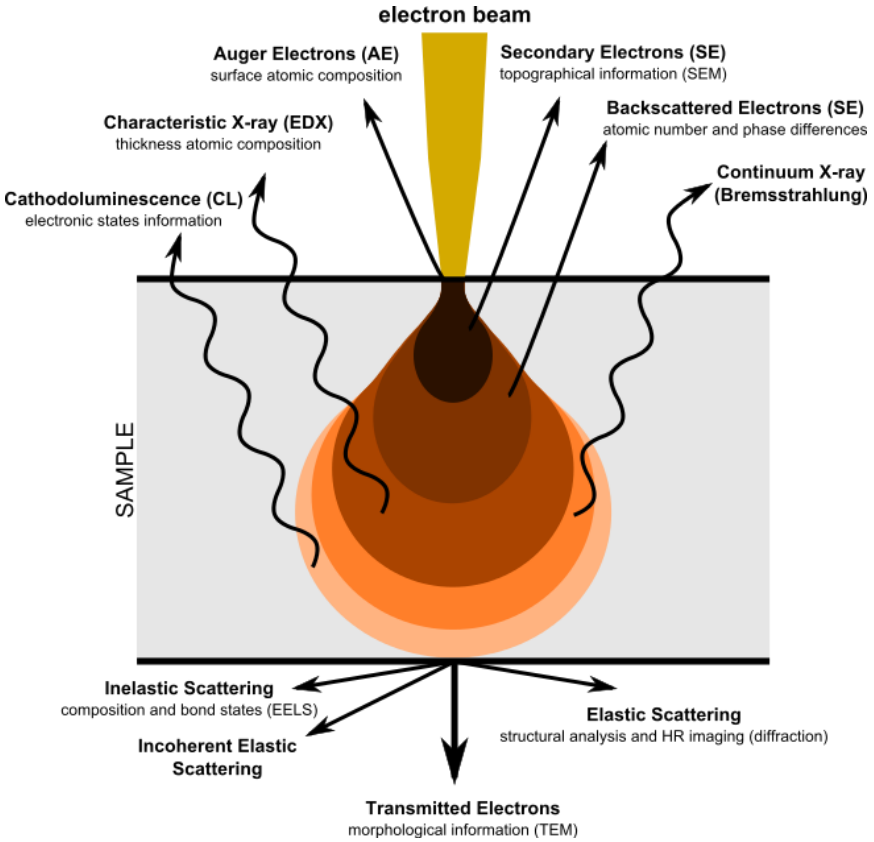

Figure 3. 23: Illustration of the interaction volume (https://commons.wikimedia.org/wiki/File:Electron_Interaction_with_Matter.svg).

When the electron beam interacts with the sample, the electron would loose energy by scattering and absorption in a volume that is in the shape of a tear as described in figure 3.23. This volume is called interaction volume and its penetration depth into the surface depends on the energy of the electron beam, atomic number and density of the sample. The interaction results in reflection of electrons by elastic scattering, emission of secondary electrons through inelastic scattering and emission of radiations like x-rays, characteristic to the sample. Interacted electrons are transmitted through the sample. The instrument is equipped with various detectors to quantify and detect the electrons and radiations generated by these various processes.

In general, in our measurements, we utilize an in-lens detector for secondary electrons that is located inside the column of the microscope and leads to efficient electron collection. We obtain morphology related information in nanowires and surface topography for our 2D layers using this detector.

3.3.7 Scanning transmission electron microscopy

Transmission electron microscopy (TEM) is a microscopy technique based on the transmission of an electron beam through a sample. The measurements in this work were

performed by C. Bougerol (images in chapter 8) or by M. I den Hertog and M. Spies (all other measurements) in an FEI Titan Themis and CM 300 microscope operated at 200 kV. They primarily used two techniques:

- High angle annular dark field scanning transmission electron microscopy (HAADF-STEM). Here a focused electron beam is raster scanned over the sample and the intensity of electrons scattered over relatively large angles is collected on an annular detector. The contrast in the image is related to the chemical nature of the atoms (proportional to the atomic mass) and the sample thickness. The influence of diffraction contrast is strongly reduced and high resolution imaging of the atomic lattice is possible. A qualitative interpretation of the images is much easier than using TEM techniques.
- High-resolution TEM (HR-TEM). Here a parallel electron beam is used and the transmitted beam is imaged on a camera. Heavier atoms and thicker regions can appear darker due to absorption of the electrons. Imaging at the atomic scale is possible. However, no direct interpretation of the images can be done due to the influence of sample thickness, defocus and diffraction contrast.

In this work, the planar samples were prepared by focused ion beam (FIB) and the nanowires were directly scratched/removed from the substrate and dispersed on electron-transparent SiN_x membranes for observation, most often using wet dispersion techniques.

4. Ge doping of III-nitrides

In this chapter, we present Ge as an alternate n-type dopant, in place of Si, for wurtzite GaN and AlGaN thin films grown by PAMBE. We first prove that Ge does not introduce any perturbation in the GaN growth. We then study the effect of doping on the structural quality and estimate the Ge incorporation. We systematically assess the effect of Ge on the electrical properties, complemented by observing optical properties for various Ge doping concentrations and Al content.

For the study of Ge doping in GaN (section 4.1), I performed the MBE growth, Hall effect measurements, PL measurements, IR reflectivity, UV transmission measurements and theoretical calculations. This work was done in close collaboration with the group of Prof. M. Eickoff at the University of Giessen (XRD, SIMS), where I worked as a visiting student for two weeks. I also collaborated with M. Jiménez-Rodriguez (AFM), C. B. Lim (XRD) and L. Amichi (APT). Results were published in " Ge doping of GaN beyond the Mott transistion", A. Ajay et al., J. Phys. D: Appl. Phys. ***49****, 445301 (2016)* [129].

Regarding the study of Ge doping in AlGaN (section 4.2), I was in charge of XRD and worked in collaboration with R. Blasco for PL and Hall measurements, and with my PhD supervisor Dr. E. Monroy for the MBE growth. The RBS/C and PIXE studies were performed by Dr. K. Lorenz, Dr. L. C. Alves at the Instituto Superior Tecnológico, Bobadela LRS, Portugal.

4.1 Ge doping of GaN

Silicon has been, so far, the preferred n-type dopant in wurtzite GaN even though it contributes to an increase in the density of edge type dislocations, leading to larger tensile stress [36–38]. In the case of GaN on silicon substrates, tensile strain is highly problematic since the mismatch of thermal expansion coefficients requires careful strain engineering to prevent crack propagation [130]. Si doping above the Mott transition[1] density of GaN (≈10^{19} cm^{-3}) is also reported to cause surface roughening and crack propagation [37]. In nanowire structures, the radial distribution of Si is inhomogeneous with a tendency to migrate towards the side walls [34]. At high doping levels this tends to degrade the nanowire morphology [131].

Ge, like Si, is a shallow donor in GaN, with a theoretical activation energy of 31.1 meV [39]. Moreover, the ionic radius of a Ge atom is comparable to that of Ga and the metal-nitrogen bond length changes by only 1.4% with Ge, while it changes 5.5% with Si [40]. Hence Ge can occupy the Ga lattice site causing far less lattice distortion than other dopants like Si and O. Also like Si, the DX-state of Ge is unstable in GaN and does not affect doping efficiency [40].

Ge was recently reintroduced as a highly favorable dopant for GaN, and, at the beginning of this PhD work, several reports on Ge-doped GaN synthesized using HVPE [132,133] and MOVPE [134–137] already existed. On the contrary, using plasma assisted MBE, data was scarce. Thin films displaying carrier concentrations up to 4×10^{20} cm^{-3} were published [138,139], and Ge-doped nanowires with metallic conductivity were demonstrated [140–142].

[1] The Mott transition is a change in the material behavior from semiconducting to metallic.

These efforts also lead to the observation of ISB transitions in Ge-doped GaN/AlN nanowires [35,143]. However, there was still a large void regarding the effect of Ge doping on the PAMBE growth kinetics and properties of planar GaN:Ge.

Here, we made extensive efforts in understanding the growth kinetics of Ga while using PAMBE for growing Ge-doped GaN. We expand on the existing literature of highly Ge-doped GaN thin films by combining studies on electrical properties with a comprehensive analysis on the optical properties. The dependence on the carrier concentration of the optical properties is specifically demonstrated.

4.1.1 Effect of Ge on the growth kinetics of GaN

As described in chapter 2, n.i.d. Ga-face GaN was grown by PAMBE under slightly Ga-rich conditions, with a 2-ML-thick self-regulated Ga adlayer on the growing surface [104]. This Ga adlayer is known to be extremely sensitive to the presence of dopants, and this can be understood by studying the desorption process of the adlayer during a growth interruption. For example, it has been shown that Si does not introduce any perturbation in Ga kinetics, whereas Mg inhibits the formation of the Ga adlayer by segregating at the growth front [144–146]. For Mg, this segregation drastically reduces the window of Ga fluxes that can be used for the growth of planar GaN.

To analyze the effect of Ge on the adatom kinetics, we had studied the Ga desorption during a growth interruption after the deposition of 7 nm Ge-doped GaN for various Ge fluxes. For this experiment, the GaN growth rate was 0.5 ML/s at a substrate temperature of T_S= 720°C. The Ga flux was chosen to be ≈0.7 ML/s, so that the 2 ML Ga adlayer is dynamically stable during the growth of n.i.d. GaN, and an increase of the Ga flux by 7% leads to the accumulation of Ga on the growing surface. The Ge cell temperature was varied from 720°C to 1000°C.

Figure 4.1 represents RHEED intensity transients generated by the Ga desorption after the growth of n.i.d GaN and Ge-doped GaN for Ge cell temperatures T_{Ge} = 800°C, 900°C, 950°C and 1000°C. The growth was interrupted at time t = 0 by closing the Ge, Ga and N cells simultaneously. Before each measurement of Ga desorption from GaN:Ge, we deposited 7 nm of n.i.d GaN and recorded the Ga desorption from the undoped surface as a reference.

During the experiment, with time, there can be variations in the shape (Intensity) and desorption time (i.e. the duration of the transient) of the RHEED transient during Ga desorption. The variations in the shape can occur (see for instance the difference between the various transients recorded for n.i.d GaN in figure 4.1) due to a modification of the surface morphology during the growth, a change in the position of the sample, a change in the angle of incidence of the RHEED electron beam, or the choice of the section of the RHEED pattern that is analyzed. In contrast, variations of the desorption time, are due to changes in the sample temperature or in the amount of Ga accumulated on the surface as more and more

layers are added after each GaN deposition. Therefore, in our analysis, we included for each Ge cell temperature a measurement of the desorption transient after the growth of n.i.d. GaN and another one after the growth of GaN:Ge, recorded immediately after the former one, and we analyzed the same section of the RHEED pattern in both cases. Following this procedure, when comparing these two transients, the drifts due to substrate temperature and relative position of the RHEED and the surface are negligible, and the differences, if any, are only due to the surface morphology and amount of Ga on the surface. We observe in figure 4.1 that differences between the transients associated to different temperatures of the Ge cell can be present. Here, a difference in the desorption curve can be due to the required time interval between measurements, and can also be due to the difficulty to guarantee that the relative position of RHEED and surface remain stable over time (minutes).

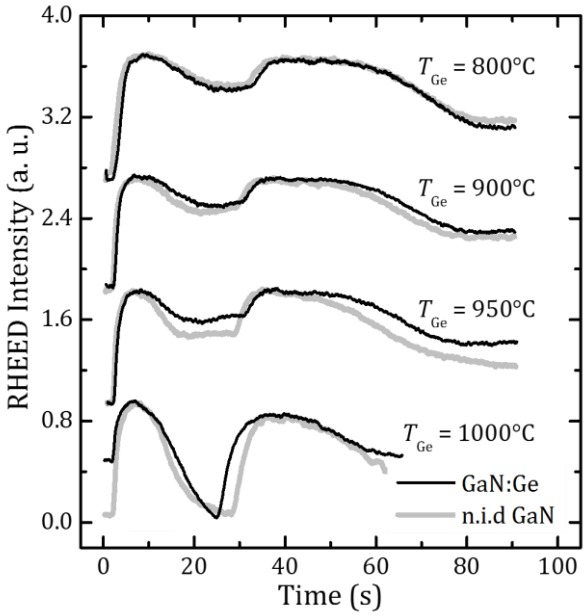

Figure 4.1: RHEED intensity transients during the desorption of Ga after the growth of n.i.d GaN and GaN:Ge for different Ge cell temperatures (modified from ref. [129]).

On the basis of this analysis, we see that, in figure 4.1 the RHEED intensity increases sharply after the growth interruption, which indicates that there is no accumulation of Ga forming droplets or clusters. Then, in both cases (n.i.d. GaN and GaN:Ge), the evolution of the RHEED intensity after the growth interruption presents two distinct oscillations. The two transients do not overlap perfectly; however, the difference in the time to the first inflection point in the RHEED transient points to a difference in the Ga coverage during growth lower than 0.5 ML. Therefore, it can be concluded rightly that the RHEED intensity transients remain unaltered in presence of a Ge flux, i.e. Ge does not perturb the Ga kinetics on the GaN (0001) growth front.

4.1.2 Effect on the structural quality

Following our demonstration that Ge does not perturb the Ga kinetics during the growth of GaN (0001), we grew Ge-doped GaN thin films with a thickness of 675 nm using the 2 ML Ga-adlayer regime on 1 µm thick AlN-on-sapphire templates. A ≈ 40 nm AlN buffer layer was grown on the substrate prior to the growth of GaN. This was done to improve the quality of the AlN surface with respect to the commercial substrate, exposed to air. All the samples are listed in table 4.1.

Sample name	**Sample code**	**T_{Ge} (°C)**	**Δω (arcsec)**	**ε_{zz} (%)**	***n*** **(cm^{-3})**	**ρ (Ωcm)**	**E_G at 300 K (eV)**	**E_{Urb} at 300 K (meV)**
E3495	A	720	133	0.25±0.02	7.8×10^{17}	8.1×10^{-2}	3.432	52.2
E3496	B	760	392	0.211±0.003	1.0×10^{18}	1.71×10^{-1}	3.436	53.3
E3482	C	800	120	0.084±0.008	2.4×10^{18}	2.61×10^{-2}	3.42	58.9
E3483	D	850	60	0.166±0.003	1.3×10^{19}	6.03×10^{-3}	3.43	66.0
E3484	E	875	100	0.207±0.008	3.1×10^{19}	3.27×10^{-3}	3.438	72.4
E3480	F	900	287	0.29±0.01	6.8×10^{19}	6.00×10^{-3}	3.484	94.9
E3485	G	925	115	0.244±0.003	1.5×10^{20}	8.75×10^{-4}	3.522	117
E3481	H	950	296	0.242±0.003	2.6×10^{20}	5.51×10^{-4}	3.58	132
E3487	I	1000	193	0.317±0.003	6.7×10^{20}	6.90×10^{-4}	3.671	198
E3488	X	n.i.d.	237	0.236±0.003	--	--	3.443	46.9

Table 4.1: Description of samples under study: Ge cell temperature (T_{Ge}), FWHM of the x-ray rocking curve (Δω), strain along the (0001) axis (ε_{zz}), room-temperature carrier concentration (n) measured from Hall effect and resistivity (ρ), bandgap (E_G) and Urbach's tail energy (E_{Urb}) extracted from transmission measurements at room temperature.

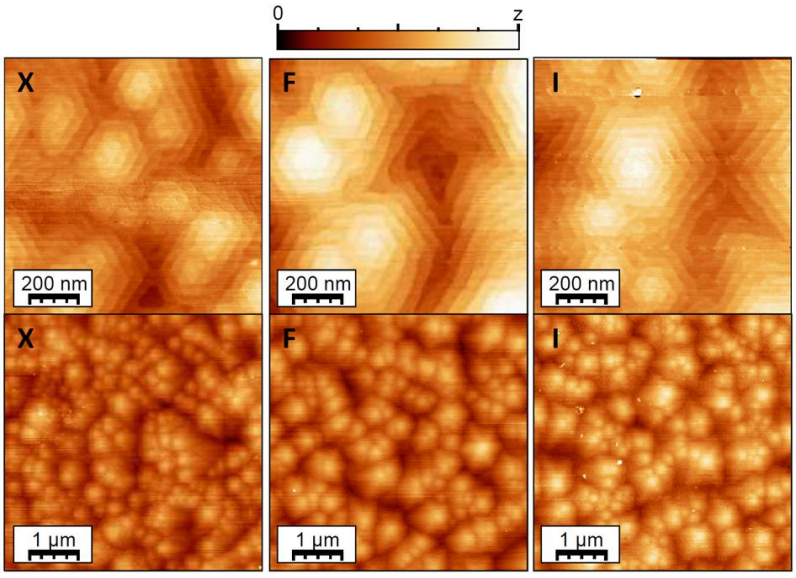

Figure 4.2: AFM images of samples X, F and I. (Top: 1×1 μm^2 surface: z range 0–5 nm. Down: 5×5 μm^2 surface: z range 0–9 nm) (modified from ref. [129]).

After the growth, the surface morphology was analyzed by AFM with the results presented in figure 4.2. Regardless of the doping level, all the samples present monoatomic terraces and hexagonally-shaped hillocks characteristic of PAMBE grown GaN, without the observation of cracks or pits. Looking at the top row in figure 4.2 one can have the feeling that there is a change of morphology. This is due to local variations since in the larger-range figures in the bottom row, the surfaces are indeed similar. The average number of hillocks in all the samples has been estimated to be approximately (1.0±0.6)×10^6 cm^{-2}. The rms roughness of these surfaces in 5×5 μm^2 images is measured to be 0.9±0.3 nm, for all the samples. These results demonstrate that there is no significant effect of Ge on the surface morphology.

The structural quality was further examined by HRXRD. From ω−2θ scans of the (0002) GaN reflection, the average strain of the c-lattice parameter of GaN was estimated to ε_{zz} = 0.22±0.07%. The value of ε_{zz} for all the samples is listed in table 4.1, and it does not show any clear trend as a function of the Ge concentration. This tensile strain along c is the result of the compressive in-plane stress imposed by the AlN substrate, in good agreement with previous studies of the plastic relaxation of GaN on AlN when growing by PAMBE in the 2 ML Ga-adlayer regime [109]. Also the FWHM of the ω-scan of the (0002) reflection of GaN:Ge can be compared to the n.i.d reference sample in table 4.1. For all the layers, the FWHM remains in the range of 190 ± 110 arcsec without any systematic influence of the Ge incorporation. In fact, the variation in the FWHM from sample to sample correlates very well with the variation of the same parameter for their respective AlN templates, i.e. the influence of the substrate on the GaN mosaicity is more important than any effect related to Ge doping.

4.1.3 Determination of Ge incorporation and carrier concentration

To analyze the incorporation of Ge, all samples were studied by time-of-flight secondary ion mass spectrometry (ToF-SIMS). The depth profile of GaN:Ge sample H and the n.i.d. reference sample X are depicted in figures 4.3 (a) and 4.3 (b). The depth profiles were studied in negative ion mode with 25 keV Bi^+ as primary ion species and 1 keV Cs^+ ions for the sputter process. For the quantification of the Ge concentration, we used the method of relative sensitivity factors (RSFs) and we used three reference samples with different Ge concentrations, which were grown by MOVPE.

A uniform Ge signal throughout the thickness of the GaN layers was found in the samples doped with Ge. Oxygen and trace amounts of silicon and carbon, seen in all samples including the reference, had no specific dependence on T_{Ge} and can be concluded to be almost constant from sample to sample. It should be noted that these unintentional n-type dopants (Si and O) are two and three orders of magnitude lower than Ge.

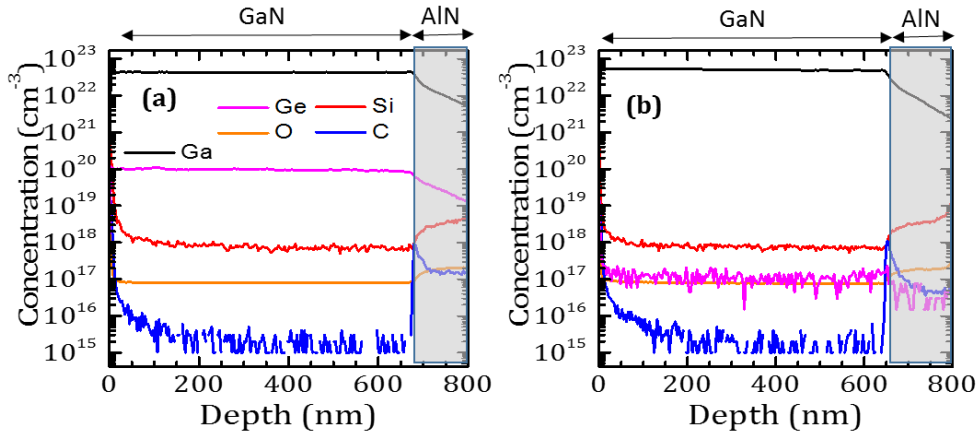

Figure 4.3: ToF-SIMS profiles of samples H (a) and X (b) (modified from ref. [129]).

The Ge atom incorporation in the most heavily doped sample (I) was additionally studied by Atom Probe Tomography (APT) in a CAMECA Flextap system, operated in laser pulsing mode with a UV laser at a temperature of 40 K. Sample I was modified to be in the shape of a needle by using a focused ion beam (FIB), and APT was performed by sequential field effect evaporation of individual atoms located at the needle-shaped sample. The chemical nature of the evaporated atoms was obtained from time-of-flight mass spectrometry and the elemental composition of the material was computed from the proportion of atoms of each species. Distribution of Ge and Ga in sample I, computed from this analysis, is shown in figure 4.4. Ge is homogenously distributed, without any indication of clustering. The mass spectrum of sample I shows the presence of the various Ge isotopes in agreement with their natural abundance. After quantification, $(9.4\pm0.5)\times10^{20}$ cm^{-3} has been obtained as the concentration of Ge. The large error bar is due to the fact that the peaks attributed to Ge ions (Ge^{2+}, Ge_2X^{2+}) are very close to those of Ga.

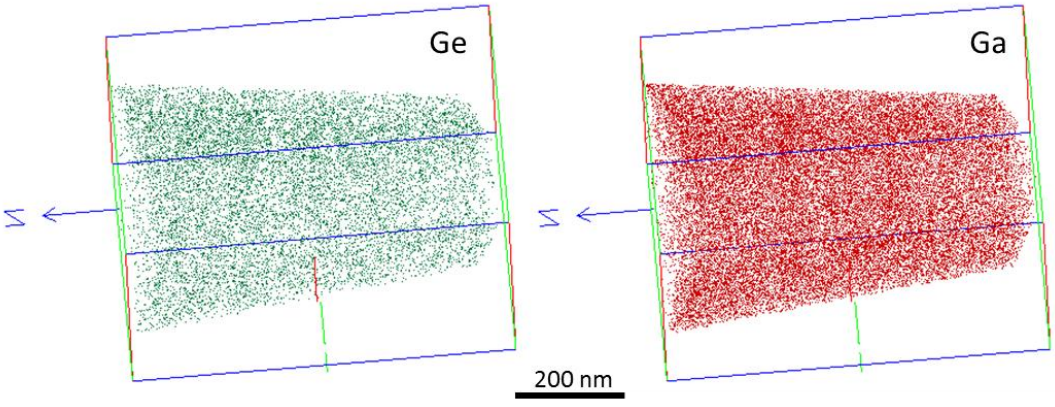

Figure 4.4: Distribution of Ge and Ga in the needle-shaped sample I.

Free carrier concentrations, *n*, were measured using Hall Effect technique at 300 K using Van der Pauw method. We recorded *n* of up to 6.7×10^{20} cm^{-3} for the sample grown with the highest Ge cell temperature (1000°C) as detailed in table 4.1. This corresponds to a Ge mole

fraction higher than 1.5% in the layer. As illustrated in figure 4.5 (a), *n* scales exponentially with T_{Ge} following,

$$n \propto \exp\left(-\frac{E_{Ge}}{kT_{Ge}}\right) \qquad \text{(equation 4.1)}$$

where E_{Ge} = 3.42 eV is the thermal evaporation energy of Ge [147] and *k* Is the Boltzmann constant. Our studies are in line with previously conducted studies for Si doped GaN, with E_{Si} = 4.05 eV [147]. The free carrier concentration extracted from Hall effect measurements at room temperature scales linearly with the Ge signal obtained from ToF-SIMS, as shown in figure 4.5 (b), confirming that the variation in carrier concentration is indeed due to Ge incorporation.

The resistivity at 300 K (in table 4.1) decreases over two orders of magnitude when increasing the free carrier concentration from 7.9×10^{17} cm^{-3} to 6.7×10^{20} cm^{-3}, reaching a lowest value of 6.90×10^{-4} Ωcm (sample I).

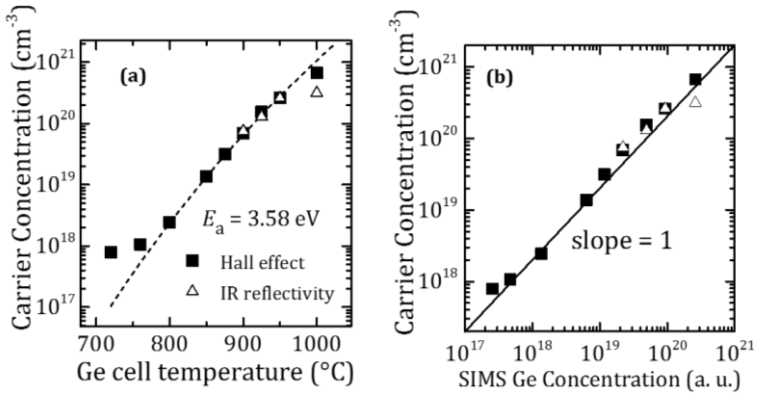

Figure 4.5: (a) Evolution of carrier concentration, *n*, with the Ge cell temperature. (b) Comparison of *n* and Ge ToF-SIMS concentration showing a linear relationship. (*n* is measured by Hall effect and IR reflectivity) (modified from ref. [129]).

Reflectivity measurements were performed using FTIR to study bulk plasma oscillations. Plasma oscillations of the free electron gas density, similar to plasmon resonances in metals, can be observed for samples that are heavily doped. We utilized TM-polarized light at 70° incidence and the resulting spectrum was corrected for the system response by dividing it by the reflectivity measurement of an Au film using the same experimental conditions. The experiment was repeated for other incident angles to identify interference oscillations. Especially TE-polarized light showed interference fringes associated to the thickness of the GaN layer. The carrier concentration of the most heavily doped samples (samples F–I) was estimated from the plasma frequency, ω_p, using MWIR reflectivity measurements with TM-polarized light, see figure 4.6.

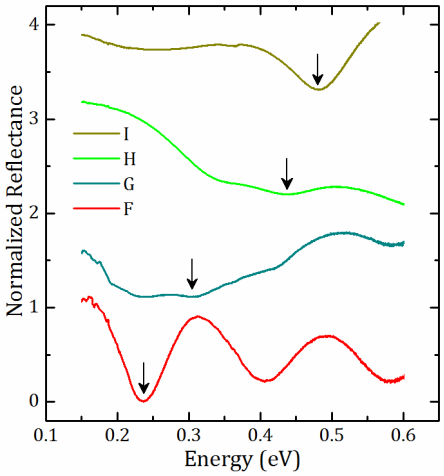

Figure 4.6: IR reflectance measured in samples F, G, H and I for TM-polarized light at an angle of incidence of 70°. The features associated to the free carrier plasma are marked by arrows. Other features are due to interference phenomena, as verified by changing the angle of the light (modified from ref. [129]).

According to the Drude–Lorentz model, the plasma frequency of the free carrier plasma is given by

$$\omega_p^2 = \frac{nq^2}{m_e^* \varepsilon_s \varepsilon_0} \qquad \text{(equation 4.2)}$$

where q is the elementary charge, ε_0 is the vacuum permittivity, ε_s = 9.38 is the static dielectric constant of GaN, and m^*_e = 0.231 m_0 is the electron effective mass in GaN. The estimated free carrier concentrations are illustrated in figures 4.5 (a) and (b), and are similar to the data obtained from Hall effect measurements.

Figures 4.7 (a) and (b) describe the variation of carrier concentration and resistivity with temperature, respectively, in samples with doping levels up to the density of the Mott transition (≈1–1.5×10^{19} cm^{-3} in GaN at room temperature [148,149]). We estimate an activation energy E_a from the Arrhenius equation,

$$n \propto \exp\left(-\frac{E_a}{kT_{Ge}}\right) \qquad \text{(equation 4.3)}$$

The activation energies extracted from figure 4.7 (a) decrease from 19.5 meV for the lowest doped sample A, to 12.4 meV for sample B, and 9.7 meV for sample C. The decrease in activation energy is in accordance with the decrease in average distance between the impurity atoms which results in the average potential as seen by an electron to decrease [150]. As a result, sample D (n = 1.3×10^{19} cm^{-3}) starts to exhibit metallic behavior, marked clearly by almost zero activation energy and low resistivity at room temperature, indicating Mott transition. Mathematically, this effective activation energy can be described by

$$E_a = E_I - \alpha(n)^{1/3} \qquad \text{(equation 4.4)}$$

where E_I is the activation energy of a single isolated Ge impurity atom in GaN (theoretically estimated at E_I = 31.1 meV by Wang and Chen [39]), and α is a proportionality constant. The

value of α determined by the empirical fit is α = (1.6±0.3)×10^{-5} meV.cm, close to the α = (2.1±0.2)×10^{-5} meV.cm reported for Si donors in GaN [151].

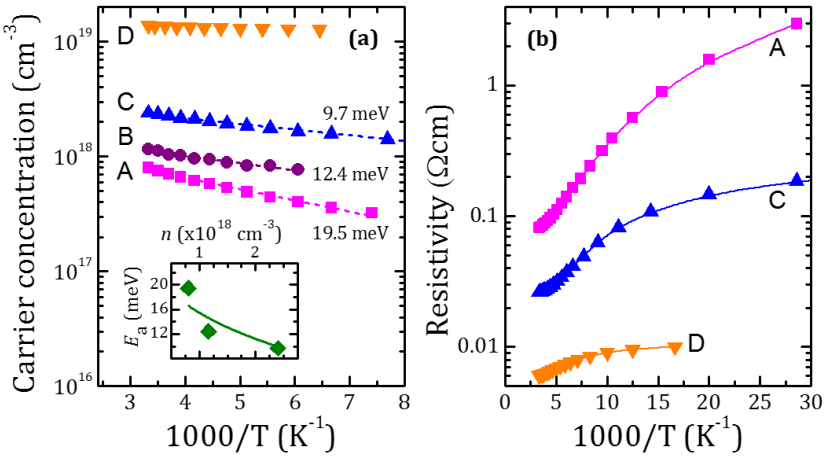

Figure 4.7: Variation of (a) free carrier concentration and (b) resistivity with temperature for various GaN:Ge samples with carrier densities up to the Mott transition. Dashed lines in (a) correspond to exponential fits leading to the activation energy (Ea) values as indicated in the figure. Inset: Variation of Ea as a function of the carrier concentration. The solid line is a fit to $E_a = E_I - \alpha(n)^{1/3}$ (modified from ref. [129]).

4.1.4 Effect on optical properties

The normalized PL spectra at low temperature (T = 5 K) and room temperature are displayed in figures 4.8 (a) and (b), respectively. The PL spectra at 5 K of n.i.d. GaN (sample X) show excitonic emission near the band edge, around 3.515 eV. Regardless of the temperature, as the Ge concentration increases for samples A to C, a redshift is noticed which is consistent with bandgap renormalization [152] (BGR) due to electron-electron and electron-ion interaction. Further increase of carrier concentration (samples D to I) causes a blue-shift of the emission due to additional contributions from the Burstein-Moss effect [153] (BME), i.e. the lower energy states in the conduction band become significantly filled, and the Fermi level is positioned inside the conduction band. Also, the emission spectra of samples D to I are systematically broadened with the increase in carrier concentration. Their shape corresponds to the Kane density of states for the conduction band multiplied by the Fermi-Dirac distribution [154]. Our observations are similar to the description in ref. [155], which used GaN doped with Si in the range of 8.7×10^{17} cm^{-3} to 1.4×10^{19} cm^{-3} synthesized using HVPE, and Ge for dopant concentrations in the range of 3.4×10^{19} cm^{-3} to 1.6×10^{20} cm^{-3}, synthesized using MOVPE.

The PL transition energies are shifted with respect to their values for relaxed GaN due to the compressive in-plane stress resulting from the AlN substrate. From the strain estimated from the HRXRD in table 4.1, the bandgap should be larger by 28 meV on average with respect to its relaxed value (following ref. [156]). In the same note, the variation of the strain state

between the samples results in a shift of the excitonic transitions of the order of ±7 meV (standard deviation).

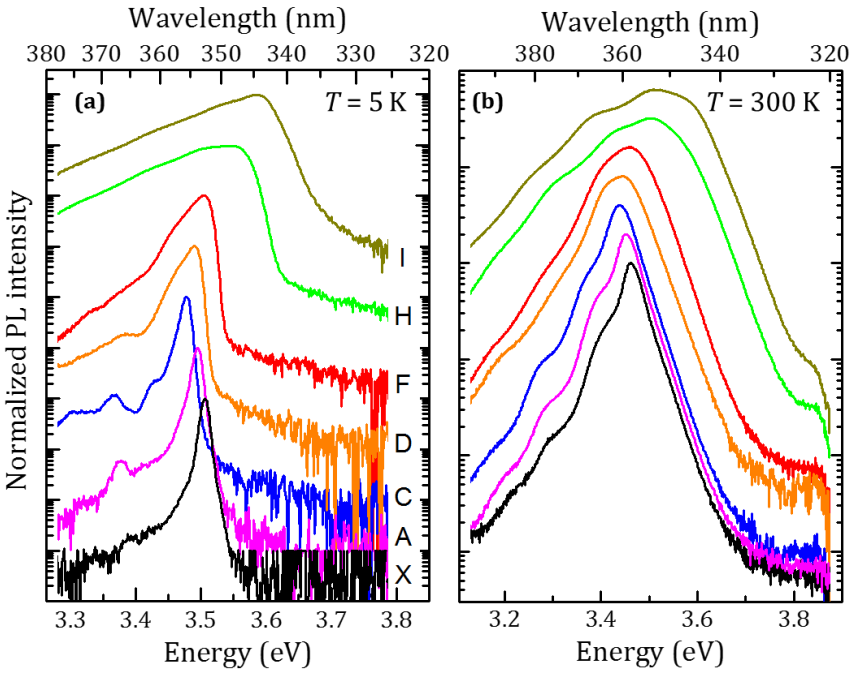

Figure 4.8: Normalized PL spectra at (a) 5 K and (b) 300 K. The spectra are vertically shifted for clarity (modified from ref. [129]).

The evolution of the bandgap, E_G, at room temperature was studied by optical transmission in the range of 320 nm to 420 nm. Measurements were performed under normal incidence, using a 450 W Xe-arc lamp coupled to a Gemini-180 double monochromator. The apparent bandgap energy was determined from a Tauc's plot[2] which is displayed in the inset of figure 4.9 (a). The bandgap values thus extracted for each sample are provided in table 4.1 and also in figure 4.9 (a). Similar to the low-temperature PL emission, the value of E_G first redshifts (samples A to C) and then blue-shifts (samples D to I) with increasing carrier concentration, as illustrated in figure 4.9 (a).

The increase in doping concentration affects the slope of the absorption edge that can be described by the introduction of an Urbach energy[3] ΔE_{Urb} in the expression for the optical absorption known as Urbachs's empirical rule:

$$\alpha(\lambda) = \alpha_0 \exp[(hc/\lambda - E_0)/\Delta E_{Urb}] \qquad \text{(equation 4.5)}$$

[2] A Tauc's plot shows the quantity energy of the light (E) on the abscissa and the quantity $(\alpha E)^{1/r}$ on the ordinate, where α is the absorption coefficient of the material. In the case of direct allowed transitions, r = ½. The resulting plot has a distinct linear regime which denotes the onset of absorption. Thus, extrapolating this linear region to the abscissa yields the energy of the optical band gap of the material.

[3] Urbach energy is the width of the absorption edge and it is an estimate of the degree of absorption edge smearing due to crystal lattice disordering

where hc/λ is the photon energy, α_0 and E_0 are material-dependent fitting parameters. The values of ΔE_{Urb} extracted from transmission measurements are summarized in table 4.1, showing a monotonous increase with the carrier concentration, as expected.

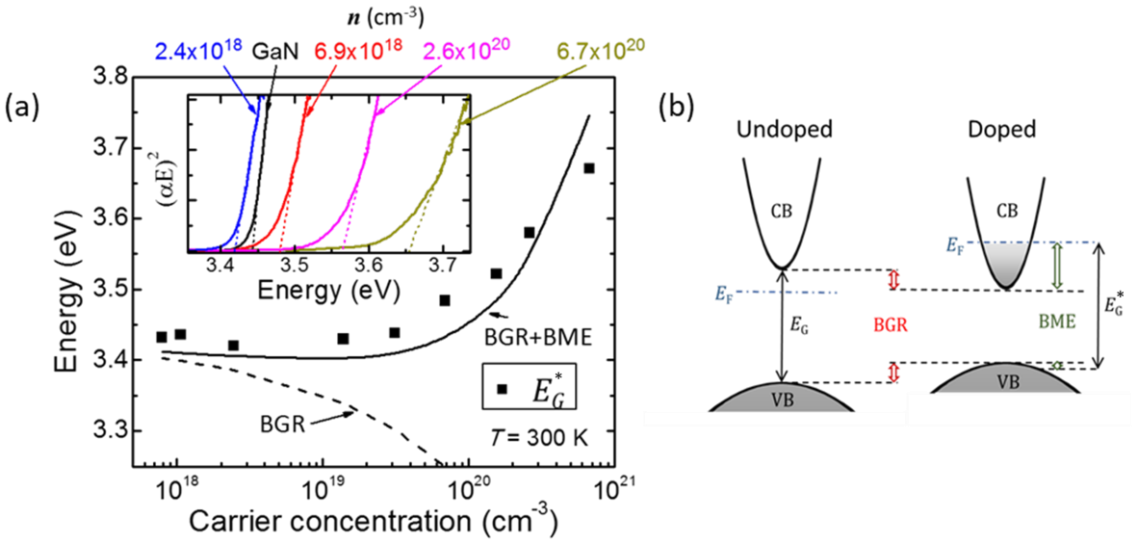

Figure 4.9: (a) Variation of the bandgap energy obtained from Tauc's plot as a function of the carrier concentration. The dashed line corresponds to the calculation of $\Delta E_{BGR} + E_0$ where E_0 is the bandgap energy of the n.i.d sample X, and the solid line corresponds to the calculation of $E_G = \Delta E_{BME} + \Delta E_{BGR} + E_0$. Inset: Tauc's plot of selected samples. (b) Schematics describing BGR and BME (Modified from ref. [129]).

The shift of the apparent bandgap with the free carrier concentration is given by the superposition of BGR and BME, i.e. $\Delta E = \Delta E_{BME} + \Delta E_{BGR}$. We estimate individual contributions analytically similar to ref. [155]. The BGR shift itself has two contributions due to electron-electron and electron-ion interactions (ΔE_{ee} and ΔE_{ei}, respectively), which can be approximated as

$$\Delta E_{ee} = -\frac{q^2 k_F}{2\pi^2 \varepsilon_s \varepsilon_0} - \frac{q^2 k_{TF}}{8\pi \varepsilon_s \varepsilon_0}\left[1 - \frac{4}{\pi}\arctan\left(\frac{k_F}{k_{TF}}\right)\right] \qquad \text{(equation 4.6)}$$

$$\Delta E_{ei} = -\frac{q^2 n}{\varepsilon_s \varepsilon_0 a_B^* - k_{TF}^3} \qquad \text{(equation 4.7)}$$

where $k_F = (3\pi^2 n)^{1/3}$ is the Fermi vector, $k_{TF} = 2\sqrt{k_F/(\pi a_{B-}^*)}$ is the inverse Thomas-Fermi screening length, $a_{B-}^* = 4\pi\varepsilon_s\varepsilon_0\hbar^2/(m_e^* q^2)$ is the effective Bohr radius of the electron. On the other hand, the shift induced by the BME follows the equation

$$\Delta E_{BMS} = \frac{\hbar^2 k_F^2}{2\mu^*} \qquad \text{(equation 4.8)}$$

where μ^* is the reduced effective mass.

The contribution of BME and BGR on the apparent bandgap are illustrated in figure 4.9 (b). The contribution from excitonic effects, influenced by the carrier concentration, is weak

at high carrier densities and is hence neglected here. A plot of $E_G = \Delta E + E_0$ versus *n* is displayed in figure 4.9 (a), showing good agreement with the bandgap values obtained from Tauc's plot. E_0 was taken as the bandgap of sample X. Therefore, the observed trends in optical properties both in absorption and emission can be directly correlated with the measured trend in carrier concentration, *n* and Ge incorporation.

4.2 Ge doping of AlGaN

AlGaN alloys are studied extensively as contact layers of UV LEDs and laser diodes. For these applications, conductive AlGaN alloys with high Al content are necessary. Hence the role of dopants, impurities and defects in such systems have to be understood. Silicon (Si) is used for the n-type doping, but achieving highly conductive n-type $Al_xGa_{1-x}N$ for x > 0.70 is proven difficult. Beyond this threshold, a sharp increase in the donor activation energy [157–159] and resistivity [160] was observed. Carrier compensation by deep level defects, including deep Si DX centers, has often been speculated. DX centers are formed when a shallow donor impurity undergoes a large bond-rupturing displacement and becomes a deep acceptor by trapping electrons. This heavily drops the carriers available for conduction. Different calculations support that Si forms a deep DX center in $Al_xGa_{1-x}N$ [40,41,161,162]. Thus, Park and Chadi [161] predicted the onset of DX behavior for Si to occur at x > 0.24, whereas Boguslawski and Bernholc [40] predicted that Si-related DX centers are stable at x > 0.60, and Gordon et al. [41] obtained an onset of DX transition for x = 0.94. Experimental results are also contradictory, e.g. some studies suggested Si to be a DX center in $Al_xGa_{1-x}N$ for x > 0.5 [42], others for x ≥ 0.84 [163], and some show indications of self-compensation for high doping levels ([Si] > 3×10^{19} cm^{-3}) for x ≥ 0.42 [164].

Ge doping was possible in GaN as it was a shallow donor like Si. However, there is very little information about its behavior in $Al_xGa_{1-x}N$. Gordon et al. [41] predicted the onset of the DX transition for Ge in AlGaN at x = 0.52. However, at the beginning of my PhD, to our knowledge, there were no experimental studies of Ge doping of AlGaN. In view of the results obtained for GaN, it was interesting to explore its behavior in the ternarly alloy.

4.2.1 Structural properties and Al content

Ge-doped $Al_xGa_{1-x}N$ thin films of thickness 675 nm were grown by PAMBE. The samples were grown, first for low Al content (<40%), for varying Ge concentrations in the range 10^{19} to 10^{21} cm^{-3} (T_{Ge} = 840°C, 928°C, 1011°C) for constant Al composition of 12%, 24%, and 36%. Then we varied the Al cell temperature to introduce more Al keeping a constant Ge cell temperature of 1011°C. A GaN reference sample was also made at the same Ge cell temperature. The list of samples and their properties are recorded in table 4.2.

The Al content of selected samples was measured by using Rutherford backscattering spectroscopy (RBS) using 1.8 MeV He^+ ions and a silicon surface barrier detector at a scattering

angle of 160°. As an example, the RBS spectrum of sample A7G3 is displayed in figure 4.10. The data is fitted using NDF code [165]. Based on these measurements, the estimation of Al content for all the samples is presented in table 4.2.

Sample name	**Sample code**	**Al content (%)**	**T_{Ge} (°C)**	**n (cm^{-3})**	**ρ (Ωcm)**	**PL peak at 5K (nm)**	**ε_{xx} (%)**
E3763	A0G3	0	1011	1.3×10^{21}	2.1×10^{-4}	341.5	–0.12
E3743	A1G1	12±1 (*)	840	1.0×10^{19}	9.8×10^{-3}	321.5	–0.18
E3745	A1G2	12±1 (*)	928	2.1×10^{20}	1.1×10^{-3}	332.0	–0.11
E3746	A1G3	12±1 (*)	1011	1.2×10^{21}	2.9×10^{-4}	332.0	–0.11
E3747	A2G1	24±1 (*)	840	6.2×10^{18}	4.7×10^{-2}	319.5	–0.18
E3751	A2G2	24±1	928	6.7×10^{19}	6.4×10^{-3}	319.8	–0.11
E3753	A2G3	24±1 (*)	1011	4.5×10^{20}	8.4×10^{-4}	316.1	–0.14
E3752	A3G1	36±1 (*)	840	2.8×10^{18}	8.6×10^{-2}	301.0	–0.17
E3750	A3G2	36±1 (*)	928	9.8×10^{18}	3.7×10^{-2}	302.0	–0.28
E3754	A3G3	36±1	1011	5.6×10^{19}	5.8×10^{-3}	302.0	–0.22
E3764	A4G3	47±1	1011	2.4×10^{20}	6.2×10^{-3}	283.0	–0.31
E3765	A5G3	53±1	1011	4.9×10^{19}	3.4×10^{-2}	280.0	–0.15
E3782	A6G3	64±1	1011	1.2×10^{18}	1.4	275.0	–0.33
E3783	A7G3	66±1	1011	--	3.8	272.0	–0.35

(*) Estimation from RBS measurements in other samples.

Table 4.2: Description of samples under study: Al content obtained from RBS, Ge cell temperature (T_{Ge}), room-temperature carrier concentration (n) and resistivity (ρ) from Hall effect measurements, PL peak energy of band-to-band transitions at 5 K.

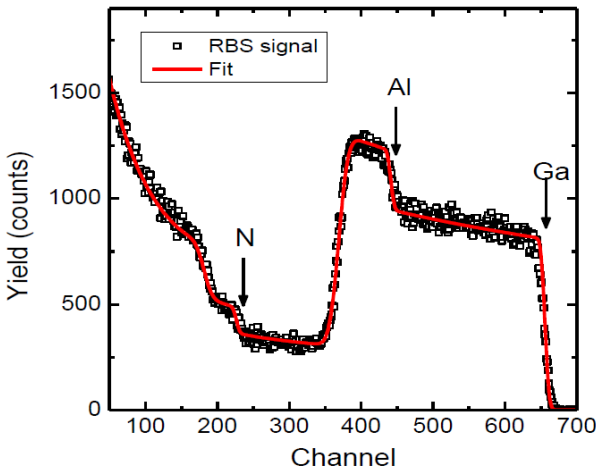

Figure 4.10: RBS spectrum of Ge doped AlGaN (66%) with fit generated by NDF code.

The Ge distribution in samples A5G3, A5G3, A6G3 and A7G3 was studied by using particle-induced X-ray emission (PIXE), as illustrated by the 530×530 μm^2 elemental maps in figure 4.11. The average Ge concentration extracted from the PIXE data is in the range of 0.12-1.5×10^{21} cm^{-3}. The large error bar is due to the proximity of the signals from Ga and Ge. The images show that high Al mole fraction (> 40%) leads to inhomogeneous Ge incorporation

with tens-of-µm-sized areas with large clustering. In the Ge-rich regions, the Ge concentrations reaches values around 3×10^{21} cm^{-3}.

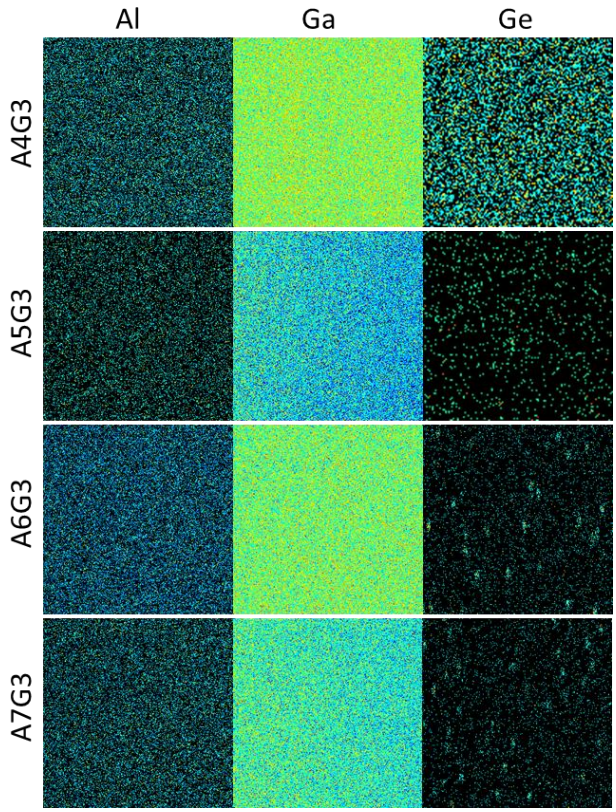

Figure 4.11: Elemental (Al, Ga, Ge) PIXE maps from samples A5G3, A5G3, A6G3 and A7G3. All the images represent a 530×530 μm^2 surface. Al and Ga appear homogeneously distributed in the samples, whatever the Ga/Al ratio. In contrast, the samples with higher Al mole fraction (A6G3 and A7G3) presents inhomogeneous Ge incorporation, with tens-of-µm-sized areas with large clustering.

The structures were further analyzed by x-ray diffraction using symmetric ω–2θ scans of the (0002) reflection for all the samples and the asymmetric (−1015) reflection for selected samples. From the angular location of the symmetric reflection, it is possible to extract the lattice parameter *c*. From this value, and assuming that the strain is biaxial, we calculated the in-plane strain, ε_{xx}, with the results summarized in table 4.2 and figure 4.12 (a). Let us remind here that the lattice mismatch between GaN and the AlN template is ≈ 2.6%. The AlGaN samples feel an important compressive stress at the beginning of the growth, and the mismatch relaxes progressively, as observed for binary compounds grown under metal excess [109]. The strain that remains after growth is around ε_{xx} = 0.12±0.04% and increases with the Al mole fraction of the layers, as illustrated in figure 4.12 (a). The slow relaxation process of the AlGaN layer manifests in the elongation of the (−1015) reflection towards more negative Q_x and smaller Q_z (Q_x, Q_z are the reciprocal space vectors) in figure 4.12 (b), which contrasts with the Q_x symmetry of the reflection from the AlN substrate. These features (magnitude of the residual strain and asymmetry of the XRD reflections) do not depend on the Ge content of the layers, being present for both low and heavily doped samples.

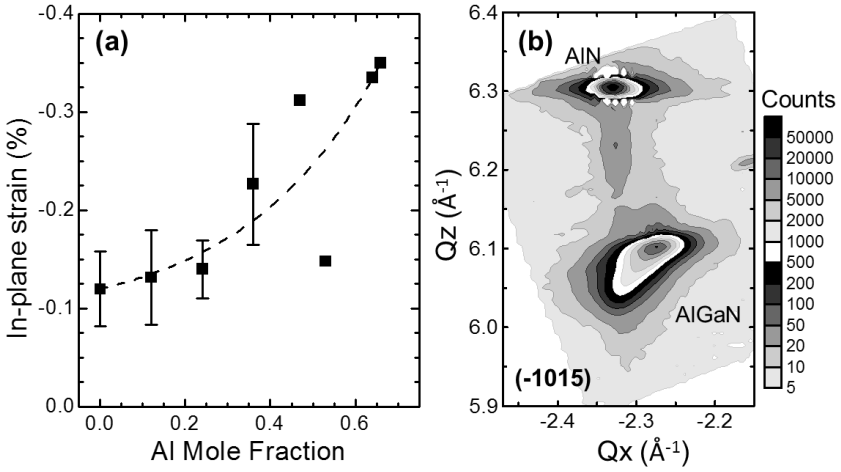

Figure 4.12: (a) In-plane strain in the AlGaN:Ge layers extracted from ω–2θ scans around the (0002) reflection. (b) Reciprocal space map of sample A3G3 showing the (−1015) reflections of the Ge-doped AlGaN layer and the AlN template.

4.2.2 Electrical properties

The evolution of free carrier concentration, *n* and the resistivity ρ, with increase in Al content was studied by the Hall effect technique at 300 K using the Van der Pauw method. The results are presented in table 4.2. For low Al content, x < 0.4, the data is plotted in figure 4.13 (a) as a function of the temperature of the Ge cell. Results are compared with the case of GaN (dashed line taken from section 4.1 and sample A0G3), which is consistent with $n \propto \exp(-E_{Ge}/k_B T_{Ge})$ where E_{Ge} = 3.58 eV is the thermal evaporation energy of Ge, and k_B is the Boltzmann constant. For x = 0.12, results are approximately the same as for GaN. On the contrary, increasing the Al mole fraction to x = 0.24 leads to a decrease of the carrier concentration to 40% of the value for GaN, but maintains the slope of the trend, which points to the dopant level getting deeper into the bandgap. For x = 0.36, the carrier concentration decreases further and we observe that the variation with T_{Ge} starts to deviate from the trend for GaN. This is understood as a variation in the nature of the dopant, which is not only getting deeper in the bandgap but also self-compensating. This Al concentration is well below the predicted value for the onset of the DX configuration, but it could be related to the initiation of the clustering process that was described above.

For the highest Ge cell temperature used in this study, T_{Ge} =1011°C (leading to $n = 1.3\times10^{21}$ cm^{-3} in GaN, sample A0G3), the variation of *n* and ρ with the Al content is plotted in figure. 4.13 (b). A significant decrease in n is observed for x ≥ 0.24. At the highest Al composition of x = 0.66, we report a resistivity of 3.8 Ωcm. For this sample, reliable measurements of *n* were not possible due to the high resistance.

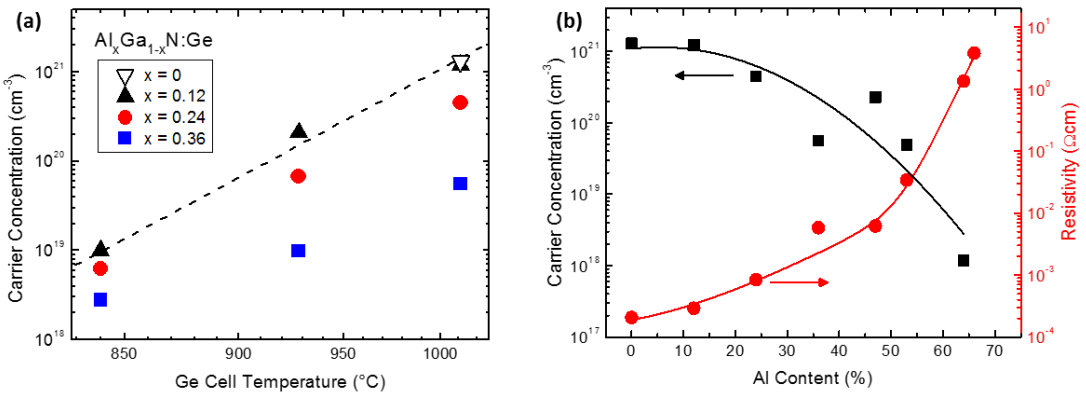

Figure 4.13: (a) Variation of the carrier concentration at room temperature measured by Hall effect as a function of the temperature of the Ge cell. Experimental values for Ge-doped $Al_xGa_{1-x}N$ (x = 0, 0.12, 0.24, and 0.36) are presented. The dashed line indicates the variation in the case of GaN. (b) Evolution of the carrier concentration and resistivity with the Al concentration in $Al_xGa_{1-x}N$ layers with [Ge] = 1×10^{21} cm^{-3}.

Temperature dependent Hall effect (77 K to 300 K) measurements were carried out to determine the effective activation energy, E_a. The E_a of the samples are derived in a similar method to that in section 4.1.3 by using equation 4.3. The E_a value extracted is plotted against Al content in figure 4.14. For the same Al content, the activation energy is lower (≈5-10 meV) for the highest T_{Ge} than in more lightly doped samples. This is due to the increased Ge concentration, above Mott concentration, which readily places carriers in the conduction band. In the lightly doped samples, the carriers require a finite energy before being available for conduction. However as Al content is increased for the same Ge concentration, we find that E_a increases for both T_{Ge}, reaching ≈40 meV for the highest Al content.

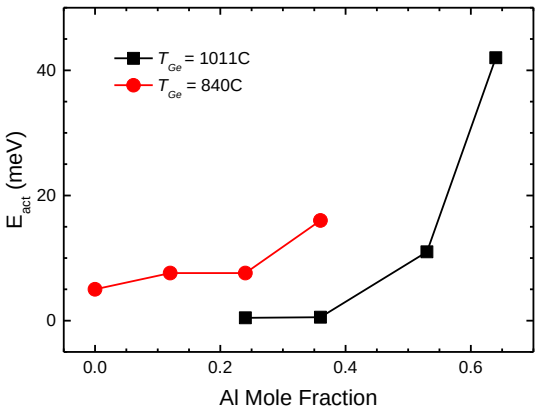

Figure 4.14: Ionization energy E_a as a function of Al content for the lowest and highest Ge cell temperatures T_{GE}.

4.2.3 Optical properties

The normalized low temperature (T = 5 K) PL spectra of the $Al_xGa_{1-x}N$ samples with the highest doping level (T_{Ge} = 1011°C) is displayed in figure 4.15 (a). The spectra are dominated by the band-to-band emission, which blueshifts with increasing Al content. The PL peak positions of all the samples are provided in table 4.2 from where we can infer that, for a constant Al content, we observe a blueshift with increasing Ge incorporation due to band filling. However, as Al content is increased, the blueshift with Ge incorporation becomes less significant due to the lower density of free carriers.

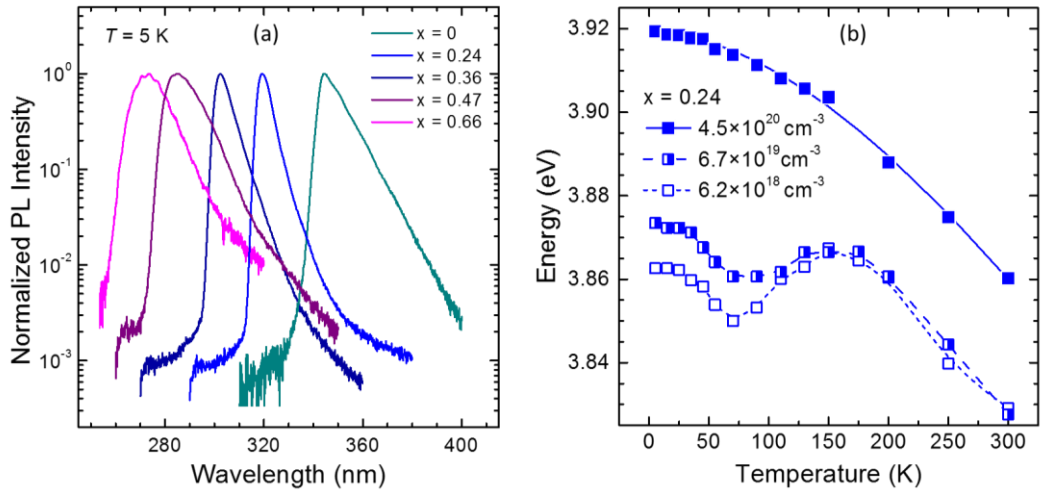

Figure 4.15: (a) Normalized Low temperature (5 K) PL spectra of the highest doped samples (T_{Ge} = 1011°C). (b) Temperature dependent PL peak positions of samples with 24% Al.

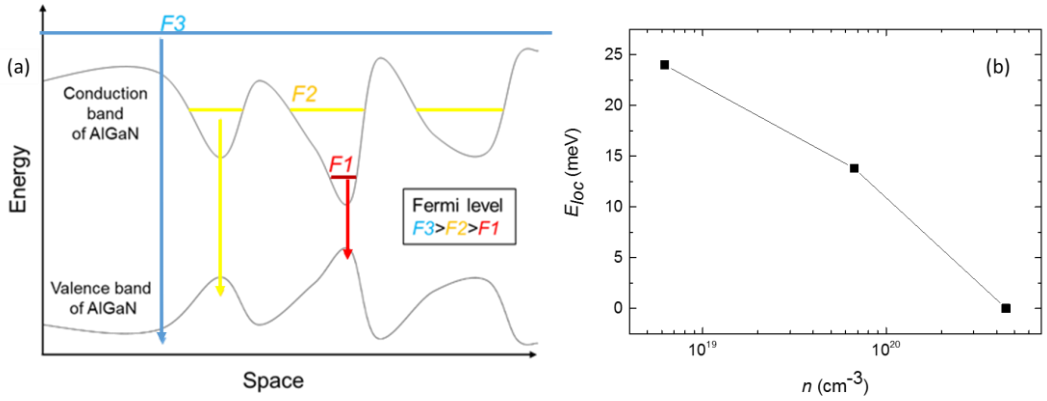

Figure 4.16: (a) Illustration of carrier localization caused by alloy fluctuations and subsequent screening for increasing Fermi energy, (b) Variation of E_{loc} as a function of carrier concentration.

Figure 4.15 (b) describes the variation of band-to-band emission energies (PL peak position E_{PL}) with temperature for samples with x = 0.24. For the lower doping levels, the evolution presents an S-shape behavior, with a blueshift between 70 K and 150 K. This is explained by the fact that the low-temperature emission is dominated by transitions of carriers localized in alloy fluctuations [114,166]. As temperature is increased beyond 150 K,

carriers get thermally delocalized, and E_{PL} follows Varshni's law (equation 2.2). For the highly doped sample, even at low temperatures, the potential fluctuations due to the alloy inhomogeneities are screened, as the Fermi level already lies further inside the conduction band. Here, the temperature variation of the PL peak energy readily follows the Varshni's law. This process of screening of the fluctuations is described in figure 4.16 (a). For these samples, the shift in PL peak energy at 5K with respect to that described by Varshni's law was used to calculate a localization energy, E_{loc}, obtaining the values that are plotted in figure 4.16 (b). For the samples with the lowest doping level, the estimated localization energy, E_{loc} = 23±3 meV. Such a localization energy can be justified by alloy fluctuations in the order of x ± 0.01. Similar PL data for samples with an Al content of x = 0.36 gave the same value of localization energy, indicating similar alloy fluctuations.

The evolution of the PL Intensity I_{PL} with temperature is represented in figure 4.17 for samples with the highest T_{Ge}. The intensity follows the equation [167]

$$I_{PL} = \frac{I_0}{1+A\exp\left(-\frac{E_a}{kT}\right)} \qquad \text{(equation 4.9)}$$

where I_0 is the PL intensity at 0 K, A is the ratio of the non radiative and radiative recombinations, and E_a is the thermal activation energy of the non-radiative recombination process. With increasing Al content we see an increase in slope of the curve at high temperature, which is resulting from an increase in non-radiative processes. This is evident by the increase in A with increase in Al content as displayed in table 4.3. The onset of non-radiative recombination remains at the same temperature for all samples, i.e. the thermal activation energy does not vary significantly as shown in the table 4.3.

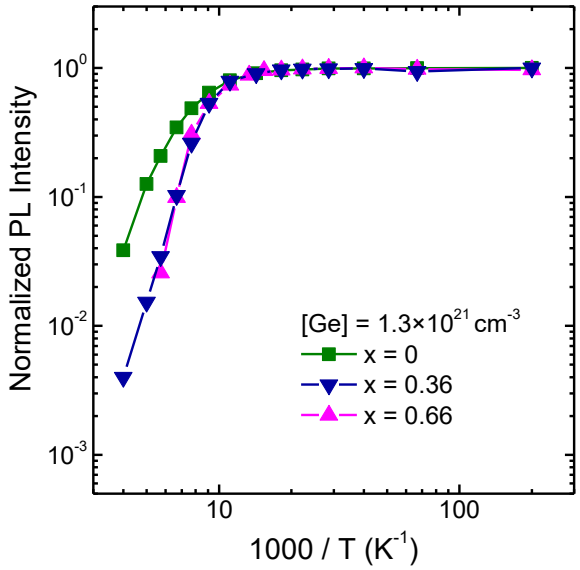

x	E_a	A
0	46±5	115±40
0.36	50±21	1700±900
0.66	65±16	1400±900

Figure 4.17: Temperature variation of PL intensity in various Ge-doped $Al_xGa_{1-x}N$ samples grown with T_{Ge} = 1011°C.

Table 4.3: Variation of E_a and A with Al content, x, in $Al_xGa_{1-x}N$.

4.3 Conclusion

From these studies we conclude that the presence of Ge flux (≤1000°C) during the growth of wurtzite GaN does not perturb the Ga growth kinetics. We grew Ge-doped GaN thin films with carrier concentrations of up to 6.7×10^{20} cm^{-3} at 300 K, well beyond the Mott density. The Ge concentration and free carrier density were found to scale linearly with the Ge flux in the studied range. All the GaN:Ge layers presented smooth surface morphology with atomic terraces, without traces of pits or cracks, and the mosaicity of the samples has no noticeable dependence on the Ge concentration. The variation of the GaN:Ge bandgap with the carrier concentration is consistent with theoretical calculations of the bandgap renormalization due to electron-electron and electron-ion interaction, and the Burstein-Moss effect.

We grew Ge-doped $Al_xGa_{1-x}N$ thin films with Al mole fraction up to x = 0.64. We successfully demonstrated that Ge does not induce any structural or optical degradation in AlGaN samples with x < 0.4. For higher Al compositions, Ge rich clusters were observed. Keeping the Ge concentration constant to [Ge] = 1×10^{21} cm^{-3}, Hall Effect measurements at room temperature show a gradual decrease of the carrier concentration when increasing the Al mole fraction. This decrease is already noticeable in samples with x = 0.24. Samples with x = 0.64-0.66 remain conductive (σ = 0.8-0.3 $\Omega^{-1}cm^{-1}$), but the carrier concentration drops to 1×10^{18} cm^{-3}, which implies a donor activation of 0.1%. From the optical point of view, the low temperature PL is dominated by the band-to-band emission. When increasing the doping concentration, the PL blueshifts due to band filling. Furthermore, from the evolution of the PL peak position with temperature, we observe the screening of the localization induced by fluctuations of the alloy composition.

5. Growth of GaN nanowire by MBE

In this chapter, we present the development of GaN nanowires grown by PAMBE on Si(111) substrates. The insertion of a thin AlN buffer layer is necessary to improve the vertical alignment of the wires. However, the presence of AlN results in huge 2D undergrowth. To solve this problem, we develop a low-temperature AlN growth process. We then make an analysis of the impact of the gallium flux and substrate temperature on the coalescence and growth rate of the nanowires.

For this study, I performed the MBE growth and SEM measurements. Part of the work concerning the growth of the AlN pre-buffer was published in, "ISB Absorption in Si- and Ge-Doped GaN/AlN Heterostructures in Self-Assembled Nanowire and 2D layers", A. Ajay et al., Phys. Stat. Sol. B 254, 1600734 (2017) [168].

5.1 Substrate preparation and buffer layer

Self-assembled, N-polar GaN nanowires were synthesized on Si(111) using nitrogen-rich conditions in PAMBE. We used various shapes and sizes of the Si(111) substrate, including 1.5×1.5 cm^2 squares, quarters of 4" wafers, and 3×3 cm^2 squares. First, the substrates were degreased with organic solvents, which included dichloromethane, acetone and methanol, in an ultrasound bath. Then, they were mounted in custom-designed molybdenum sample holders where samples are held between two plates by metal 'fingers'. This allows direct heating of the substrate. A GaN nanowire sample and the corresponding sample holder front plate and back plates are shown in figure 5.1 (a), (b) and (c) respectively. Note that the areas marked by the four fingers of the front plate can be clearly seen on the sample.

The extremities of the sample close to the finger were too cold for any nanowire growth to happen. From the center of the sample to a circle of ≈ 2 cm in diameter, the samples remain homogeneous in characteristics. Between this first circle and a second circle that is larger in radius by 0.5 cm, the temperature is ≈ 5°C lower than at the center. This was estimated by comparing samples grown with substrate temperatures differing by 5°C. Beyond the second circle, the temperature is largely inhomogeneous.

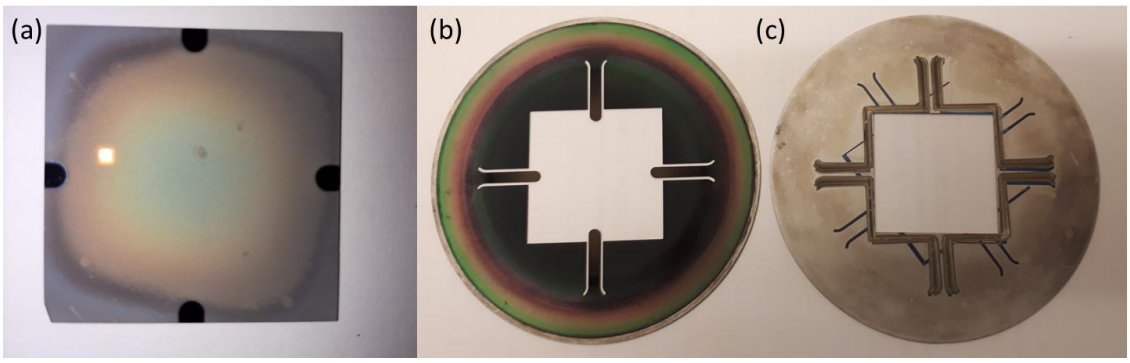

Figure 5.1: (a) A sample containing GaN nanowires on Si(111) of dimension 3×3 cm^2. (b) Front plate and (c) back plate of the corresponding sample holder.

The following describes the preparation of the substrate surface once it is placed inside the growth chamber. It is well known that oxide-free Si(111) exhibits surface reconstructions depending on the temperature. At temperatures above 850°C, a 1×1 structure is obtained, which converts to a 7×7 reconstruction when cooled down [169]. We have used this transition as temperature reference for all the substrate temperature values provided in this chapter. The growth process starts by baking the substrate for 5 min at high temperature (880ºC) to remove the native oxide. During the baking process we observed an unreconstructed 1×1 pattern with strong Kikuchi lines using RHEED. It evolved slowly towards the 7×7 reconstruction as the sample was cooled down to a temperature of 810°C, as depicted in Fig 5.2(a).

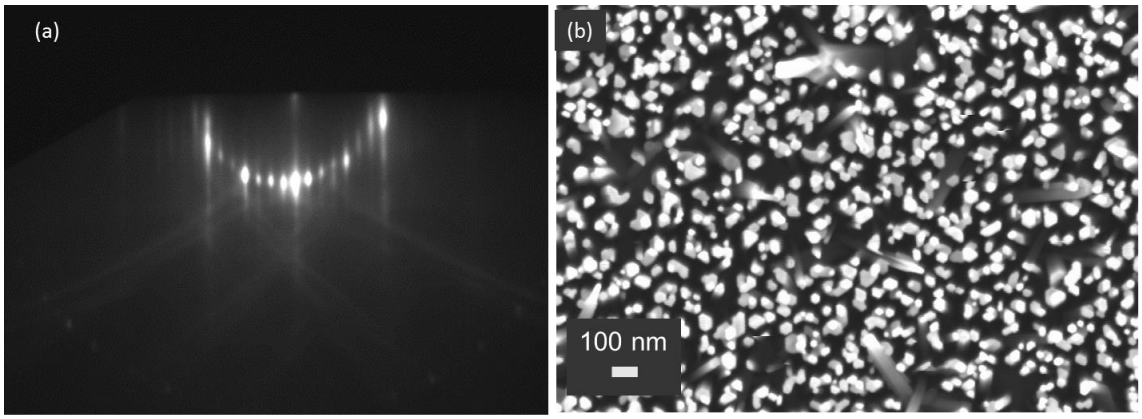

Figure 5.2: RHEED images of (a) 7×7 reconstruction of Si(111), (b) GaN nanowires grown directly on Si(111) at 810ºC.

As a first approach, GaN nanowires were directly grown on the substrate by keeping the nitrogen flux fixed at the value required to produce planar GaN layers at a growth rate of 0.50±0.01 ML/s under N-limited conditions. The Ga flux was kept below that value (Φ_{Ga} = 0.429 ML/s), to ensure nitrogen-rich conditions, and the substrate temperature was T_S = 790°C.[4] At these growth conditions, we observe a spotty RHEED pattern overlapping with a faint ring-like pattern. The resulting self-assembled GaN nanowires are described in the SEM image in figure 5.2(b) showing that the nanowires were slightly tilted, as reported in previous studies [170].

In order to improve the nanowire orientation, we added a 1.2-nm-thick AlN buffer layer prior to the GaN deposition at the same substrate temperature. The AlN buffer was expected to grow in a 2D regime (i.e. slightly Al-rich conditions) which was confirmed by a streaky RHEED pattern [171]. We grew three samples at different growth temperatures of 750ºC, 770ºC and 790ºC with the same impinging Ga flux (Φ_{Ga} = 0.429 ML/s), to rule out any substrate

[4] Note that the desorption of Ga is relevant (in comparison with the growth rate) for temperatures higher than 700°C, to the point that at 720°C the Ga desorption flux is comparable to the growth rate. In this chapter, the value of Φ_{Ga} is given in terms of impinging flux, knowing that the density of adsorbed Ga is much lower (to be precise, Φ_{Ga} multiplied by the sticking coefficient, which depends on the substrate temperature).

temperature related uncertainty (samples listed in table 5.1). For all growth temperatures under investigation, the presence of such an AlN buffer layer leads to an improved perpendicularity of the nanowires with respect to the substrate surface, as shown in Figure 5.3, but it results also in parasitic 2D growth of GaN between the nanowires and decreased nanowire density compared to samples grown at the same conditions without the buffer layer. This has been attributed to the fact that the AlN buffer presents mixed polarity [172,173].

Sample name	T_s	Φ_{Ga}	**Growth time**
E3545	750°C	0.429 ML/s	3 h
E3544	770°C	0.429 ML/s	3 h
E3550	790°C	0.429 ML/s	3 h

Table 5.1. Samples with AlN buffer layer that is grown at the same temperature as the growth temperature where T_s is the temperature of the substrate and Φ_{Ga} is the impinging Ga flux.

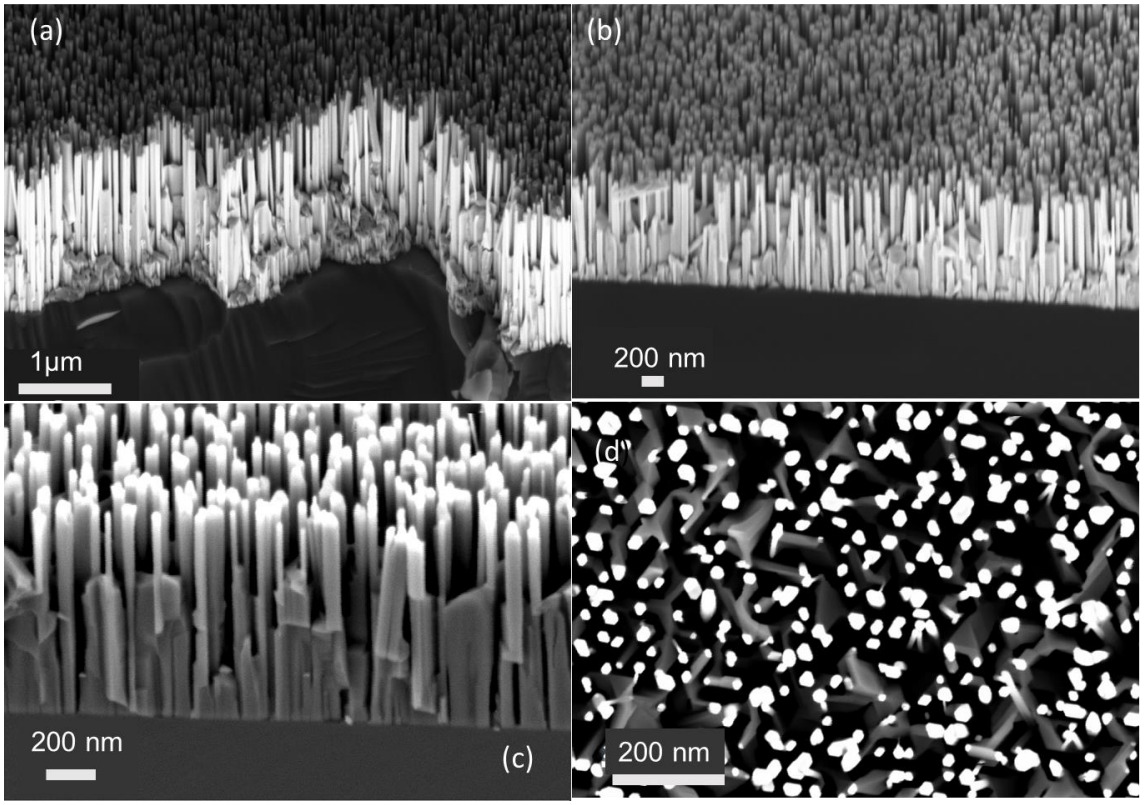

Figure 5.3: Tilted view SEM images (a) E3545 (T_s=750°C), (b) E3550 (T_s=790°C) and (c) E3544 T_s=770°C). The GaN undergrowth is clearly visible. (d) Top view SEM images of E3544. The undergrowth is still visible, however note that the nanowires are well separated (modified from ref. [168]).

In order to obtain GaN nanowires without GaN undergrowth, we used a two-step growth procedure for AlN similar to the works of Schenk, *et al.* [174] and Musolino, *et al*. [175]. After baking the substrate, it was cooled down to 200°C, and we deposit 1.2 nm of AlN at stoichiometric conditions at this low temperature. At this point, the RHEED pattern evolves from the 7×7 reconstruction to the pattern in figure 5.4(a). An 8-nm-thick AlN buffer layer was then grown at stoichiometric conditions at 670°C. This resulted in the characteristic 1×1

RHEED pattern of stoichiometric AlN, in figure 5.4(b). GaN nanowires were then grown at a substrate temperature around 780°C, for the same Ga flux as for the samples in table 5.1. The RHEED pattern during the growth was the spotty wurtzite pattern shown in figure 5.4(c). The resulting GaN nanowires are displayed in the SEM image in figure 5.4(d), which shows no parasitic 2D growth and nanowires oriented perpendicular to the substrate surface. All the nanowires discussed hereforth contain the AlN buffer layer grown using this two-step growth procedure.

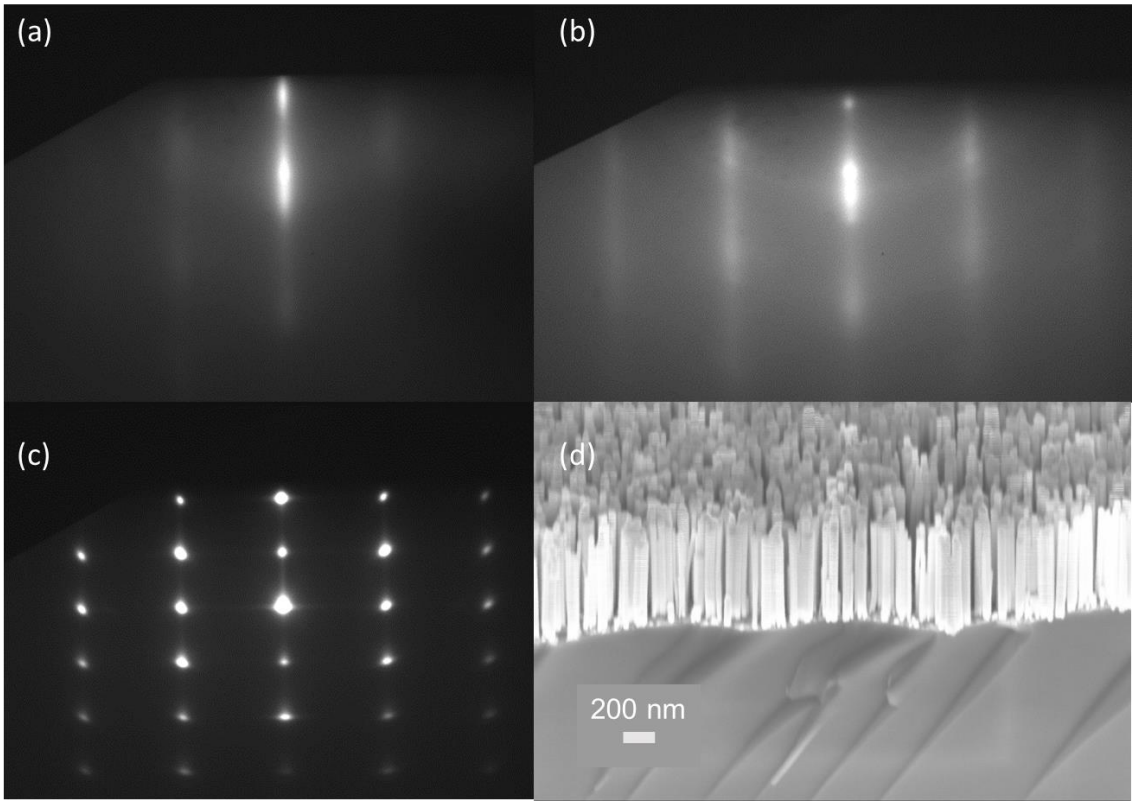

Figure 5.4: RHEED images of (a) 1.2-nm-thick AlN on Si(111) (the diffraction pattern of Si is still visible below the 1×1 reconstruction of AlN), (b) 1×1 pattern of stoichiometric AlN after deposition of the buffer layer, and (c) spotty wurtzite pattern during the growth of GaN nanowires on an AlN buffer layer. (d) SEM image (tilted at 45°) of GaN nanowires grown on Si(111) using an AlN buffer made using the two-step growth procedure described in this manuscript. (Modified from ref. [168]).

5.2 Influence of growth temperature and Ga flux

The effect of temperature and Ga flux on GaN nanowire growth has been widely addressed in the literature [123,170,176]. This section describes our study to find the right growth window to obtain well separated GaN nanowires. Figure 5.5 presents SEM images of nanowires grown under substrate temperatures and Ga fluxes as indicated. The total growth time is always 3 hours. The average height of the nanowires is mentioned on top of the respective SEM images. It can be noticed that for a fixed Ga flux, increasing the substrate temperature beyond a certain threshold leads to a decrease in the total height of the nanowires and increased variation in nanowire height. For example, for an impinging Ga flux

of 0.338 ML/s, the total height changes from 600-650 nm to 350-550 nm for a change in substrate temperature from 780°C to 785°C. Increasing the substrate temperature by approximately 10°C, results in the absence of nanowires due to enhanced GaN decomposition.

Increasing the maximum nanowire height, without coalescence, requires increasing the Ga impinging flux. In turn, for higher Ga fluxes, the growth of nanowires requires a higher substrate temperature to avoid coalescence, and there is a larger window of substrate temperatures between highly-coalesced nanowires and the absence of nanowires.

Note that, in the investigated windows, the maximum nanowire growth rate is still far from the thickness of a planar GaN layer grown under N-limited conditions (≈ 1.3 µm) at 720°C (our standard planar growth conditions). This is due to the important GaN decomposition that takes place at the high growth temperatures used for nanowire growth.

Figure 5.6 presents a more detailed analysis of nanowires grown at the same Ga flux of 0.429ML/s, only varying the substrate temperature between 755°C and 795°C. Increasing the growth temperature resulted in thinner nanowires, decreased coalescence and decreased nanowire density. This is due to enhanced adatom diffusion and desorption, and increased GaN decomposition [118]. Even though the coalescence was sharply reduced at the highest growth temperature, there was still coalescence between a few wires, resulting in the formation of bundles [177]. The average distance between the wires for the sample grown at 795°C was 33±10 nm, calculated by sampling the shortest distance between nearest nanowires that are not coalesced. Such large interwire distances are highly valuable for growing GaN nanowires containing MQWs of Al(Ga)N, as an AlN shell forms around the nanowires, which increases the effective nanowire diameter.

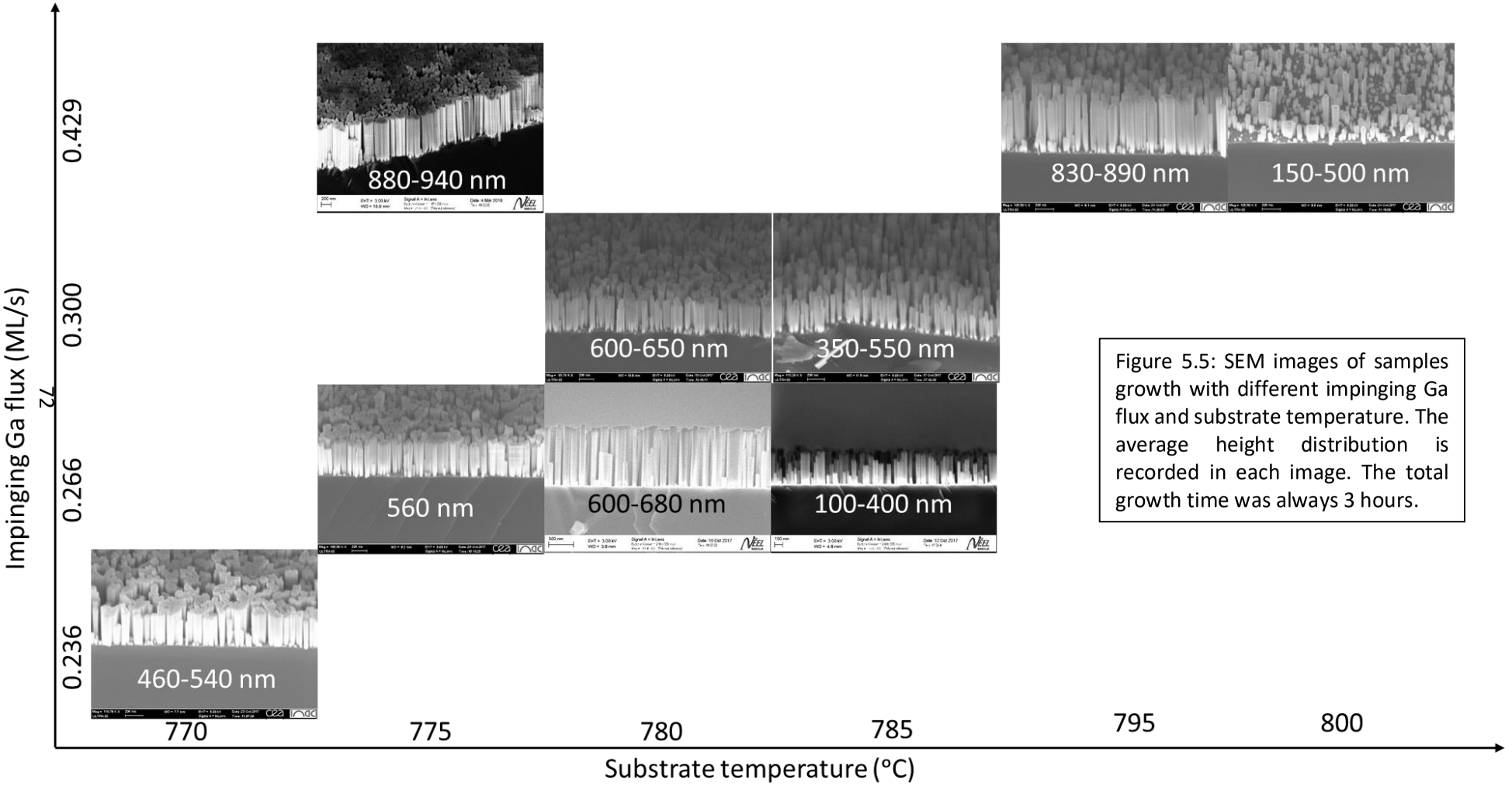

Figure 5.5: SEM images of samples growth with different impinging Ga flux and substrate temperature. The average height distribution is recorded in each image. The total growth time was always 3 hours.

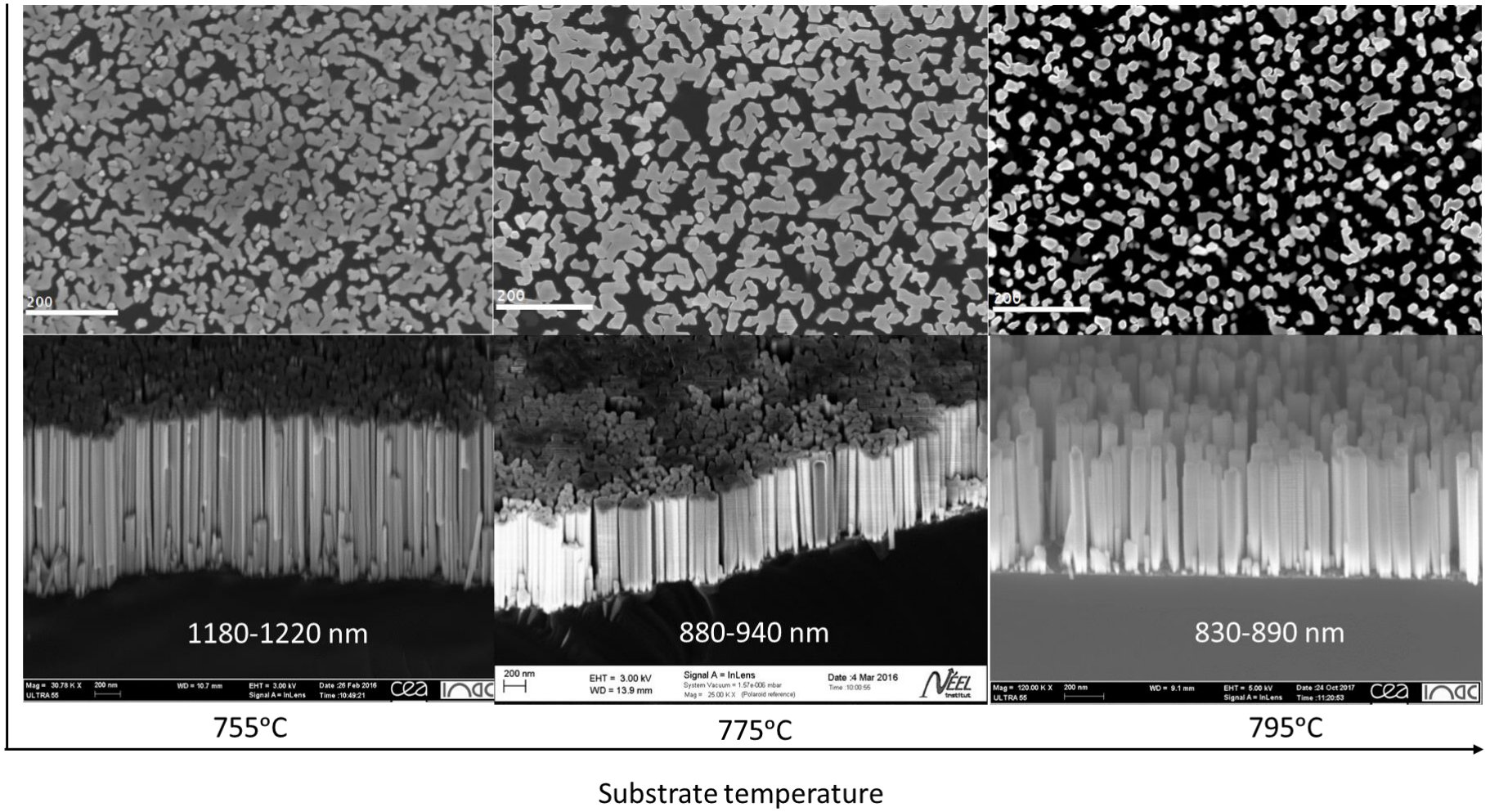

Figure 5.6: SEM (top view on top, bird's eye on bottom) images of samples grown at different temperatures. The average height distribution is recorded in each image. The total growth time was always 3 hours.

5.3 Conclusion

Here, we have presented a study on the synthesis of self-assembled GaN nanowires on Si(111) using PAMBE. We observed that a thin AlN buffer layer can be used to improve the nanowire alignment perpendicular to the substrate. However, we noticed the appearance of undesirable GaN undergrowth when the AlN buffer layer is grown at the same temperature as the nanowires. To overcome this issue, we developed a two-step low temperature AlN buffer growth process. We then analyzed the impact of the impinging gallium flux and substrate temperature on the coalescence and growth rate of the nanowires, on substrates prepared with such two-step AlN buffer layer. To increase the nanowire growth rate, we need to increase the impinging Ga flux, and to prevent coalescence at high Ga fluxes, we need to increase the substrate temperature. Growth at higher substrate temperature results in thinner, less densely packed nanowires due to the enhanced adatom diffusion, desorption and increased GaN decomposition.

6. GaN/AlN heterostructures for the short-wavelength IR range

In this chapter, we present a study of GaN/AlN heterostructures designed to absorb in the SWIR spectral range, considering both planar structures and nanowire heterostructures. In sections 6.1 and 6.2, we assess the effect of the nature of the n-type dopant, either Ge or Si, and the dopant concentration on the structure geometry and on the optical properties. In this work, I performed the MBE growth, HRXRD, SEM, TEM image analysis, Hall effect measurements, time-resolved/continuous-wave PL measurements, FTIR measurements and theoretical calculations. I worked together with C. B. Lim for the characterization of planar heterostructures (HRXRD, continuous-wave PL and FTIR). TEM images were obtained by Dr. M. I. den Hertog. The complete study was published in "Effect of doping on the ISB absorption in Si- and Ge-doped GaN/AlN heterostructures", A. Ajay et al., Nanotechnol. ***28*** *405204 (2017)* [178] *and "Effect of Ge-doping on the short-wave, mid- and far-IR ISB transitions in GaN/AlGaN heterostructures", C.B Lim et al., Semicond. Sci. Technol.* ***32*** *125002 (2017)* [179].

Finally, in section 6.3 we introduce top-down nano/micropillar heterostructures, also absorbing in the SWIR. For this study, I performed theoretical calculations and XRD measurements, working in collaboration with Dr. D. A Browne and Dr. E. Monroy. The samples were grown by Dr. E. Monroy, and the top-down etching and optical characterization were performed by Dr. J. Lähnemann. The complete study has been submitted for publication [180].

6.1 Ge vs Si doping in planar GaN/AlN heterostructures

N-type doping is a critical parameter in controlling the performance of ISB photodetectors or modulators because of the need to populate subbands in the conduction band. While a variety of GaN based ISB devices has been demonstrated, these devices are primarily based on a planar geometry and utilize Si as a dopant. For example, see the topical review ref. [181]. Based on the advancements in Ge doping in GaN thin films (discussed in chapter 4), it became interesting to assess the performance of planar ISB structures as a function of the nature of the dopant, either Ge or Si.

6.1.1 Sample structure

The planar samples under study contain 25 periods of GaN/AlN (≈ 1.8 nm / 3 nm), designed to present an ISB transition at 0.729 eV (1.70 µm) for low doping levels. The samples were grown using PAMBE on AlN-on-sapphire templates. A 340-nm-thick GaN buffer layer was deposited on the substrate before growing the heterostructure. This GaN buffer layer is partially strained on the AlN allowing the growth of heterostructures without cracking [109]. The GaN QWs in the samples were doped with Ge or Si with different doping densities as described in table 6.1. The dopant cell temperature to free carrier concentration ratio was

calibrated using Hall effect measurements on doped GaN thin films. The growth finishes with the deposition of a 30 nm AlN cap, to avoid the influence of surface charges. Figures 6.1 (a) and (b) describe the structure of the samples and the corresponding band structure simulated using 1D calculations in nextnano[3], respectively.

Figure 6.1 (c) presents XRD ω-2θ scans of exemplary samples PS3 and PG3, together with a simulation of sample PG3. The GaN/AlN MQW period of all the samples extracted from the intersatellite distance in ω-2θ scans is summarized in table 6.1. The deviations of the thickness from the nominal values are similar for both Si-and Ge-doped samples, i.e. they are not related to the nature of the dopant. Information on the mosaicity of the samples could be obtained from the FWHM of the ω scan of the zero-order reflection (MQW peak 0 in figure 6.1). The average FWHM of ω scans was 0.18±0.01° and 0.14±0.01° for Si-doped and Ge-doped MQWs, respectively, to be compared with 0.056±0.006° for the AlN substrate. The increased broadening of the heterostructures compared to the substrate is due to strain relaxation. Comparing the heterostructures, Ge-doped heterostructures systematically present ≈22% narrower rocking curves than their Si-doped counterparts on average for all doping levels.

Sample	Code	Dopant	n (cm^{-3})	Period (nm)	$\Delta\omega_{MQW}$ (°)	$\Delta\omega_{subs}$ (°)	ISB FWHM (meV)	Absorption per pass (%)	τ_{PL} (ns)
E3515	PS0	Si	1×10^{18}	4.8±0.1	0.163	0.057	-	-	11.6
E3517	PG0	Ge	1×10^{18}	4.8±0.1	0.106	0.053	-	-	7.9
E3522	PS1	Si	3×10^{19}	4.8±0.1	0.199	0.056	85	2.1	7.3
E3523	PG1	Ge	3×10^{19}	4.8±0.1	0.167	0.046	94	1.8	11.6
E3524	PS2	Si	1×10^{20}	4.8±0.1	0.180	0.061	108	8.9	3.2
E3525	PG2	Ge	1×10^{20}	4.7±0.1	0.154	0.058	90	6.6	5.6
E3588	PS3	Si	3×10^{20}	4.4±0.1	0.176	0.057	189	9.5	3.5
E3587	PG3	Ge	3×10^{20}	4.3±0.1	0.149	0.063	110	8.6	2.5

Table 6.1: Description of samples under study: dopant nature, dopant concentration (*n*), MQW period from XRD, FWHM of ω-scan of the MQW ($\Delta\omega_{MQW}$) and the substrate ($\Delta\omega_{subs}$), FWHM of the ISB absorption, absorption per pass, and decay time of the PL (τ_{PL}).

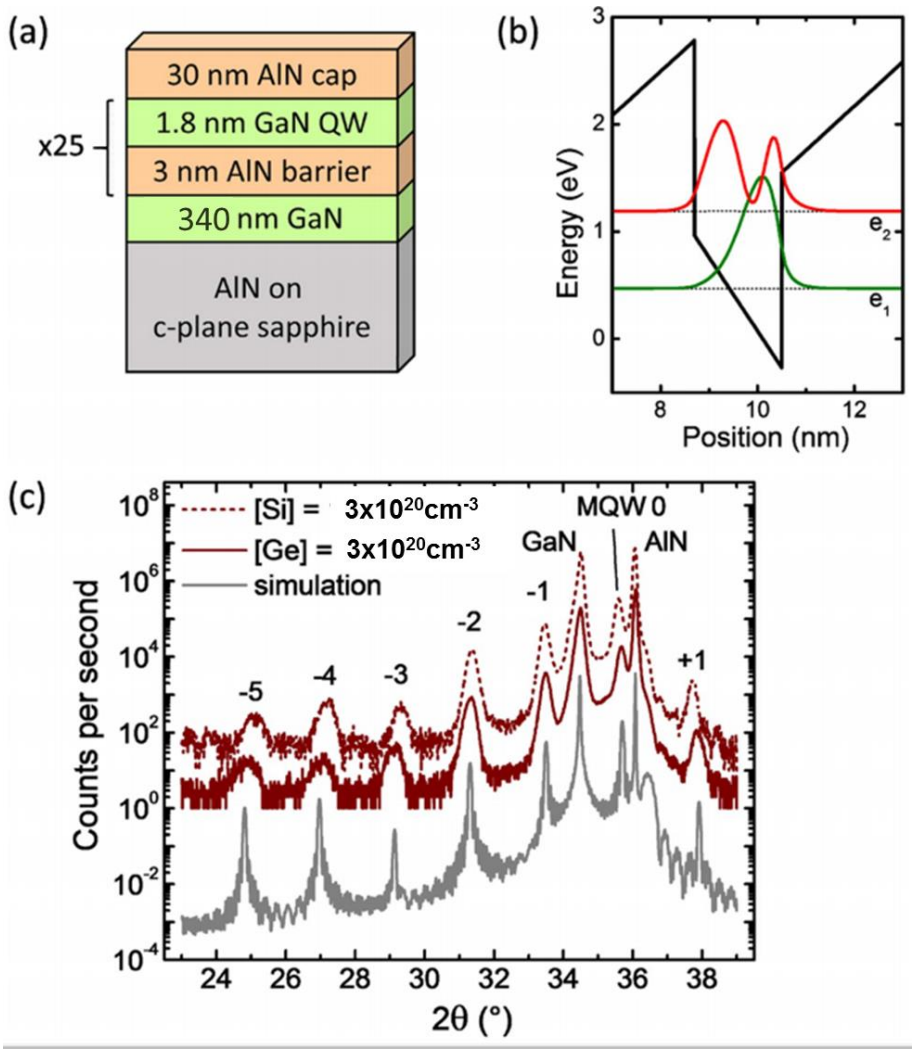

Figure 6.1: (a) Sketch of the GaN/AlN planar MQWs under study. (b) Band structure of a single quantum well, calculated using 1D nextnano[3]. (c) XRD ω-2θ scans of (0002) reflection of samples PS3 and PG3, and simulation of PG3 (modified from ref. [179]).

6.1.2 Optical properties

The band-to-band properties at 5 K of the MQWs were studied using PL spectroscopy, and the resulting spectra are displayed in figure 6.2. For both Ge- and Si- doping, the spectra present a multi-peak structure resulting from monolayer fluctuations of the well thickness [73]. When increasing the dopant density, a blueshift is clearly visible, which is assigned to the screening of the electric field by free carriers [182]. The broadening of the emission peak can be attributed to the Burstein-Moss effect (BME) [153]. We observe that the shift in emission energy and broadening is similar for both dopants.

Simulations of the electronic structure as a function of the QW thickness and for the various doping levels were performed using the 1D nextnano[3] Schrodinger-Poisson solver, with the results presented in figure 6.3. The solid lines describe the calculated emission wavelength (or energy) associated with the transition between the lowest electron energy

level, e_1, in the conduction band and the highest hole level, h_1, in the valence band of the QWs. For these calculations, the AlN barrier was chosen to be 3 nm in all the cases (the error in the e_1–h_1 transition associated with this choice is negligible). The impact of the screening of the electric field due to doping is significantly reduced in smaller QWs compared to large QWs. This is explained by the fact that free carrier screening effects scale with the ratio between the well thickness and the Debye length [182], the latter defined as

$$\lambda_D = \sqrt{\frac{\varepsilon_r \varepsilon_0 k_B T}{q^2 N_D}} \qquad \text{(equation 6.1)}$$

where $\varepsilon_r \varepsilon_0$ is the dielectric constant times the vacuum permittivity, $k_B T$ is the thermal energy, q is the electron charge and N_D is the dopant density.

Experimental data are also superimposed to the theoretical calculations in figure 6.3. These data are represented with a set of error bars where the horizontal error bar represents the uncertainty in the well thickness and the vertical error bar represents the spectral width at 90% intensity of PL peak wavelengths obtained for Si- and Ge- doping. The experimental blueshift shows the same trend as the theoretical expectations.

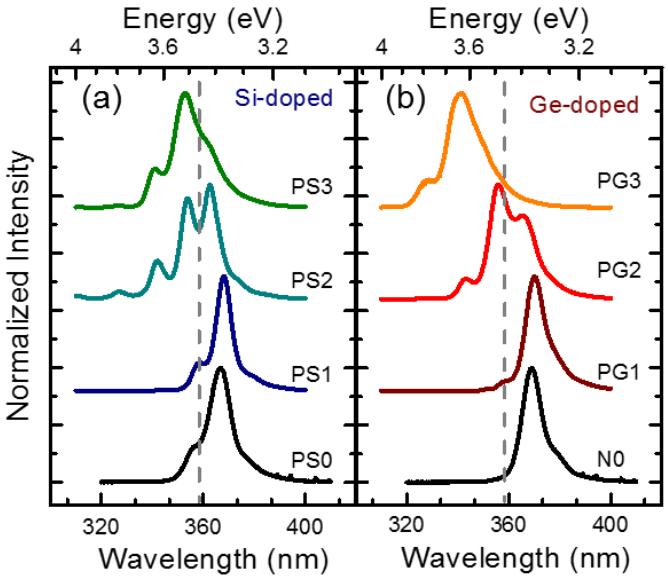

Figure 6.2: Low temperature PL intensity of all the samples under investigation. Dotted line shows GaN bandgap energy at 5 K (modified from ref. [178]).

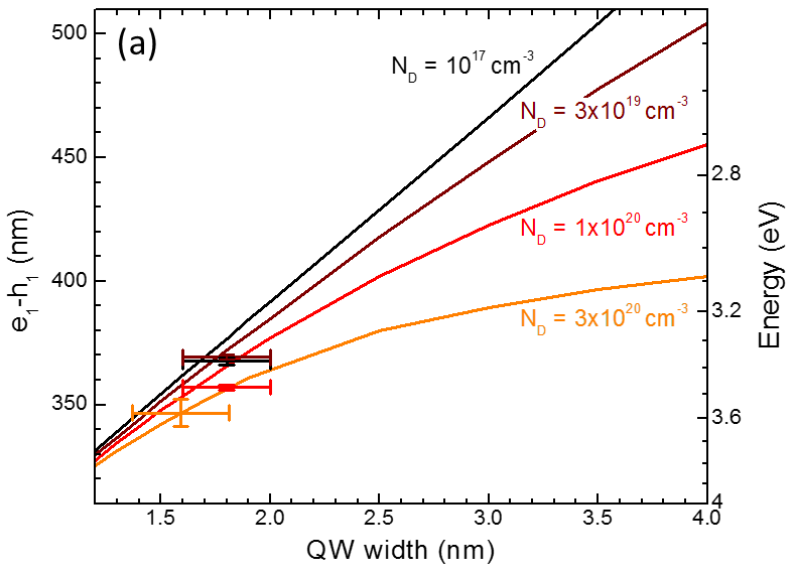

Figure 6.3: Theoretically calculated values of e_1-h_1 transitions (solid lines) and data points corresponding to PL peaks. Horizontal error bar represents the uncertainty in the well thickness and the vertical error bar represents the spectral width at 90% intensity (modified from ref. [178]).

To study the effect of free carriers on the screening of the internal electric field in the QWs, we performed time-resolved PL studies at an excitation power of 250 µW, with pulse width of 200 fs. The laser was augmented with a cavity damper section with a base pulse repetition rate of 54 MHz, allowing the period between pulses to be varied from 20 to 500 ns. Further experimental details can be found in section 3.4.3. The PL decay time constants measured for the planar samples with different doping levels are recorded in table 6.1. We observe that with increase in doping concentration the decay time constants decrease consistently for both dopants. This is consistent with the onset of screening of the internal electric field by free carriers.

The ISB properties of the samples were accessed using room temperature FTIR measurements. The measured absorption in the SWIR range, for TM-polarized light, is displayed in figure 6.4. ISB absorption is observed in samples with both Si as well as Ge doping and is well covering the 1.55 µm (0.799 eV) wavelength. As mentioned before, such heterostructures based on Si-doping had been extensively studied and are well documented in ref. [181]. For Ge-doped heterostructures we observe absorption covering 1.75 µm to 1.45 µm. The absorption is due to transitions from the first to the second electronic level in the QWs (e_1-e_2). The observed multi-peak spectral profile arises from in-plane monolayer fluctuations in the QWs in line with previous observations [33,73]. The magnitude of absorption per pass is recorded in table 6.1, however the error associated with these calculations (error in waveguide length and incident angle) is as high as ±20%. The magnitude of absorption scales approximately linearly with doping densities except for PG3 and PS3, where we observe saturation. This is due to the fact that the Fermi level approaches the excited state e_2 for such heavily doped samples.

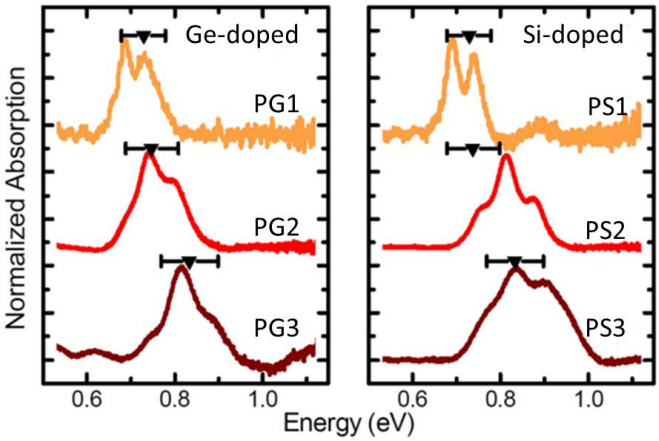

Figure 6.4: Room-temperature absorption spectra for TM-polarized light. Black triangles mark the transition energies calculated using nextnano[3] and corrected to account for the exchange interaction and depolarization shift. (modified from ref. [179]).

With increasing doping concentration, the absorption is blueshifted for both dopants, which is due to the many-body effects, explained in section 2.3.2. In particular, we are concerned by exchange interactions and depolarization shift. 1D calculations using nextnano[3] were performed to find the transition energy, $E_{21} = e_2 - e_1$, considering a doping density of 1×10^{17} cm^{-3}. Based on equations 2.25-2.27 the magnitude of the exchange interaction ΔE_{exch} and depolarization shift were calculated and used to correct E_{21}. Corrected values are recorded as black triangles in figure 6.4. The error bar corresponds to ±1 ML fluctuations of the well thickness. We see that for both Si- and Ge- doped samples, the spectral shift agrees with theoretical expectations.

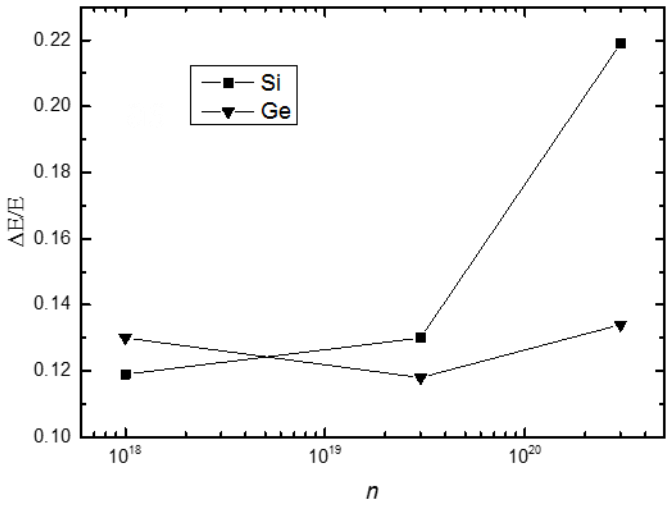

Figure 6.5: Normalized broadening (ΔE/E) of the ISB absorption peak as a function of the doping density *n*. (modified from ref. [179]).

The FWHM (ΔE) of the ISB absorption of the samples are given in table 6.1. Figure 6.5 represents the normalized broadening (ΔE/E) for various dopant concentrations. Si-doping clearly leads to a strong broadening of the absorption. This is most possibly arising from

interface roughness, and not due to scattering of ionized impurities or electron-electron interactions, which should be similar for both dopants.

6.1.3 Conclusion for Ge vs Si doping in planar GaN/AlN heterostructures

We synthesized GaN/AlN planar heterostructures with similar periodicity, varying dopant type (Si and Ge) and dopant concentration in the GaN sections. It was clear from x-ray diffraction studies that in these strongly lattice-mismatched heterostructures (GaN/AlN), highly Si-doped samples exhibit a larger broadening of the ω scans with respect to Ge doped samples, which points to a better structural quality of the Ge-doped samples. With increasing dopant concentration, the heterostructures exhibited a blueshift of the PL peak emission due to the screening of the internal electric field by free carriers. However, we do not observe any dependence of the band-to-band properties on the dopant nature. Regarding ISB transitions, we present Ge-doped planar heterostructures exhibiting ISB absorption associated to the transition from first to second electronic level in the QWs, covering the range of 1.45–1.75 µm. Identical behavior was observed in the Si-doped heterostructures used as a reference. Blueshift and broadening of the ISB transitions associated to many-body effects, including the exchange interaction and depolarization shift, have been observed. The broadening of the transition is larger in the case of Si-doped samples, which points to a higher heterointerface roughness in this case. To the best of our knowledge, these results constitute the first systematic study of ISB transitions in Ge-doped planar GaN based structures.

6.2 Ge vs. Si doping in GaN/AlN nanowire heterostructures

On the other hand, using nanowires instead of planar heterostructures in ISB devices can lead to a better performance due to lower electrical cross-sections, and the design flexibility associated to the possibility of elastical release of misfit strain. However, the field of nanowire ISB transitions is still in the nascent phase. Tanaka et al. [32] reported ISB absorption centered at 1.77 µm (= 0.7 eV) with FWHM ≈ 230 meV in a GaN/AlN (1 nm/2.7 nm) nanowire heterostructure with the AlN barriers doped with Si at 2×10^{19} cm^{-3}. In this configuration, it is assumed that the electrons from the donor levels in the AlN barriers should be transferred to the GaN wells. Studies in GaN/AlN planar heterostructures showed an improvement of the ISB absorption linewidth if the doping is performed directly in the GaN wells [33]. However, at the beginning of my PhD work, to the best of our knowledge, there was no report on ISB absorption in GaN/AlN nanowire heterostructures with Si-doped GaN wells. Difficulties were attributed to the fact that Si migrated towards the nanowire sidewalls and degraded the nanowire morphology. Replacing Si by Ge, Beeler et al, [35] demonstrated GaN:Ge/AlN (4-8 nm /4 nm) nanowire heterostructures with ISB absorption in the SWIR, but with an absorption linewidth around 400 meV.

At the start of my PhD, there was no report on ISB absorption in GaN/AlN nanowire heterostructures with Si-doped GaN QWs. Here, we assess the optical properties (band-to-band and ISB) of n-type doped GaN/AlN nanowire heterostructures, using the same concentration of Ge and Si dopants in the GaN sections as in section 6.1 for planar structures, i.e. varying the concentrations in the 1×10^{18} to 3×10^{20} cm^{-3} range. The structures are designed to display ISB transitions in the SWIR, around 1.55 µm. This work is, to our knowledge, the first observation of many-body effects on the ISB absorption of Si-doped GaN/AlN nanowire heterostructures. This observation is particularly relevant since it proves that, with our growth conditions, Si can efficiently dope the GaN nanowires without material degradation.

6.2.1 Sample structure

The nanowire heterostructures consisted of 30 periods of GaN/AlN (≈ 1.8 nm / 3 nm) MQWs on top of a GaN base, as described in Figure 6.6 (a). Self-assembled (000–1)-oriented GaN nanowires were synthesized on floating-zone Si(111) substrates using nitrogen-rich conditions. The growth started with the deposition of an AlN buffer using a two-step procedure, as described in section 5.1. Then, a 700 nm long GaN base was grown at a substrate temperature T_S = 810°C and with a growth rate of 330 nm/h. The GaN/AlN MQW was then deposited. The GaN QWs were grown using the same nitrogen-rich conditions used to grow the GaN base and the AlN barriers were grown at stoichiometry. The GaN QWs were doped with Ge or Si following the same doping densities as of the planar heterostructures, as described in table 6.2. The heterostructure was then capped with 30 nm of GaN. This is necessary as the sample crystal structure is inverted with respect to the planar samples and the GaN cap has a lower polarization module than the heterostructure. This ensures the pinning of the Fermi level at the conduction band at the heterostructure/cap interface. The choice of pinning the Fermi level at the topmost heterointerface in both planar and nanowire heterostructures aims at reducing the sensitivity of the structures to {0001} surface states.

Sample name	Sample Code	Dopant nature	n (cm^{-3})	Period thickness (nm)	PL peak position (nm)	PL decay constant (ns)
E3571	N0	-	n.i.d.	4.4±0.2	345	14.0
E3572	NG1	Ge	3×10^{19}	4.6±0.2	336	16.0
E3573	NS1	Si	3×10^{19}	4.6±0.2	339	15.3
E3592	NG2	Ge	1×10^{20}	4.6±0.2	336	10.2
E3593	NS2	Si	1×10^{20}	4.3±0.2	338	8.9
E3594	NG3	Ge	3×10^{20}	4.1±0.2	336	3.3
E3595	NS3	Si	3×10^{20}	4.6±0.2	337	5.4

Table 6.2: Description of nanowire samples under study: Dopant nature, Dopant concentration (*n*), heterostructure period from XRD, PL peak position and PL decay time constant.

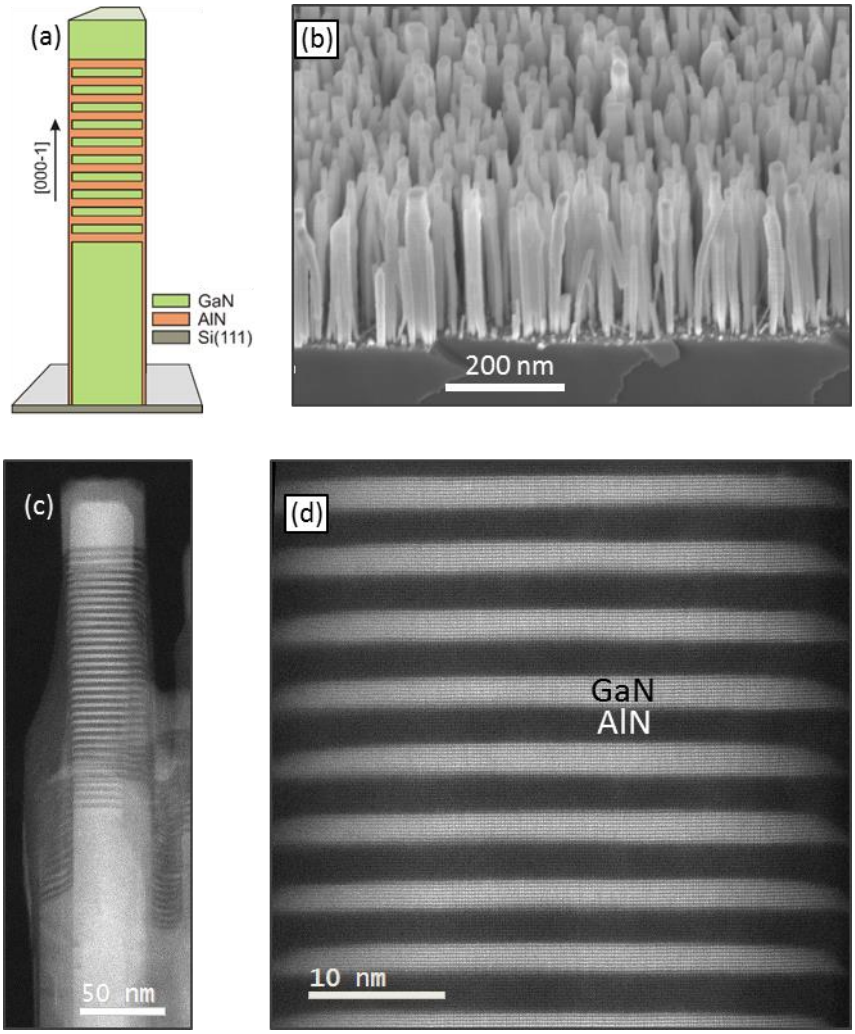

Figure 6.6: (a) Schematic representation of the nanowire heterostructures, (b) SEM (c), (d) HAADF-STEM observation in [1-100] direction of a nanowire from NG1 at two different magnifications with dark/bright contrast corresponding to AlN/GaN (modified from ref. [178]).

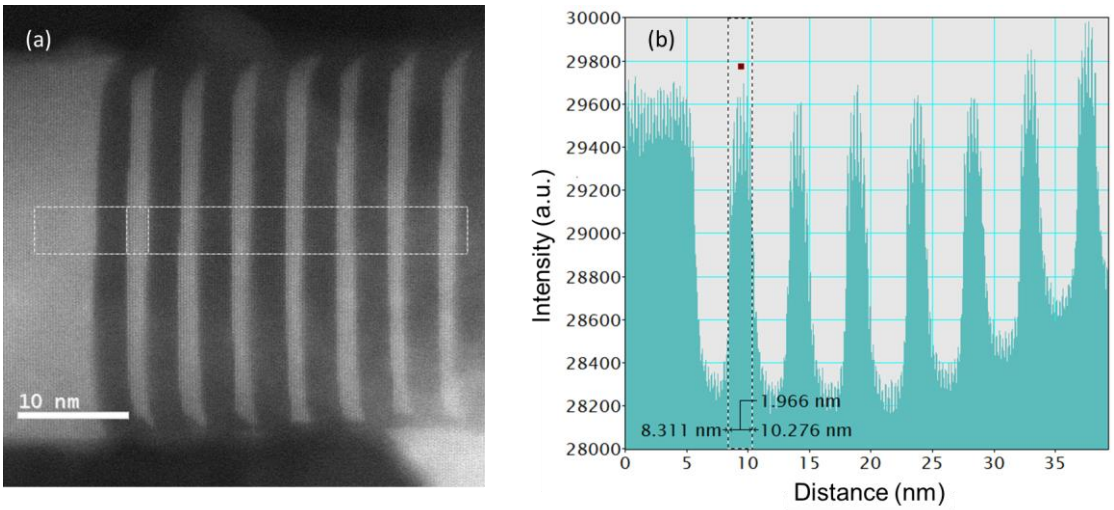

Figure 6.7: (a) Profiled area for statistical analysis on a HAADF-STEM image using Gatan Microscopy suite, (b) Corresponding intensity of the selected area with the calculated QW thickness

The as-grown nanowires were studied using SEM (similar to figure 6.6 (b)), and nanowires dispersed on SiN_x membranes were studied using HAADF-STEM (similar to figure 6.6 (c), (d)). Based on SEM observations, it was confirmed that the coalescence of the wires, if present, generally occurs in the early stages of the growth, and is therefore away from the active region. The diameter of the wires were in the range of 40 nm to 60 nm. Both SEM and HAADF-STEM images did not show any morphological change (in terms of nanowire diameter, density or facet orientation) as a function of the doping level or the nature of the dopant.

HAADF-STEM images of samples NS1 and NG2 (2 nanowires per sample), similar to figures 6.6(c), (d), were used for a statistical analysis of the well and barrier thickness using the Gatan Microscopy Suite software. Contrast variation between GaN (bright) and AlN (dark), due to the difference in atomic mass, is visualized in an intensity profile that was used to measure the thickness of the different layers in the heterostructure. An intensity profile of a selected region in figure 6.7 (a) is displayed in figure 6.7 (b). According to the analysis, the average thicknesses were 2.0±0.3 nm for GaN and 2.8±0.3 nm for AlN. The first two-three QWs are characterized by a higher irregularity in the thickness, which can deviate up to two monolayers (≈ 0.5 nm) from the average. Analysis also shows the presence of a ≈ 5 nm-thick AlN shell surrounding the nanowire heterostructures, which is known to introduce a uniaxial compressive strain in the wells [35]. The shell thickness was observed to gradually decrease as we move away from the substrate.

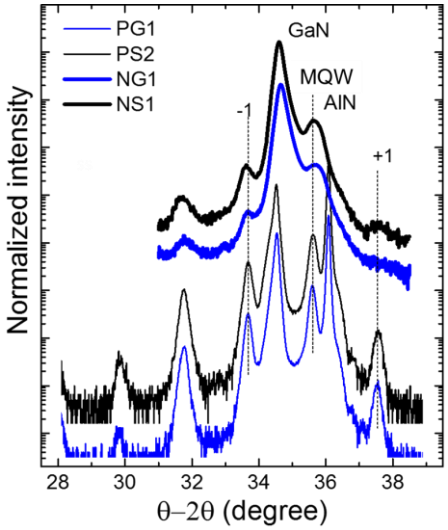

Figure 6.8: ω-2θ scans around the (0002) reflection of samples with similar doping and similar heterostructure dimensions (modified from ref. [168]).

Both nanowire and planar heterostructures were analyzed by HRXRD. Figure 6.8 presents the ω-2θ scan of the (0002) reflection GaN/AlN heterostructures of the same dopant concentration (3×10^{19} cm^{-3}), both nanowire and planar with both dopants. The average period extracted from the inter-satellite angular distance is presented in table 6.2. Comparing nanowires and planar heterostructures, nanowires clearly present broadened peaks resulting from increased inhomogeneity in heterostructure period along the growth axis from wire to

wire. The error bar in the period is calculated using extremities of the FWHM of the reflection peak.

6.2.2 Optical properties

The low temperature (5 K) PL of the samples is displayed in figure 6.9. In the spectrum of N0, the GaN stem of the nanowires contributes to a peak emission around 360 nm, which indicates that the stem is significantly strained due to the AlN shell, compared to the unstrained GaN (expected at ≈ 357 nm). For the same nanowire sample, the transition related to the heterostructure (at ≈ 345 nm) is blueshifted by 30 nm with respect to the lightly doped planar samples (PS0 and PG0, see figure 6.4 and table 6.1). The variation in thickness between the samples can only justify a blueshift of 10 nm, significantly smaller than what is observed. This additional blueshift arises from the uniaxial compressive strain along the growth axis which is imposed by the presence of the AlN shell in nanowire heterostructures, as previously observed and modeled [35,183,184].

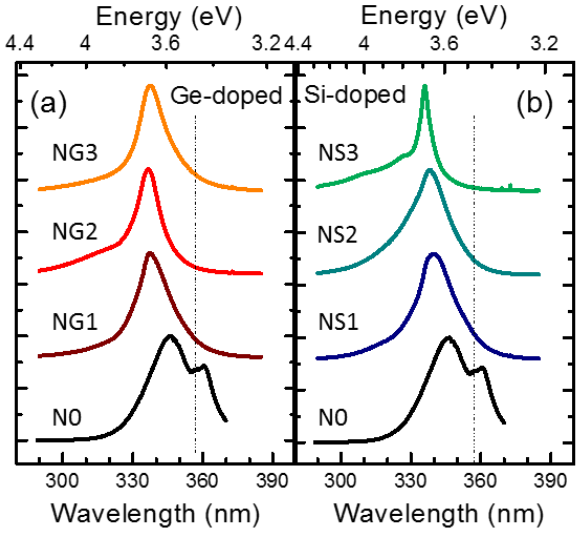

Figure 6.9: PL emission peaks of the nanowire heterostructures at 5K. The dotted line indicates the emission wavelength expected for an unstrained GaN nanowire (modified from ref. [178]).

For the doped nanowires, we observe a slight blueshift, which can be attributed to the screening of the internal electric field in the heterostructure that increases with doping. To understand the magnitude of this blueshift, we performed 3D simulations using nextnano[3]. We assumed an AlN barrier thickness of 3 nm, an AlN shell of 5 nm, and varied the GaN QW thickness and doping levels based on the details provided in section 3.1. The results of the simulations are presented in figure 6.10, in terms of wavelength associated with transitions between e_1 and h_1 in the QWs. The experimental PL peak positions are represented as data points in figure 6.10, in addition to the PL peaks from ref. [35]. The horizontal error bar represents the uncertainty in the well thickness and the vertical error bar represents the PL peak wavelengths obtained for Si- and Ge- doping.

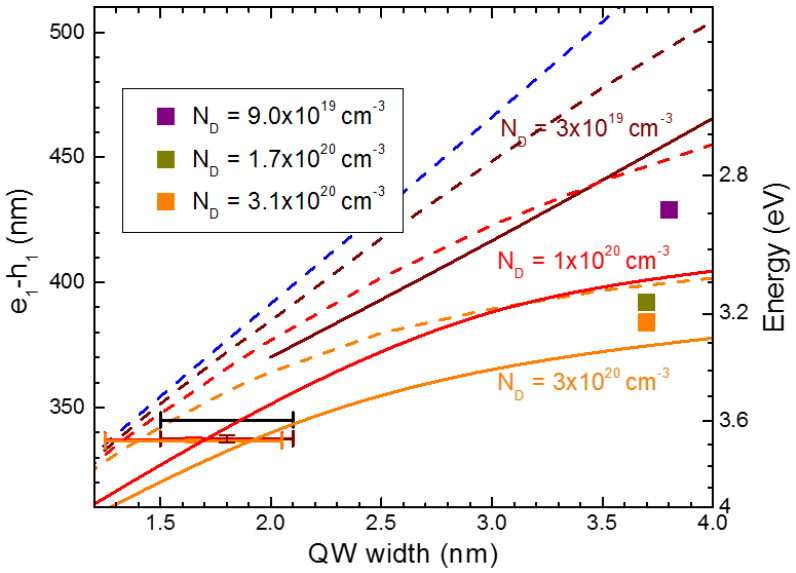

Figure 6.10: Calculated values of e_1-h_1 transitions (solid lines) from 3D calculations using nextnano[3] and data points corresponding to PL peaks. Horizontal error bars represents the uncertainty in the well thickness and vertical error bars represent the spectral width at 90% intensity. Dotted lines are 1D calculations from figure 6.3 for comparison. Colored squares are data points from reference [35] (modified from ref. [178]).

We performed time-resolved PL studies with the same optical conditions as for the planar samples in section 6.1.2. The PL decay time constants measured for the nanowires with different doping levels are recorded in table 6.2, and displayed in figure 6.11, together with data from planar samples, from table 6.1. This representation allows us to study the effect of free carriers and geometry (nanowire and planar) on the screening of the internal electric field in the QWs. Very similar decay times were observed for Si- or Ge-doped samples with similar doping levels. Regardless of the geometry, the decay time constant decreases with increasing doping. This is consistent with the onset of screening of the internal electric field by free carriers. This can be illustrated by nextnano[3] calculations provided in figure 6.12 (a) and (b). These show the axial conduction band and valence band profiles along the center of a nanowire. An increase in doping causes screening of the internal electric field that results in a better overlap of electron and hole wave functions.

In addition, we observe that the decay time constant in the nanowires is systematically longer than in their planar counterparts. Note that this remains true in spite of the slightly smaller well width. The increased decay time constant for the nanowires is explained by the occurrence of lateral separation of the electron and hole wave functions due to the lateral electric field induced by the shear component of the strain in the GaN nanodisks, as discussed in [143] and also due a contribution from the Fermi level at the surface. The same effect is illustrated in figure 6.12 (c) and (d), showing electron and hole band profiles in the radial direction.

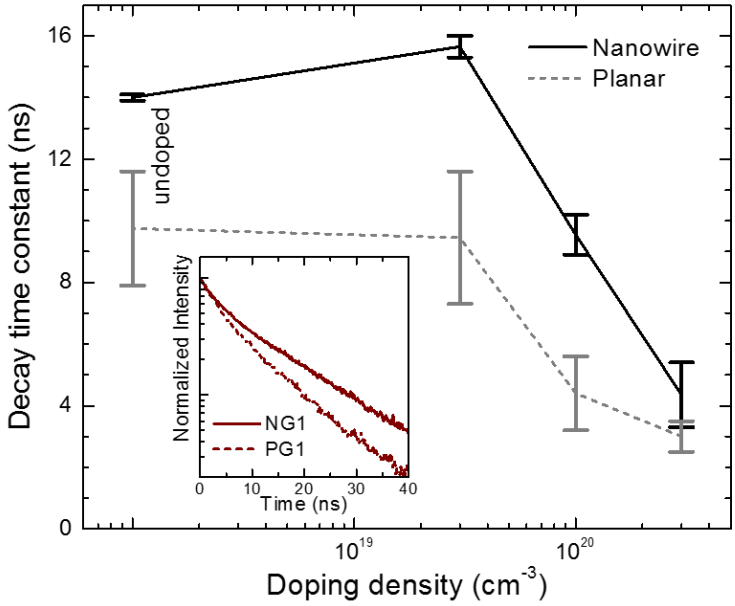

Figure 6.11: Decay time constant extracted from time-resolved PL as a function of doping density. The vertical error bar indicates the values obtained for Si- and Ge-doped samples for the same dopant concentration. Inset: normalized decay of the PL intensity as a function of time for NG1 and PG1. The laser pulse arrives at time t = 0 (modified from ref. [178]).

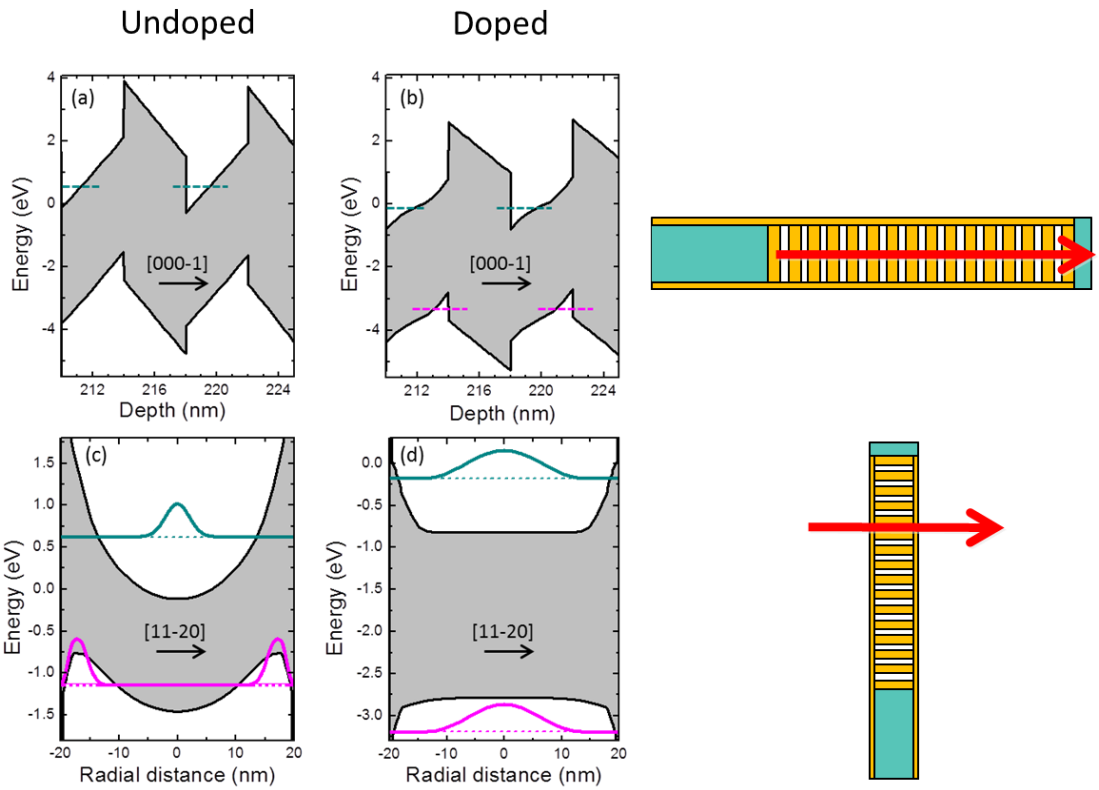

Figure 6.12: (a)-(d) Calculation of conduction and valence band profiles. (a), (b) Profile along [000-1] taken at the center of the nanowire as indicated by arrows in the diagrams on the right side. The ground electron and hole levels are indicated by dashed lines. (c), (d) Radial profile. The squared wave functions of the ground electron and hole states are indicated (modified from ref. [143]).

The ISB properties of the doped nanowire samples were accessed using room temperature FTIR measurements. Measurements were made with identical conditions on sample N0 as a reference. The measured absorption spectra for TM-polarized light are displayed in figure 6.13. The recorded absorption corresponds to the transition between the ground electron level of the GaN QWs and the first excited electron level associated to confinement along the growth axis (namely s-p_z transition). The absorption peak lies around 1.39–1.55 µm for Si-doped sample NS1 and 1.37–1.53 µm for Ge-doped sample NG1. 3D calculations of the nanowire quantum confined ground and excited states were performed using nextnano[3] using the **k.p** model. For a doping concentration of 3×10^{19} cm^{-3}, the s-p_z transition is calculated at 0.729 eV, which is indicated by arrows in figure 6.13.

Further, in NS2 and NG2 samples, we observe a blueshift with respect to NS1, NG1, which can be attributed to many-body effects. Transitions from the highest doped nanowires (NG3 and NS3) of 3×10^{20} cm^{-3} could not be clearly discerned, probably due to the huge broadening of the transition. When considering 3D calculations, many-body effects due to doping could not be taken into account to calculate the ISB transitions for samples with higher doping levels. An approach similar to the planar samples taking into account the 3D calculations is beyond the scope of this work, but the results from the 1D calculations can be used as a guideline to the expected blueshift.

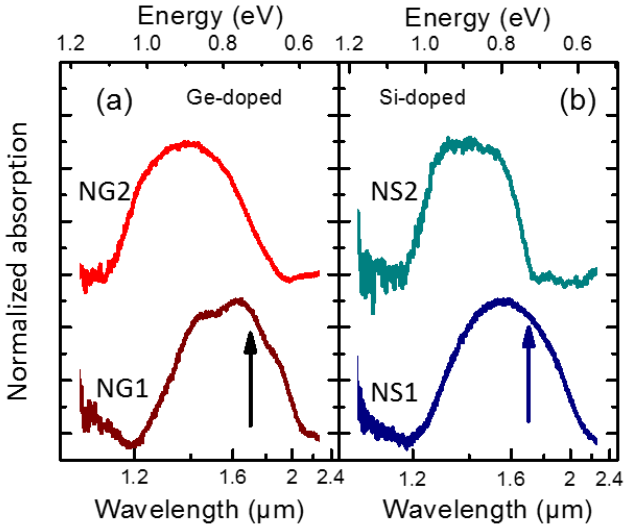

Figure 6.13: Room-temperature absorption spectra for TM-polarized light. Arrows mark the transition energies estimated using 3D calculations in nextnano[3] (modified from ref. [178]).

Compared to the planar samples in section 6.1, the large, inhomogeneous broadening of these absorption peaks is due to thickness/diameter variations in the nanowire ensemble. This is amplified in the case of nanowires due to the measurement strategy, which uses light incident at nearly grazing angle of 5°, as explained in section 3.4.4. In contrast to planar structures, the existing thickness monolayer fluctuations along the nanowire growth axis cannot be resolved due to their overlap with fluctuations of the diameter of the disks. This is

similar to observations in GaN/ AlN quantum dots grown by the Stranski-Krastanov method [185].

As mentioned before, in the previous report of Ge-doped GaN nanowire heterostructures, the absorption was spread over a wider spectral region (1.58–1.95 µm) [35] with a FWHM around 400 meV. In our case, because of the smaller QWs, we were able to tune the absorption to the telecommunication spectral region, with a better FWHM of 200 meV. The large QWs used in ref. [35] (> 3 nm) require high doping levels to absorb at 1.55 µm (by blueshifting the fundamental transition with many-body effects). This inherently leads to broadening of the transitions.

6.2.3 Conclusion for Ge vs Si doping in nanowire GaN/AlN heterostructures

We synthesized GaN/AlN nanowire heterostructures, with active regions designed to absorb around 1.55 µm. The nanowire structures were comparable in design to the planar structures in section 6.1. We varied the dopant type (Si and Ge) and dopant concentration in the GaN QWs. The samples exhibit defect free active regions regardless of dopant nature.

We found that for both nanowire and planar geometries, the PL peak energy, linewidth and decay time constant were not influenced by the choice of dopant (Si or Ge). However, it was observed that nanowire heterostructures consistently present longer PL decay times than their planar counterparts with identical active regions and doping level. This experimental evidence confirms the existence of an in-plane piezoelectric field in nanowires associated to the sheer component of the strain tensor, leading to lateral electron–hole separation.

We reported the first observation of ISB absorption in Si-doped GaN/AlN nanowire heterostructures with varying doping levels, which also leads to an improved FWHM of 200 meV for the ISB absorption at 1.55 µm, compared to previous reports of Ge-doped nanowires. Si-doped and Ge- doped nanowires behaved identical, indicating that the choice of dopant is not a hindrance for observing ISB transitions in nanowires. However, we observe an inhomogeneous broadening in the samples that was associated to geometry fluctuations, regardless of doping. This means that the homogeneity between individual nanowires across the sample wafer is the limiting factor rather than the dopant. Based on this study, we can conclude that both Si- and Ge-doped nanowires are potentially suitable for the fabrication of GaN/AlN heterostructures for the study of ISB optoelectronic phenomena. They are both promising for fabricating planarized nanowire based ISB devices.

6.3 Top-down heterostructures

Trying to keep the advantages of nanowire heterostructures while reducing the inhomogoneinity associated to self-assembled growth, we explored an alternative approach consisting in the fabrication of top-down micro/nanopillars. This procedure combines the

growth control of planar heterostructures and the optical advantages of the nanowire geometry, with the risk associated to damage during the etching process and the presence of dislocations in the initial planar structure. With III-As heterostructures, nano- and micropillar arrays for THz emission have already been demonstrated by lithographically defined top-down etching [43–45]. Such a process using GaN/AlN heterostructures has not been attempted so far. Here, we investigate top-down etched nano/micro-pillar arrays capable of having ISB absorption at the telecommunication wavelengths. The active region is similar to those discussed previously.

6.3.1 Sample structure

The samples were derived from a planar heterostructure sample similar to those discussed in section 6.1. This parent sample, grown by PAMBE, consisted of an active region of 39 periods of GaN/AlN (1.5 nm / 2.8 nm). It was grown on a 1-µm-thick AlN-on-sapphire template followed by a 200-nm-thick GaN buffer layer, which is partially strained on the AlN template, thus allowing the growth of a crack-free active region. The active region was capped with 30 nm of AlN. The GaN QWs were doped with Si of concentration 2.6×10^{19} cm^{-3}.

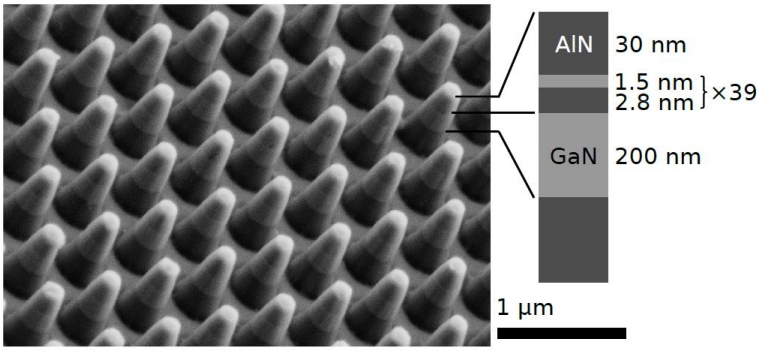

Figure 6.14: SEM image of TD3 and an illustration of the layer stacks (modified from ref [180]).

	TD0 (as grown)	TD1	TD2	TD3	TD4
Diameter (µm)	-	1.5	0.4	0.2	0.1
Pitch (µm)	-	3.0	1.2	0.6	0.3
Period (nm)	4.3	4.0	4.2	4.2	4.4
c_{GaN} (Å)	5.208	5.192	5.185	5.183	5.186
ε_z (%)	0.46	0.15	0.03	-0.03	0.04
$\Delta\omega_{he}$ (°)	0.18	0.38	0.44	0.28	0.44
$\Delta\omega_{AlN}$ (°)	0.06	0.06	0.06	0.05	0.05
$\Delta\omega_{GaN}$ (°)	0.16	0.42	0.33	0.30	0.43
I_{PL} (10K) (normalized)	1	0.68	0.73	0.96	0.65
I_{PL} (300K) / I_{PL} (10K)	0.1	0.08	0.07	0.03	0.05
λ_{FTIR} (as grown) (µm)	-	-	1.43	1.54	1.51
λ_{FTIR} (etched) (µm)	-	-	1.38	1.42	1.47
$FWHM_{FTIR}$ (as grown) (µm)	-	-	0.28	0.33	0.32
$FWHM_{FTIR}$ (etched) (µm)	-	-	0.28	0.31	0.4

Table 6.3: Description of nanowire samples under study: (From top to bottom) Diameter and pitch of the etched samples, period of the active region, out-of-plane lattice constant (c_{GaN}) and strain (ε_z) extracted from ω-2θ scans around (0002) reflections, FWHM of various peaks ($\Delta\omega_{he}$, $\Delta\omega_{AlN}$ and $\Delta\omega_{GaN}$) from ω scans around (0002) reflections, PL intensity (I_{PL}) at various temperatures, absorption wavelength (λ_{FTIR}) and FHWM of the absorption.

Pillars were etched using a top-down process to produce samples with various diameters and pitches that are summarized in table 6.3. A Ti/Ni (5/50 nm) etch mask of appropriate circular structures on a hexagonal grid was defined by lift-off. The pattern was written by laser lithography for pillars with a diameter d = 1.5 µm and electron beam lithography for diameters d = 0.4, 0.2 and 0.1 µm. A 3 min etch leads to an etch depth of approximately 1100 nm. The material around the pillars was removed with an inductively-coupled plasma (ICP) etch. The metal mask was removed with $FeCl_3$ and HF. An exemplary SEM image of a sample after etching is shown in figure 6.14, together with an illustration of the various layers in the sample.

The influence of the top down processing on the sample structure and quality was analyzed using HRXRD. The heterostructure period extracted from ω-2θ scans like in figure 6.15 (a) are summarized in table 6.3. The variation in the period is due to the gradient of the growth rate along the wafer surface, arising from radial variations of adatom influx. If we normalize the intensity of the diffractogram by the intensity of the reflection from the AlN substrate, we realize that the intensity of the reflections from the MQW and from the GaN buffer layer in the etched samples have decreased to about 10% of the as-grown value. This decrease is due to the decrease in the amount of material to 10% of the original after etching. On the other hand, if we look at the angular location, the reflections assigned to the heterostructure do not present any significant angular shift with etching. On the contrary, the reflection associated to GaN exhibits a clear, systematic shift towards larger angles in the etched structures, which is an indication of strain relaxation.

The strain state of the GaN buffer is estimated by examining the out-of-plane deformation, which is $\varepsilon_{zz} = (c-c_0)/c_0$ where c is the measured out-of-plane lattice constant and c_0 is 5.185 Å. ε_{zz} is summarized in table 6.3. The GaN buffer is highly relaxed for samples with diameter ≤ 0.4 µm. The FWHM of the ω scans around the (0002) reflection of the heterostructure $\Delta\omega_{he}$, the AlN template $\Delta\omega_{AlN}$ and the GaN buffer layer $\Delta\omega_{GaN}$ are summarized in table 6.3. After etching, we observe an increase in $\Delta\omega_{GaN}$ and $\Delta\omega_{he}$, which is an indication of strain relaxation towards the side walls of the pillars.

Reciprocal space maps (RSMs) around the (-2025) reflection of samples TD0 and TD4 are displayed in figure 6.15 (b) and (c). The position of the GaN buffer layer shifts in the etched sample TD4, whereas the position of the heterostructure remains unchanged, consistent with the observation from ω-2θ scans. We also extracted the average in-plane lattice parameter from the RSM. Combining this with the out-of-plane lattice parameter extracted from ω-2θ scans, we estimate an average Al composition of 65±1% in the heterostructure, and that it is fully relaxed. This is consistent with the heterostructure period consisting of 1.5 nm of GaN and 2.8 nm AlN. This implies that the strain state of the heterostructure is practically insensitive to the strain state of the buffer layer. This in agreement with ref. [186], which

points at the fact that full relaxation of similar GaN/AlN superlattices can be achieved after the growth of about 10 GaN/AlN periods independent of the substrate.

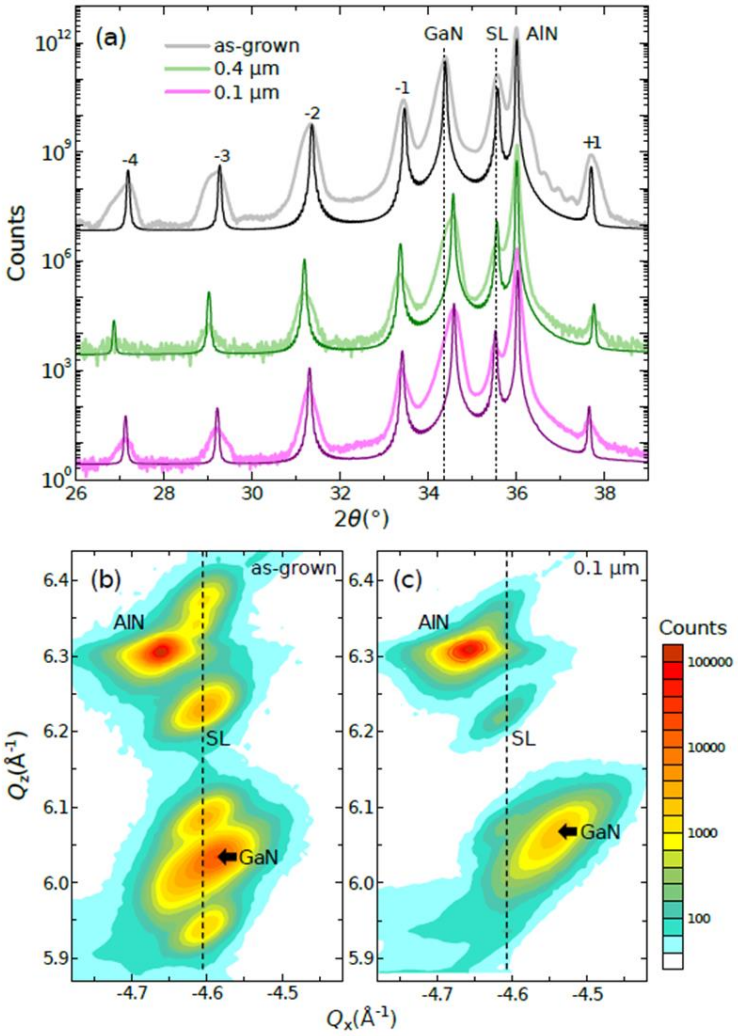

Figure 6.15: a) ω-2θ scans around the (0002) reflection of as-grown and etched samples with d = 0.4 µm and 0.1 µm. Superimposed in a darker color are the simulated profiles. Reciprocal space maps around the (-2025) reflection are shown for (b) as-grown TD0 and (c) etched into nanopillars with d = 0.1 µm TD4. The vertical dashed line indicates the in-plane wavevector of the heterostructure (modified from ref [180]).

6.3.2 Optical properties

To get a first idea about the impact of the top-down processing on the optical characteristics, we have studied the PL emission of the heterostructures both at low temperature (10 K) and room temperature. Selected measurements are displayed in figure 6.16. The PL peaks for all the samples are at the same position (with an error bar of ±0.5 nm). The emission is centered around 343 nm at room temperature and around 339 nm at 10 K. In

comparison, 3D calculations using nextnano[3] predict interband transitions at 342 nm at 300 K and 335 nm at 10 K, in good agreement with the experimental results, confirming the validity of our calculations (note that excitonic effects are not taken into account by the software).

However, the attenuation of the peak intensities at 10K after etching amounts to less than a factor of 2. Note that with etching we have removed 80% to 90% of the sample material (depending on the diameter to etch ratio of the pillars). The fact that the attenuation is not consistent with the magnitude of material removal indicates increased coupling of light for the pillar array as compared to the planar layers. The PL intensity (I_{PL}) at 300 K is decreased with respect to the intensity at 5K for both as grown and etched samples, as expected. The I_{PL}(300 K) / I_{PL}(10 K) ratio shows a trend to smaller values with decreasing feature size, with the reduction being limited to a factor of 3 in the case of the sample with a diameter of 0.2 µm. Apparently, the processing induces some nonradiative defects at or close to the surface, which are activated at room temperature. However, it is a notable result that, even for the smallest pillar diameter, the non-radiative recombination is only moderately enhanced. Note that no additional processing for defect removal or surface passivation has been applied after the ICP etching process.

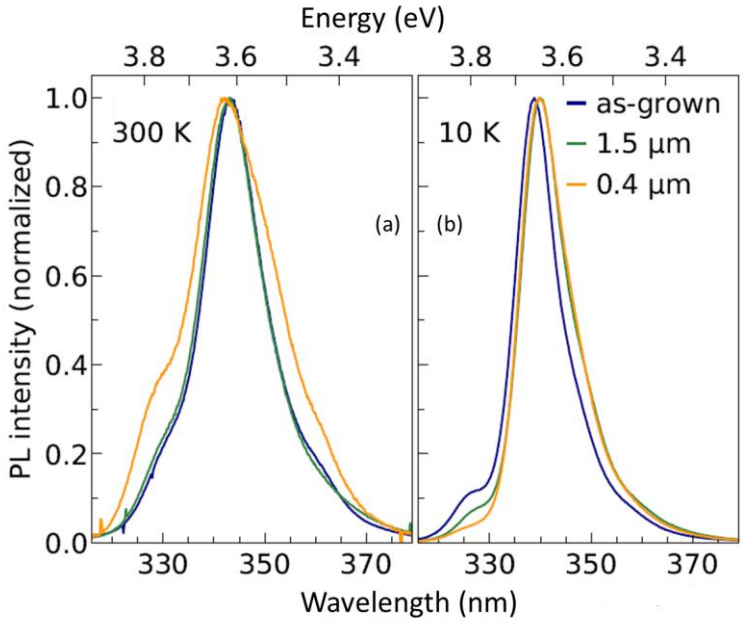

Figure 6.16: PL of selected samples (a) at 300K, (b) at 10K (modified from ref [180]).

Room temperature FTIR spectroscopy measurements were carried out, using TM/TE polarized light, to study ISB transitions in the samples. Normalized transmittance with TM polarized light through the samples are displayed in figure 6.17. The reason why transmittance is discussed in this section to describe ISB transitions, contrary to absorption in other sections, is due to the enhanced photonic crystal effects and differences in absorption with respect to the as-grown reference sample due to strain relaxation.

Figure 6.17 (a), for example, displays transmittance at various angles of incidence compared to a measurement of the corresponding as-grown sample piece before etching. The

as-grown sample exhibits a dip in intensity at 1.5 µm (0.8 eV) corresponding to ISB absorption. As a comparison, 3D calculations using nextnano[3], and including many-body effects, put the theoretical value at 1.53 µm (0.81 eV). After the sample is etched down to micropillars with d = 1.5 µm, the spectra exhibit several absorption related dips in intensity, which shift with the measurement angle. These features in the spectra can be attributed to the fact that the micropillar array constitutes a two-dimensional photonic crystal with a lattice constant on the order of the investigated wavelength range [45].

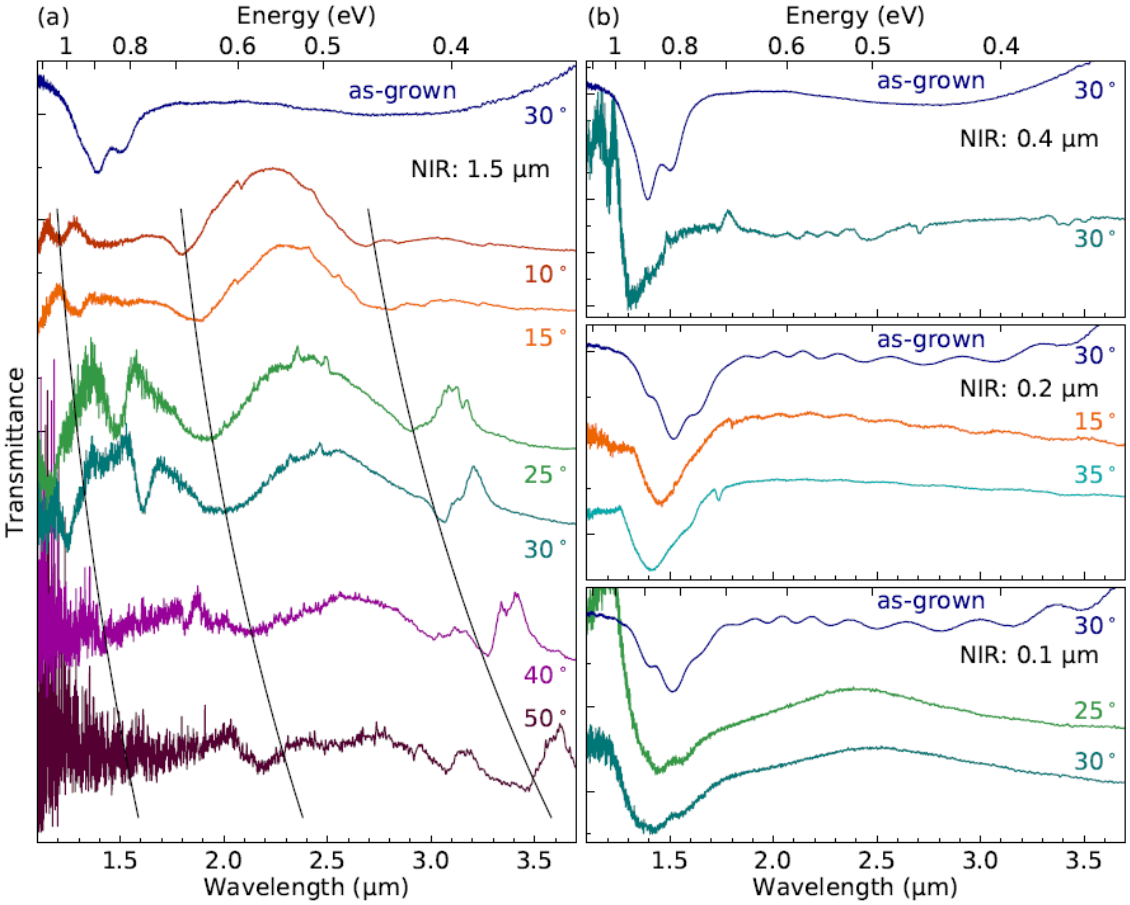

Figure 6.17: FTIR transmittance of the as-grown compared with the top-down-processed samples for samples with diameter, (a) d = 1.5 µm, (b) d = 0.4, 0.2, and 0.1 µm (top to bottom) for the different panels. The incident angle θ_{in} is indicated for each curve. The black lines in (a) show the dependence of the effective lattice constant on the incident angle (modified from ref [180]).

For samples with smaller diameters, the normalized transmittance spectrum of the samples, displayed for both as-grown and after etching in Figure 6.17, shows ISB absorption at 1.5 µm. The dip in intensity does not shift with increasing angles, confirming its origin from ISB transitions. In line with the PL intensity, we do not have a significant degradation of the ISB absorption FWHM (table 6.3). Furthermore, the magnitude of the absorption dip at an angle of 30-35° is 67±8% in the as-grown samples and 72±12% in the samples etched into

nanopillars, which means that there is no degradation of the total ISB absorption in spite of the fact that 80%-90% of the material is removed on etching.

6.3.3 Conclusion for top-down heterostructures

We fabricated micro- and nanopillars with various pillar diameters and pitch by top-down processing of planar GaN/AlN MQW structures. The top-down processing resulted in a relaxation of the strain in the GaN buffer layer. However, analyzing the reciprocal space maps showed that the GaN/AlN heterostructures were already fully relaxed for the as-grown samples and the relaxation was retained on etching. The PL emission of the heterostructure does not show any spectral shift for the processed samples. We showed that the improved in- and outcoupling of light for the pillar arrays compensates for the removal of a large part of the active region material through etching as seen from the PL intensity variations at 10 K. Only at room temperature, the non-radiative recombination at the pillar sidewalls has a moderate effect on the PL intensity.

Concerning the IR absorption, we showed that when the spacing of the pillar array is comparable to the probed wavelengths, photonic crystal resonances dominate the absorption spectra. For subwavelength pillar arrays, where these resonances are at much shorter wavelengths than the ISB absorption, the absorption is clearly observed. We have shown that the magnitude and linewidth of the ISB absorption is preserved in spite of the low filling factor even when 80% or 90% of the material is etched away.

6.5 General conclusions

In summary, we synthesized GaN/AlN planar heterostructures with similar periodicity, varying dopant type (Si and Ge) and dopant concentration in the GaN sections. The Ge-doped planar heterostructures showed ISB absorption associated to the transition from the first to second electronic level in the QWs, covering the range of 1.45–1.75 µm. Identical behavior was observed in the Si-doped heterostructures used as a reference. To the best of our knowledge, these results constitute the first systematic study of ISB transitions in Ge-doped planar GaN based structures.

We reported the first observation of ISB absorption in Si-doped GaN/AlN nanowire heterostructures with varying doping levels, which also lead to an improved FWHM of 200 meV for the ISB absorption at 1.55 µm, compared to previous reports of Ge-doped nanowires. Based on this study we can conclude that both Si- and Ge-doped nanowires are potentially suitable for the fabrication of GaN/AlN heterostructures for the study of ISB optoelectronic phenomena. They are both promising for fabricating planarized nanowire based ISB devices. However, the ISB absorption linewidth, in the order of 200 meV, is significantly larger than that observed in planar structures, due to the inhomogeneities associated to the self-assembled growth process.

Trying to reduce the inhomogeneities while keeping the advantages of the nanowire geometry, we also presented a systematic analysis of ISB absorption in group-III-nitride micro- and nanopillars for different pillar diameters. We showed that when the spacing of the pillar array is comparable to the probed wavelengths, photonic crystal resonances dominate the absorption spectra, but when these resonances are at much shorter wavelengths than the ISB absorption, the absorption is clearly observed. Therefore, this work is opening the pathway for a microstructured group-III-nitride quantum-well IR photodetector and can be seen as a motivation to pursue the investigation of group-III-nitride pillars also for ISB emitter structures.

7. GaN/Al(Ga)N heterostructures for the mid-wavelength IR range

In this chapter, we present a study on the ISB characteristics of GaN/AlN and GaN/$Al_{0.4}Ga_{0.6}N$ nanowire heterostructures structurally designed to absorb in the MWIR region. To redshift the ISB absorption, we follow two approaches. First, we increase the GaN well width in GaN/AlN heterostructures from 1.5 to 5.7 nm, which leads to a redshift of the ISB absorption from 1.4 to 3.4 µm. Second, we replace the AlN barriers by an $Al_{0.4}Ga_{0.6}N$ ternary alloy, thereby reducing the effects of polarization, which leads to a redshift of the ISB transition to the 4.5 to 6.4 µm range.

*In this work, I performed the MBE growth, HRXRD, PL, SEM and FTIR measurements. STEM analysis was performed by Dr M. I. den Hertog and M. Spies. Theoretical calculations were performed by me and Dr E. Monroy. I was assisted by R. Blasco and J. Polaczyński with PL and SEM measurements respectively. The complete study was accepted for publication as, "Intersubband absorption in GaN nanowire heterostructures at mid-infrared wavelengths", Nanotechnology **29** 385201 (2018)* [187].

In the previous chapter, we reported about doping control and improved ISB transitions in nanowires. However, considering this work and ref. [35], the observation of ISB absorption in GaN/AlN nanowire heterostructures was still limited to 1.3-1.95 µm. It is hence important at this point to venture further to longer wavelengths, which can be attained either by using larger QWs or by using AlGaN ternary alloys as QW barriers, thus reducing the internal electric field in the wells.

7.1 Sample design

The samples under study, their dopant concentration, Al content in the barriers, and other structural/optical properties are listed in table 7.1. We consider three different nominal architectures for the nanowire heterostructures:

i) samples A1 to A3 consisted of 30 periods of GaN/AlN (4 nm / 3 nm) QWs,
ii) sample B1 contained 19 periods of GaN/AlN (6 nm / 3 nm) QWs, and
iii) samples C1 to C3 consisted of 30 periods of GaN/$Al_{0.4}Ga_{0.6}N$ (4 nm / 3 nm).

The reduction in the number of periods in (ii) aimed at keeping the active region thickness approximately constant.

For comparison purposes, table 7.1 contains also samples NS1 and NS2 from section 6.2 containing a GaN/AlN superlattice with similar AlN barriers (≈ 2.7 nm) and thinner GaN wells (1.7 and 1.8 nm, respectively).

The growth of the entire nanowire except for the heterostructure was kept consistent with the growth of nanowires from section 6.2.1. Hence, a similar growth procedure is detailed here. Self-assembled (000–1)-oriented GaN nanowires with the above mentioned

heterostructures were synthesized using PAMBE. They were grown on floating-zone Si(111) substrates using nitrogen-rich conditions. The growth started with the deposition of an AlN buffer using a two-step procedure, as described in section 5.1. Then, a 700 nm long GaN base was grown at a substrate temperature T_S = 810°C and with a growth rate of 330 nm/h. The GaN/(Al,Ga)N MQW was then deposited. The GaN QWs were grown using the same nitrogen-rich conditions used to grow the GaN base and the AlN barriers were grown at stoichiometry. A 2 nm section in the center of the GaN QWs was doped with Si at various concentrations. The calibration of the dopant density was performed by Hall effect characterization using the Van der Pauw method on Si-doped planar GaN layers. The entire heterostructure was then capped with 30 nm of GaN.

Note that samples A1 to A3 present a similar geometry as S1-S4 in ref. [35], displaying ISB absorption in the 1.60-1.95 µm range. However, we have significantly reduced the doping level, in an attempt to reduce the spectral blueshift of the ISB absorption due to many-body effects. Note that the surface doping density in ref. [35], was 3.6 and 12×10^{13} cm^2 (using Ge as a dopant), to be compared with 0.2 to 2×10^{13} cm^{12} in this work (using Si as a dopant).

Sample	**Al (%)**	**[Si] (cm^{-3})**	**Period (nm)**	**GaN width (nm)**	**PL peak (nm)**	**e_1-h_1 3D (nm)**	**IR absorption peak (µm)**	**e_1–e_2 1D (µm)**
NS1	100	3×10^{19}	4.6±0.2	1.8±0.2	339±4	325	1.55±0.11	1.72
NS2	100	1×10^{20}	4.3±0.2	1.7±0.2	338±3	323	1.41±0.11	1.63
A1	100	1×10^{19}	7.0±0.3	3.7±0.3	445±9	453	1.74±0.13	2.21
A2	100	3×10^{19}	6.3±0.2	3.3±0.2	412±5	422	1.87±0.13	2.18
A3	100	1×10^{20}	6.8±0.2	3.7±0.2	430±12	425	1.78±0.12	2.18
B1	100	1×10^{19}	8.6±0.2	5.7±0.3	490±19	562 504(*)	3.4±0.5, 1.45±0.13	2.6 3.0(*)
C1	40	1×10^{18}	6.2±0.2	3.7±0.4	368±3	358	--	4.9
C2	40	1×10^{19}	6.6±0.2	4.0±0.4	365±3	365	--	4.8
C3	40	1×10^{20}	5.7±0.3	3.7±0.4	362±2	351	6.4-4.5	4.6

(*) Introducing 2 nm of graded alloy at the bottom interface of the well.

Table 7.1: Structural and optical characteristics of the nanowire heterostructures: Al concentration in the barriers, Si concentration in the 2 nm doped region in the QWs, superlattice period (GaN+AlN) measured by XRD, GaN width estimated from the XRD and TEM measurements, PL peak wavelength with error bar representing the spectral width at 90% of the maximum intensity, theoretical calculation of the e_1–h_1 transition in the wells at 5 K using the nextnano^3 software in 3D, IR absorption peak wavelength with error bar representing the spectral width at 90% of the maximum absorption, theoretical calculation of the e_1–e_2 transition in the wells using the nextnano^3 software in 1D.

7.2 Structural properties

The morphology of the as-grown nanowire ensemble was studied by SEM using a Zeiss Ultra 55 or a Zeiss 55 microscope. Figure 7.1 presents tilted (≈ 45°) SEM images of samples A1 and C1, containing GaN/AlN and GaN/AlGaN superlattices, respectively. The images present

the typical morphology of self-assembled GaN wires grown by PAMBE, without bending or deformation of the nanowire shape due to the presence of the heterostructures.

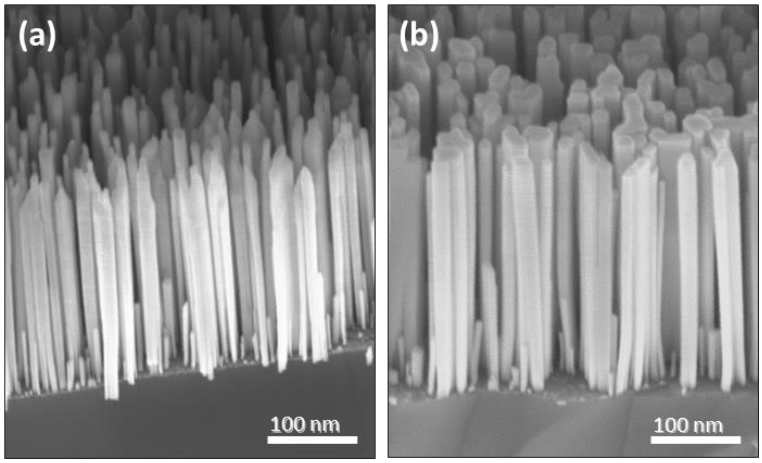

Figure 7.1 Tilted (45°) SEM images of samples (a) A1 and (b) C1 (modified from ref. [187]).

The average thickness of one period of the GaN+(Al,Ga)N MQWs was extracted from the inter-satellite angular distance of the XRD θ-2θ scan around the (0002) reflection. The results are listed in table 7.1, and exemplary diffractograms of samples A1, C3, and B1 are show in figure 7.2, together with simulations using the Rigaku HRXRD plugin of the Smart Lab Studio II software. The simulations considered planar layers with the structural parameters of the MQWs in table 7.1, and their strain state was considered as the only fitting parameter.

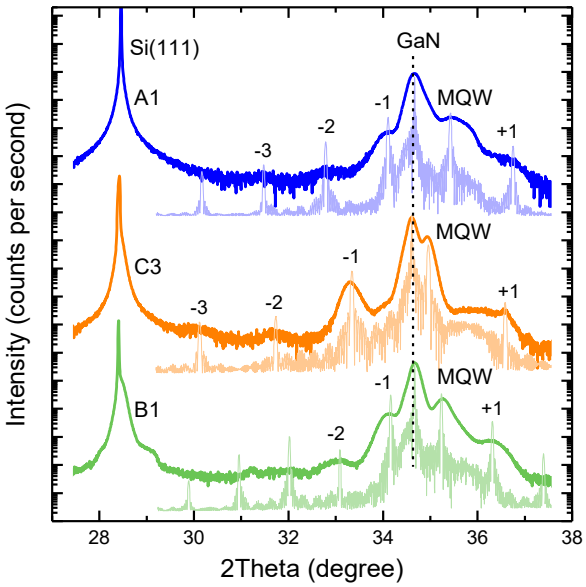

Figure 7.2 XRD θ-2θ scan of samples A1, C3 and B1. The scans are vertically shifted for clarity. Lighter shades are simulated data. Labels indicate the (111) reflection of the Si substrate, the (0002) reflection of the GaN stem, and the (0002) reflection of the MQW with its satellites (modified from ref. [187]).

Detailed structural studies were conducted using HAADF-STEM performed on a probe-corrected FEI Titan Themis microscope operated at 200 kV. The GaN width indicated in the

table 7.1 is an estimation based on the statistical analysis of HAADF-STEM images of selected samples. HAADF-STEM images of the active region of sample A1 with GaN/AlN MQWs with 4-nm-thick GaN wells are shown in figure 7.3 (a) and (b). The well/barrier interfaces are chemically sharp, and we observe the presence of a ≈ 5-nm-thick AlN shell surrounding the GaN/AlN heterostructure, see for example figure 7.3 (b), which has been commonly observed on such nanowire heterostructures before [184,188,189], and is due to the low mobility of Al atoms on the nanowire sidewalls at the growth temperature [30].

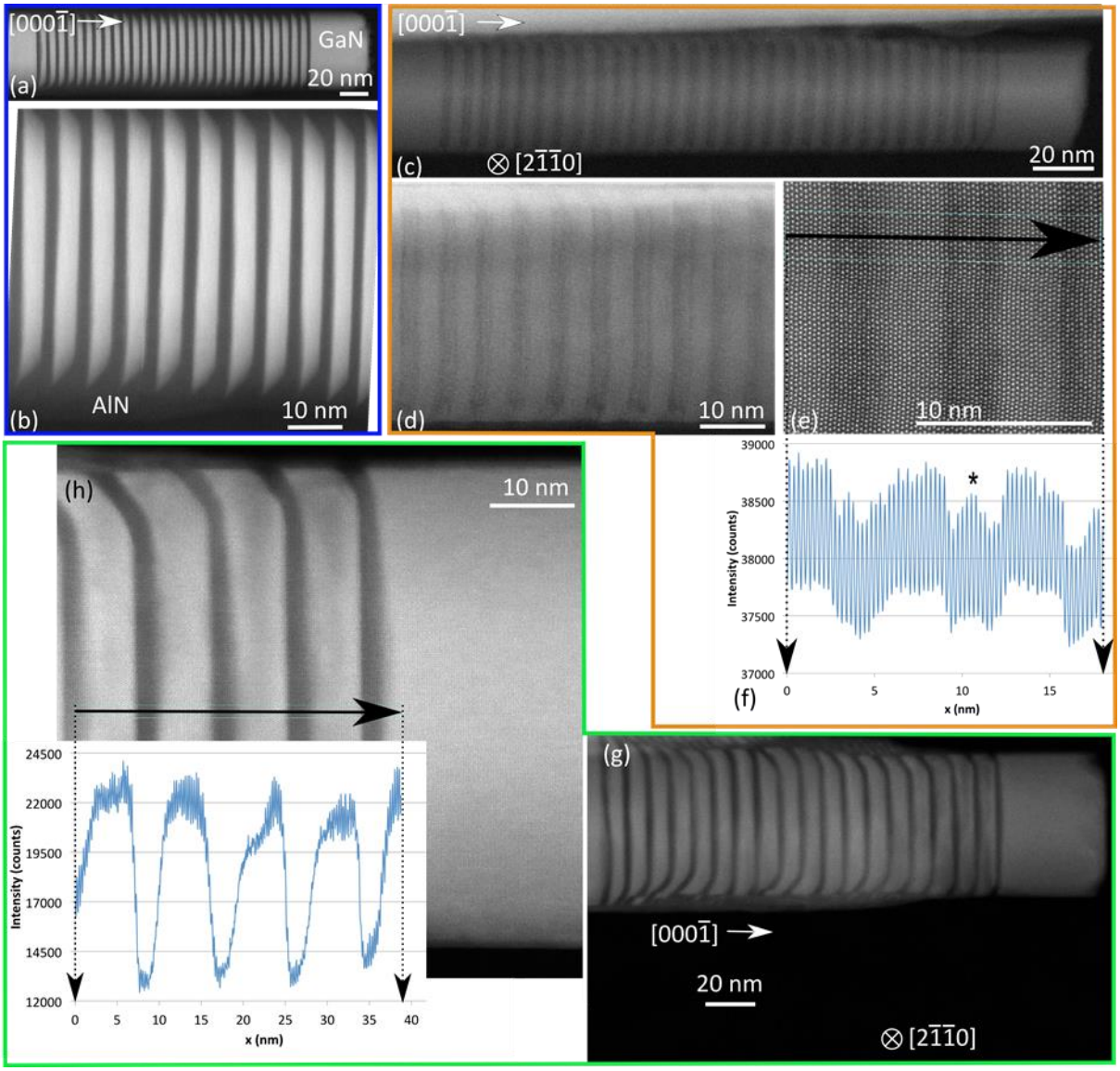

Figure 7.3: HAADF-STEM images and corresponding intensity profiles of the active region of a nanowire from samples (a,b) A1, (c,d,e,f) C2 and (g,h) B1. Dark/bright contrast corresponds to Al-rich/Ga-rich areas. (f) The "*" symbol in (f) indicates a region of higher intensity corresponding to increased Ga content in the AlGaN barrier (modified from ref. [187]).

The shell thickness gradually decreases as we move towards the cap. The first two or three QWs are characterized by a narrower width and higher irregularity in the thickness,

which can deviate up to two monolayers (±0.5 nm) from the average. The broadening of the disks occurs during the growth, in an attempt to partially relieve the strain induced by the lattice mismatch between AlN and GaN. The first QWs are grown under different misfit stress conditions: the GaN stem, which is originally relaxed, becomes compressively strained along the growth axis during the growth of the MQW, due to the formation of the AlN shell [190]. The strain stabilizes after the growth of about 3 MQW periods [35,191], which leads in turn to the stabilization of the well width and diameter.

Similar HAADF-STEM images of the active region of sample C2 with GaN/AlGaN MQWs are displayed in figures 7.3 (c), (d), (e) and (f). The nanowires present an Al-rich shell that envelops the MQWs and the stem. This shell is thinner (about 3-nm at the stem/MQW interface) than in the case of the binary MQWs, and its Al composition is higher than that of the barriers, although difficult to determine precisely. The ternary compound represents a reduction of misfit in comparison to AlN. Therefore, the diameter and width of the GaN wells is more homogeneous along the structure. However, the image contrast reveals certain composition inhomogeneities in the barriers. In some barriers we observe a brighter region in the center indicating a more Ga-rich region (see the "*" labelled region in figure 7.3 (f)). Moreover, near the nanowire sidewall, we first find a darker contrast followed by a brighter contrast in the AlGaN barrier indicating radial composition inhomogeneities (see bottom region of figure 7.3 (d)).

Figure 7.3 (g) and (h) present HAADF images of sample B1, the GaN/AlN heterostructure with ≈ 6 nm GaN wells. From the intensity profile in the inset of figure 7.3 (h) we see that the interface of AlN grown on GaN is sharper than the interface of GaN grown on AlN, which extends by around 1.5-2 nm. Note that this asymmetry can influence the confinement of carriers in the well, as it will be discussed later. Asymmetry at the interfaces, involving intermixing or alloying, is often found in GaN/AlN MQWs in nanowires with large wells, and it is explained by the strain evolution of GaN during the growth process [191]. Indications of graded GaN-AlN interfaces are also reported in Ga-polar GaN/AlN QWs grown by metalorganic vapor phase epitaxy [192], and are attributed to the instability of the GaN/AlN interface under strain [193]. In this latter case, it is possible to attenuate the interdiffusion by forcing a compressive strain in the layers [192] and reducing the growth temperature [194], which can be combined with a pulsed injection process [195]. However, in the case of nanowire growth, such tuning of the growth conditions leads also to modifications of the nanowire diameter and shape.

7.3 Optical properties

The band-to-band behavior of these samples was studied by low-temperature PL at 5K. The PL peak wavelengths are summarized in table 7.1. As an example, the inset of figure 7.4 presents the PL spectra of samples NS1, A1 and B1, illustrating how the emission redshifts with increasing QW width in GaN/AlN heterostructures. In most of the samples, a weak PL emission from the GaN stem is visible at around 360 nm (3.44 eV), for example for sample A1

in the inset of figure 7.4. This indicates that the stem is significantly strained due to the AlN shell, as the unstrained GaN emits rather at 357 nm (3.47 eV) as observed in the PL studies in section 6.2.2.

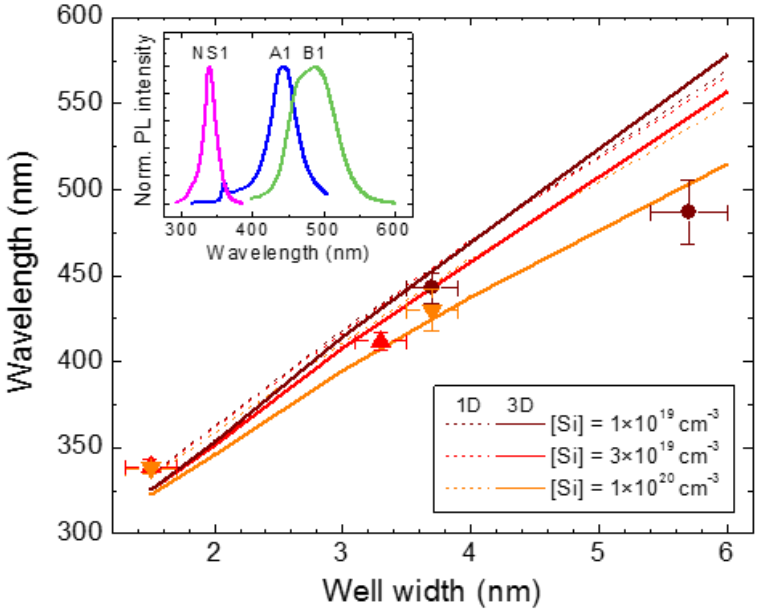

Figure 7.4: Theoretical value of the e1-h1 transition in GaN/AlN nanowires with varying well thickness, calculated using the nextnano[3] software in 3D (solid lines) and 1D (dashed lines). Data points indicate the PL peak wavelength of the samples under study, with horizontal error bars representing the uncertainty in the well thickness and vertical error bars representing the spectral width at 90% of the maximum PL intensity (simulations and experimental data at 5 K). Inset: Normalized low temperature (5 K) PL spectra of samples NS1, A1 and B1. (Modified from ref. [187]).

In figure 7.4, the peak emission wavelength of the GaN/AlN samples under study is compared with theoretical calculations. Note that the experimental points are plotted with a horizontal error bar that represents the error in the determination of the GaN well width, and a vertical error bar that indicates the spectral width at 90% of the maximum intensity. Theoretical calculations were performed in 1D (dashed lines) and 3D (solid lines) for various doping levels, indicated by different colors. In general, the result of 3D calculations deviates slightly from the 1D approximation due to the strain distribution in the wire, particularly the effect of the compressive stress along the nanowire axis imposed by the presence of the AlN shell. Increase in doping for the same QW dimensions results in blueshifting of the PL emission due to screening of the internal electric field. For higher doping levels, the deviation between 1D and 3D calculations becomes more significant, since it is easier to screen the internal electric field in the nanowire geometry, as previously demonstrated [142,143].

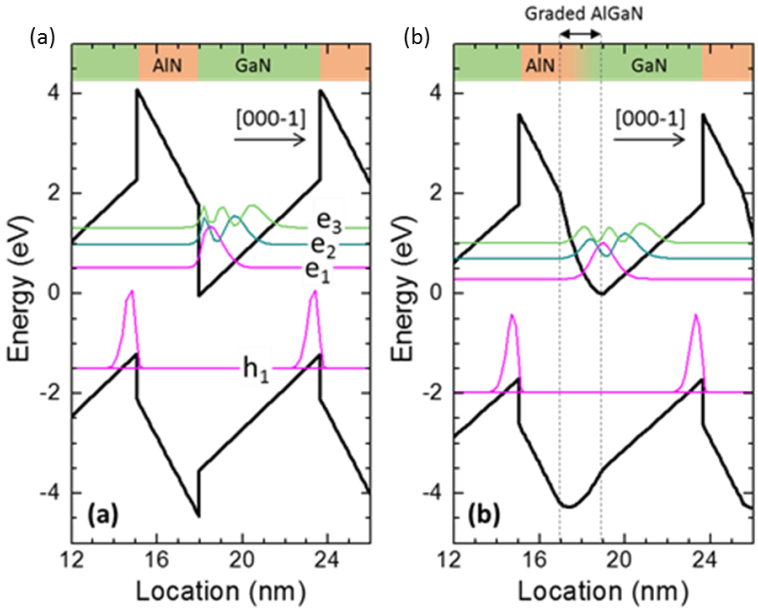

Figure 7.5: Calculations of the band diagram of a GaN/AlN multi-quantum-well structure with the dimensions of B1, presenting (a) sharp GaN/AlN interfaces, and (b) a 2-nm graded interface (first interface of the well along the [000-1] growth axis). The squared wave functions for the three first electron levels (e1, e2, e3) and the first hole level (h1) are also represented. The calculations were made in 1D using the self-consistent 8-band **k·p** Schrödinger-Poisson solver of nextnano[3] (modified from ref. [187]).

The experimental points match the theoretical calculations within their error bars, with the exception of sample B1, emitting at 490±19 nm, which is far from the 562 nm theoretically predicted. The explanation to this discrepancy is found looking back at the structural characterization of the sample. Structural characterization had, in the previous section, showed that the first interface of the well along the growth axis presents a GaN-AlN intermixing area that can extend 1.5-2 nm. To visualize the effect of such an interface on the band diagram, figure 7.5 (a) and (b) presents 1D calculations of the band diagram of a GaN/AlN MQW structure with the dimensions of B1. We compare a structure (a) with sharp GaN/AlN interfaces and (b) with a 2-nm graded interface (first interface of the well along the growth axis, in agreement with our observations). The squared wave functions for the three first electron levels (e_1, e_2, e_3) and the first hole level (h_1) are also displayed in the figure 7.5. Due to the sign of the electric field in the wire, the graded interface corresponds to the area of highest probability of localization of the electrons within the well. Therefore, the shape of the electron wave functions is very sensitive to the interface quality. As the interface gets broader, the electron and hole wave functions get closer along the growth axis and the e_1–h_1 transition energy blueshifts. Considering the geometry of B1, the theoretical wavelength associated to the e_1–h_1 transition becomes 504 nm (see table 7.1), now within the error bar of the experimental value (490±19 nm).

In the case of GaN/AlGaN heterostructures i.e., samples C1-C3, their emission spectra are clearly blueshifted with respect to GaN/AlN samples of similar dimensions (PL peak between 362-368 nm for samples C1-C3, to be compared with peaks between 430-445 nm for

samples A1-A3), due to the reduction in the internal electric field when lowering the Al content. The experimental emission wavelength shows good agreement with 3D calculations of the electronic levels, as shown in table 7.1.

Room-temperature FTIR spectroscopy was used to study the ISB absorption in these heterostructures. Transmission dips assigned to ISB absorption appear only at grazing angles between 5-20° and for TM-polarized light. To correct the spectral variation of the light intensity and the effect of the substrate, spectra are divided by the transmittance of a reference sample containing undoped GaN nanowires with the same total length as the ISB samples. The transmittance of this reference sample is very similar to that of the samples with GaN/(Al,Ga)N heterostructures when measured at larger angles of incidence (≈ 30-50°), both for TE and TM polarized light. This is explained by the decrease of the ISB absorption at large incidence angles, in agreement with the polarization selection rules [80].

The normalized absorption spectra for TM polarization are displayed in figure 7.6. The absorption bands are about 250-300 meV broad. Within the GaN/AlN samples (NS1-NS2, A1-A3 and B1), the absorption shifts to lower energies (longer wavelengths) for increasing well width. The longest peak absorption wavelength is 3.4±0.5 μm, obtained for B1, which is the longest intraband absorption wavelength reported in GaN/AlN nanowires, to the best of our knowledge. In the case of B1, a broader and less intense secondary absorption band appears at higher energies (peak absorption wavelength ≈ 1.45±0.13 μm).

The ISB absorption bands presented here are significantly narrower than results in ref. [35], where a FWHM of about 400 meV was measured. This is explained by the higher uniformity of the heterostructure dimensions along the nanowire axis, in terms of both diameter and thickness. On the other hand, here the transitions appear redshifted in comparison to ref. [35]. The difference is particularly striking when comparing sample S6 in ref. [35] (6 nm GaN / 4 nm AlN, absorbing at 1.74 μm) with B1 (5.7 nm GaN / 2.9 nm AlN, absorbing at 3.4 μm). Interpretation of these results requires careful comparison with simulations taking into account the surface doping density (e.g. [Ge] = 5×10^{13} cm^{-2} for S6 vs. [Si] = 2×10^{12} cm^{-2} for B1) and the resulting many-body effects.

The experimental peak absorption wavelengths are compared with 1D calculations in table 7.1. Unfortunately, the complexity of the problem did not allow a systematic calculation in 3D using the nextnano^3 software, due to the high number of laterally-confined electron states located at energies between the ground electron state e_1 and first vertically-confined state e_2. However, given the proximity of 1D and 3D calculations, in figure 7.4 and section 6.2, 1D calculations should provide a reasonable description of the intraband phenomena. The theoretical values presented in the table are corrected to account for the blueshift associated to the exchange interaction and plasmon screening or depolarization [80,82], as described in ref. [196].

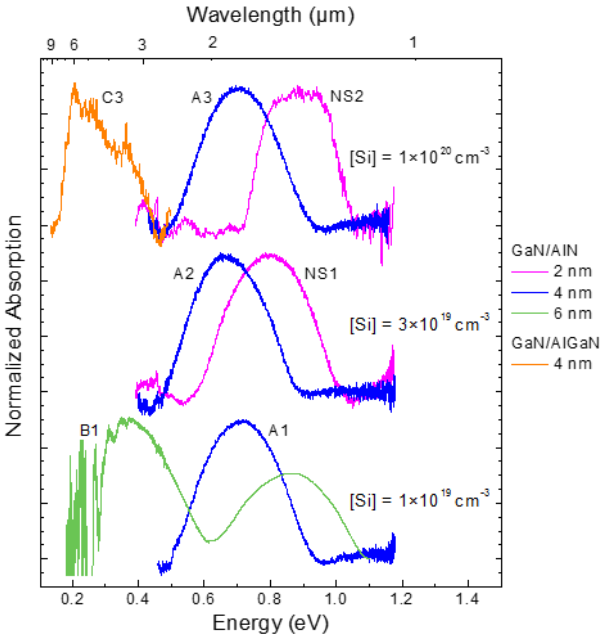

Figure 7.6: Normalized IR absorption for TM-polarized light measured at grazing incidence (≈ 10°). Spectra from samples with different doping levels are vertically shifted for clarity (modified from ref. [187]).

The peak intraband absorption of samples NS1-NS2 and A1-A3 follows the theoretical trend for e_2–e_1, keeping always slightly blueshifted with respect to the calculations. This deviation could be explained as due to the error associated to modelling the structure as 1D (see figure 9.8 in section 9.1.3 which compares results of 1D and 3D calculations in nanowires containing GaN/AlN heterostructures with and without AlN shell). On the contrary, sample B1 appears strongly redshifted with respect to the theory (experimentally at 3.4±0.5 μm, expected at 2.6 μm). Looking back at figure 7.5, the location of the electron levels is very sensitive to the presence of the graded interface. Taking into account the results in figure 7.5(b) with a 2-nm-thick linearly graded interface, the predicted e_2–e_1 energy is 3.0 μm, within the error bar of the experimental result, whereas the secondary absorption at higher energy is assigned to transitions to higher electron states. Note that the energy difference between e_3 and e_1 would explain a transition at 1.7 μm.

The optical behavior of B1, with a blueshift of the interband emission and a redshift of the intraband absorption with respect to theoretical calculations, could be misinterpreted as a decrease of the quantum confined Stark effect in the nominal structure, which has often been claimed in GaN/AlN nanowire heterostructures [183]. A decrease of the internal electric field could be justified by defect-assisted strain relaxation or by the compressive effect of the AlN shell (the latter was already taken into account in our model). Our results here show that it is important to perform advanced structural studies to assess the quality of the heterointerfaces in order to understand the origin of the optical features, and distinguish between interface-related and defect-related phenomena.

In the case of nanowires containing GaN/$Al_{0.4}Ga_{0.6}N$ heterostructures, FTIR transmission measurements did not reveal any indication of intraband absorption in samples C1 and C2.

However, C3, the most heavily doped sample, presents an absorption band at 6.4-4.5 µm that appears only for TM-polarized light and under grazing incidence. This band is slightly redshifted with respect to the expectations (4.6 µm obtained from 1D calculations), which can be justified by the strain distribution in the heterostructure due to the presence of the AlN shell.

7.4 Conclusion

In conclusion, we synthesized self-assembled GaN/AlN and GaN/$Al_{0.4}Ga_{0.6}N$ nanowire heterostructures structurally designed to absorb in the MWIR wavelength region. In the case of GaN/AlN heterostructures in GaN nanowires, we varied the GaN well width from 1.5 to 5.7 nm. Heterostructures with 1.5-4 nm wells present sharp GaN/AlN interfaces. However, in larger wells (5.7 nm), one of the GaN/AlN heterointerfaces was not sharp but rather a graded alloy, which extends by around 1.5-2 nm and has strong influence on the electron wave functions in the well. Increasing the GaN well width in the heterostructures, we observe a redshift of the PL emission and a redshift of the ISB absorption from 1.4 to 3.4 µm, at room temperature. The results agress well with theoretical models, taking into account the structural characteristics (including AlN shell and GaN/AlN interface sharpness or intermixing) and many-body effects associated to the doping level. For GaN/$Al_{0.4}Ga_{0.6}N$ heterostructures, the ternary compound represents a reduced polarization, which leads to the blueshift of the band-to-band transitions and redshift of the ISB transitions. As a result, we obtained TM-polarized absorption in the 4.5-6.4 µm wavelengths.

8. Nonpolar heterostructures for the far-IR range

In this chapter, we assess the possibility to observe ISB transitions in the 1.5–9 THz frequency range in nonpolar m-plane GaN/AlGaN MQWs, covering most of the 7–10 THz band inaccessible to GaAs based technologies. Such nonpolar structures present inhomogeneities of the Al composition in the barriers along the growth axis, however we did not identify any extended structural defects introduced by the epitaxial process. We study the effect of varying the Si doping concentration and we explore the effect of using Ge as a dopant.

For the study of ISB transitions using non-polar m-plane GaN/AlGaN, I performed the AFM, PL and FTIR measurements, in collaboration with C. B. Lim. XRD characterization was performed by J. Schörmann, and C. B. Lim was in charge of the MBE growth. STEM measurements were performed by C. Bougerol and B. Haas. Results were published in "Nonpolar m-plane GaN/AlGaN heterostructures with ISB transitions in the 5–10 THz band", C. B. Lim et al., Nanotechnology ***26****, 435201 (2015)* [47].

Regarding the study of the effect of the doping concentration and the nature of the dopant on non-polar m-plane GaN/AlGaN, I performed the AFM and PL. I assisted C. B. Lim in FTIR measurements. C. B. Lim was in charge of the MBE growth. STEM measurements were performed by C. Bougerol. Results were published in "Effect of doping on the far-IR ISB transitions in nonpolar m-plane GaN/AlGaN heterostructures", C. B. Lim et al., Nanotech. ***27****, 145201 (2016) and "Effect of Ge-doping on the short-wave, mid and far-IR ISB transitions in GaN/AlGaN heterostructures", Semicond. Sci. Technol.* ***32*** *125002 (2017)*

Using c-plane GaN/AlN QWs, the ISB absorption can be tuned in the 1.0–3.5 µm wavelength range by changing the QW thickness from 1 to 7 nm [73,194,197–199]. In addition to QWs, we have explored the use of nanowires in this spectral region. However, to shift the absorption towards longer wavelengths, it is necessary to reduce the polarization-induced internal electric field even further, which can be attained by using ternary AlGaN barriers with reduced Al mole fraction. Varying the geometry and composition of the barriers, the ISB absorption in AlGaN/GaN QWs can be tailored to cover the range up to 10 µm [200–205]. Reducing the ISB transition energy below 60 meV (wavelength > 20 µm) requires further band engineering to compensate the internal electric field in the QWs, which is only achieved by implementation of complex multi-layer QW designs [206–209]. The use of nonpolar crystallographic orientations, particularly the m-plane, is a promising alternative to obtain GaN/AlGaN QWs without internal electric field [46–48].

We have recently reported that the (1-100) *m*-plane is the best nonpolar crystallographic orientation for ISB applications, based on comparative results with the (11-20) *a*-plane [48]. MWIR ISB absorption in the 4.0 to 5.8 µm (310 to 214 meV) range has been observed on m-plane GaN/AlGaN MQWs [48,210], and photodetection at 7.5 and 9.3 µm (165 and 133 meV, respectively) has been demonstrated at 14 K using m-InGaN/(Al)GaN MQWs [211]. ISB absorption in the 3.77–6.31 THz window (15.6–26.1 meV) using nonpolar *m*-GaN/AlGaN MQWs was first shown by Edmunds et al. [46].

High doping levels are known to significantly perturb the IR absorption spectrum. In the SWIR, the exchange interaction (dominant many-body mechanism) leads to a blueshift of the ISB transitions in c-plane GaN/AlN MQWs [14]. In the MWIR, using c- and m-plane GaN/AlGaN MQWs, high doping levels lead to the broadening of the ISB transition. Also, the expected redshift due to the screening of the internal electric field is over-compensated by the blueshift induced by exchange interaction and the now dominant depolarization [15, 16]. Moreover, results from section 6.1 have shown that Ge is a potential dopant for ISB technology.

In this chapter, we extend the study to cover the 1.5–9 THz frequency range with nonpolar *m*-plane GaN/AlGaN MQWs. We explore the effect of both Si and Ge doping on the low-temperature ISB absorption of nonpolar m-plane GaN/ AlGaN MQWs designed for ISB absorption in the THz range (FIR).

8.1 Sample design and growth

The samples under study consist of 40-period *m*-plane GaN/AlGaN MQWs grown by PAMBE. They were grown on free-standing semi-insulating (s.i.) Fe-doped *m*-GaN platelets sliced from (0001)-oriented GaN boules synthesized by hydride vapor phase epitaxy (resistivity > 10^6 Ωcm, dislocation density < 5×10^6 cm^{-2}). The samples were grown at a substrate temperature T_s = 720°C and with a nitrogen-limited growth rate of 0.5 ML/s (≈ 450 nm/h). Growth was performed under the optimum conditions for *c*-GaN, i.e. slightly Ga-rich conditions.

For ISB transitions in the FIR region, we used larger QWs than in the SWIR and MWIR region. The QW widths were varied so that we obtain ISB absorption in the range of 4.8-8 THz (19.7-33 meV) as indicated in table 8.1. The barriers were designed to be around 20 nm to avoid coupling between the wells. They were composed of AlGaN with Al content below 10%, which reduces the lattice mismatch in the structure. The GaN wells were homogeneously doped with silicon at a concentration of 3×10^{18} cm^{-3} and, to prevent surface effects, the MQW structures were capped with a 50 nm AlGaN layer with the same Al content as the barriers. Figure 8.1 shows (a) a sketch of the sample structure and (b) the band diagram of sample E3419m calculated using 1D nextnano[3].

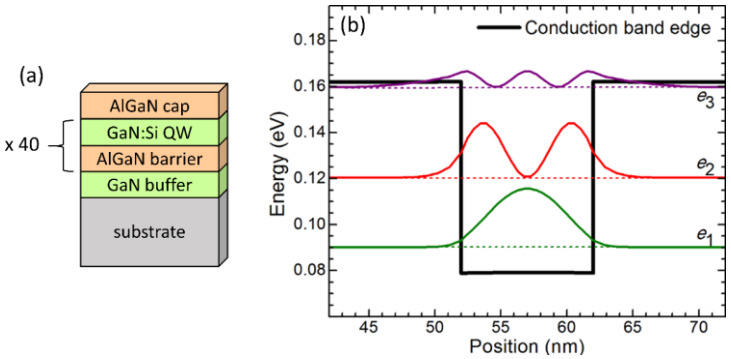

Figure 8.1: (a) Sketch of the sample structure. (b) Conduction band diagram with the three first electronic states and their square wave functions of a QW in the center of the active region of sample E3419m (Modified from ref. [47]).

Sample	t_{QW} (nm)	t_B (nm)	x_B (%)	Period (nm)	$\Delta\omega_{MQW}$ (arcsec)	$\Delta\omega_{GaN}$ (arcsec)	simulated e_2-e_1 (meV)	ISB central energy [window] (meV)
E3420m	9.5	21.7	8	31.2	Δωc = 35 Δωa = 34	Δωc = 34 Δωa = 39	33	25.4 [13.4-37.4]
E3419m	10.0	18.5	7.5	28.5	Δωc = 38 Δωa = 35	Δωc = 35 Δωa = 36	30.5	27.1 [18.1-36.1]
E3424m	10.4	21.2	7.5	31.6	Δωc = 22 Δωa = 31	Δωc = 24 Δωa = 39	30.3	21.3 [6.3–36.3]
E3423m	12.9	21.1	6	34.1	Δωc = 38 Δωa = 28	Δωc = 42 Δωa = 29	19.7	20.9 [7.9–33.9]

Table 8.1: Structural and optical characteristics of the *m*-plane GaN/AlGaN MQWs: QW and barrier thickness (t_{QW} and t_B, respectively); Al composition of the barriers (x_B); MQW period measured by HR-XRD; FWHM of the ω-scan of the (3-300) x-ray reflection of the MQWs ($\Delta\omega_{MQW}$) and of the GaN substrate ($\Delta\omega_{GaN}$), measured in the *c* and *a* directions ($\Delta\omega_c$ and $\Delta\omega_a$, respectively); simulated ISB transition energy; measured ISB transition energy window and central energy.

The samples for studying the effect of doping consisted of a series of 40 periods of *m*-plane GaN/AlGaN (10 nm GaN/18.5 nm $Al_{0.075}Ga_{0.925}N$) MQW structures where the doping densities in the GaN QW was varied using both Si and Ge as dopant. The list of samples are provided in table 8.2. The entire structure of the sample is identical to the sample E3419m but with different doping densities. They hence follow the structure described in figure 8.1 (a).

Sample	Dopant	n_S (cm^{-2})	$\Delta\omega_{MQW}$ (arcsec)	$\Delta\omega_{GaN}$ (arcsec)	ISB central energy (meV)	absorption per pass (%)
E3445m	Si	3×10^{12}	23	22	35.5	9.1
E3447m	Si	1×10^{12}	44	33	28.2	10.0
E3448m	Si	3×10^{11}	20	19	31.0	7.3
E3449m	Si	1×10^{11}	35	35	27.6	2.9
E3643m	Ge	5×10^{12}	48	40	24.1	13
E3541m	Ge	2×10^{12}	46	38	23.5	19

E3540m	Ge	5×10^{11}	52	42	25.1	19

Table 8.2: Structural and optical characteristics of the m-plane GaN/AlGaN MQWs: doping concentration[5]; FWHM of the ω-scan of the (3-300) x-ray reflection of the MQWs and of the GaN substrate measured with the c direction in the diffraction plane; measured ISB transition energy; ISB absorption per pass.

8.2 Structural characterization

Figure 8.2 shows the surface of a typical sample measured by AFM. We observe surfaces with a smooth morphology down to the atomic scale, having an RMS roughness of 0.28 nm. We did not observe significant differences as a function of the doping level or the nature of the dopant. The systematic atomic steps are indicative of step flow growth. This is a convincing proof of not having very serious distortions in the QW structures. Similar structures with higher Al content in the barriers were reported to have a degraded morphology [212]. Indicating a significant improvement of the sample morphology when reducing the Al mole fraction in the barriers, i.e. when reducing the lattice mismatch in the structure. However, a few cracks (between 1 and 5 cracks within an overall distance of 5 mm) propagating along the *a* direction were observed in nanostructures with a total MQW thickness above 1.2 µm and an average Al composition around 5%, which is in agreement with ref. [213]. This is consistent with the higher tensile stress along the *c* direction (GaN/AlN lattice mismatch = 3.9%) with respect to the in-plane *a* direction (GaN/AlN lattice mismatch = 2.4%).

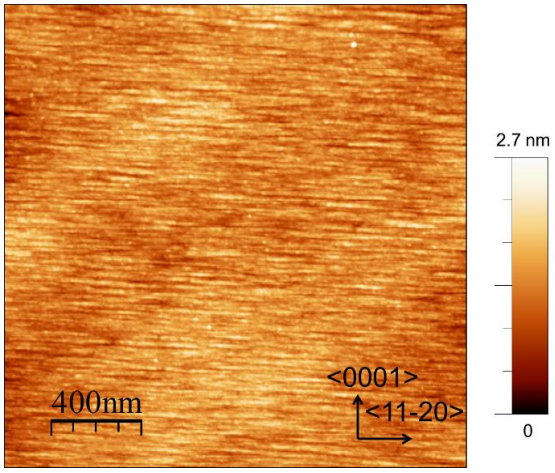

Figure 8.2: AFM image of sample E3540m showing smooth surface morphology (RMS = 0.28 nm), comparable to that observed on the Si-doped FIR structures (modified from ref. [179]).

For the first set of samples, the varying well width, the periodicity and the average Al contents of the structures were measured by HRXRD. Figure 8.3 displays ω-2θ scans along the (3-300) reflection of samples E3420m and E3423m, together with simulations assuming that

[5] Doping concentration is described here in cm^{-2} for ease of calculation and for comparison with literature. The conversion follows, n_S (cm^{-2}) = n(cm^{-3})×thickness of the quantum well.

the quantum structures are fully strained on the GaN substrate. The periods of the MQWs extracted from the inter-satellite distance are summarized in table 8.1. The FWHM of the ω-scans were measured for the substrate and the MQW zero-order (3-300) reflection with the *c*-axis and the *a*-axis in the plane of diffraction ($\Delta\omega_c$ and $\Delta\omega_a$, respectively). Both $\Delta\omega_c$ and $\Delta\omega_a$ remain in the 30±8 arcsec range for all the MQWs, and these values are similar to those measured for the substrate reflections. This is probably indicative for the absence of extended defects like dislocations or stacking faults.

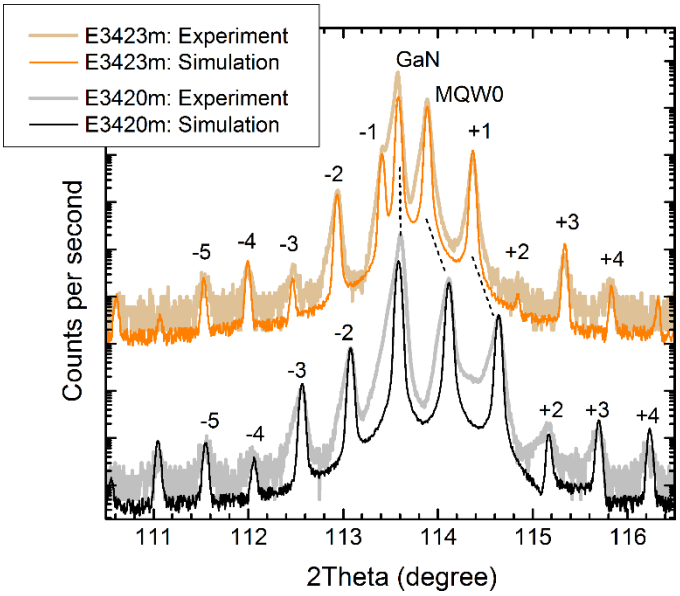

Figure 8.3: HR-XRD ω-2θ scans of the (3-300) reflection of samples E3420m and E3423m. Simulations assume the structures fully strained on the GaN substrate (Modified from ref. [47]).

We verified that there is no significant variation of the HR-XRD diffractograms for Ge- and Si-doped samples, as illustrated in figure 8.4, which displays the ω-2θ scans around the (3-300) reflection of E3643m (Ge-doped) and E3445m (Si-doped).

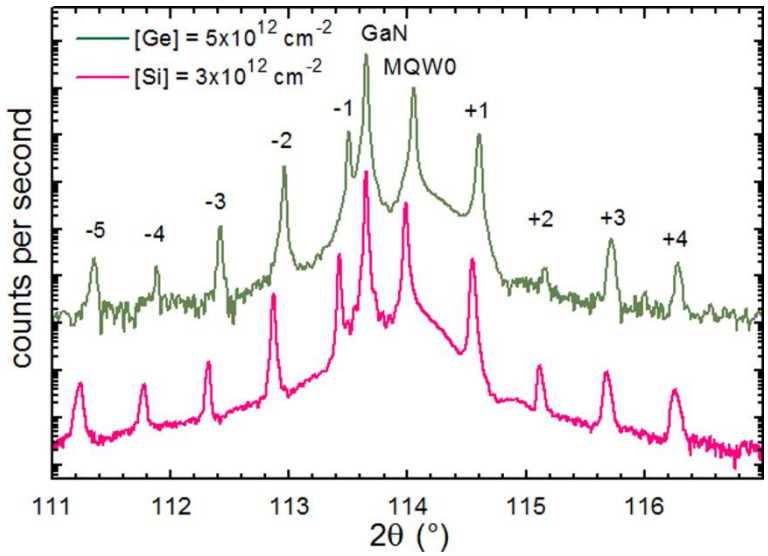

Figure 8:4: HR-XRD ω-2θ scans of the (3-300) reflection of samples E3643m (Ge-doped) and E3445m (Si-doped).

The structures were further analyzed by HAADF-STEM and HRTEM. Figure 8.5 (a) and (b) show cross-section HAADF-STEM images covering the entire MQWs of sample E3419m, viewed along (a) <0001> and (b) <11-20> respectively. The QW interfaces are uniform along the two perpendicular directions, confirming the 2D nature. It is quite clear that no dislocations or stacking faults appear in the epitaxial layers, which was further confirmed by HRTEM measurements (not shown).

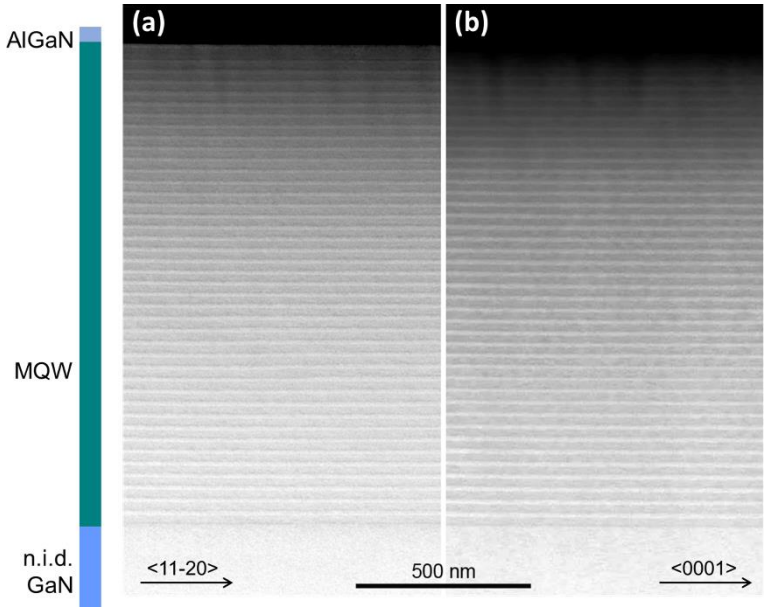

Figure 8.5 Cross-section HAADF-STEM images of sample E3419m viewed (a) along <0001>, and (b) along <11-20>. Dark layers correspond to the AlGaN barriers/cap and bright layers correspond to GaN (Modified from ref. [47]).

Figure 8.6 (a) presents a HAADF-STEM view of part of the heterostructure in the middle of the sample E3419m (same as in figure 8.5). We find that the AlGaN barriers have an inhomogeneous contrast with dark lines parallel to the QW interfaces. This contrast is

assigned to alloy inhomogeneity along the growth axis, as confirmed by the absence of extended defects in the high-resolution image in figure 8.6 (b). From the intensity profile extracted from figure 8.6 (a), the alloy fluctuations in the barriers reach ± 30% of the average concentration. This fluctuation has been qualitatively confirmed by EDX analysis.

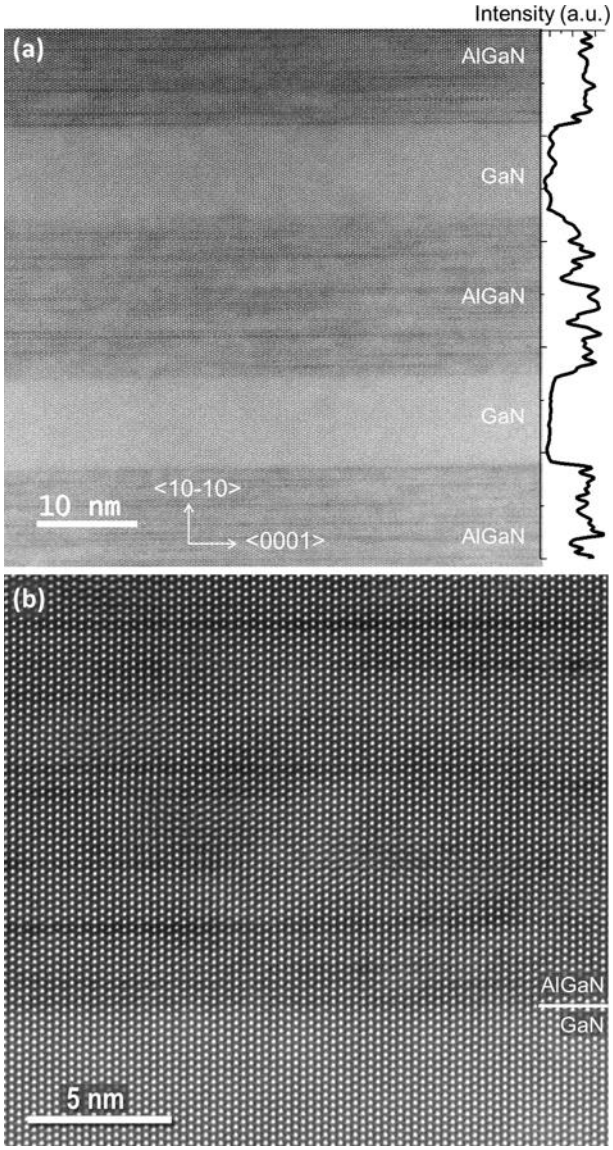

Figure 8.6: (a) Cross-section HAADF-STEM image of sample E3419m viewed along <11-20> and intensity profile along <10-10>. (b) High-resolution HAADF-STEM image of the barrier/QW interface showing that the variations of contrast in the image are not associated to structural defects. Layers with dark and bright contrast correspond to the AlGaN barriers and GaN QWs, respectively (Modified from ref. [47]).

Similar STEM studies were performed on Ge-doped sample E3541m and the results are displayed in figure 8.7, similar to the Si-doped E3419m, alloy inhomogeneities are visible in the AlGaN barriers.

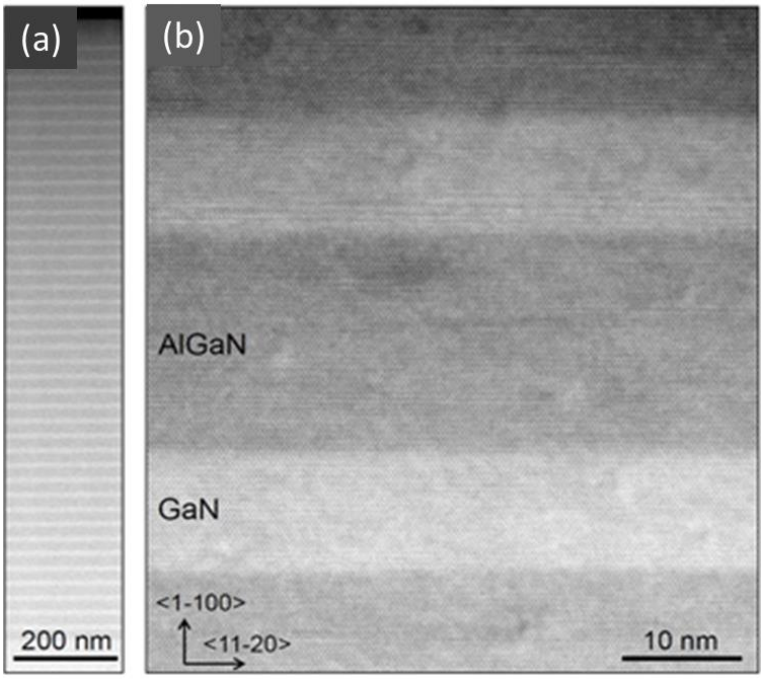

Figure 8.7: Cross-section HAADF-STEM images of (a), (b) Ge-doped sample E3541m viewed along <0001>. The images show two QWs in the middle of the stack. Clear areas correspond to GaN, darker contrast reveals the presence of aluminum. (Modified from ref. [196])

8.3 Optical characterization

We performed temperature-dependent PL measurements on these samples. Figure 8.8 (a) shows a typical PL spectrum of the series, obtained for E3423m as a function of temperature in the range 5 to 300 K. The low temperature spectrum (with the highest peak intensities) is dominated by the excitonic line associated to the MQWs (indicated as MQW peak), together with its LO-phonon replicas. At high energy, the emission from the AlGaN cap layer is visible, but it is rapidly quenched for increasing temperatures. The AlGaN cap layer peak position is consistent with the estimated AlGaN band gap. Figure 8.8 (b) shows the variation of the MQW peak intensity versus temperature. Two decay pathways can be distinguished. We can calculate the corresponding activation energies E_a and E_b extracted from,

$$I = \frac{I_0}{1+\alpha_1 \exp\left(-\frac{E_a}{kT}\right)+\beta_1 \exp\left(-\frac{E_b}{kT}\right)} \qquad \text{(equation 8.1)}$$

where I is the PL intensity, I_0 the PL peak intensity, α_1 and β_1 are constant parameters, k is the Boltzmann constant, and T is the sample temperature during the measurement.

The MQW line shows a low activation energy (E_a = 4.6±0.3 meV) at lower temperatures and a higher activation energy (E_b = 43±5 meV) at higher temperatures. The first activation energy is related to the thermal detrapping of donor bound states to free exitons [167], i.e.

the excitons that are trapped around donor impurities obtain energy to become free excitons. The higher activation is the energy required for the activation of non-radiative recombination, since the decrease in intensity is due to an increase in a non-radiative recombination process [214].

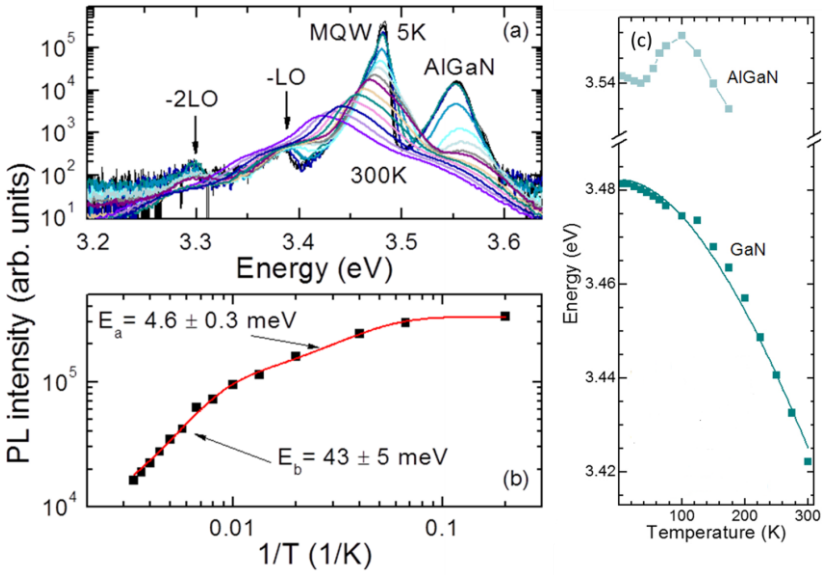

Figure 8.8 (a) Variation of the PL spectrum of sample E3423m as a function of temperature, from 5 to 300 K. (b) Variation of the PL intensity of the MQW-related PL peak with temperature. Squares correspond to the experimental data and the red solid line corresponds to the fit to equation 8.1 (c) Temperature dependent energy of GaN and AlGaN interband transitions in sample E3423m and fit to the Varshni law (Modified from ref. [212])

The thermal shift of the GaN MQW transition is presented in figure 8.8 (c) and is well described by the Varshni law (equation 2.2), with the Varshni and Debye coefficients α_V = 0.590 meV/K and β_D = 600 K, respectively, which is in complete agreement with the temperature-induced bandgap quenching in *c*-GaN/AlN MQWs described by ref. [215].

The high-energy line around 3.55 eV is associated to the emission from the AlGaN cap layer. Taking into account the penetration depth of the laser (excitation at 244 nm) and the geometry of the sample, the PL emission originates only from the cap layer and the two or three topmost QWs.

On the other hand, the thermal shift of AlGaN presents a marked S-shaped behavior, characteristic of AlGaN alloys [114,166]. For temperatures above 100 K, the emission redshifts following the semiconductor band gap *i.e*. the PL energy follows the Varshni law. However while increasing the temperature, the emission first blueshifts up to about 100 K and this is attributed to the transition from localized to extended bandtail states. Such localization could originate from variations of thickness, interface roughness, or alloy inhomogeneity. In our case, the STEM images revealed sharp interfaces and regular QWs. In addition, having such large QWs makes a variation of thickness unlikely to induce such localization. However the

STEM images have shown alloy fluctuations and the origin of the inhomogeneous potential distribution leading to exciton localization can be easily assigned to the alloy inhomogeneity.

The effect of the doping density on the PL emission energy and broadening is negligible in the range under study. This is due to the fact that, first, in nonpolar QWs there is no electric field to be screened by carriers, and second, the surface dopant densities used should not have a large effect on the band-to-band transition (the shift due to band filling is < 60 meV, and it is partially compensated by bandgap renormalization [152]).

The ISB absorption of the samples was characterized by FTIR spectroscopy performed at 5 K. Using sample E3419m as an example, figure 8.9 (a) illustrates typical TE- and TM-polarized THz transmission measurements, and figure 8.9 (b) compares the same transmission spectrum for TM-polarized light with that of the substrate. The inset of figure 8.9 (a) shows a magnified view. The apparent noise superimposed on all the spectra is an oscillation with nearly-regular periodicity in energy, which is assigned to a Fabry-Pérot interference. Using the refractive index of GaN in the FIR range from ref. [216], the cavity length associated to the interference is ≈ 350 μm, corresponding to the overall thickness of the samples. The transmission spectra for TE-polarized light present additional Fabry-Pérot oscillations associated to the MQW layers. In contrast, the transmission spectrum for TM-polarized light exhibits an easily discernible broad dip, in the 3-8 THz range in the case of sample E3419m, which is assigned to ISB absorption, following the polarization selection rule. This is confirmed by comparing the TM-polarized spectra of the sample and substrate (figure 8.9 (b)). In the inset of figure 8.9 (b), we display the normalized broadening of the absorbance (energy broadening divided by the central energy) as a function of the doping density in the MQWs. Hollow square symbols are extracted from ref. [46], and the full round symbol corresponds to our work.

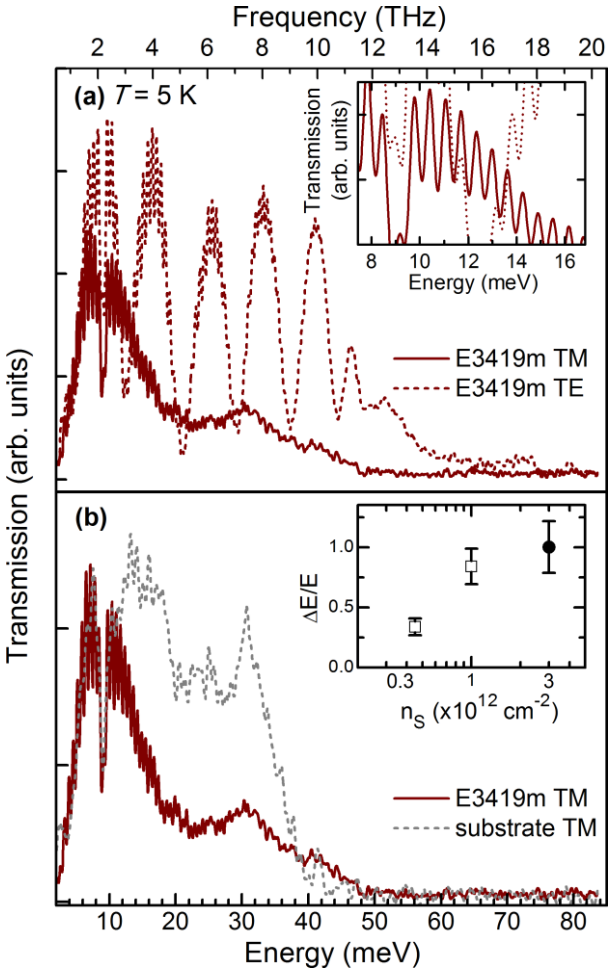

Figure 8.9: (a) Transmission spectra of TM and TE-polarized light of sample E3419m measured in the THz range at 5 K. Inset: Magnification of the transmission spectra showing Fabry-Pérot oscillations. (b) Transmission spectra of TM-polarized light of sample E3419m and of the substrate, measured in the THz range. Inset: Normalized broadening of the absorbance as a function of the doping density in the MQWs. Hollow square symbols are extracted from ref. [46], and the full round symbol corresponds to this work. (Modified from ref. [47])

We can define the normalized absorbance as $A = 1 - TM_{MQW}/TM_{sub}$, where TM_{MQW} and TM_{sub} are the TM-polarized transmission of the MQWs and of the substrate, respectively. Figure 8.10 presents the normalized absorbance of the samples under study for TM-polarized light, extracted from the transmission measurements. TM-polarized absorption is observed over a broad spectral window, ranging from 6.3 to 37.4 meV (1.5 to 9 THz). The extreme values and the peak energy of the absorption band are summarized in table 8.1. The central energy decrease from 27.1 to 20.9 meV (6.5 to 5 THz) as the QW width increases is consistent with the trend of the simulations. The entire ISB absorption window ranging from 6.3 to 37.4 meV (1.5 to 9 THz), provides experimental evidence that ISB transitions in GaN MQWs can cover the THz spectral range forbidden to GaAs. These results complete the work of ref. [46], which demonstrated THz ISB absorption (15.6-26.1 meV) in *m*-plane GaN/AlGaN MQWs. The broad absorption bands are consistent with the doping density in the QWs, *i.e.* at least three times higher than in Ref. [46], as illustrated in the inset of figure 8.9 (b).

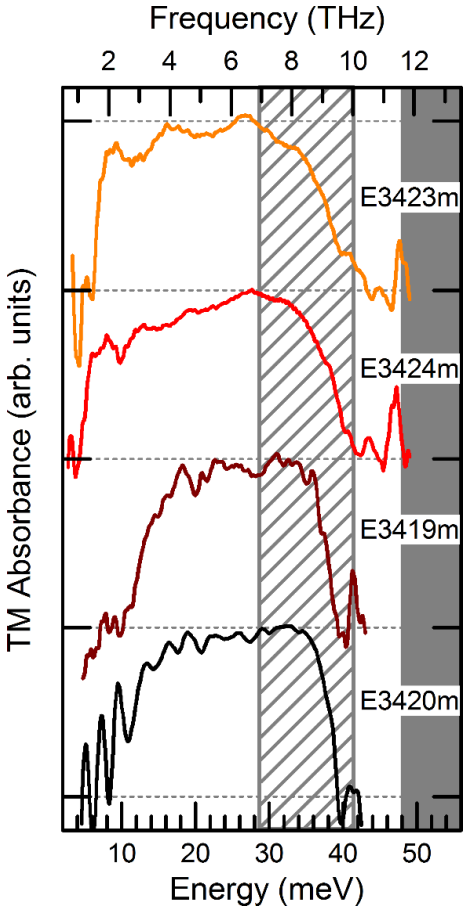

Figure 8.10: Normalized absorbance of TM-polarized light for the samples under study in the THz range at 5 K. Data are vertically shifted for clarity. The striped and shadowed areas represent the phonon absorption bands of GaAs and GaN, respectively. (Modified from ref. [47])

The measured ISB transition energies for different doping densities and dopants are recorded in table 8.2 and the normalized absorbance is displayed in figure 8.11 (a) and (b). For the Si doped samples, with increase in doping densities, we observe an increase in transition energy. For equivalent doping densities, the Ge-doped structures show ISB absorption peaks with smaller energy broadening than for the Si-doped structures. When increasing the Ge doping density, we observe a slight widening of the ISB absorption peak and no shift of the ISB energy. However we have to note that high doping density results in higher absorption which saturates when the Fermi level approaches the first excited electron state e_2 (the Fermi level is calculated to reach e_2 for a doping concentration of 2.3×10^{12} cm^{-2}).

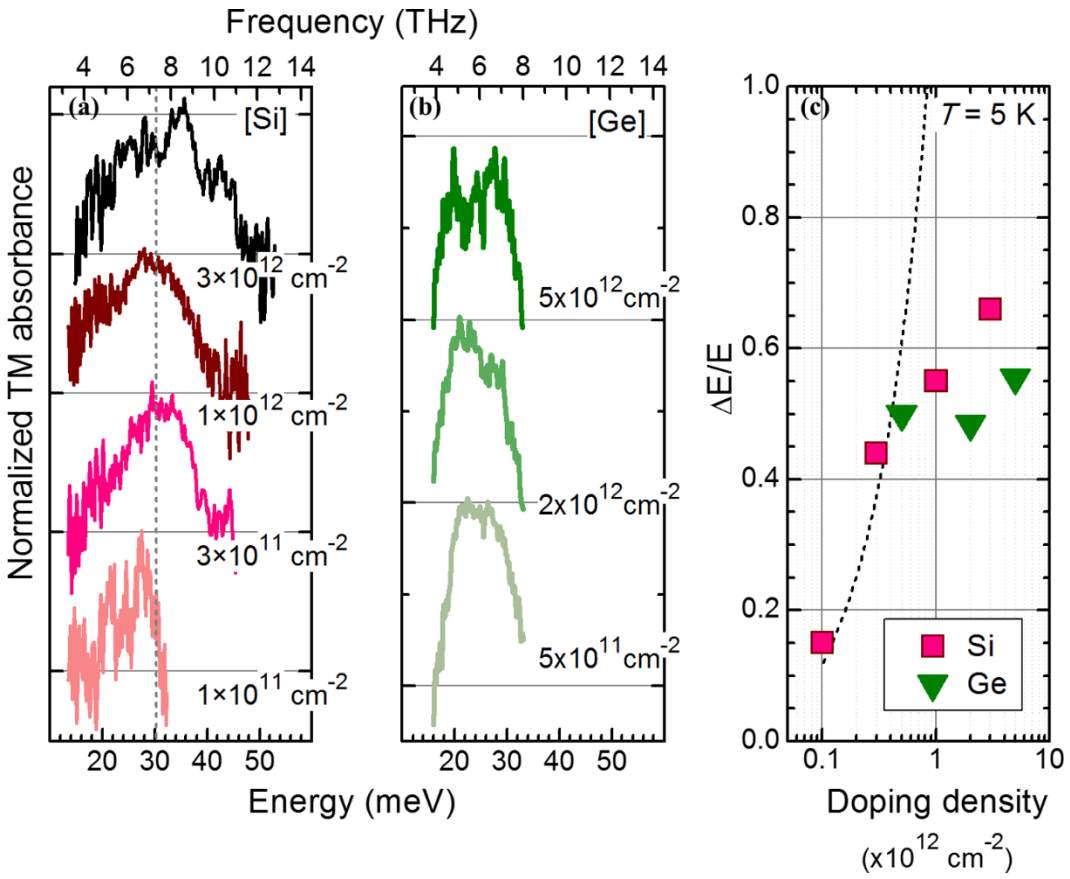

Figure 8.11: Normalized absorbance of TM-polarized light of (a) Si-doped (b) Ge-doped samples at T = 5 K. Data are vertically shifted for clarity. The dashed line indicates the theoretical ISB transition energy. (c) Normalized linewidth of the absorbance as a function of the doping density in the MQWs. The dashed line indicates the theoretical trend, not taking into account the population of the first excited state. (Modified from ref. [196])

The normalized linewidths (energy broadening divided by the peak energy, $\Delta E/E$) of the absorbance spectra are plotted in figure 8.11 (c), and are compared to theoretical calculations. These calculations were based on the models in ref. [217,218], and we calculated the normalized linewidth at low doping density (1×10^{11} cm^{-2}) taking into account the scattering by interface roughness (dominant at this low doping density), longitudinal acoustic and optic phonons and alloy disorder. In our estimation, we set the mean height of the roughness parameter to Δ = 0.2 nm and adjusted the correlation length to λ = 70 nm, values that are consistent with AFM measurements. When increasing the Si concentration, the scattering by ionized impurities becomes dominant and sets a linear dependence of the linewidth on the doping density. From our experiment, increasing the doping concentration by one order of magnitude increases the normalized linewidth by a factor of 4.4.

With increase in dopants, the transition in figure 8.11 (a) of Si-doped samples presents a blueshift that is assigned to many-body effects as described in section 2.3.2, namely exciton shift, exchange interaction and plasmon screening. Note that, from our calculations, the exciton shift for the considered doping densities is of the order of 10^{-14} meV, *i.e.*, negligible. The experimental results present a blueshift, as predicted by theory for the Si-doped samples

as shown in figure 8.12. However, the magnitude of the shift in the most heavily doped samples (E3445m and E3447m) is smaller than expected. The deviation might be attributed to the population of the excited electron state, consistent with the saturation of the absorption. Our study completes the recent work of ref. [218] on *m*-GaN/AlGaN MQWs showing ISB transitions in the MWIR region. They had developed a model that both calculates the blueshift caused by many-body effects on the transition energy, and quantifies the effect of scattering, mainly due to interface roughness, LO phonons, and ionized impurities, on the ISB absorption linewidth.

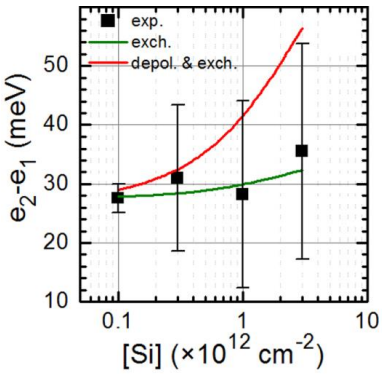

Figure 8.12 ISB transition energy as a function of the doping density in the MQWs and theoretical evolution considering the exchange interaction (green) and both the exchange interaction and the depolarization shift (red). The error bars illustrate the absorption linewidth (Modified from ref. [196]).

8.4 Conclusions

In summary, we have designed a series of nonpolar *m*-plane GaN/AlGaN MQWs by varying the dimensions and Al compositions to separate the two confined electronic levels by 20–33 meV (corresponding to 4.8–8 THz transitions), and decouple these transitions from the neighboring wells. These low-Al-composition MQWs (Al composition in the AlGaN alloy below 10% and average Al concentration in the heterostructure below 6%) displayed flat and regular layers in the two perpendicular in-plane directions *a* and *c*, and a very good crystalline quality. Extended defects, like stacking faults or dislocations, were not present. Only when the total heterostructure thickness exceeded 1.2 µm, we observed cracks propagating along the *a* direction. Inhomogeneities of the Al composition in the barriers were observed along the growth axis *m*. Optically, the structures showed low-temperature ISB absorption in the 6.3 to 37.4 meV (1.5 to 9 THz) range, providing an experimental demonstration of the possibility for GaN to cover a large part of the 7–10 THz band forbidden to GaAs-based technologies. However, the demonstrated ISB absorption are spectrally broad, with a normalized bandwidth close to 1, which is attributed to the high Si doping density (n_s = 3×10^{12} cm^{-2}).

Based on this result, we further study the effect of doping density on such FIR structures. We have designed a series of nonpolar m-plane GaN/AlGaN MQWs (10 nm GaN/18.5 nm $Al_{0.075}Ga_{0.925}N$) for ISB absorption at 30 meV (7.3 THz). To probe the effect of doping on the structural and optical properties of the nanostructures, the Si and Ge doping density in the wells was varied in the range of 1×10^{11} cm^{-2} to 5×10^{12} cm^{-2}. Structurally, the QWs were

uniform with flat interfaces and no extended defects related to the epitaxial growth, but they showed nm-sized alloy inhomogeneities in the AlGaN barriers. All the structures display ISB absorption in the THz range at 5 K. However, a saturation of the absorption is observed at 1×10^{12} cm^{-2}, and the magnitude of the blueshift and broadening increases less than theoretically predicted for the samples with higher doping levels. This is explained by the presence of free carriers in the excited electron level due to the increase of the Fermi level energy. Results for low doping levels are comparable for MQWs doped with Si or Ge. However, for high doping levels, there is a systematic improvement when using Ge as a dopant, which manifests in narrower absorption bands independent of the spectral region, and this effect is therefore valid for different QW size, barrier composition and crystallographic orientations.

9. Single nanowire photodetectors

In this chapter, we present the first single nanowire ISB photodetector (NW-QWIP), using GaN/AlN nanowire heterostructures that exhibit ISB transitions around 1.55 µm. In parallel, using band-to-band transitions, we report a single nanowire UV photodetector incorporating an AlN/GaN/AlN heterostructure. Such a device shows a UV response that is linear with the optical power when the nanowire diameter is small enough to ensure a complete depletion of the wire.

For the study of the ISB photodetector (section 9.1), I performed the MBE growth, SEM measurements and theoretical calculations to understand the electronic structure of the nanowire. The STEM measurements were performed by my supervisor Dr. M. I. den Hertog. The single nanowire contacting, photo-response and I-V characteristics were studied by Dr. J. Lähnemann. Results were published in "Near-IR ISB Photodetection in GaN/AlN Nanowire", J. Lähnemann et al., Nano Lett. ***17****, 6954-6960 (2017)* [219].

For the study of the single-nanowire UV photodetector (section 9.2), I performed the MBE growth, SEM measurements and was involved in the device design. The theoretical calculations were performed by M. Spies and Dr. E. Monroy. The STEM measurements and analysis were performed by M. Spies and my supervisor Dr. M. I. den Hertog. The single nanowire contacting was performed by M. A. Luong, M. Spies and J. Polaczyński. The photo-response and I-V characteristics were studied by M. Spies, J. Lähnemann and J. Polaczyński. Results were published in "Effect of the nanowire diameter on the linearity of the response of GaN-based heterostructured nanowire photodetectors", M. Spies et al., Nanotechnology ***29****, 255204. (2018)* [220].

9.1 Quantum well infrared photodetector

The demonstration of ISB absorption in nanowire ensembles, described in chapter 6 and 7 of this document, together with the demonstration of resonant tunneling transport [221,222] in single nanowires, highlight the possibility of using GaN nanowires with GaN/AlN heterostructures as nanowire ISB photodetectors. The nanowire ensembles presented in section 6.2 are particularly interesting for this application, as they were shown to absorb around the telecommunication wavelength of 1.55 µm at room temperature. Based on current planar technologies, an obvious material choice for nanowire ISB devices would be GaAs/AlAs. However, the pronounced crystal polytypism in GaAs nanowires obtained through the bottom-up approach [223] impedes the application as ISB devices, and the top-down strategy (patterning and etching) appears as the only alternative for this material system so far [45]. In contrast, for GaN/AlN, the bottom-up method [224] yields the necessary low density of structural defects in spite of the lattice mismatch [225].

In this section, we demonstrate the feasibility of ISB photodetection in nanowire-based devices using GaN/AlN MQWs embedded in GaN nanowires. The active region is similar to that of the samples in section 6.2, having already demonstrated ISB absorption. We study

photocurrent characteristics of contacted nanowires under near-IR and SWIR illumination that allow us to unambiguously assign the observed signal to ISB transitions in the embedded QWs.

9.1.1 Nanowire growth and device fabrication

The nanowires investigated in this study were grown on floating-zone Si(111) substrates by PA MBE under N-rich conditions at a substrate temperature of T_S = 782°C and with a growth rate of 330 nm/h. The sample was prepared following the cleaning procedure and the two-step AlN buffer layer growth process as described in section 5.1. Following the nanowire nucleation and the growth of the 1200 nm long GaN stem, a 39-period GaN/AlN MQW was formed at the same growth temperature by periodic switching of Ga and Al fluxes. The GaN quantum disks were synthesized using the same nitrogen-rich conditions that apply to the GaN base, while the AlN sections were deposited with an impinging Al flux equivalent to the active nitrogen flux. Finally, the structure was capped with a 1000-nm-long GaN segment. To facilitate current collection, both the stem and cap, except the regions 25 nm below and 100 nm above the MQWs, were doped n-type with Si to a concentration of 3×10^{18} cm^{-3}. To populate the electron ground state in the quantum disks, the GaN disks were Si-doped to a concentration of 3×10^{19} cm^{-3}.

A SEM image of the as-grown nanowire ensemble and the schematics of the above described structure can be found in figure 9.1 (a) and (b).

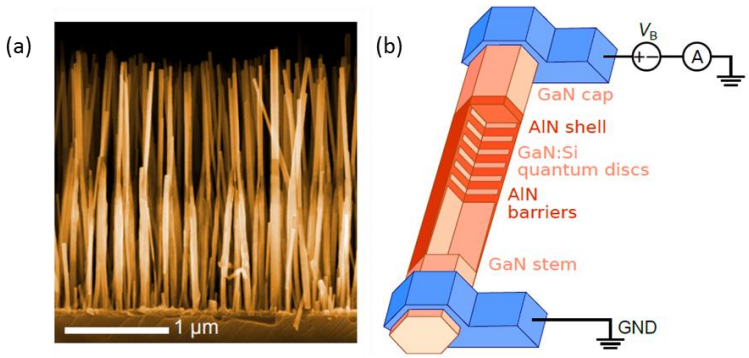

Figure 9.1: SEM image of the as-grown nanowire sample and (b) Sketch of the investigated nanowire heterostructures, depicting also the contact scheme for photocurrent measurements (modified from ref[219])

To allow photocurrent measurements and STEM imaging of the same nanowires, the as-grown nanowires were dispersed on an array of custom-made Si_3N_4 membranes [226]. The nitride membranes have a window size of 200 µm and were fabricated from an n++ silicon (100) wafer covered on both sides with a SiO_2 layer (200 nm) for additional electrical insulation and with a stoichiometric Si_3N_4 layer (40 nm). Both layers were deposited by low-pressure chemical vapor deposition. Using laser lithography and reactive ion etching, windows and cleavage lines were opened in the Si_3N_4 and SiO_2 layers on one side of the wafer. The etching of the silicon and SiO_2 was continued in a KOH bath, leaving only membranes of the top Si_3N_4 layer. Another optical lithography step, combined with electron beam evaporation of Ti/Au

(10 nm/50 nm) and subsequent lift-off, was used to define contact pads and marker structures on the front side of the membrane chips. To disperse nanowires on such membranes, the as-grown sample was sonicated in ethanol, and droplets of the solution were then deposited on the membranes. Multiple nanowires are contacted, and these single contacted nanowires will be referred to as NW1, NW2, NW3 and NW4.

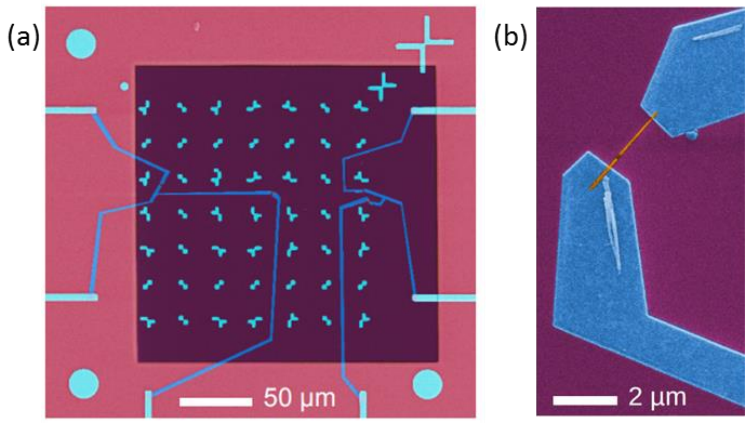

Figure 9.2: (a) Overview of a 200×200 µm^2 TEM compatible membrane with four contacted nanowires. The dark violet square is the electron transparent Si_3N_4 membrane window, supported by a Si chip (light violet). The light blue areas are pre-deposited contact leads and marker structures defined by optical lithography, whereas the darker blue contact lines are defined by electron beam lithography. (b) Close-up view of a contacted nanowire (orange) (modified from ref[219](supporting information))

9.1.2 Characterization and modeling

HAADF-STEM images of NW 1, presented in Figures 9.3 (a)-(c), demonstrate that the nanowire incorporates regular MQWs with a thickness of 1.6±0.3 nm for the GaN wells and 3.1±0.4 nm for the AlN barriers. The AlN shell, generated by lateral growth when depositing the AlN barriers, exhibits a maximum thickness around 5 nm, which decreases toward the top of the MQWs. Shadow effects during the growth, due to the directionality of MBE, also lead to a reduction of the shell thickness along the nanowire base as we move away from the MQWs. The individual nanowires have a diameter of 30−50 nm. However, in the case of the structure in figure 9.3, due to the coalescence of the nanowire stems, two nanowires with well-separated MQWs are contacted in parallel.

Using the dimensions of the wells and barriers extracted from the STEM images, we have performed calculations of the band structure and energy levels in the nanowire MQWs to determine the expected ISB transition energies. The band structure and transition energies in the nanowire heterostructures were calculated in 1D and 3D with the nextnano^3 software employing the material parameters for GaN and AlN described in section 3. For 3D calculations, the nanowire was modeled as a hexahedral prism consisting of a 100 nm long GaN section followed by a 20-period AlN/GaN stack and capped with 125 nm of GaN. The geometrical dimensions were defined as follows: radius of the GaN stem of 30 nm, GaN well thickness of 1.6 nm, AlN barrier thickness of 3.1 nm, and AlN shell thickness of 2 nm. The n-

type residual doping was fixed to 3×10^{17} cm^{-3}. The stem and cap were n-type doped at a concentration of 3×10^{18} cm^{-3}, except a region 25 nm below and 100 nm above the MQWs. The doping of the disks was set to 3×10^{19} cm^{-3}. The structure was defined on a GaN substrate to provide a reference in-plane lattice parameter and was embedded in a rectangular prism of air, which allowed elastic strain relaxation. To simulate the effect of surface states, the Fermi level was pinned 0.6 eV below the GaN bandgap at the GaN cap-air interface [92] and 2.1 eV below the AlN band gap at the AlN shell-air interface [93]. Additionally, 1D calculations were performed by simulating a segment of the MQW containing three QWs with periodic boundary conditions.

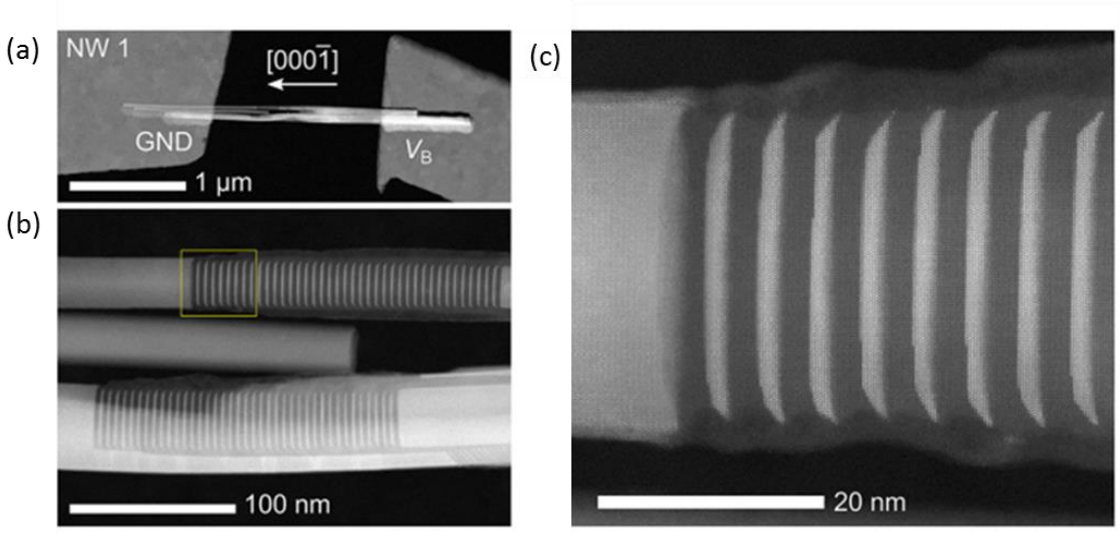

Figure 9.3: (a) Overview HAADF STEM image of NW 1 and (b) detail of the GaN (bright)/AlN (dark) MQWs. (c) Zoom HAADF STEM image of the region marked in (b) viewed along the [2-1-10] direction. Both the growth direction and the contacting convention are labeled in (a) (modified from ref[219]).

Figure 9.4 (a) shows a cross-sectional view of the thus calculated energy of the conduction band edge. A profile of the conduction band energy taken along the central axis of the nanowire is depicted in figure 9.4 (b). It exhibits the polarization-induced sawtooth structure typical for III-nitride QWs. Whereas, for the lowermost well, the conduction band lies above the Fermi level, from the second well onward, doping pushes the conduction band below the Fermi level. Note that ISB absorption is only expected in QWs containing electrons in the ground state of the conduction band. We calculated the ISB transition energy and wave functions of the electron ground state (e_1) and the first excited electron state associated with the vertical confinement (e_{2z}) in the 10th QW. The (1-100) cross-sectional view of the squared wave functions $|\Psi(x,z)|^2$ (with x = ⟨11-20⟩ and z = ⟨0001⟩) associated with e_1 and e_{2z} are given in figure 9.4 (c). Both wave functions show a maximum probability of finding the electron at the center of the nanowire. Note that this situation, which should facilitate the observation of ISB absorption, might not be given for other well dimensions or doping levels [35]. This situation emphasizes the importance of the 3D calculations in combination with a reconstruction of the exact structure by STEM imaging. The e_1–e_{2z} transition energy is 0.76 eV (1.64 µm).

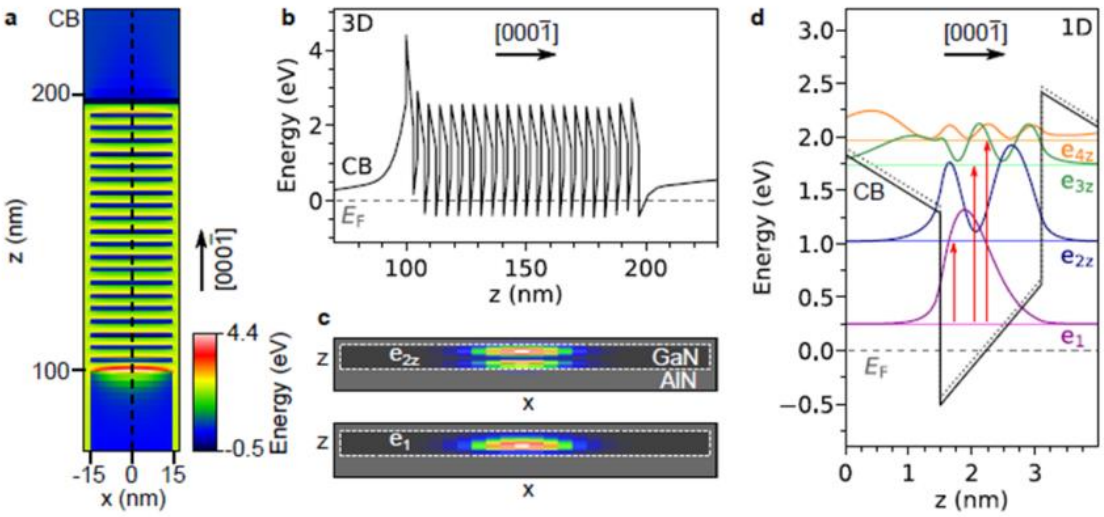

Figure 9.4: (a) Color-coded cross-sectional view of the conduction band (CB) edge as obtained from 3D calculations of the strain and bands in the nanowire heterostructure. (b) Conduction band profile along the [000-1] direction in the center of the nanowire as marked by the dashed line in (a). The gray dashed line indicates the Fermi level (E_F). (c) Cross-sectional view of the spatial extension of the wave functions ($|\Psi(x,z)|^2$) for the electron ground state (e_1) and the first excited electron state induced by the vertical confinement (e_{2z}) as obtained from **k·p** calculations in the tenth QW. (d) 1D **k·p** calculations of the energy levels and wave functions in the QWs giving energies of 0.77, 1.4, and 1.71 eV for the e_1–e_{2z}, e_1–e_{3z} and e_1–e_{4z} transitions (as marked by the red arrows), respectively. The dotted profile shows the CB edge from the 3D calculation in (b) for comparison (modified from ref[219]).

Using 3D calculations, the large number of laterally confined levels prevents us from calculating higher-order levels induced by the vertical confinement. Therefore, we turn to a 1D approximation, as depicted in figure 9.4 (d). This approach is legitimate as the band profile does not deviate significantly from the one extracted from the 3D calculation for the center of the nanowire (dotted line in figure 9.4 (d)). The resulting transition energies for e_1–e_{2z}, e_1–e_{3z} and e_1–e_{4z} are 0.77, 1.48, and 1.71 eV (corresponding to wavelengths of 1.61, 0.84, and 0.72 µm), respectively. For doped QWs, many-body corrections to these transition energies have to be taken into account [35,80]. However, for our thin QWs and moderate doping densities, the correction is smaller than 10 meV and will thus be considered as negligible.

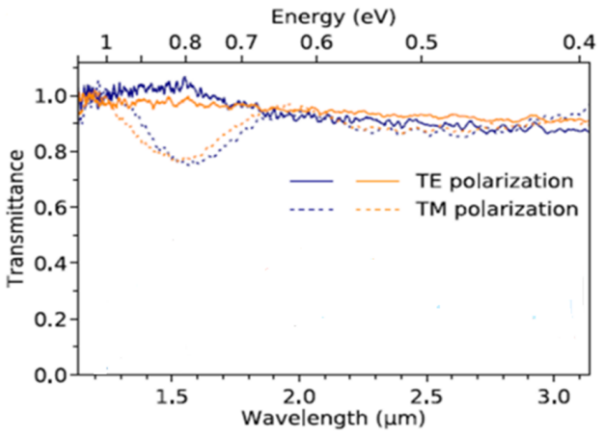

Figure 9.5: FTIR transmittance of the nanowire ensemble measured for TE (solid) and TM (dashed) polarized light at two different positions on the sample (modified from ref. [219]).

To probe the ISB absorption in the nanowire ensemble (as-grown), we employed room-temperature FTIR spectroscopy at grazing incidence. The polarization dependent FTIR transmittance in figure 9.5 exhibits an absorption-related dip between 1.2 and 1.8 µm (or 0.7−1 eV) for TM polarized light, while it is constant across the SWIR spectral range for the TE polarization. The energy range of this absorption feature agrees well with the predicted e_1-e_{2z} transition energy of 0.77 eV, with a relative line width ΔE/E = 20%. The broadening and Gaussian shape of the dip, comparable to results obtained in GaN/AlN QDs synthesized by the Stranski−Krastanov method, are attributed to the dispersion of the QW size in the nanowire ensemble. This is consistent with results obtained in section 6.2.

9.1.3 Device characterization

The current−voltage (I−V) characteristics of the nanowires were investigated with an Agilent 4155C semiconductor parameter analyzer directly connected to the nanowires. The positive bias is conventionally defined as to have a higher dark current in the forward direction. The end of the nanowire to which the positive bias was applied is indicated in figure 9.6 (c). For the measurement of the photocurrent as a function of the optical power, the nanowires were connected to the 10^6 A/V transimpedance amplifier integrated in a lock-in amplifier (Stanford Research Systems SR830). The laser illumination was chopped at 647 Hz (unless indicated) and the nanowires biased at 1 V. The error bars correspond to three times the standard deviation for measurements averaged over 90 s.

The dark and under illumination at 1.55 µm I−V characteristics of the nanowires are presented in figure 9.6 (a) and (b) in linear and logarithmic scales. All nanowires show a rectifying behavior for the dark current. In figure 9.6 (b) two major components can be distinguished: a linear ($I \propto V$) regime for low bias (up to 0.1−0.5 V), followed by an increase with the third power of the voltage ($I \propto V^3$), which is an indication of space charge limited transport [227,228].

Note that the degree of rectification varies between the individual nanowires, but also the current levels and thus the conductivity changes from nanowire to nanowire. Following the convention of bias direction, the bias is applied to the stem for NW 1 and NW 2 and to the cap for NW 3 and NW 4 (see column (c) of figure 9.6) and hence the rectification cannot be linked to the asymmetry of the heterostructure resulting from the internal electric fields or the presence of the AlN shell. Instead, a Schottky-type barrier seems to be formed at the contacts, whose barrier height differs between the contacts of the different nanowires, in the dark and under continuous-wave IR laser illumination.

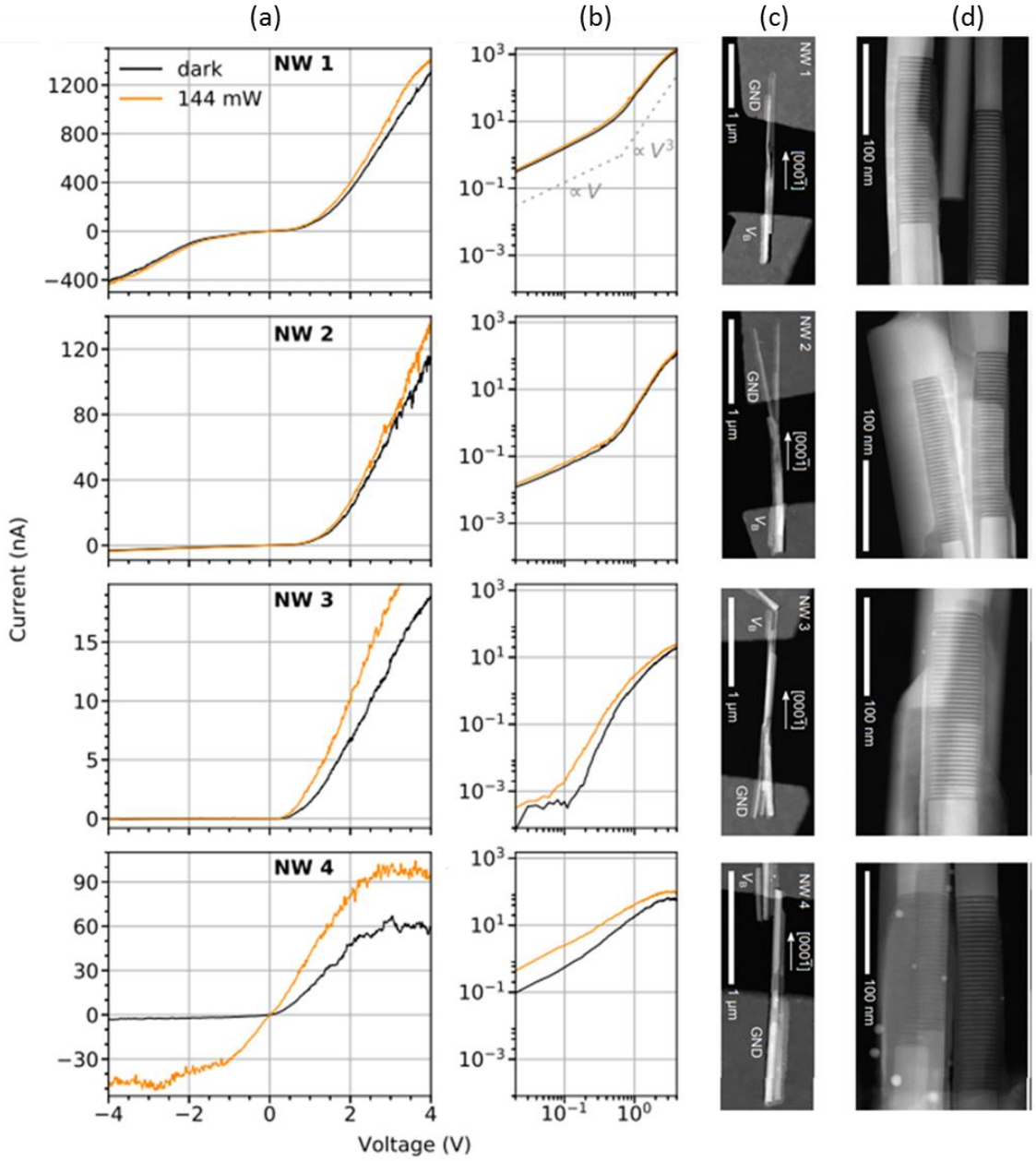

Figure 9.6: Each row corresponds to one nanowire as indicated. For the columns, current-voltage characteristics in the dark (black) and under continuous wave IR laser illumination at 1.55 µm (orange) for all four investigated in (a) linear scale and (b) logarithmic scale. (c) Overview of the contacted nanowires. The growth direction, as well as the contacting convention are marked. (d) Detail of the GaN (bright)/AlN (dark) MQW (modified from ref. [219]).

Under illumination, the current increases both in the forward and reverse directions, though more pronounced in the forward direction. We can further correlate the photocurrent characteristics (column (a) and (b)) of the different nanowires with their STEM images (column (c) and (d)) in figure 9.6. The micrographs reveal that some of the nanowires exhibit an additional GaN shell around the AlN shell that envelops the MQW and part of the nanowire stem. Such an outer GaN shell creates a shunt conduction path [222,226] and most of the applied bias voltage drops across the AlN barrier between the GaN shell and the core of the

nanowire stem instead of across the MQWs. The reduced barrier width will increase the dark current, while the missing external potential across the MQWs hinders the collection of the electrons excited by ISB absorption in the quantum disks. As we always have more than one MQW per nanowire, we essentially have several conductors connected in parallel. Therefore, the photocurrent should largely originate from MQWs without continuous GaN shell. In turn, the dark current can be attributed to the MQWs with an additional GaN shell, where the resistance is determined only by the thickness of the AlN barrier between shell and stem and not by the full stack of barriers in the MQWs. Indeed, the strongest IR photoresponse can be seen for NW 1, the lowest for NW 2. While both of the MQWs in NW 2 are surrounded by significant GaN shells, the right MQWs in NW 1 do not have any outer GaN shell. At the same time, the left MQWs in NW 1 contain a much thinner AlN barrier between core and outer shell than for NW 2, which results in the higher dark current observed for NW 1. The STEM images of NW 3 and NW 4 give a less clear picture due to the superposition of several MQWs. However, NW 4, which does not appear to have any GaN shell, exhibits both a low dark current and a high photocurrent.

To remove the contribution from the dark current, we measured the photocurrent under chopped illumination (647 Hz, unless mentioned otherwise) using a lock-in amplifier with a spot diameter of 2 mm. The photocurrent as a function of the incident laser power at 1.55 µm and under 1 V bias is shown in figure 9.7 (a) for the four nanowires. Strikingly, the photocurrent shows a linear increase over more than 3 orders of magnitude. The result is confirmed at various laser wavelengths, as illustrated in Figure 9.7 (b). The values of β given in the legends of the graphs are the power law coefficients determined from fitting the relation $I \propto P^{\beta}$ to the data, where I is the photocurrent and P is the laser power. Note that $\beta = 1$ indicates that the photoresponse is linear.

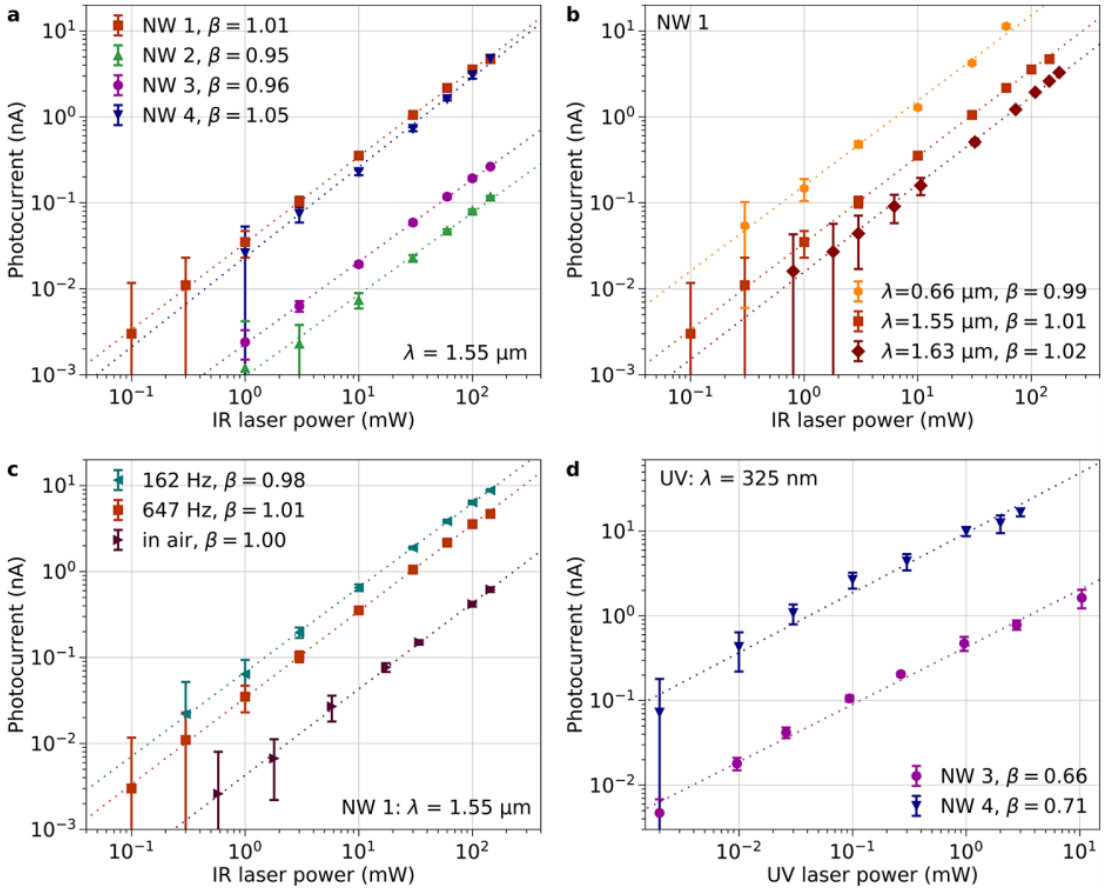

Figure 9.7: Linearity of the ISB photocurrent for (a) four different nanowires (NWs 1–4) measured in vacuum at an illumination wavelength of 1.55 µm (b) NW 1 measured at different wavelengths, as well as (c) NW 1 measured at different chopping frequencies in vacuum and in air (laser chopped at 647 Hz). For comparison, panel d gives the photoresponse under UV illumination for NWs 3 and 4 in vacuum (laser chopped at 86 Hz). All measurements are carried out at a bias of 1 V (modified from ref. [219]).

The observed linear trend is usually not obtained in single nanowire interband photodetectors [228–232]. Indeed, the band-to-band photocurrent under UV illumination shows a sublinear dependence on the laser power also for our sample, as demonstrated in figure 9.7 (d) for NW 3 and NW 4. This sublinearity is generally attributed to the importance of surface states, either as nonradiative recombination centers, or as surface charges affecting the nanowire conductivity [228,229]. Therefore, the linear power dependence confirms, on the one hand, that IR illumination has no effect on the Fermi level pinning at the nanowire sidewall surfaces, and on the other hand, that the measured photocurrent originates from a mechanism different from the band-to-band photocurrent, with low sensitivity to surface states. Theoretical calculations using 3D nextnano^3 simulations for various QW sizes were performed during a previous study [35]. The results displayed in figure 9.8 show the low sensitivity to surface states of ISB transitions.

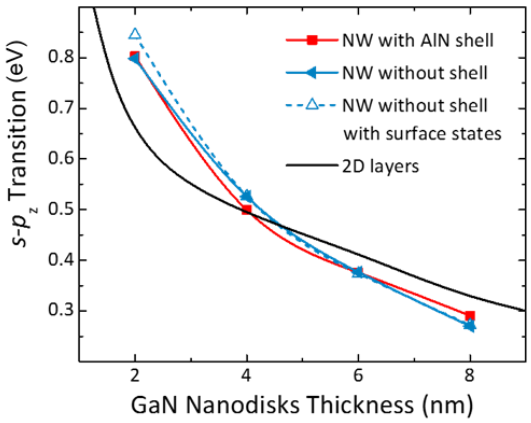

Figure 9.8: Theoretical energy of the ISB transition energy as a function of the GaN nanowire QW (nanodisk) thickness. The transition energy in the case of GaN/AlN planar QWs is also shown (2D layers) for comparison (modified from ref. [35]).

The linear behavior was reproduced for different chopping frequencies and with the nanowire in air, as shown in figure 9.7 (c). The photocurrent increases for lower chopping frequencies for all nanowires, which is attributed to the resistance × capacitance (RC) frequency response of the lock-in amplifier electronics. However, when measuring in air, there is an additional difference in surface state occupation, which modulates the conductivity of the nanowire.

We have estimated the responsivity for NW 1 considering the nanowire surface exposed to the laser as the active photodetector area. Note that the detection cross-section of a nanowire is expected to be larger than this surface [233]. We obtain values of 0.6±0.1 A/W and 1.1±0.2 A/W at chopping frequencies of 647 and 162 Hz, respectively (the values are averaged over the different excitation levels in Figure 9.7 (c).

The spectral response of the nanowire photodetectors has been obtained by measuring the photocurrent under illumination from laser diodes operating at various wavelengths across the near-IR and SWIR spectral range, as given in figure 9.9 (a) for NW 1 and NW 2. The shape of the spectral response is independent of the incident optical power as shown in the inset to figure 9.9 (a). The response reaches a maximum in the 1.3 to 1.55 µm range. It goes down around 1.0 µm but then increases again for shorter wavelengths, which can be attributed to transitions from e_1 to higher excited states (e_{3z}, e_{4z}), for which also the extraction of the carriers from the quantum disks should be facilitated. The wavelengths corresponding to the e_1–e_{3z} and e_1– e_{4z} transitions were predicted to be 0.84 and 0.72 µm. Note that the restrictions for transitions between levels with the same parity, which is forbidden in square QWs, is waived in GaN/AlN due to the asymmetry introduced by the internal electric field.

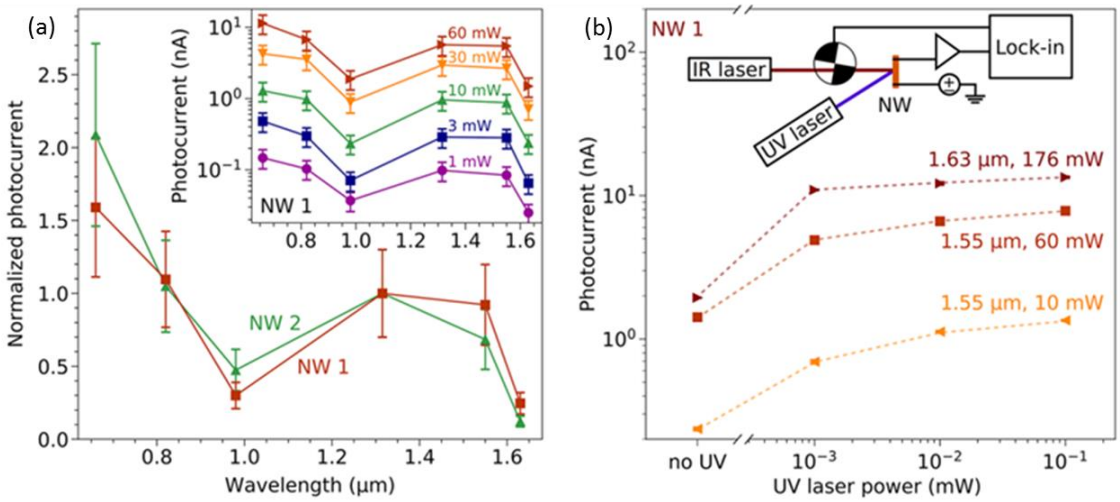

Figure 9.9: Normalized spectral photocurrent response for two nanowires (NW 1 and NW 2) measured at 1 V bias. The response has been averaged over several different illumination powers. The inset shows the spectral response of NW 1 at different illumination levels on a semilogarithmic scale. The error bars account for the uncertainty in the calculation of the impinging irradiance due to the error in estimation of the spot size for the different laser diodes. (b) Evolution of the ISB photocurrent under additional continuous-wave bias illumination using an UV laser (as sketched in the inset) measured on NW 1. The trend is given for different values of impinging laser power and wavelength. The dashed lines serve as guides to the eye (modified from ref[219]).

Finally, figure 9.9 (b) shows that the ISB photocurrent from the nanowire increases when adding a continuous-wave UV illumination to the chopped IR illumination, as sketched in the inset. UV illumination should lead to an enhancement of the ISB photocurrent due to the photo-generated carriers that increase the population of the ground electron level in the conduction band. However, a UV laser power of only 1 µW improves the measured ISB photocurrent by a factor 2−3, while further increasing the UV illumination power up to 100 µW only leads to a moderate additional increase of the photocurrent. Assuming a carrier lifetime around 10 ns (section 6.2.2) and assuming that the impinging laser power is fully absorbed in the QWs (unrealistic upper-bound scenario), the number of photo-generated carriers would be $\approx 4\times10^{15}\,cm^{-3}$, which is several orders of magnitude lower than the doping level. Therefore, the increase of the photoresponse should be due to the effect of the UV illumination on surface states, which shifts the Fermi level higher toward the conduction band, and improves the conductivity of the stem/cap segments [228,229] and in turn enhances the carrier collection. Therefore, while providing further evidence that the photocurrent originates from ISB transitions, this experiment also indicates that a moderate increase of the stem/cap doping, as well as of the quantum disk doping, are pathways for a further improvement of the photoresponse.

9.2 Single nanowire photodetectors for ultraviolet

Band-to-band nanowire photoconductors are characterized by high photocurrent gains, which can reach 10^6, and strong spectral contrast above and below the bandgap. A general

feature in nanowire photoconductors is the fact that the photocurrent scales sublinearly with the impinging laser power, which has been shown for single GaN nanowires regardless of the presence of heterostructures [228,229,231,234,235], as well as for nanowires of other material systems such as ZnTe [236], ZnO [237,238], InP [239], CuO [240], and GaAs [241]. This sublinearity of the response hampers the use of such devices for the quantification of the radiant fluence, and restricts their application domain to digital detection. The high photocurrent gain and the sublinearity have been related to the light-induced reduction of the depletion layer at the nanowire sidewalls [228,231,232,237,242]. Indeed, the large surface to volume ratio in nanowires makes them very sensitive to surface effects (presence of charge traps or Fermi level pinning, which can be modified by adsorbed species). In the case of undoped GaN nanowires, Sanford et al. reported an improvement of the linearity in nanowires with small diameter (≈100 nm), which they attributed to the total depletion of the nanowires associated with the axial electric field generated by asymmetric Schottky-like contacts [231].

In this section, we study single-nanowire ultraviolet photodetectors incorporating an AlN/GaN/AlN heterostructure. The influence of the heterostructure is confirmed by the rectifying behavior of the current–voltage characteristics in the dark, and by the asymmetry of the photoresponse in magnitude and linearity. We analyze in detail the effect of diameter and doping on the bandstructure influencing the photoresponse of these single nanowire photodetectors.

9.2.1 Nanowire design, growth and device fabrication

The samples under study are GaN nanowires incorporating an AlN/GaN/AlN heterostructure (see figure 9.10 (a)) to enhance the responsivity at low bias, as a consequence of the internal electric field generated by the large difference in spontaneous and piezoelectric polarization between GaN and AlN. The heterostructure is surrounded by segments of undoped GaN (each 130 nm long), while the ends of the nanowires are doped at 8×10^{17} cm^{-3} to facilitate Ohmic contacts. For the design of the heterostructure, we calculated the band profile using the nextnano^3 8×8 **k·p** self-consistent Schrödinger–Poisson solver using the parameters listed in section 3.1. The result is illustrated in figure 9.10 (c). The heterostructure consists of two 10 nm thick AlN insertions, separated by 2.3 nm of GaN. As self-assembled nanowires grow along the [000-1] crystallographic axis [226], the polarization induced depletion region is located below the heterostructure. In turn, accumulation of free electrons occurs on top of the heterostructure. To avoid the risk of covering the depletion region when depositing the contacts, the wire is asymmetric, with the heterostructure located towards the top of the nanowire.

Under illumination, the depletion region is expected to separate charge carriers, as illustrated in figure 9.10 (c). The presence of the GaN/AlN heterostructure favors the collection of photo-generated electrons, but it is an obstacle for hole transport. The field-emission transport through such a barrier should be negligible. However, transport through relatively large AlN barriers has been experimentally observed [243,244]. The strong band bending in the heterostructure favors a generation-recombination current that involves holes from the

stem and electrons from the cap region. In the case of a single barrier, transport proceeds via interband Zener tunneling [243]. In our case, where two barriers are involved, the states in the intermediate GaN section should play a role as intermediate states in the transport process.

These GaN nanowires were synthesized by PAMBE on n-Si(111) substrates. The growth rate of the GaN nanowires was ≈0.11 nm s^{-1} and the substrate temperature was T_S = 810°C. The sample was prepared following cleaning procedures and the two-step AlN buffer layer growth process as described in section 5.1. In the sample under study, the nanowire base consists of a 2.5-µm-long GaN stem doped with Ge ([Ge] = 8×10^{17} cm^{-3}), and followed by a 130 nm long undoped GaN segment. This was followed by the AlN/GaN/AlN (10 nm/2.3 nm/10 nm) heterostructure and by a 130-nm-thick undoped GaN segment, which is finally capped with a Ge-doped ([Ge] = 8×10^{17} cm^{-3}) GaN segment of about 410 nm length. During the growth of the AlN barriers, a thin AlN shell forms around the GaN stem and the AlN/GaN/AlN heterostructure, as indicated in the scheme in figure 9.10 (a). An SEM image of the as-grown nanowire ensemble can be seen in figure 9.10 (b), where the arrows on the side of the SEM image mark the location of the heterostructure.

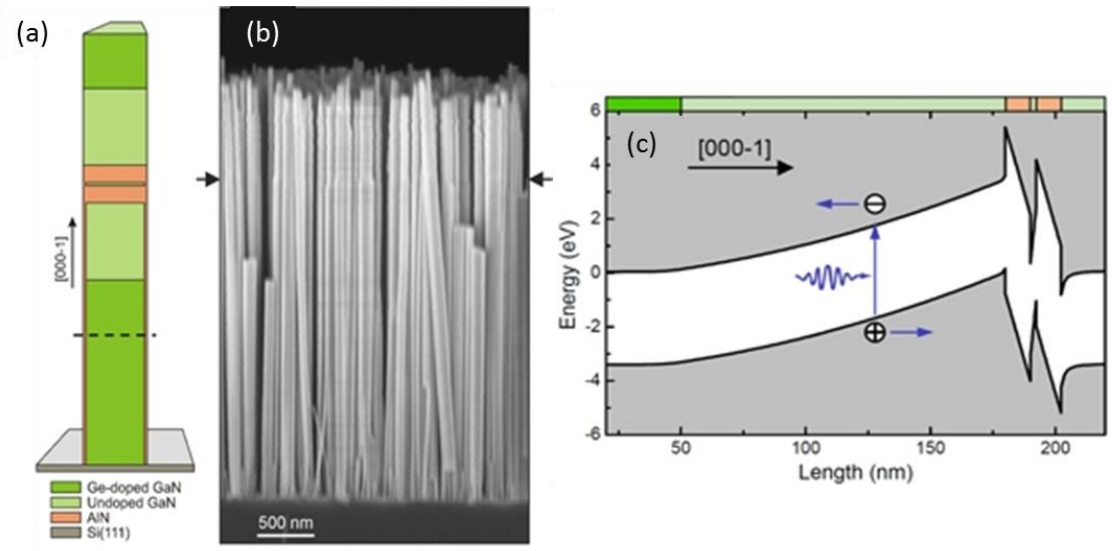

Figure 9.10: (a) Schematic of the nanowires under study. (b) SEM image of the as-grown nanowire ensemble. The position of the insertion can be identified on the top quarter of the nanowires as the growth of the strained GaN on the AlN insertion results in a slight reduction of the nanowire diameter. (c) 1D simulation of the photoactive part of the nanowire showing the band bending due to the AlN insertions. Electron-hole pairs photo-generated in the space charge region will get separated by the internal electric field, as depicted schematically (modified from ref[220]).

The as-grown nanowire ensemble is sonicated in isopropanol and dispersed on sets of Si_3N_4 membranes fabricated on Si(100) where it is electrically contacted. The fabrication of the membrane and the contacting of the nanowires have been detailed in section 9.1.1. The example of a contacted nanowire can be seen in figure 9.11 (c).

The structural properties of the nanowires were probed both by HAADF STEM and TEM using a probe corrected FEI TITAN Themis working at 200 kV and a CM 300 working at 300 kV. TEM and STEM characterization of the contacted nanowires on the Si_3N_4 reveals that the nanowire diameters lie in the 40 to 160 nm range due to bundling of nanowires as commonly observed in GaN nanowires. In case of a bundle of nanowires the average diameter is measured with error bars representing the standard deviation. The Figure 9.11 (a) and (b) describes STEM images of a bundle and single nanowire.

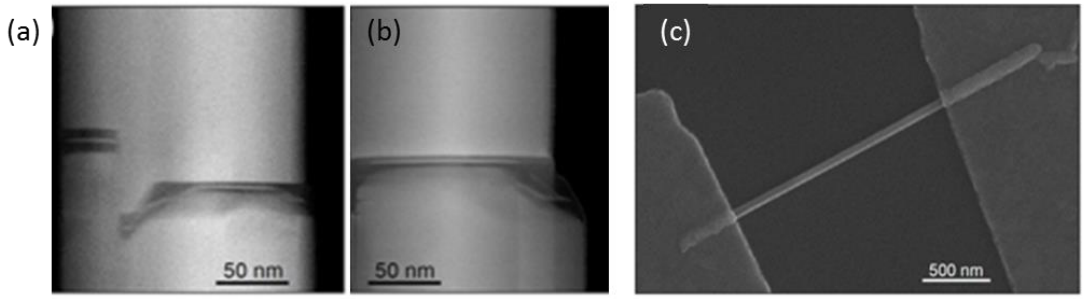

Figure 9.11: HAADF STEM images of (a) a bundle of nanowires and (b) a single nanowire, respectively. (c) SEM image of a contacted nanowire (modified from ref[220]).

Note that the thickness of the layers in the AlN/GaN/AlN heterostructure is not critical, within certain limits. Increasing the size of the AlN barriers would have the positive impact of decreasing the dark current, but it would lead to problems for the collection of photo-generated holes. Therefore, if a larger heterostructure were desired, it should be implemented as an AlN/GaN MQW structure. However, if several periods were added, the heterostructure would start showing its own contribution to the spectral response, particularly when positive bias is applied to the cap [245]. On the other hand, a thinner heterostructure would result in a reduction of the electric field in the stem. This would decrease the extension of the depletion region where the charge carrier separation takes place.

9.2.3 Ultaviolet photoresponse

The I–V characteristics in the dark exhibit a strongly rectifying behavior, as illustrated in figure 9.12 for two typical specimens. The asymmetry of the I–V curve is explained by the electronic asymmetry presented in figure 9.10 (c), which results from the polarization fields in wurtzite III-nitride heterostructures. The band profile resembles that of a Schottky diode, where the cap layer plays the role of the metal Schottky contact. Consistently, forward bias in figure 9.12 corresponds to a positive voltage being applied to the nanowire cap with respect to the stem. Following the interpretation for the case of a single AlN insertion [226], the reverse current is associated to a leakage path through the barriers, involving a GaN shell, surface conduction or the coalescence of multiple wires [229]. Under forward bias, among the set of nanowires under study, we observe a strong dispersion of the dark current, varying from a few nanoamperes to microamperes at +1 V bias.

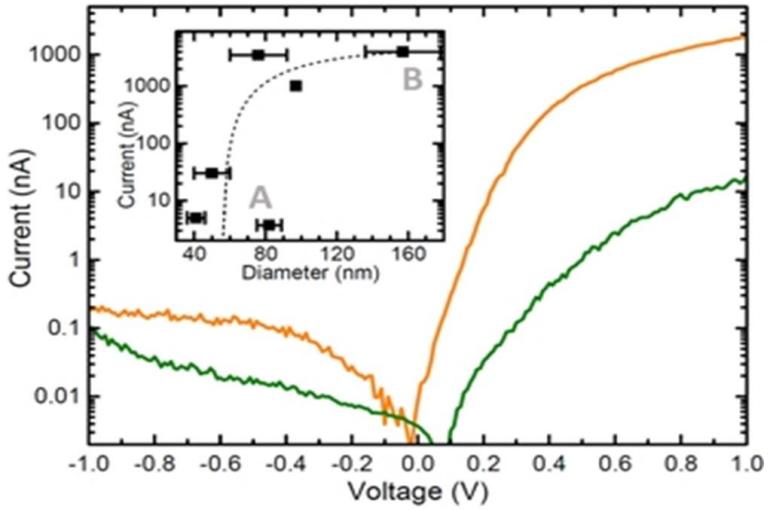

Figure 9.12: I–V characteristics (in dark) of two typical nanowires, one with small diameter of 80 nm. Inset: dark current at +1 V bias as a function of the diameter of the nanowires measured by STEM in proximity of the AlN/GaN/AlN insertion. The error bars account for the different diameters of nanowires in a bundle. The dotted line is a guide to the eye. Nanowires with diameters ≥ 80 nm present a dark current in the μA range (group B) (modified from ref[220]).

We studied STEM images of 10 nanowire bundles (19 nanowires) and they show no correlation of the dark current with the number of nanowires that are effectively contacted or with possible fluctuations in the thickness of the AlN barriers. However, there is a correlation between the dark current and the nanowire diameter, as illustrated in the inset of figure 9.12. For clarity, we have divided the studied nanowires into two groups: those with dark current in the nanoampere range at +1 V bias—we shall call them group A from here on and those that display microampere-ranged currents at the same bias—we shall call them group B. As shown in the inset of figure 9.12, the limit between the two groups is found for a diameter of ≈80 nm.

The variation of the photocurrent as a function of the UV irradiance was studied at 325 nm using an unfocused continuous-wave HeCd laser (spot diameter on the sample ≈ 1 mm), chopped at 33 Hz (unless indicated). The nanowire is biased and connected in series with a $\times 10^6$ V/A transimpedance amplifier, which is read out by a Stanford Research Systems SR830 lock-in amplifier. Figures 9.13 (a) and (b) present typical results for specimens in groups A and B, respectively at zero and negative bias. The values of β given in the legends of the graphs are the power law coefficients determined from fitting the relation $I \propto P^{\beta}$ to the data, where I is the photocurrent and P is the laser power. Note that β = 1 indicates that the photoresponse is linear. In both figures 9.13 (a) and (b), the photocurrent at zero bias scales sublinearly with the impinging irradiance, which is consistent with previous reports on samples containing GaN/AlN MQWs [245] and with the nanowires studied earlier in this chapter, in section 9.1. This behavior differs however from the observations in planar photodetectors [246]. Planar photovoltaic devices are systematically linear since the photocurrent is due to the linear

generation of electron–hole pairs separated by the internal electric field. The deviation from this behavior in the case of nanowires reveals the involvement of an additional mechanism in the zero-bias photoresponse, which remains unknown at this moment.

Under −100 mV bias, nanowires in groups A and B exhibit different behaviors. Figure 9.13(a) displays a linear photocurrent behavior for group A, whereas the photoresponse of group B in figure 9.13 (b) remains sublinear. Group A already shows a significant improvement of the linearity for bias voltages as low as −10 mV.

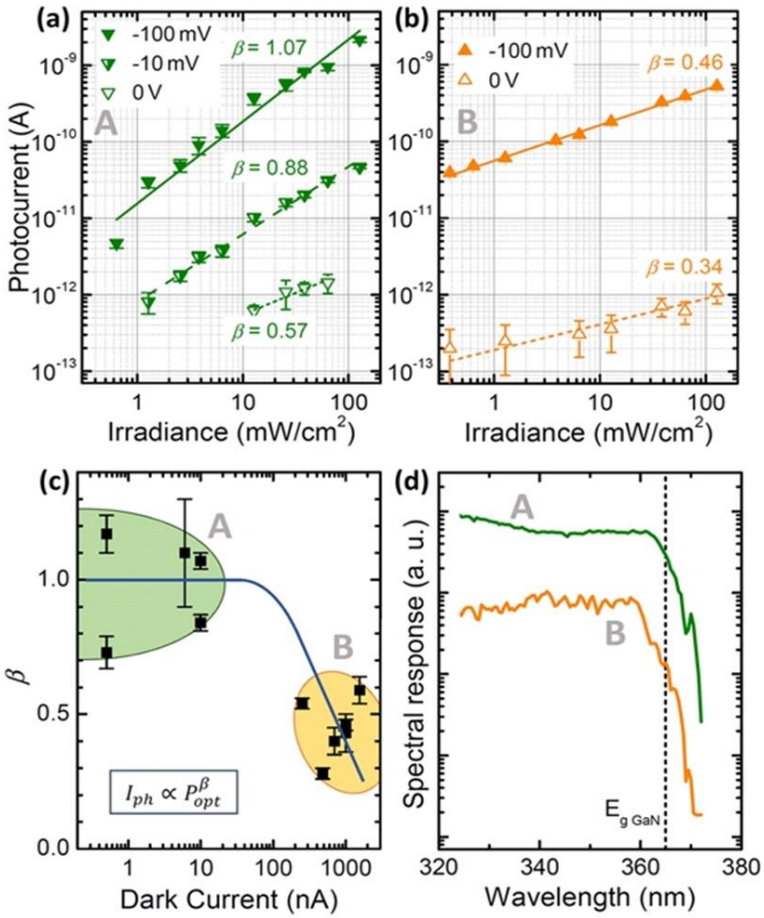

Figure 9.13: Photocurrent measurements as a function of the irradiance (impinging laser power per unit of surface) at 325 nm for: (a) a typical group-A nanowire (diameter 80 nm). Bias is indicated in the legends. The values of β are indicated in the figure. (b) for a typical group B NW (diameter>80 nm). Lines are fits to $I_{ph} = AP_{opt}^{\beta}$, where I_{ph} is the photocurrent, $P_{opt}$is the impinging optical power and A and β are proportionality constants. (c) Variation of β as a function of the dark current (measured at +1 V). The solid line is a guide to the eye. (d) Spectral response measurements for typical group-A and group-B nanowire. The dashed line marks the wavelength of the GaN band gap at room temperature (modified from ref. [220]).

Figure 9.13(c) displays a summary of the values of β (at −100 mV) as a function of the dark current through the nanowire (at +1 V) for all the nanowires in this study. The nanowires in group A present β = 1.0±0.2, i.e. their photocurrent scales linearly with the optical power within the error bars of the measurement, whereas the nanowires in group B clearly show a

sublinear behavior, with $\beta = 0.45 \pm 0.11$. Note that, for these linearity measurements, the range of bias voltages applied to the nanowires was chosen to keep the maximum photocurrent lower than 10 μA, to prevent device failure. This implies that the maximum applied voltage was in the range of −1 V (lower for some of the specimens). In the devices where a linear behavior is observed (group A), the linearity improves with bias, without any indication of degradation at higher bias.

To verify that the photocurrent induced by UV illumination stems from the GaN nanowires, we have recorded the spectral response for both sets of devices. The spectral response has been measured using the same read-out configuration, but exciting with light from a 450 W xenon lamp passed through a Gemini 180 Jobin-Yvon monochromator. In general, the bias was chosen to keep the maximum photocurrent lower than 10 μA to prevent device failure. All measurements were carried out at room temperature. The results are presented in figure 9.13(d). In both cases (groups A and B), the absorption exhibits a sharp cutoff around 365 nm, which corresponds well to the band gap of GaN at room temperature. This experiment confirms that in both cases a potential leakage photocurrent through the silicon substrate is negligible.

If we approximate the exposed photodetector area by the in-plane cross-section of the contacted nanowire (on average, 1.5 μm × 80 nm), we can estimate that the typical responsivity (geometric mean) for an irradiance of 10 mW cm^{-2} is around 0.3 A/W at zero bias. At a bias of −100 mV, the typical responsivity, measured under the same conditions and calculated in the same manner, increases to around 20 A/W for nanowires in group A, and up to around 700 A/W for nanowires in group B. The increase of the responsivity with the nanowire diameter is consistent with previous reports on GaN nanowire photodetectors [230,231].

To confirm the role of the heterostructure in the responsivity of the nanowires, we have compared the photocurrent under forward and reverse bias. Under reverse bias, the response is expected to be dominated by the presence of the space charge region, which separates photo-generated electrons and holes. The response is hence expected to resemble that of a Schottky diode (low dark current and linear response with the optical power) [247]. In contrast, under forward bias, the space charge region disappears and the nanowire resembles a photoresistor (high dark current and sublinear response).

Figure 9.14 presents the variation of the photocurrent as a function of the UV irradiance in a specimen from group A measured at +1 and −1 V bias. As expected, the photoresponse scales linearly with the irradiance under reverse bias ($\beta = 0.96 \pm 0.06$) only, whereas forward bias results in a strongly sublinear behavior ($\beta = 0.61 \pm 0.05$). This asymmetric behavior is a confirmation of the role of the AlN/GaN/AlN heterostructure in the photoresponse.

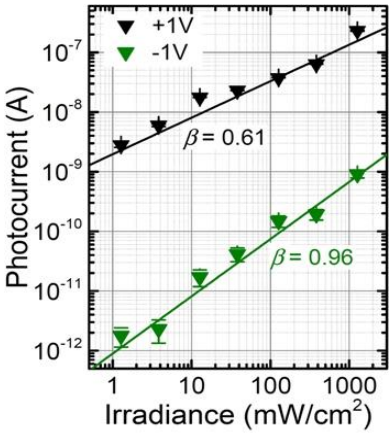

Figure 9.14: Photocurrent measurements as a function of the irradiance at 325 nm for a typical group-A nanowire measured under forward and reverse bias (modified from ref[220]).

9.2.2 Simulations and discussions

The drastic reduction of the dark current in nanowires with a diameter below ≈ 80 nm has been observed previously in GaN nanowires [30], and it was explained by the presence of a space charge layer extending inwards from the nanowire sidewalls. In the report by Calarco et al. [230], total depletion of the GaN nanowires was obtained for a diameter of 85 nm, when the residual doping level was 6.25×10^{17} cm^{-3}. We performed 3D calculations of the band profile using the nextnano^3 software using the parameters listed in section 3.1. The nanowire was modeled as a hexahedral prism consisting of a 150 nm long n-type GaN segment followed by 130 nm of undoped GaN, an AlN/GaN/AlN (10 nm/2.3 nm/10 nm) heterostructure, 130 nm of undoped GaN, and 50 nm of n-type GaN. The n-type doping density and residual doping were fixed to 8×10^{17} cm^{-3} and 1×10^{17} cm^{-3}, respectively. The structure was defined on a GaN substrate to provide a reference in-plane lattice parameter, and was embedded in a rectangular prism of air to include elastic strain relaxation. Different diameters, namely 50, 60, 80 and 120 nm, were considered.

Regarding the treatment of the surface, we have fixed the Fermi level at the AlN sidewalls of the stem at 2.1 eV below the AlN conduction band [93]. On the contrary, in the cap region, we have fixed the Fermi level at the GaN/air interface at 0.6 eV below the conduction band [91,92]. However, this latter value has no critical influence on the results, since the area of the cap exposed to light is small and the polarization-induced accumulation of electrons at the upper AlN/GaN heterointerface screens the effect of the surface.

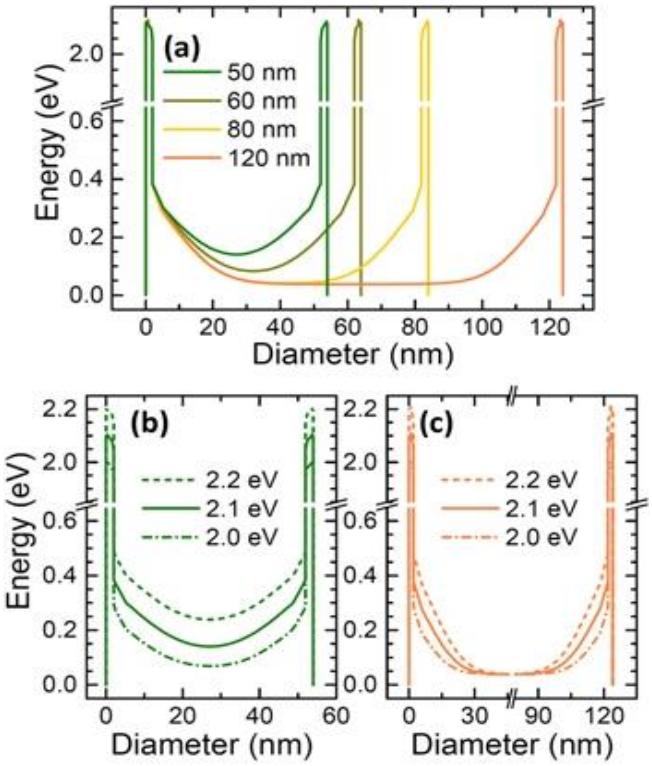

Figure 9.15: Cross-sectional view of the band structure in the doped stem region of the nanowire, 200 nm below the undoped region (a) for nanowire diameters of 50, 60, 80, 120 nm, with the Fermi level pinned 2.1 eV below the conduction band edge of AlN. With decreasing diameter, the difference in energy between Fermi level and the lowest point in the conduction band increases from 38 to 140 meV. In (b) and (c), the Fermi level pinning is varied between 2.0, 2.1 and 2.2 eV for nanowires with diameters of 50 nm and 120 nm, respectively. (modified from ref. [220]).

The results of the simulations are summarized in figure 9.15 (a), which displays the cross-sectional view of the conduction band structure in the doped stem region extracted 200 nm below the first GaN/AlN heterointerface (see dashed line in figure 9.10 (a)). For nanowires with a diameter of 60 nm, the space charge regions extending from opposite sidewalls touch each other, and the location of the conduction band edge in the center of the nanowire increases by about 100 meV when decreasing the nanowire diameter from 80 to 50 nm. This confirms the full depletion of the thin nanowires and justifies the drastic drop in the dark current.

UV illumination is known to unpin the Fermi level at the nanowire sidewalls. This phenomenon has been experimentally studied by Pfüller et al [248], and it was attributed to photo-induced desorption of oxygen from the nanowire sidewalls. Therefore, to simulate the effect of ultraviolet illumination, we have analyzed the consequences of changing the position of the Fermi level at the surface in the range of 2.0–2.2 eV below the conduction band edge of the AlN shell. Taking a look at the simulations of a nanowire with a diameter of 50 nm (group A) (figure 15 (b)), we observe that changes to the Fermi level pinning shift the radial position of the conduction band as a whole across the nanowire, but the shape of the potential profile is not modified. In other words, the component of the electric field along the nanowire

diameter seen by photo-generated electrons is approximately the same in all cases, with its maximum value at the GaN/ AlN interface being 210 kV/cm (± 3%).

In a nanowire with diameter of 120 nm (group B) (figure 9.15 (c)), we note a different behavior. When the location of the Fermi level pinning changes from 2.2 to 2.0 eV below the conduction band edge of the AlN shell, the maximum radial electric field varies from 360 to 240 kV/cm (by more than 30%). At the same time, the space charge region at the sidewalls of the nanowire shrinks, increasing the extent of the central conducting channel in the nanowire. Therefore, in thick nanowires (group B), light induces not only a linear increase in the carrier concentration, but also a nonlinear variation in the diameter of the conducting channel that such carriers have to traverse to be collected. This explains also the enhancement of the responsivity with the nanowire diameter. The responsivity is linked to the total number of photo-generated carriers, i.e. it should increase with the square of the nanowire radius.

To this dependence, we have to add the variation of the conductivity due to the change in the diameter of the central conducting channel in the stem. Both phenomena are relatively independent. In small, fully depleted nanowires, the variation of the responsivity with the diameter will be given by the change in the total amount of photo-generated carriers. In large, partially depleted wires, it is the modulation of the conductive section that dominates, which can lead to a huge photocurrent gain. A theoretical analysis of both contributions can be found in [249].

9.3 Conclusion

In this chapter, we have presented GaN/AlN nanowire MQW structures that show SWIR ISB detection around 1.55 µm. Using the dimensions extracted from STEM measurements, 3D simulations were carried out explaining the observed absorption. In general, unlike the UV band-to-band photocurrent, the IR photocurrent scales linearly with the incident illumination power. This linearity confirms that the UV and IR photocurrents are generated by different mechanisms, the latter being less sensitive to surface-related phenomena, as expected for ISB transitions in a nanowire heterostructure. We also observed an increase of the IR photoresponse under additional UV illumination due to the modification of surface states. In conclusion, this work is a proof-of-principle study of ISB nanowire photodetectors.

On the other hand, we have demonstrated single-nanowire UV photodetectors consisting of a GaN nanowire with an embedded AlN/GaN/AlN heterostructure, which generates an electric field along the nanowire axis as a result of the difference in polarization between III-nitride compounds with wurtzite crystal structure. The influence of the heterostructure is confirmed by the rectifying behavior of the I-V characteristics in the dark, and by the asymmetry of the photoresponse in magnitude and linearity. Under reverse bias (negative bias on the cap segment), the detectors behave linearly with the impinging optical power when the nanowire diameter remains below a certain threshold (≈80 nm). This is

explained by the linearity of the photogeneration process, the separation of photo-generated carriers induced by the axial electric field, and the fact that illumination does not have a significant effect on the radial electric field. In the case of nanowires that are not fully depleted (diameter > 80 nm), the light-induced change in the Fermi level at the sidewalls results in a variation of the diameter of the central conducting channel in the stem, which leads to an overall nonlinear photoresponse.

10. Conclusions and perspectives

10.1 Conclusions

The purpose of this work was to explore the use of GaN nanowires for ISB applications. Therefore, we first developed a growth process for GaN nanowires using PAMBE trying to improve their morphology and vertical alignment. Thus, nanowires were grown on a low temperature AlN buffer layer, and we analyzed the impact of the impinging gallium flux and substrate temperature on their coalescence and growth rate.

Doping is crucial to improve the ISB performance of our heterostructures. Therefore, our initial task was to study the feasibility of Ge as an alternative n-type dopant, and we performed a comparative analysis of Si- and Ge-doped GaN/AlN heterostructures in both planar and nanowire geometries, all of them absorbing in the SWIR region. Additionally, we fabricated nanowires via top-down patterning of planar layers, to reduce the linewidth of the ISB absorption in the SWIR. We then tried to extend the ISB absorption in GaN-based nanowire heterostructures towards the unexplored MWIR spectral region. Finally, to reach the FIR spectral region, we also investigated planar structures with alternative crystallographic orientations, namely the nonpolar m-plane of GaN.

As an ultimate target, this PhD work also aimed at developing devices based on single nanowires, and we presented innovative approaches to the fabrication of nanowire IR and UV photodetectors.

10.1.1 Conclusions for the study of Ge as n-type dopant

We demonstrated that the use of Ge as a dopant in GaN during the growth in PAMBE does not affect the growth kinetics of GaN. We grew Ge-doped GaN thin films with maximum carrier concentrations of up to 6.7×10^{20} cm^{-3} at 300 K, well beyond the Mott density. The Ge concentration and free carrier density scale linearly with the Ge flux in the studied range. All the GaN:Ge layers present smooth surface morphology with atomic terraces, without trace of pits or cracks, and the mosaicity of the samples has no noticeable dependence on the Ge concentration. The variation of the GaN:Ge band gap with the carrier concentration is consistent with theoretical calculations of the band gap renormalization due to electron-electron and electron-ion interaction, and the Burstein-Moss effect. These results validate the use of Ge in GaN for applications requiring high doping levels.

We then successfully grew Ge-doped $Al_xGa_{1-x}N$ thin films with $x \leq 0.66$. We demonstrated that Ge does not induce any structural or optical degradation in AlGaN samples with $x < 0.4$. For higher Al compositions, Ge rich clusters were observed. Keeping the Ge concentration constant at 1×10^{21} cm^{-3}, Hall effect measurements at room temperature showed a gradual decrease of the carrier concentration when increasing the Al mole fraction.

The decrease is already noticeable in samples with x = 0.24. Samples with x = 0.64-0.66 remain conductive (σ = 0.8-0.3 $\Omega^{-1}cm^{-1}$), but the carrier concentration drops to 1×10^{18} cm^{-3}, which implies a donor activation of 0.1%. From the optical point of view, the low temperature PL was dominated by the band-to-band emission. When increasing the doping concentration, the PL blueshifts due to band filling. Furthermore, from the evolution of the PL peak position with temperature, we observe the screening of the localization induced by fluctuations of the alloy composition.

In the range of Al concentrations that we addressed, the behavior of Ge dopant does not represent a drastic improvement over Si in transport properties. However, we should keep in mind that we present the first report on Ge-doped AlGaN, to the best of our knowledge, and there is a huge dispersion in the data on Si-doped AlGaN in the literature. Conductivity values vary drastically across reports and this suggests a dependence on growth conditions. Therefore, it is difficult to compare our data on Ge doped AlGaN with literature on Si doped AlGaN, but our observation of conductivity up to 66% of Al content is extremely promising.

To assess the potential of using Ge as a dopant in ISB devices, we peformed a comparative study of Si-doped and Ge-doped planar GaN/AlN heterostructures absorbing in the SWIR. X-ray diffraction studies showed that in these strongly lattice-mismatched heterostructures, highly Si-doped samples exhibit a larger broadening of the ω scans with respect to Ge doped samples, which points to a better structural quality of the Ge-doped samples. Both the Ge- and Si-doped samples displayed ISB absorption in the range of 1.45 to 1.75 μm. The broadening of the transition is larger in the case of Si-doped samples, which points to a higher heterointerface roughness in this case. To the best of our knowledge, these results constitute the first systematic study of ISB transitions in Ge-doped planar GaN based structures.

Additionally, we peformed a comparative study of Si-doped and Ge-doped nanowire GaN/AlN heterostructures absorbing in the SWIR. We reported the first observation of ISB absorption in Si-doped GaN/AlN nanowire heterostructures with varying doping levels, with comparable performance to their Ge-doped counterparts. Based on this study, we conclude that both Si- and Ge-doped nanowires are potentially suitable for the fabrication of GaN/AlN nanowire heterostructures. In both cases, we obtained an improved FWHM of 200 meV for the ISB absorption at 1.55 μm, compared to previous reports. However, the ISB absorption linewidth remains significantly larger than that observed in planar structures, due to the inhomogeneities associated to the self-assembled growth process. This means that the homogeneity between individual nanowires across the sample wafer is the limiting factor rather than the dopant.

10.1.2 Extension of ISB transition in GaN nanowires towards longer wavelengths

We extend this technology towards longer wavelengths, to absorb in the MWIR spectral region. For this purpose, we synthesized self-assembled GaN/AlN and GaN/$Al_{0.4}Ga_{0.6}N$ nanowire heterostructures. In the case of GaN/AlN heterostructures in GaN nanowires, we varied the GaN well width from 1.5 to 5.7 nm. Heterostructures with 1.5-4 nm wells present sharp GaN/AlN interfaces. However, in larger wells (5.7 nm) one of the GaN/AlN heterointerfaces was not sharp but rather a graded alloy, which extends by around 1.5-2 nm and has strong influence on the electron wave functions in the well. Increasing the GaN well width in the heterostructures, we observe a redshift of the PL emission and a redshift of ISB absorption from 1.4 to 3.4 µm, at room temperature. The results fit well with theoretical models, taking into account the structural characteristics (including AlN shell and GaN/AlN interface sharpness or intermixing) and many-body effects associated to the doping level. For GaN/$Al_{0.4}Ga_{0.6}N$ heterostructures, the ternary compound represents a reduction of polarization, which leads to the blueshift of the band-to-band transitions and redshift of the ISB transitions. As a result we obtained TM-polarized absorption in the 4.5-6.4 µm wavelengths.

10.1.3 Top-down nanowires

Trying to reduce the inhomogeneities while keeping the advantages of the nanowire geometry, we also presented a systematic analysis of ISB absorption in top-down etched micro- and nanopillars containing GaN/AlN heterostructures absorbing in the SWIR domain. We show that when the spacing of the pillar array is comparable to the probed wavelengths, photonic crystal resonances dominate the absorption spectra. However, when these resonances are at much shorter wavelengths than the ISB absorption, the absorption is clearly observed, without any degradation of its magnitude or linewidth.

10.1.4 Non-polar orientations to attain the FIR spectral region

To extend the GaN-based ISB technology to the FIR, we have designed a series of nonpolar *m*-plane GaN/AlGaN MQWs by varying the dimensions and Al compositions to separate the two confined electronic levels by 20–33 meV (corresponding to 4.8–8 THz transitions), and decouple these transitions from the neighboring wells. These low-Al-composition MQWs (Al composition in the AlGaN alloy below 10% and average Al concentration in the heterostructure below 6%) displayed flat and regular layers in the two perpendicular in-plane directions *a* and *c*, and a very good crystalline quality. These structures showed low-temperature ISB absorption in the 6.3 to 37.4 meV (1.5 to 9 THz) range, providing an experimental demonstration of the possibility for GaN to cover a large part of the 7–10 THz band forbidden to GaAs-based technologies. However, the demonstrated ISB absorption is

spectrally broad, with a normalized bandwidth close to 1, which is attributed to the high Si doping density (n_s = 3×10^{12} cm^{-2}). Based on this result, we further study the effect of doping density on such FIR structures. We have designed a series of nonpolar m-plane GaN/AlGaN MQWs (10 nm GaN/18.5 nm $Al_{0.075}Ga_{0.925}N$) for ISB absorption at 30 meV (7.3 THz), where the Si and Ge doping density in the wells was varied in the range of 1×10^{11} cm^{-2} to 5×10^{12} cm^{-2}. Increasing the doping level leads to an enhancement and blueshift of the absorption peak energy, together with an increase of the linewidth for Si, and also slightly for Ge doping. However, a saturation of the absorption is observed at 1×10^{12} cm^{-2}, and the magnitude of the blueshift and broadening increases less than theoretically predicted for the samples with higher doping levels. This is explained by the presence of free carriers in the excited electron level due to the increase of the Fermi level energy. Results for low doping levels are comparable for MQWs doped with Si or Ge. However, for high doping levels, there is a systematic improvement when using Ge as a dopant, which manifests in narrower absorption bands independent of the spectral region, and this effect is therefore valid for different QW size, barrier composition and crystallographic orientations.

10.1.5 Single nanowire photodetectors

We presented GaN/AlN nanowire MQW structures that show SWIR ISB photodetection around 1.55 µm. Using the dimensions extracted from STEM measurements, 3D simulations were carried out explaining the observed absorption. Unlike the UV band-to-band photocurrent, the IR photocurrent scales linearly with the incident illumination power. This linearity confirms that the UV and IR photocurrents are generated by different mechanisms, the latter being less sensitive to surface-related phenomena, as expected for ISB transitions in a nanowire heterostructure. In conclusion, this work is a proof-of-principle study of ISB nanowire photodetectors.

On the other hand, we have demonstrated single-nanowire UV photodetectors consisting of a GaN nanowire with an embedded AlN/GaN/AlN heterostructure. The influence of the heterostructure is confirmed by the rectifying behavior of the I-V characteristics in the dark, and by the asymmetry of the photoresponse in magnitude and linearity. Under reverse bias (negative bias on the cap segment), the detectors behave linearly with the impinging optical power when the nanowire diameter remains below a certain threshold (≈ 80 nm). This is explained by the linearity of the photogeneration process, the separation of photo-generated carriers induced by the axial electric field, and the fact that illumination does not have a significant effect on the radial electric field in a depleted nanowire. In the case of nanowires that are not fully depleted (diameter > 80 nm), the light-induced change in the Fermi level at the sidewalls results in a variation of the diameter of the central conducting channel in the stem, which leads to an overall nonlinear photoresponse.

10.2 Perspectives

The III-nitride nanowire ISB technology is at its nacent phase. With proof-of-concept demonstrations of ISB detection for a single nanowire, we have also set direction and standards for single nanowire devices in general. The future is expected to see a lot of applications of nanowires, in flexible electronics, high efficient optoelectronic devices, implantable devices etc. The reproducibility, control and processing of nanowires has drastically developed over the last decade. However, it is still far-away from industrial mass production necessary for the majority of applications, although a few processes exist, like planarization. Advanced manipulation techniques for single nano-objects are being developed, and this will help in processing and building newer and better devices.

In ISB nanowire devices, a main bottleneck is the large absorption linewidth due to inhomogenities in the nanowire dimensions along the length, and from nanowire to nanowire. The linewidth can be improved by better control of the growth rate from wire to wire across the ensemble. An idea would be to use alternative substrates that lead to more homogeneous and well separated self-assembled nanowires. There exist only few of such studies, using substrates like TiN; however, ISB transitions in nanowires grown on such substrates have not been studied, and the presence of pollutants and incorporation of dopants in such wires should be carefully analyzed. Another approach would be the use of patterned substrates or the various methods of localized growth that are under development, which could also provide an answer to the homogeneity problem. Then, we did suggest an alternative solution for better control of dimensions in this thesis, namely a top-down approach. This method should be brought further, to develop complete devices with nanowire ensembles.

Regarding the distribution and efficiency of dopants in GaN nanowires, with and without heterostructures, there is still a lot to be understood. Such studies on doping are essential for a transition towards development of nanowire devices, and progress in characterization techniques like EDX or APT will shine new light on this topic.

We have demonstrated ISB absorption in a single-nanowire QWIP operating in the SWIR. The next systematic development would be to extend the demonstration of single nanowire devices to MWIR and FIR. More importantly, it is necessary to fabricate planarized devices from self-assembled nanowire ensembles, to compare their performance with planar devices. Potential advantages are to be validated, and limitations are to be identified.

In general, manipulating nanowires, nanobatteries and nanoelectromechanical systems open up possibilites to develop self sustainable devices at the nanoscale that could fuel quantum technologies of the future. The future also brings in an emergent and exotic phenomenon like mjorana fermions that could be observed at a semiconductor nanowire and superconductor interface. Due to immense possibilities, it is hard to guess the phenomena one would be studying with nanowires 20 years into the future from 2018.

References

[1] Herschel W 1800 Experiments on the Refrangibility of the Invisible Rays of the Sun. By William Herschel, LL. D. F. R. S. *Philos. Trans. R. Soc. Lond.* **90** 284–92

[2] Beeler M, Trichas E and Monroy E 2013 III-nitride semiconductors for intersubband optoelectronics: a review *Semicond. Sci. Technol.* **28** 074022

[3] Rogalski and Chrzanowski 2002 Infra red devices and techniques **10** 111–36

[4] Rogalski A. 2012 History of infrared detectors *Opto-Electron. Rev.* **20** 279

[5] Long D and Schmit J L 1970 Mercury-Cadmium Telluride and Closely Related Alloys *Semiconductors and Semimetals* vol 5 (edited by R.K. Willardson, Albert C. Beer, Elsevier) pp 175–255

[6] Esaki L and Sakaki H 1977 New Photoconductor *IBM Tech. Discl. Bull.* **20** 2456–7

[7] West L C and Eglash S J 1985 First observation of an extremely large-dipole infrared transition within the conduction band of a GaAs quantum well *Appl. Phys. Lett.* **46** 1156–8

[8] Levine B F, Choi K K, Bethea C G, Walker J and Malik R J 1987 New 10 µm infrared detector using intersubband absorption in resonant tunneling GaAlAs superlattices *Appl. Phys. Lett.* **50** 1092–4

[9] Suzuki N and Iizuka N 1997 Feasibility Study on Ultrafast Nonlinear Optical Properties of 1.55-µm Intersubband Transition in AlGaN/GaN Quantum Wells *Jpn. J. Appl. Phys.* **36** L1006–8

[10] Hofstetter D, Baumann E, Giorgetta F R, Théron R, Wu H, Schaff W J, Dawlaty J, George P A, Eastman L F, Rana F, Kandaswamy P K, Leconte S and Monroy E 2009 Photodetectors based on intersubband transitions using III-nitride superlattice structures *J. Phys. Condens. Matter* **21** 174208

[11] Wang Z, Reimann K, Woerner M, Elsaesser T, Hofstetter D, Baumann E, Giorgetta F R, Wu H, Schaff W J and Eastman L F 2006 Ultrafast hole burning in intersubband absorption lines of GaN/AlN superlattices *Appl. Phys. Lett.* **89** 151103

[12] Hofstetter D, Schad S-S, Wu H, Schaff W J and Eastman L F 2003 GaN/AlN-based quantum-well infrared photodetector for 1.55 µm *Appl. Phys. Lett.* **83** 572–4

[13] Hofstetter D, Baumann E, Giorgetta F R, Graf M, Maier M, Guillot F, Bellet-Amalric E and Monroy E 2006 High-quality AlN/GaN-superlattice structures for the fabrication of narrow-band 1.4 µm photovoltaic intersubband detectors *Appl. Phys. Lett.* **88** 121112

[14] Baumann E, Giorgetta F R, Hofstetter D, Golka S, Schrenk W, Strasser G, Kirste L, Nicolay S, Feltin E, Carlin J F and Grandjean N 2006 Near infrared absorption and room temperature photovoltaic response in AlN/GaN superlattices grown by metal-organic vapor-phase epitaxy *Appl. Phys. Lett.* **89** 041106

[15] Hofstetter D, Baumann E, Giorgetta F R, Guillot F, Leconte S and Monroy E 2007 Optically nonlinear effects in intersubband transitions of GaN/AlN-based superlattice structures *Appl. Phys. Lett.* **91** 131115

[16] Giorgetta F R, Baumann E, Guillot F, Monroy E and Hofstetter D 2007 High frequency (f=2.37 GHz) room temperature operation of 1.55 μm AlN⁄GaN-based intersubband detector *Electron. Lett.* **43** 185–7

[17] Hofstetter D, Baumann E, Giorgetta F R, Théron R, Wu H, Schaff W J, Dawlaty J, George P A, Eastman L F, Rana F, Kandaswamy P K, Leconte S and Monroy E 2009 Photodetectors based on intersubband transitions using III-nitride superlattice structures *J. Phys. Condens. Matter* **21** 174208

[18] Rosencher E and Bois P 1991 Model system for optical nonlinearities: Asymmetric quantum wells *Phys. Rev. B* **44** 11315–27

[19] Hofstetter D, Di Francesco J, Kandaswamy P K, Das A, Valdueza-Felip S and Monroy E 2010 Performance Improvement of AlN/GaN-Based Intersubband Detectors by Using Quantum Dots *IEEE Photonics Technol. Lett.* **22** 1087–9

[20] Gendron L, Carras M, Huynh A, Ortiz V, Koeniguer C and Berger V 2004 Quantum cascade photodetector *Appl. Phys. Lett.* **85** 2824

[21] Giorgetta F R, Baumann E, Graf M, Yang Q, Manz C, Kohler K, Beere H E, Ritchie D A, Linfield E, Davies A G, Fedoryshyn Y, Jackel H, Fischer M, Faist J and Hofstetter D 2009 Quantum Cascade Detectors *IEEE J. Quantum Electron.* **45** 1039–52

[22] Vardi A, Bahir G, Guillot F, Bougerol C, Monroy E, Schacham S E, Tchernycheva M and Julien F H 2008 Near infrared quantum cascade detector in GaN⁄AlGaN⁄AlN heterostructures *Appl. Phys. Lett.* **92** 011112

[23] Sakr S, Crozat P, Gacemi D, Kotsar Y, Pesach A, Quach P, Isac N, Tchernycheva M, Vivien L, Bahir G, Monroy E and Julien F H 2013 GaN/AlGaN waveguide quantum cascade photodetectors at λ ≈ 1.55 μm with enhanced responsivity and ∼40 GHz frequency bandwidth *Appl. Phys. Lett.* **102** 011135

[24] Huang M H, Mao S, Feick H, Yan H, Wu Y, Kind H, Weber E, Russo R and Yang P 2001 Room-temperature ultraviolet nanowire nanolasers *Science* **292** 1897–9

[25] Huang Y, Duan X and Lieber C M 2004 Nanowires for Integrated Multicolor Nanophotonics *Small* **1** 142–7

[26] Qian F, Li Y, Gradecak S, Park H-G, Dong Y, Ding Y, Wang Z L and Lieber C M 2008 Multi-quantum-well nanowire heterostructures for wavelength-controlled lasers *Nat. Mater.* **7** 701–6

[27] Krogstrup P, Jørgensen H I, Heiss M, Demichel O, Holm J V, Aagesen M, Nygard J and Fontcuberta i Morral A 2013 Single-nanowire solar cells beyond the Shockley–Queisser limit *Nat. Photonics* **7** 306–10

[28] Zibik E A, Grange T, Carpenter B A, Porter N E, Ferreira R, Bastard G, Stehr D, Winnerl S, Helm M, Liu H Y, Skolnick M S and Wilson L R 2009 Long lifetimes of quantum-dot intersublevel transitions in the terahertz range *Nat. Mater.* **8** 803–7

[29] Tredicucci A 2009 Quantum dots: Long life in zero dimensions *Nat. Mater.* **8** 775–6

[30] Songmuang R, Ben T, Daudin B, González D and Monroy E 2010 Identification of III–N nanowire growth kinetics via a marker technique *Nanotechnology* **21** 295605

[31] Rigutti L, Jacopin G, Bugallo A D L, Tchernycheva M, Warde E, Julien F H, Songmuang R, Galopin E, Largeau L and Harmand J-C 2010 Investigation of the electronic transport in GaN nanowires containing GaN/AlN quantum discs *Nanotechnology* **21** 425206

[32] Tanaka K, Ikuno K, Kasai Y, Fukunaga K, Kunugita H, Ema K, Kikuchi A and Kishino K 2008 Ultrafast intersubband relaxation dynamics at 1.55 μm in GaN/AlN multiple quantum disk nanocolumns *J. Lumin.* **128** 1084–6

[33] Kandaswamy P K, Guillot F, Bellet-Amalric E, Monroy E, Nevou L, Tchernycheva M, Michon A, Julien F H, Baumann E, Giorgetta F R, Hofstetter D, Remmele T, Albrecht M, Birner S and Dang L S 2008 GaN/AlN short-period superlattices for intersubband optoelectronics: A systematic study of their epitaxial growth, design, and performance *J. Appl. Phys.* **104** 093501

[34] Fang Z, Robin E, Rozas-Jiménez E, Cros A, Donatini F, Mollard N, Pernot J and Daudin B 2015 Si Donor Incorporation in GaN Nanowires *Nano Lett.* **15** 6794–801

[35] Beeler M, Hille P, Schörmann J, Teubert J, de la Mata M, Arbiol J, Eickhoff M and Monroy E 2014 Intraband Absorption in Self-Assembled Ge-Doped GaN/AlN Nanowire Heterostructures *Nano Lett.* **14** 1665–73

[36] Romano L T, Van de Walle C G, Ager J W, Götz W and Kern R S 2000 Effect of Si doping on strain, cracking, and microstructure in GaN thin films grown by metalorganic chemical vapor deposition *J. Appl. Phys.* **87** 7745

[37] Fritze S, Dadgar A, Witte H, Bügler M, Rohrbeck A, Bläsing J, Hoffmann A and Krost A 2012 High Si and Ge n-type doping of GaN doping - Limits and impact on stress *Appl. Phys. Lett.* **100** 122104

[38] Nenstiel C, Bügler M, Callsen G, Nippert F, Kure T, Fritze S, Dadgar A, Witte H, Bläsing J, Krost A and Hoffmann A 2015 Germanium - the superior dopant in n-type GaN *Phys. Status Solidi RRL - Rapid Res. Lett.* **9** 716–21

[39] Wang H and Chen A-B 2000 Calculation of shallow donor levels in GaN *J. Appl. Phys.* **87** 7859–63

[40] Bogusławski P and Bernholc J 1997 Doping properties of C, Si, and Ge impurities in GaN and AlN *Phys. Rev. B* **56** 9496–505

[41] Gordon L, Lyons J L, Janotti A and Van de Walle C G 2014 Hybrid functional calculations of D X centers in AlN and GaN *Phys. Rev. B* **89** 085204

[42] Skierbiszewski C, Suski T, Leszczynski M, Shin M, Skowronski M, Bremser M D and Davis R F 1999 Evidence for localized Si-donor state and its metastable properties in AlGaN *Appl. Phys. Lett.* **74** 3833–5

[43] Amanti M I, Bismuto A, Beck M, Isa L, Kumar K, Reimhult E and Faist J 2013 Electrically driven nanopillars for THz quantum cascade lasers *Opt. Express* **21** 10917

[44] Krall M, Brandstetter M, Deutsch C, Detz H, Andrews A M, Schrenk W, Strasser G and Unterrainer K 2014 Subwavelength micropillar array terahertz lasers *Opt. Express* **22** 274–82

[45] Krall M, Brandstetter M, Deutsch C, Detz H, Andrews A M, Schrenk W, Strasser G and Unterrainer K 2015 From Photonic Crystal to Subwavelength Micropillar Array Terahertz Lasers *IEEE J. Sel. Top. Quantum Electron.* **21** 780–91

[46] Edmunds C, Shao J, Shirazi-HD M, Manfra M J and Malis O 2014 Terahertz intersubband absorption in non-polar m-plane AlGaN/GaN quantum wells *Appl. Phys. Lett.* **105** 021109

[47] Lim C B, Ajay A, Bougerol C, Haas B, Schörmann J, Beeler M, Lähnemann J, Eickhoff M and Monroy E 2015 Nonpolar m-plane GaN/AlGaN heterostructures with intersubband transitions in the 5–10 THz band *Nanotechnology* **26** 435201

[48] Lim C B, Beeler M, Ajay A, Lähnemann J, Bellet-Amalric E, Bougerol C and Monroy E 2015 Intersubband transitions in nonpolar GaN/Al(Ga)N heterostructures in the short and mid-wavelength infrared regions *J Appl Phys* **118** 014309

[49] Vurgaftman I and Meyer J R 2003 Band parameters for nitrogen-containing semiconductors *J. Appl. Phys.* **94** 3675–96

[50] Morkoç H, Strite S, Gao G B, Lin M E, Sverdlov B and Burns M 1994 Large-band-gap SiC, III-V nitride, and II-VI ZnSe-based semiconductor device technologies *J. Appl. Phys.* **76** 1363–98

[51] Haskell B A, Wu F, Matsuda S, Craven M D, Fini P T, DenBaars S P, Speck J S and Nakamura S 2003 Structural and morphological characteristics of planar (1120)a-plane gallium nitride grown by hydride vapor phase epitaxy *Appl. Phys. Lett.* **83** 1554–6

[52] Gardner N F, Kim J C, Wierer J J, Shen Y C and Krames M R 2005 Polarization anisotropy in the electroluminescence of m-plane InGaN–GaN multiple-quantum-well light-emitting diodes *Appl. Phys. Lett.* **86** 111101

[53] Chichibu S F, Kagaya M, Corfdir P, Ganière J-D, Deveaud-Plédran B, Grandjean N, Kubo S and Fujito K 2012 Advantages and remaining issues of state-of-the-art m-plane freestanding GaN substrates grown by halide vapor phase epitaxy for m-plane InGaN epitaxial growth *Semicond. Sci. Technol.* **27** 024008

[54] Dridi Z, Bouhafs B and Ruterana P 2003 First-principles investigation of lattice constants and bowing parameters in wurtzite AlxGa1−xN, InxGa1−xN and InxAl1−xN alloys *Semicond. Sci. Technol.* **18** 850

[55] Vurgaftman I and Meyer J R 2003 Band parameters for nitrogen-containing semiconductors *J. Appl. Phys.* **94** 3675–96

[56] Levinshteĭn M E, Rumyantsev S L and Shur M 2001 *Properties of advanced semiconductor materials: GaN, AlN, InN, BN, SiC, SiGe* (New York: Wiley)

[57] Xu Y-N and Ching W Y 1993 Electronic, optical, and structural properties of some wurtzite crystals *Phys. Rev. B* **48** 4335–51

[58] Santic B 2003 On the hole effective mass and the free hole statistics in wurtzite GaN *Semicond. Sci. Technol.* **18** 219–24

[59] Ramos L E, Teles L K, Scolfaro L M R, Castineira J L P, Rosa A L and Leite J R 2001 Structural, electronic, and effective-mass properties of silicon and zinc-blende group-III nitride semiconductor compounds *Phys. Rev. B* **63** 165210

[60] Figge S, Kröncke H, Hommel D and Epelbaum B M 2009 Temperature dependence of the thermal expansion of AlN *Appl. Phys. Lett.* **94** 101915

[61] Roder C, Einfeldt S, Figge S and Hommel D 2005 Temperature dependence of the thermal expansion of GaN *Phys. Rev. B* **72** 085218

[62] Kim K, Lambrecht W R L and Segall B 1996 Elastic constants and related properties of tetrahedrally bonded BN, AlN, GaN, and InN *Phys. Rev. B* **53** 16310–26

[63] Wright A F 1997 Elastic properties of zinc-blende and wurtzite AlN, GaN, and InN *J. Appl. Phys.* **82** 2833–9

[64] Takagi Y, Ahart M, Azuhata T, Sota T, Suzuki K and Nakamura S 1996 Brillouin scattering study in the GaN epitaxial layer *Phys. B Condens. Matter* **219**–**220** 547–9

[65] Polian A, Grimsditch M and Grzegory I 1996 Elastic constants of gallium nitride *J. Appl. Phys.* **79** 3343–4

[66] Yamaguchi M, Yagi T, Azuhata T, Sota T, Suzuki K, Chichibu S and Nakamura S 1997 Brillouin scattering study of gallium nitride: elastic stiffness constants *J. Phys. Condens. Matter* **9** 241

[67] Deger C, Born E, Angerer H, Ambacher O, Stutzmann M, Hornsteiner J, Riha E and Fischerauer G 1998 Sound velocity of AlxGa1−xN thin films obtained by surface acoustic-wave measurements *Appl. Phys. Lett.* **72** 2400–2

[68] McNeil L E, Grimsditch M and French R H 1993 Vibrational Spectroscopy of Aluminum Nitride *J. Am. Ceram. Soc.* **76** 1132–6

[69] Bernardini F, Fiorentini V and Vanderbilt D 1997 Spontaneous polarization and piezoelectric constants of III-V nitrides *Phys. Rev. B* **56** R10024–7

[70] Zoroddu A, Bernardini F, Ruggerone P and Fiorentini V 2001 First-principles prediction of structure, energetics, formation enthalpy, elastic constants, polarization, and piezoelectric constants of AlN, GaN, and InN: Comparison of local and gradient-corrected density-functional theory *Phys. Rev. B* **64** 045208

[71] Ambacher O, Foutz B, Smart J, Shealy J R, Weimann N G, Chu K, Murphy M, Sierakowski A J, Schaff W J, Eastman L F, Dimitrov R, Mitchell A and Stutzmann M 2000 Two dimensional electron gases induced by spontaneous and piezoelectric polarization in undoped and doped AlGaN/GaN heterostructures *J. Appl. Phys.* **87** 334–44

[72] Mitin V V, Sementsov D I and Vagidov N Z 2012 *Quantum mechanics for nanostructures* (Cambridge; New York: Cambridge University Press)

[73] Tchernycheva M, Nevou L, Doyennette L, Julien F, Warde E, Guillot F, Monroy E, Bellet-Amalric E, Remmele T and Albrecht M 2006 Systematic experimental and theoretical investigation of intersubband absorption in GaN/AlN quantum wells *Phys. Rev. B* **73** 125347

[74] Farrell R M, Young E C, Wu F, DenBaars S P and Speck J S 2012 Materials and growth issues for high-performance nonpolar and semipolar light-emitting devices *Semicond. Sci. Technol.* **27** 024001

[75] Harrison P 2005 *Quantum wells, wires, and dots: theoretical and computational physics of semiconductor nanostructures* (Hoboken, NJ: Wiley)

[76] Szczech J R, Higgins J M and Jin S 2011 Enhancement of the thermoelectric properties in nanoscale and nanostructured materials *J. Mater. Chem.* **21** 4037–55

[77] Kamgar A, Kneschaurek P, Dorda G and Koch J F 1974 Resonance Spectroscopy of Electronic Levels in a Surface Accumulation Layer *Phys. Rev. Lett.* **32** 1251–4

[78] West L C and Eglash S J 1985 First observation of an extremely large-dipole infrared transition within the conduction band of a GaAs quantum well *Appl. Phys. Lett.* **46** 1156–8

[79] Kasap S O and Capper P 2006 *Springer handbook of electronic and photonic materials* (New York: Springer)

[80] Liu H C and Capasso F 2000 *Intersubband transitions in quantum wells: Physics and device applications* (San Diego, CA: Academic Press)

[81] Bandara K M S V, Coon D D, O B, Lin Y F and Francombe M H 1989 Erratum: Exchange interactions in quantum well subbands [Appl. Phys. Lett. 53, 1931 (1988)] *Appl. Phys. Lett.* **55** 206

[82] Bandara K M S V, Coon D D, O B, Lin Y F and Francombe M H 1988 Exchange interactions in quantum well subbands *Appl. Phys. Lett.* **53** 1931–3

[83] Shtrichman I, Metzner C, Ehrenfreund E, Gershoni D, Maranowski K D and Gossard A C 2001 Depolarization shift of the intersubband resonance in a quantum well with an electron-hole plasma *Phys. Rev. B* **65** 035310

[84] Allen S J, Tsui D C and Vinter B 1976 On the absorption of infrared radiation by electrons in semiconductor inversion layers *Solid State Commun.* **20** 425–8

[85] Bloss W L 1989 Effects of Hartree, exchange, and correlation energy on intersubband transitions *J. Appl. Phys.* **66** 3639–42

[86] Ando T 1977 Inter-subband optical transitions in a surface space-charge layer *Solid State Commun.* **21** 133–6

[87] Ando T 1977 Inter-subband optical absorption in space-charge layers on semiconductor surfaces *Z. Für Phys. B Condens. Matter Quanta* **26** 263–72

[88] Birner S, Zibold T, Andlauer T, Kubis T, Sabathil M, Trellakis A and Vogl P 2007 nextnano: General Purpose 3-D Simulations *IEEE Trans. Electron Devices* **54** 2137–42

[89] Birner S 2011 *Modeling of semiconductor nanostructures and semiconductor–electrolyte interfaces* PhD Thesis (Garching b. München: Technische Universität München)

[90] Bertelli M, Löptien P, Wenderoth M, Rizzi A, Ulbrich R, Righi M, Ferretti A, Martin-Samos L, Bertoni C and Catellani A 2009 Atomic and electronic structure of the nonpolar GaN(1-100) surface *Phys. Rev. B* **80** 115324

[91] Van de Walle C G and Segev D 2007 Microscopic origins of surface states on nitride surfaces *J. Appl. Phys.* **101** 081704

[92] Lymperakis L, Weidlich P H, Eisele H, Schnedler M, Nys J-P, Grandidier B, Stiévenard D, Dunin-Borkowski R E, Neugebauer J and Ebert P 2013 Hidden surface states at non-polar GaN (10-10) facets: Intrinsic pinning of nanowires *Appl. Phys. Lett.* **103** 152101

[93] Reddy P, Bryan I, Bryan Z, Guo W, Hussey L, Collazo R and Sitar Z 2014 The effect of polarity and surface states on the Fermi level at III-nitride surfaces *J. Appl. Phys.* **116** 123701

[94] Ambacher O 1998 Growth and applications of Group III-nitrides *J. Phys. Appl. Phys.* **31** 2653–710

[95] Bernardini F, Fiorentini V and Vanderbilt D 1997 Spontaneous polarization and piezoelectric constants of III-V nitrides *Phys. Rev. B* **56** R10024–7

[96] Wright A F 1997 Elastic properties of zinc-blende and wurtzite AlN, GaN, and InN *J. Appl. Phys.* **82** 2833–9

[97] Polian A, Grimsditch M and Grzegory I 1996 Elastic constants of gallium nitride *J. Appl. Phys.* **79** 3343–4

[98] Park S-H 2000 Crystal Orientation Effects on Electronic Properties of Wurtzite GaN/AlGaN Quantum Wells with Spontaneous and Piezoelectric Polarization *Jpn. J. Appl. Phys.* **39** 3478–82

[99] Rinke P, Winkelnkemper M, Qteish A, Bimberg D, Neugebauer J and Scheffler M 2008 Consistent set of band parameters for the group-III nitrides AlN, GaN, and InN *Phys. Rev. B* **77** 075202

[100] Chin V W L, Tansley T L and Osotchan T 1994 Electron mobilities in gallium, indium, and aluminum nitrides *J. Appl. Phys.* **75** 7365

[101] Lim C B 2017 *Hétérostructures GaN/Al(Ga)N pour l'optoélectronique infrarouge : orientations polaires et non-polaires* PhD Thesis (Grenoble: Université Grenoble Alpes)

[102] Cho A Y and Arthur J R 1975 Molecular beam epitaxy *Prog. Solid State Chem.* **10** 157–91

[103] Ohring M 2001 *Materials Science of Thin Films* (Elsevier)

[104] Adelmann C, Brault J, Mula G, Daudin B, Lymperakis L and Neugebauer J 2003 Gallium adsorption on (0001) GaN surfaces *Phys. Rev. B* **67** 165419

[105] Mula G, Adelmann C, Moehl S, Oullier J and Daudin B 2001 Surfactant effect of gallium during molecular-beam epitaxy of GaN on AlN (0001) *Phys. Rev. B* **64** 195406

[106] Neugebauer J, Zywietz T, Scheffler M, Northrup J, Chen H and Feenstra R 2003 Adatom Kinetics On and Below the Surface: The Existence of a New Diffusion Channel *Phys. Rev. Lett.* **90** 056101

[107] Lieberman M A and Lichtenberg A J 2005 Chemical Kinetics and Surface Processes *Principles of Plasma Discharges and Materials Processing* (Hoboken, NJ, USA: John Wiley & Sons, Inc.) pp 285–325

[108] Myoung J M, Gluschenkov O, Kim K and Kim S 1999 Growth kinetics of GaN and effects of flux ratio on the properties of GaN films grown by plasma-assisted molecular beam epitaxy *J. Vac. Sci. Technol. Vac. Surf. Films* **17** 3019–28

[109] Bellet-Amalric E, Adelmann C, Sarigiannidou E, Rouvière J L, Feuillet G, Monroy E and Daudin B 2004 Plastic strain relaxation of nitride heterostructures *J. Appl. Phys.* **95** 1127–33

[110] Northrup J, Neugebauer J, Feenstra R and Smith A 2000 Structure of GaN(0001) : The laterally contracted Ga bilayer model *Phys. Rev. B* **61** 9932–5

[111] Kotsar Y 2012 *Puits quantiques GaN/Al(Ga)N pour l'opto´electronique inter-sous-bande dans l'infrarouge proche, moyen et lointain* PhD Thesis (Grenoble: Université de Grenoble)

[112] Adelmann H C 2002 *Growth and strain relaxation mechanisms of group III nitride heterostructures* PhD Thesis (Grenoble: Université Joseph Fourier)

[113] Iliopoulos E and Moustakas T D 2002 Growth kinetics of AlGaN films by plasma-assisted molecular-beam epitaxy *Appl. Phys. Lett.* **81** 295–7

[114] Monroy E, Daudin B, Bellet-Amalric E, Gogneau N, Jalabert D, Enjalbert F, Brault J, Barjon J and Dang L S 2003 Surfactant effect of In for AlGaN growth by plasma-assisted molecular beam epitaxy *J. Appl. Phys.* **93** 1550–6

[115] Sears G W 1955 A growth mechanism for mercury whiskers *Acta Metall.* **3** 361–6

[116] Ruth V and Hirth J P 1964 Kinetics of Diffusion-Controlled Whisker Growth *J. Chem. Phys.* **41** 3139–49

[117] Blakely J M and Jackson K A 1962 Growth of Crystal Whiskers *J. Chem. Phys.* **37** 428–30

[118] Calleja E, Ristić J, Fernández-Garrido S, Cerutti L, Sánchez-García M A, Grandal J, Trampert A, Jahn U, Sánchez G, Griol A and Sánchez B 2007 Growth, morphology, and structural properties of group-III-nitride nanocolumns and nanodisks *Phys. Status Solidi B* **244** 2816–37

[119] Yoshizawa M, Kikuchi A, Mori M, Fujita N and Kishino K 1997 Growth of self-organized GaN nanostructures on Al2O3(0001) by RF-radical source Molecular beam epitaxy *Jpn. J. Appl. Phys.* **36** L459–62

[120] Sanchez-Garcia M A, Calleja E, Monroy E, Sanchez F J, Calle F, Muñoz E and Beresford R 1998 The effect of the III/V ratio and substrate temperature on the morphology and properties of GaN- and AlN-layers grown by molecular beam epitaxy on Si(111) *J. Cryst. Growth* **183** 23–30

[121] Calarco R, Meijers R J, Debnath R K, Stoica T, Sutter E and Lüth H 2007 Nucleation and Growth of GaN Nanowires on Si(111) Performed by Molecular Beam Epitaxy *Nano Lett.* **7** 2248–51

[122] Fernández-Garrido S, Kong X, Gotschke T, Calarco R, Geelhaar L, Trampert A and Brandt O 2012 Spontaneous Nucleation and Growth of GaN Nanowires: The Fundamental Role of Crystal Polarity *Nano Lett.* **12** 6119–25

[123] Fernández-Garrido S, Grandal J, Calleja E, Sánchez-García M A and López-Romero D 2009 A growth diagram for plasma-assisted molecular beam epitaxy of GaN nanocolumns on Si(111) *J. Appl. Phys.* **106** 126102

[124] Hestroffer K, Leclere C, Bougerol C, Renevier H and Daudin B 2011 Polarity of GaN nanowires grown by plasma-assisted molecular beam epitaxy on Si(111) *Phys. Rev. B* **84** 245302

[125] Chichibu S F, Setoguchi A, Uedono A, Yoshimura K and Sumiya M 2000 Impact of growth polar direction on the optical properties of GaN grown by metalorganic vapor phase epitaxy *Appl. Phys. Lett.* **78** 28–30

[126] Massimo Sandal, Fabrizio Benedetti, Alberto Gomez-Casado, Marco Brucale, Bruno Samorì and Massimo Sandal F B 2009 Hooke: an open software platform for force spectroscopy *Bioinformatics* **25** 1428–30

[127] Schroder D K 2005 Frontmatter *Semiconductor Material and Device Characterization* (Hoboken, NJ, USA: John Wiley & Sons, Inc.) pp i–xv

[128] Smith K K 1981 Photoluminescence of semiconductor materials *Thin Solid Films* **84** 171–82

[129] Ajay A, Schörmann J, Jiménez-Rodriguez M, Lim C B, Walther F, Rohnke M, Mouton I, Amichi L, Bougerol C, Den Hertog M I, Eickhoff M and Monroy E 2016 Ge doping of GaN beyond the Mott transition *J. Phys. Appl. Phys.* **49** 445301

[130] Dadgar A, Fritze S, Schulz O, Hennig J, Bläsing J, Witte H, Diez A, Heinle U, Kunze M, Daumiller I, Haberland K and Krost A 2013 Anisotropic bow and plastic deformation of GaN on silicon *J. Cryst. Growth* **370** 278–81

[131] Richter T, Meijers H L R, Calarco R and Marso M 2008 Doping Concentration of GaN Nanowires Determined by Opto-Electrical Measurements *Nano Lett.* **8** 3056–9

[132] Oshima Y, Yoshida T, Watanabe K and Mishima T 2010 Properties of Ge-doped, high-quality bulk GaN crystals fabricated by hydride vapor phase epitaxy *J. Cryst. Growth* **312** 3569–73

[133] Hofmann P, Krupinski M, Habel F, Leibiger G, Weinert B, Eichler S and Mikolajick T 2016 Novel approach for n-type doping of HVPE gallium nitride with germanium *J. Cryst. Growth* **450** 61–5

[134] Nakamura S, Mukai T and Senoh M 1992 Si- and Ge-Doped GaN Films Grown with GaN Buffer Layers *Jpn. J. Appl. Phys.* **31** 2883–8

[135] Zhang X, Kung P, Saxler A, Walker D, Wang T C and Razeghi M 1995 Growth of AlxGa1−xN:Ge on sapphire and silicon substrates *Appl. Phys. Lett.* **67** 1745

[136] Dadgar A, Bläsing J, Diez A and Krost A 2011 Crack-Free, Highly Conducting GaN Layers on Si Substrates by Ge Doping *Appl. Phys. Express* **4** 011001

[137] Kirste R, Hoffmann M P, Sachet E, Bobea M, Bryan Z, Bryan I, Nenstiel C, Hoffmann A, Maria J-P, Collazo R and Sitar Z 2013 Ge doped GaN with controllable high carrier concentration for plasmonic applications *Appl. Phys. Lett.* **103** 242107

[138] Hageman P R, Schaff W J, Janinski J and Liliental-Weber Z 2004 n-type doping of wurtzite GaN with germanium grown with plasma-assisted molecular beam epitaxy *J. Cryst. Growth* **267** 123–8

[139] Gunning B P, Clinton E A, Merola J J, Doolittle W A and Bresnahan R C 2015 Control of ion content and nitrogen species using a mixed chemistry plasma for GaN grown at extremely high growth rates >9 µm/h by plasma-assisted molecular beam epitaxy *J. Appl. Phys.* **118** 155302

[140] Schäfer M, Günther M, Länger C, Müßener J, Feneberg M, Uredat P, Elm M T, Hille P, Schörmann J, Teubert J, Henning T, Klar P J and Eickhoff M 2015 Electrical transport properties of Ge-doped GaN nanowires *Nanotechnology* **26** 135704

[141] Schörmann J, Hille P, Schäfer M, Müßener J, Becker P, Klar P J, Kleine-Boymann M, Rohnke M, de la Mata M, Arbiol J, Hofmann D M, Teubert J and Eickhoff M 2013 Germanium doping of self-assembled GaN nanowires grown by plasma-assisted molecular beam epitaxy *J. Appl. Phys.* **114** 103505

[142] Hille P, Müßener J, Becker P, de la Mata M, Rosemann N, Magén C, Arbiol J, Teubert J, Chatterjee S, Schörmann J and Eickhoff M 2014 Screening of the quantum-confined Stark effect in AlN/GaN nanowire superlattices by germanium doping *Appl. Phys. Lett.* **104** 102104

[143] Beeler M, Lim C B, Hille P, Bleuse J, Schörmann J, de la Mata M, Arbiol J, Eickhoff M and Monroy E 2015 Long-lived excitons in GaN/AlN nanowire heterostructures *Phys. Rev. B* **91** 205440

[144] Lahourcade L, Pernot J, Wirthmüller A, Chauvat M P, Ruterana P, Laufer A, Eickhoff M and Monroy E 2009 Mg doping and its effect on the semipolar GaN(11-22) growth kinetics *Appl. Phys. Lett.* **95** 171908

[145] Monroy E, Andreev T, Holliger P, Bellet-Amalric E, Shibata T, Tanaka M and Daudin B 2004 Modification of GaN(0001) growth kinetics by Mg doping *Appl. Phys. Lett.* **84** 2554

[146] Northrup J E 2005 Effect of magnesium on the structure and growth of GaN(0001) *Appl. Phys. Lett.* **86** 122108

[147] Zhang Y, Evans J R G and Yang S 2011 Corrected Values for Boiling Points and Enthalpies of Vaporization of Elements in Handbooks *J. Chem. Eng. Data* **56** 328–37

[148] Binet F, Duboz J Y, Off J and Scholz F 1999 High-excitation photoluminescence in GaN: Hot-carrier effects and the Mott transition *Phys. Rev. B* **60** 4715–22

[149] Feneberg M, Lange K, Lidig C, Wieneke M, Witte H, Bläsing J, Dadgar A, Krost A and Goldhahn R 2013 Anisotropy of effective electron masses in highly doped nonpolar GaN *Appl. Phys. Lett.* **103** 232104

[150] Pearson G L and Bardeen J 1949 Electrical Properties of Pure Silicon and Silicon Alloys Containing Boron and Phosphorus *Phys. Rev.* **75** 865–83

[151] Meyer B K, Volm D, Graber A, Alt H C, Detchprohm T, Amano A and Akasaki I 1995 Shallow donors in GaN—The binding energy and the electron effective mass *Solid State Commun.* **95** 597–600

[152] Berggren K-F and Sernelius B E 1981 Band-gap narrowing in heavily doped many-valley semiconductors *Phys. Rev. B* **24** 1971–86

[153] Moss T S 1954 Theory of the Spectral Distribution of Recombination Radiation from InSb *Proc. Phys. Soc. B* **67** 775

[154] Arnaudov B, Paskova T, Goldys E M, Evtimova S and Monemar B 2001 Modeling of the free-electron recombination band in emission spectra of highly conducting n-GaN *Phys. Rev. B* **64** 045213

[155] Feneberg M, Osterburg S, Lange K, Lidig C, Garke B, Goldhahn R, Richter E, Netzel C, Neumann M D, Esser N, Fritze S, Witte H, Bläsing J, Dadgar A and Krost A 2014 Band gap renormalization and Burstein-Moss effect in silicon- and germanium-doped wurtzite GaN up to 1020 cm−3 *Phys. Rev. B* **90** 075203

[156] Yan Q, Rinke P, Janotti A, Scheffler M and Van de Walle C G 2014 Effects of strain on the band structure of group-III nitrides *Phys. Rev. B* **90** 125118

[157] Nakarmi M L, Kim K H, Zhu K, Lin J Y and Jiang H X 2004 Transport properties of highly conductive n-type Al-rich AlxGa1−xN(x⩾0.7) *Appl. Phys. Lett.* **85** 3769–71

[158] Borisov B, Kuryatkov V, Kudryavtsev Y, Asomoza R, Nikishin S, Song D Y, Holtz M and Temkin H 2005 Si-doped AlxGa1−xN(0.56⩽×⩽1) layers grown by molecular beam epitaxy with ammonia *Appl. Phys. Lett.* **87** 132106

[159] Collazo R, Mita S, Xie J, Rice A, Tweedie J, Dalmau R and Sitar Z 2011 Progress on n-type doping of AlGaN alloys on AlN single crystal substrates for UV optoelectronic applications *Phys. Status Solidi C* **8** 2031–3

[160] Mehnke F, Wernicke T, Pingel H, Kuhn C, Reich C, Kueller V, Knauer A, Lapeyrade M, Weyers M and Kneissl M 2013 Highly conductive n-AlxGa1−xN layers with aluminum mole fractions above 80% *Appl. Phys. Lett.* **103** 212109

[161] Park C H and Chadi D J 1997 Stability of deep donor and acceptor centers in GaN, AlN, and BN *Phys. Rev. B* **55** 12995–3001

[162] Silvestri L, Dunn K, Prawer S and Ladouceur F 2011 Hybrid functional study of Si and O donors in wurtzite AlN *Appl. Phys. Lett.* **99** 122109

[163] Trinh X T, Nilsson D, Ivanov I G, Janzén E, Kakanakova-Georgieva A and Son N T 2014 Stable and metastable Si negative-U centers in AlGaN and AlN *Appl. Phys. Lett.* **105** 162106

[164] Taniyasu Y, Kasu M and Kobayashi N 2002 Intentional control of n-type conduction for Si-doped AlN and AlxGa1−xN (0.42⩽x<1) *Appl. Phys. Lett.* **81** 1255–7

[165] Barradas N P, Jeynes C and Webb R P 1997 Simulated annealing analysis of Rutherford backscattering data *Appl. Phys. Lett.* **71** 291–3

[166] Cho Y-H, Gainer G H, Lam J B, Song J J, Yang W and Jhe W 2000 Dynamics of anomalous optical transitions in AlxGa1−xN alloys *Phys. Rev. B* **61** 7203–6

[167] Leroux M, Grandjean N, Beaumont B, Nataf G, Semond F, Massies J and Gibart P 1999 Temperature Dependence of Photoluminescence Intensities of Undoped and Doped GaN *Phys. Status Solidi B* **216** 605–8

[168] Ajay A, Lim C B, Browne D A, Polaczynski J, Bellet-Amalric E, den Hertog M I and Monroy E 2017 Intersubband absorption in Si- and Ge-doped GaN/AlN heterostructures in self-assembled nanowire and 2D layers *Phys. Status Solidi B* **254** 1600734

[169] Binnig G, Rohrer H, Gerber C and Weibel E 1983 7x7 Reconstruction on Si(111) resolved in real space *Phys. Rev. Lett.* **50** 120–3

[170] Songmuang R, Landré O and Daudin B 2007 From nucleation to growth of catalyst-free GaN nanowires on thin AlN buffer layer *Appl. Phys. Lett.* **91** 251902

[171] Bourret A, Barski A, Rouvière J L, Renaud G and Barbier A 1998 Growth of aluminum nitride on (111) silicon: Microstructure and interface structure *J. Appl. Phys.* **83** 2003–9

[172] Cherns D, Meshi L, Griffiths I, Khongphetsak S, Novikov S V, Farley N, Campion R P and Foxon C T 2008 Defect reduction in GaN/(0001)sapphire films grown by molecular beam epitaxy using nanocolumn intermediate layers *Appl. Phys. Lett.* **92** 121902

[173] Brubaker M D, Levin I, Davydov A V, Rourke D M, Sanford N A, Bright V M and Bertness K A 2011 Effect of AlN buffer layer properties on the morphology and polarity of GaN nanowires grown by molecular beam epitaxy *J. Appl. Phys.* **110** 053506

[174] Schenk H P D, Kipshidze G D, Kaiser U, Fissel A, Kräuβlich J, Schulze J and Richter W 1999 Investigation of two-dimensional growth of AlN(0001) on Si(111) by plasma-assisted molecular beam epitaxy *J. Cryst. Growth* **200** 45–54

[175] Musolino M, Tahraoui A, Fernández-Garrido S, Brandt O, Trampert A, Geelhaar L and Riechert H 2015 Compatibility of the selective area growth of GaN nanowires on AlN-buffered Si substrates with the operation of light emitting diodes *Nanotechnology* **26** 085605

[176] Meijers R, Richter T, Calarco R, Stoica T, Bochem H-P, Marso M and Lüth H 2006 GaN-nanowhiskers: MBE-growth conditions and optical properties *J. Cryst. Growth* **289** 381–6

[177] Kaganer V M, Fernández-Garrido S, Dogan P, Sabelfeld K K and Brandt O 2016 Nucleation, Growth, and Bundling of GaN Nanowires in Molecular Beam Epitaxy: Disentangling the Origin of Nanowire Coalescence *Nano Lett.* **16** 3717–25

[178] Ajay A, Lim C B, Browne D A, Polaczyński J, Bellet-Amalric E, Bleuse J, den Hertog M I and Monroy E 2017 Effect of doping on the intersubband absorption in Si- and Ge-doped GaN/AlN heterostructures *Nanotechnology* **28** 405204

[179] Lim C B, Ajay A, Lähnemann J, Bougerol C and Monroy E 2017 Effect of Ge-doping on the short-wave, mid- and far-infrared intersubband transitions in GaN/AlGaN heterostructures *Semicond. Sci. Technol.* **32** 125002

[180] Lähnemann J, Browne D A, Ajay A, Thomassin J-L, Bellet-Amalric E and Monroy E 2018 Near- and mid-infrared intersubband absorption in top-down GaN/AlN nano- and micropillars *ArXiv180508999 Cond-Mat*

[181] Beeler M, Trichas E and Monroy E 2013 III-nitride semiconductors for intersubband optoelectronics: a review *Semicond. Sci. Technol.* **28** 074022

[182] Riyopoulos S 2009 Electrostatically Shielded Quantum Confined Stark Effect Inside Polar Nanostructures *Nanoscale Res. Lett.* **4** 993–1003

[183] Songmuang R, Kalita D, Sinha P, den Hertog M, André R, Ben T, González D, Mariette H and Monroy E 2011 Strong suppression of internal electric field in GaN/AlGaN multi-layer quantum dots in nanowires *Appl. Phys. Lett.* **99** 141914

[184] Furtmayr F, Teubert J, Becker P, Conesa-Boj S, Morante J R, Chernikov A, Schäfer S, Chatterjee S, Arbiol J and Eickhoff M 2011 Carrier confinement in GaN/AlxGa1−xN nanowire heterostructures (0<x≤1) *Phys. Rev. B* **84** 205303

[185] Guillot F, Bellet-Amalric E, Monroy E, Tchernycheva M, Nevou L, Doyennette L, Julien F H, Dang L S, Remmele T, Albrecht M, Shibata T and Tanaka M 2006 Si-doped GaN⁄AlN quantum dot superlattices for optoelectronics at telecommunication wavelengths *J. Appl. Phys.* **100** 044326

[186] Kandaswamy P K, Bougerol C, Jalabert D, Ruterana P and Monroy E 2009 Strain relaxation in short-period polar GaN/AlN superlattices *J. Appl. Phys.* **106** 013526

[187] Ajay A, Blasco R, Polaczynski J, Spies M, den Hertog M and Monroy E 2018 Intersubband absorption in GaN nanowire heterostructures at mid-infrared wavelengths *Nanotechnology* (in press)

[188] Ristić J, Calleja E, Trampert A, Fernández-Garrido S, Rivera C, Jahn U and Ploog K H 2005 Columnar AlGaN / GaN Nanocavities with AlN / GaN Bragg Reflectors Grown by Molecular Beam Epitaxy on Si(111) *Phys. Rev. Lett.* **94** 146102

[189] Allah R F, Ben T, Songmuang R and González D 2012 Imaging and Analysis by Transmission Electron Microscopy of the Spontaneous Formation of Al-Rich Shell Structure in AlxGa1-xN/GaN Nanowires *Appl. Phys. Express* **5** 045002

[190] Laneuville V, Demangeot F, Péchou R, Salles P, Ponchet A, Jacopin G, Rigutti L, de Luna Bugallo A, Tchernycheva M, Julien F H, March K, Zagonel L F and Songmuang R 2011 Double strain state in a single GaN/AlN nanowire: Probing the core-shell effect by ultraviolet resonant Raman scattering *Phys. Rev. B* **83** 115417

[191] Himwas C, Hertog M den, Dang L S, Monroy E and Songmuang R 2014 Alloy inhomogeneity and carrier localization in AlGaN sections and AlGaN/AlN nanodisks in nanowires with 240–350 nm emission *Appl. Phys. Lett.* **105** 241908

[192] Nicolay S, Feltin E, Carlin J-F, Grandjean N, Nevou L, Julien F H, Schmidbauer M, Remmele T and Albrecht M 2007 Strain-induced interface instability in GaN⁄AlN multiple quantum wells *Appl. Phys. Lett.* **91** 061927

[193] Bogusławski P, Rapcewicz K and Bernholc J J 2000 Surface segregation and interface stability of AlN/GaN, GaN/InN, and AlN/InN {0001} epitaxial systems *Phys. Rev. B* **61** 10820–6

[194] Bayram C, Péré-Laperne N and Razeghi M 2009 Effects of well width and growth temperature on optical and structural characteristics of AlN/GaN superlattices grown by metal-organic chemical vapor deposition *Appl. Phys. Lett.* **95** 201906

[195] Yang J-S, Sodabanlu H, Sugiyama M, Nakano Y and Shimogaki Y 2009 Blueshift of intersubband transition wavelength in AlN/GaN multiple quantum wells by low temperature metal organic vapor phase epitaxy using pulse injection method *Appl. Phys. Lett.* **95** 162111

[196] Lim C B, Ajay A, Bougerol C, Lähnemann J, Donatini F, Schörmann J, Bellet-Amalric E, Browne D A, Jiménez-Rodríguez M and Monroy E 2016 Effect of doping on the far-infrared intersubband transitions in nonpolar m-plane GaN/AlGaN heterostructures *Nanotechnology* **27** 145201

[197] Iizuka N, Kaneko K and Suzuki N 2002 Near-infrared intersubband absorption in GaN/AlN quantum wells grown by molecular beam epitaxy *Appl. Phys. Lett.* **81** 1803–5

[198] Kishino K, Kikuchi A, Kanazawa H and Tachibana T 2002 Intersubband transition in (GaN)m/(AlN)n superlattices in the wavelength range from 1.08 to 1.61 μm *Appl. Phys. Lett.* **81** 1234–6

[199] Berland K, Stattin M, Farivar R, Sultan D M S, Hyldgaard P, Larsson A, Wang S M and Andersson T G 2010 Temperature stability of intersubband transitions in AlN/GaN quantum wells *Appl. Phys. Lett.* **97** 043507

[200] Bayram C 2012 High-quality AlGaN/GaN superlattices for near- and mid-infrared intersubband transitions *J. Appl. Phys.* **111** 013514

[201] Chen G, Li Z L, Wang X Q, Huang C C, Rong X, Sang L W, Xu F J, Tang N, Qin Z X, Sumiya M, Chen Y H, Ge W K and Shen B 2013 Effect of polarization on intersubband transition in AlGaN/GaN multiple quantum wells *Appl. Phys. Lett.* **102** 192109

[202] Edmunds C, Tang L, Li D, Cervantes M, Gardner G, Paskova T, Manfra M J and Malis O 2012 Near-Infrared Absorption in Lattice-Matched AlInN/GaN and Strained AlGaN/GaN Heterostructures Grown by MBE on Low-Defect GaN Substrates *J. Electron. Mater.* **41** 881–6

[203] Kandaswamy P K, Machhadani H, Bougerol C, Sakr S, Tchernycheva M, Julien F H and Monroy E 2009 Midinfrared intersubband absorption in GaN/AlGaN superlattices on Si(111) templates *Appl. Phys. Lett.* **95** 141911

[204] Péré-Laperne N, Bayram C, Nguyen-The L, McClintock R and Razeghi M 2009 Tunability of intersubband absorption from 4.5 to 5.3 μm in a GaN/Al0.2Ga0.8N superlattices grown by metalorganic chemical vapor deposition *Appl. Phys. Lett.* **95** 131109

[205] Tian W, Yan W Y, Hui X, Li S L, Ding Y Y, Li Y, Tian Y, Dai J N, Fang Y Y, Wu Z H, Yu C H and Chen C Q 2012 Tunability of intersubband transition wavelength in the atmospheric window in AlGaN/GaN multi-quantum wells grown on different AlGaN templates by metalorganic chemical vapor deposition *J. Appl. Phys.* **112** 063526

[206] Machhadani H, Tchernycheva M, Sakr S, Rigutti L, Colombelli R, Warde E, Mietze C, As D J and Julien F H 2011 Intersubband absorption of cubic GaN/Al(Ga)N quantum wells in the near-infrared to terahertz spectral range *Phys. Rev. B* **83** 075313

[207] Sudradjat F F, Zhang W, Woodward J, Durmaz H, Moustakas T D and Paiella R 2012 Far-infrared intersubband photodetectors based on double-step III-nitride quantum wells *Appl. Phys. Lett.* **100** 241113

[208] Beeler M, Bougerol C, Bellet-Amalric E and Monroy E 2013 Terahertz absorbing AlGaN/GaN multi-quantum-wells: Demonstration of a robust 4-layer design *Appl. Phys. Lett.* **103** 091108

[209] Beeler M, Bougerol C, Bellet-Amalric E and Monroy E 2014 Pseudo-square AlGaN/GaN quantum wells for terahertz absorption *Appl. Phys. Lett.* **105** 131106

[210] Kotani T, Arita M and Arakawa Y 2014 Observation of mid-infrared intersubband absorption in non-polar m-plane AlGaN/GaN multiple quantum wells *Appl. Phys. Lett.* **105** 261108

[211] Pesach A, Gross E, Huang C-Y, Lin Y-D, Vardi A, Schacham S E, Nakamura S and Bahir G 2013 Non-polar m-plane intersubband based InGaN/(Al)GaN quantum well infrared photodetectors *Appl. Phys. Lett.* **103** 022110

[212] Lim C B, Ajay A, Bougerol C, Bellet-Amalric E, Schörmann J, Beeler M and Monroy E 2017 Effect of Al incorporation in nonpolar m-plane GaN/AlGaN multi-quantum-wells using plasma-assisted molecular-beam epitaxy: Al incorporation in nonpolar m-plane GaN/AlGaN multi-QWs *Phys. Status Solidi A* **214** 1600849

[213] Young E C, Romanov A E, Gallinat C S, Hirai A, Beltz G E and Speck J S 2010 Anisotropy of tensile stresses and cracking in nonbasal plane AlxGa1−xN/GaN heterostructures *Appl. Phys. Lett.* **96** 041913

[214] Liu W, Li M F, Xu S J, Uchida K and Matsumoto K 1998 Phonon-assisted photoluminescence in wurtzite GaN epilayer *Semicond. Sci. Technol.* **13** 769–72

[215] Gačević Ž, Das A, Teubert J, Kotsar Y, Kandaswamy P K, Kehagias T, Koukoula T, Komninou P and Monroy E 2011 Internal quantum efficiency of III-nitride quantum dot superlattices grown by plasma-assisted molecular-beam epitaxy *J. Appl. Phys.* **109** 103501

[216] Ibáñez J, Hernández S, Alarcón-Lladó E, Cuscó R, Artús L, Novikov S V, Foxon C T and Calleja E 2008 Far-infrared transmission in GaN, AlN, and AlGaN thin films grown by molecular beam epitaxy *J. Appl. Phys.* **104** 033544

[217] Unuma T, Yoshita M, Noda T, Sakaki H and Akiyama H 2003 Intersubband absorption linewidth in GaAs quantum wells due to scattering by interface roughness, phonons, alloy disorder, and impurities *J. Appl. Phys.* **93** 1586–97

[218] Kotani T, Arita M and Arakawa Y 2015 Doping dependent blue shift and linewidth broadening of intersubband absorption in non-polar m-plane AlGaN/GaN multiple quantum wells *Appl. Phys. Lett.* **107** 112107

[219] Lähnemann J, Ajay A, Den Hertog M I and Monroy E 2017 Near-Infrared Intersubband Photodetection in GaN/AlN Nanowires *Nano Lett.* **17** 6954–60

[220] Spies M, Polaczyński J, Ajay A, Kalita D, Luong M A, Lähnemann J, Gayral B, den Hertog M I and Monroy E 2018 Effect of the nanowire diameter on the linearity of the response of GaN-based heterostructured nanowire photodetectors *Nanotechnology* **29** 255204

[221] Songmuang R, Katsaros G, Monroy E, Spathis P, Bougerol C, Mongillo M and De Franceschi S 2010 Quantum Transport in GaN/AlN Double-Barrier Heterostructure Nanowires *Nano Lett.* **10** 3545–50

[222] Rigutti L, Tchernycheva M, De Luna Bugallo A, Jacopin G, Julien F H, Zagonel L F, March K, Stephan O, Kociak M and Songmuang R 2010 Ultraviolet Photodetector Based on GaN/AlN Quantum Disks in a Single Nanowire *Nano Lett.* **10** 2939–43

[223] Lehmann S, Jacobsson D and Dick K A 2015 Crystal phase control in GaAs nanowires: opposing trends in the Ga- and As-limited growth regimes *Nanotechnology* **26** 301001

[224] Lu W and Lieber C M 2007 Nanoelectronics from the bottom up *Nat. Mater.* **6** 841–50

[225] Landré O, Camacho D, Bougerol C, Niquet Y M, Favre-Nicolin V, Renaud G, Renevier H and Daudin B 2010 Elastic strain relaxation in GaN/AlN nanowire superlattice *Phys. Rev. B* **81** 153306

[226] den Hertog M I, González-Posada F, Songmuang R, Rouviere J L, Fournier T, Fernandez B and Monroy E 2012 Correlation of Polarity and Crystal Structure with Optoelectronic and Transport Properties of GaN/AlN/GaN Nanowire Sensors *Nano Lett.* **12** 5691–6

[227] Rose A 1955 Space-Charge-Limited Currents in Solids *Phys. Rev.* **97** 1538–44

[228] González-Posada F, Songmuang R, Den Hertog M and Monroy E 2012 Room-Temperature Photodetection Dynamics of Single GaN Nanowires *Nano Lett.* **12** 172–6

[229] Lähnemann J, Den Hertog M, Hille P, de la Mata M, Fournier T, Schörmann J, Arbiol J, Eickhoff M and Monroy E 2016 UV Photosensing Characteristics of Nanowire-Based GaN/AlN Superlattices *Nano Lett.* **16** 3260–7

[230] Calarco R, Marso M, Richter T, Aykanat A I, Meijers R, v.d. Hart A, Stoica T and Lüth H 2005 Size-dependent Photoconductivity in MBE-Grown GaN−Nanowires *Nano Lett.* **5** 981–4

[231] Sanford N A, Blanchard P T, Bertness K A, Mansfield L, Schlager J B, Sanders A W, Roshko A, Burton B B and George S M 2010 Steady-state and transient photoconductivity in c-axis GaN nanowires grown by nitrogen-plasma-assisted molecular beam epitaxy *J. Appl. Phys.* **107** 034318

[232] Sanford N A, Robins L H, Blanchard P T, Soria K, Klein B, Eller B S, Bertness K A, Schlager J B and Sanders A W 2013 Studies of photoconductivity and field effect transistor behavior in examining drift mobility, surface depletion, and transient effects in Si-doped GaN nanowires in vacuum and air *J. Appl. Phys.* **113** 174306

[233] Xu Y, Gong T and Munday J N 2015 The generalized Shockley-Queisser limit for nanostructured solar cells *Sci. Rep.* **5** 13536

[234] González-Posada F, Songmuang R, Den Hertog M and Monroy E 2013 Environmental sensitivity of n-i-n and undoped single GaN nanowire photodetectors *Appl. Phys. Lett.* **102** 213113

[235] Chen R S, Tsai H Y, Chan C H, Huang Y S, Chen Y T, Chen K H and Chen L C 2014 Comparison of CVD- and MBE-grown GaN Nanowires: Crystallinity, Photoluminescence, and Photoconductivity *J. Electron. Mater.* **44** 177–87

[236] Cao Y L, Liu Z T, Chen L M, Tang Y B, Luo L B, Jie J S, Zhang W J, Lee S T and Lee C S 2011 Single-crystalline ZnTe nanowires for application as high-performance Green/Ultraviolet photodetector *Opt. Express* **19** 6100–8

[237] Soci C, Zhang A, Xiang B, Dayeh S A, Aplin D P R, Park J, Bao X Y, Lo Y H and Wang D 2007 ZnO nanowire UV photodetectors with high internal gain *Nano Lett.* **7** 1003–9

[238] Zhang H, Babichev A V, Jacopin G, Lavenus P, Julien F H, Yu. Egorov A, Zhang J, Pauporté T and Tchernycheva M 2013 Characterization and modeling of a ZnO nanowire ultraviolet photodetector with graphene transparent contact *J. Appl. Phys.* **114** 234505

[239] Yan X, Li B, Wu Y, Zhang X and Ren X 2016 A single crystalline InP nanowire photodetector *Appl. Phys. Lett.* **109** 053109

[240] Wang S B, Hsiao C H, Chang S J, Lam K T, Wen K H, Hung S C, Young S J and Huang B R 2011 A CuO nanowire infrared photodetector *Sens. Actuators Phys.* **171** 207–11

[241] Wang H 2013 High gain single GaAs nanowire photodetector *Appl. Phys. Lett.* **103** 093101

[242] Soci C, Zhang A, Bao X-Y, Kim H, Lo Y and Wang D 2010 Nanowire Photodetectors *J. Nanosci. Nanotechnol.* **10** 1430–49

[243] Simon J, Zhang Z, Goodman K, Xing H, Kosel T, Fay P and Jena D 2009 Polarization-induced Zener tunnel junctions in wide-band-gap heterostructures *Phys. Rev. Lett.* **103** 026801

[244] Leconte S, Guillot F, Sarigiannidou E and Monroy E 2007 Charge distribution and vertical electron transport through GaN/AlN/GaN single-barrier structures *Semicond. Sci. Technol.* **22** 107–12

[245] Spies M, den Hertog M I, Hille P, Schörmann J, Polaczyński J, Gayral B, Eickhoff M, Monroy E and Lähnemann J 2017 Bias-controlled spectral response in GaN/AlN single-nanowire ultraviolet photodetectors *Nano Lett.* **17** 4231–9

[246] Monroy E, Omnès F and Calle F 2003 Wide-bandgap semiconductor ultraviolet photodetectors *Semicond. Sci. Technol.* **18** R33–51

[247] Monroy E, Calle F, Muñoz E, Omnès F, Beaumont B and Gibart P 1999 Visible-blindness in photoconductive and photovoltaic AlGaN ultraviolet detectors *J. Electron. Mater.* **28** 240–5

[248] Pfüller C, Brandt O, Grosse F, Flissikowski T, Chèze C, Consonni V, Geelhaar L, Grahn H T and Riechert H 2010 Unpinning the Fermi level of GaN nanowires by ultraviolet radiation *Phys. Rev. B* **82** 045320

[249] Garrido J A, Monroy E, Izpura I and Muñoz E 1998 Photoconductive gain modelling of GaN photodetectors *Semicond. Sci. Technol.* **13** 563–8

Publications and conference contributions

Book chapters

[1] **Infrared emitters using III-nitride semiconductors**
A. Ajay, Y Kotsar, E Monroy
In "Nitride Semiconductor Light-Emitting Diodes (LEDs) 2nd Edition. Materials, Technologies, and Applications", edited by J.-J Huang, H.-C Kuo, and S.-C Shen (Woodhead publishing, ISBN: 9780081019429, October 2017)

[2] **Intersubband Optoelectronics using III-Nitride Semiconductors**
C. B. Lim, A. Ajay, J. Lähnemann, D. A. Browne, and E. Monroy
In "HandBook of GaN Semiconductor Materials and Devices", edited by W. Bi, H.-C. Kuo, P.-C. Ku, and B. Shen (Taylor & Francis, UK, ISBN: 9781498747134, October 2017).

[3] **III-Nitride Nanostructures for Intersubband Optoelectronics**
C. B. Lim, A. Ajay, J. Lähnemann, D. A. Browne, and E. Monroy
In "III-Nitride Materials, Devices and Nano-Structures", edited by Z. C. Feng (World Scientific Europe, UK, ISBN: 9781786343185, June 2017).

Publications in international journals

2018

[1] **Intersubband absorption in GaN nanowire heterostructures at mid-infrared wavelengths**
A. Ajay, R. Blasco, J. Polaczynski, M. Spies, J. Bleuse, M. Den Hertog, and E. Monroy
Nanotechnology **29**, 385201 (2018)

[2] **Near-and mid-infrared intersubband absorption in top-down GaN/AlN nano-and micropillars**
J. Lähnemann, D. A. Browne, A. Ajay, J-L. Thomassin, E. Bellet-Amalric and E. Monroy
arXiv:1805.08999 [cond-mat.mes-hall]

[3] **Effect of the nanowire diameter on the linearity of the response of GaN-based heterostructured nanowire photodetectors**
M. Spies, J. Polaczynski, A. Ajay, D. Kalita, M. A. Luong, J. Lähnemann, B. Gayral, M. Den Hertog, and E. Monroy
Nanotechnology **29**, 255204 (2018)

2017

[4] **Effect of Ge-doping on the short-wave, mid-and far-infrared intersubband transitions in GaN/AlGaN heterostructures**
C. B. Lim, A. Ajay, J. Lähnemann, C. Bougerol and E. Monroy
Semiconductor Science and Technology **32** (12), 125002 (2017)

[5] **Near-infrared intersubband photodetection in GaN/AlN nanowires**
J. Lähnemann, A. Ajay, M. I. Den Hertog and E Monroy
Nano Letters **17** (11), 6954 (2017)

[6] **P-i-n InGaN homojunctions (10–40% In) synthesized by plasma-assisted molecular beam epitaxy with extended photoresponse to 600 nm**
S.Valdueza-Felip, A.Ajay, L.Redaelli, M.P.Chauvat, P.Ruterana, T.Cremel, M.Jiménez-Rodríguez, K.Kheng and E.Monroy
Solar Energy Materials and Solar Cells **160**, 355 (2017)

[7] **Gallium kinetics on m-plane GaN**
C. B. Lim, A. Ajay, and E. Monroy
Applied Physics. Letters **111**, 022101 (2017)

[8] **Effect of Al incorporation in nonpolar m-plane GaN/AlGaN multi-quantum-wells using plasma-assisted molecular-beam epitaxy**
C.B. Lim, A. Ajay, C. Bougerol, E. Bellet-Amalric, J. Schörmann, M. Beeler and E. Monroy
Phys. Status Solidi A **214**, 1600849 (2017)

[9] **Effect of doping on the intersubband absorption in Si- and Ge-doped GaN/AlN heterostructures**
A. Ajay, C.B. Lim, D.A. Browne, J. Polaczynski, E. Bellet-Amalric, J. Bleuse, M. Den Hertog, and E. Monroy
Nanotechnology **28** 405204 (2017)

[10] **Intersubband Absorption in Si- and Ge-Doped GaN/AlN Heterostructures in Self-Assembled Nanowire and 2D layers**
A. Ajay, C.B. Lim, D.A. Browne, J. Polaczynski, E. Bellet-Amalric, M. Den Hertog, and E. Monroy
Phys. Status Solidi B **254,** 1600734 (2017))

2016

[11] **Ge doping of GaN beyond the Mott transition**
A. Ajay, J. Schörmann, M. Jimenez-Rodriguez, C. B. Lim, F. Walther, M. Rohnke, I. Mouton, L. Amichi, C. Bougerol, M. I. Den Hertog, M. Eickhoff, et E. Monroy
J. Phys. D: Appl. Phys. **49** 445301 (2016)

[12] **Effect of doping on the far-infrared intersubband transitions in nonpolar m-plane GaN/AlGaN heterostructures**
C.B. Lim, A. Ajay, C. Bougerol, J. Lähnemann, F. Donatini, J. Schörmann, E. Bellet-Amalric, D.A. Browne, M. Jiménez-Rodriguez, and E. Monroy
Nanotechnology **27**, 145201 (2016)

[13] **Short-wavelength, mid- and far-infrared intersubband absorption in nonpolar GaN/Al(Ga)N heterostructures**
C. B. Lim, M. Beeler, A. Ajay, J. Lähnemann, E. Bellet-Amalric, C. Bougerol, J. Schörmann, M. Eickhoff, and E. Monroy
Jpn. J. Appl. Phys. **55** 05FG05 (2016)

2015

[14] **Nonpolar m-plane GaN/AlGaN heterostructures with intersubband transitions in the 5 to 10 THz band**
C. B. Lim, A. Ajay, C. Bougerol, J. Schörmann, M. Beeler, J. Lähnemann, M. Eickhoff, and E. Monroy
Nanotechnology **26**, 435201 (2015)

[15] **Intersubband transitions in nonpolar GaN/Al(Ga)N heterostructures in the short- and mid-wavelength infrared regions**
C. B. Lim, M. Beeler, A. Ajay, J. Lähnemann, E. Bellet-Amalric, C. Bougerol, and E. Monroy
J. Appl. Phys. **118**, 014309 (2015)

[16] **Effect of the quantum well thickness on the performance of InGaN photovoltaic cells**
L. Redaelli, A. Mukhtarova, S. Valdueza-Felip, A. Ajay, C. Bougerol, C. Himwas, J. Faure-Vincent, C. Durand, J. Eymery and E. Monroy
Applied Physics Letters **105** (13), 131105

[17] **Persistence photo conductivity in Ni doped CdS**
M. M. Patidar, A. Ajay, A. D. Wala, N. Kiran, R. Panda, M. Gangrade, R. Nath and V. Ganesan
Journal of Physics: Conference Series **534** (1), 012046

[18] **Effect of the barrier thickness on the performance of multiple-quantum-well InGaN photovoltaic cells**
L. Redaelli, A. Mukhtarova, A. Ajay, A Núñez-Cascajero, S. Valdueza-Felip, J. Bleuse, C. Durand, J. Eymery and E. Monroy
Japanese Journal of Applied Physics **54** (7), 072302

Participation in international conferences

[1] (Talk) A.Ajay et al, "'III-nitride nanowire photodetectors", SPIE International Symposium on Optics + Photonics, August 2018, San Diego, USA.

[2] (Talk) A.Ajay et al, "GaN nanowires for mid-infrared intersubband optoelectronics", Compound semiconductor week, June 2018, Boston, USA.

[3] (Invited talk) A.Ajay et al, "GaN nanowires for intersubband optolectronics", EMN conference on Epitaxy, September 2017, Barcelona, Spain.

[4] (Talk) A.Ajay et al, “Germanium vs. silicon doping of GaN/AlN quantum wells and nanowire heterostructures for intersubband optoelectronics at 1.55 µm”,
International conference on Nitride Semiconductors, July 2017, Strasbourg, France.

[5] (Talk) A.Ajay et al, “Germanium vs. silicon doping of GaN/AlN nanowire heterostructures for intersubband optoelectronics at 1.55 µm”,
Nanowire week, May 2017, Lund, Sweden.

[6] (Talk) A.Ajay et al, “Ge doping in GaN thin films grown with Plasma-Assisted Molecular Beam Epitaxy”,
European Materials Research Society Spring, May 2016, Lille, France.

[7] (Poster) A.Ajay et al, “Ge and Si dopants for GaN/AlN MQWs in the short wavelength infrared: Case of nanowires and 2D layers”,
International Workshop on Nitride Semiconductors October 2016, Orlando, USA

[8] (Talk) A.Ajay et al, “Ge doping in GaN beyond the Mott transition using Plasma-Assisted Molecular Beam Epitaxy”,
International Workshop on Nitrides, October 2016, Orlando, USA.

Other contributions

[1] (Talk) “Electrical and Optical Properties of Heavily Ge-Doped AlGaN”, R. Blasco, A. Ajay, K. Lorenz, L. C. Alves and E. Monroy
Compound semiconductor week, June 2018, Boston, USA.

[2] (Poster) “Low-to-mid Al content AlInN layers deposited on Si(001) and Si(111) by RF sputtering”, R. Blasco, A. Núñez-Cascajero, A. Ajay, E. Monroy, S. Valdueza-Felip and F. B. Naranjo
Compound semiconductor week, June 2018, Boston, USA.

[3] (Poster) “Effect of the quantum wells thickness on the performance of InGaN QW photovoltaic cells”, L. Redaelli, A. Mukhtarova, S. Valdueza-Felip, C. Bougerol, A. Ajay, C. Durand, J. Eymery and E. Monroy
International Workshop on III Nitride Semiconductor, August 2014, Wroclaw, Poland.

[4] (Talk) **“**High-In-content InGaN grown by plasma-assisted MBE for solar cells: In incorporation and strain relaxation mechanisms”
S. Valdueza-Felip, E. Bellet-Amalric, A. Núñez-Cascajero, L. Redaelli, A. Ajay, M.P. Chauvat, P. Ruterana, K. Lorenz, E. Alves and E. Monroy
International Workshop on III Nitride Semiconductor, August 2014, Wroclaw, Poland.

[5] (Invited talk) “Effect of n-type doping on GaN/AlGaN nanostructures: Si vs. Ge doping”, A. Ajay, C. B. Lim, D. A. Browne, J. Lähnemann, C. Bougerol, M. I. den Hertog, and E. Monroy
Processus Ultimes d’Epitaxie de Semiconducteurs, GDR Pulse, July 2016, Marseille, France.

[6] (Talk) “Effect of Al incorporation in nonpolar m-plane GaN/AlGaN multi-quantum-wells using plasma-assisted molecular-beam epitaxy”, C. B. Lim, A. Ajay, C. Bougerol, J. Schörmann, and E. Monroy
EMRS Fall Meeting, September 2016, Warsaw, Poland.

[7] (Invited talk) “Nonpolar m-plane GaN epitaxy using plasma-assisted MBE for infrared optoelectronics” Caroline B. Lim, A. Ajay, C. Bougerol, E. Bellet-Amalric, J. Schörmann, D. A. Browne, and E. Monroy
EMN Meeting on Epitaxy, September 2016, Budapest, Hungary.

[8] (Poster) “Effect of Si and Ge doping in GaN/AlGaN multi-quantum-wells with intersubband transitions”, C. B. Lim, A. Ajay, and Eva Monroy,
International Workshop on Nitride Semiconductors October 2016, Orlando, USA.

[9] (Talk) “Doping of nonpolar m-plane GaN/AlGaN multi-quantum wells with intersubband transitions in the THz range: Effect of Si and Ge doping”, C. B. Lim, A. Ajay, C. Bougerol, J. Schörmann, D. A. Browne, and E. Monroy,
International Workshop on Nitride Semiconductors October 2016, Orlando, USA.

[10] (Invited) “Intersubband transitions in the THz using GaN quantum wells”, C. B. Lim, A. Ajay, C. Bougerol, J. Schörmann, D. A. Browne, M. Beeler and E. Monroy
Photonics West (SPIE), January 2017, San Francisco, U.S.A.

Glossary

AFM	Atomic force microscopy
APT	Atom Probe Tomography
BGR	Bandgap Normalization
BME	Burstein–Moss effect
FIB	Focused Ion Beam
FIR	Far-infrared
FTIR	Fourier transform infrared spectroscopy
FWHM	Full Width at Half Maximum
HAADF-STEM	High Angle Annular Dark Field Scanning Transmission Electron Microscopy
HR-TEM	High resolution transmission electron microscopy
HR-XRD	High resolution x-ray diffraction
HVPE	Hydride Vapour Phase Epitaxy
IR	Infrared
ISB	Intersubband
LWIR	Long-wavelength Infrared
MBE	Molecular Beam Epitaxy
ML	Mono Layer
MOVPE	Metal Organic Vapour Phase Epitaxy
MQW	Multi-Quantum Well
MWIR	Mid wavelength infrared
PL	Photoluminescence
QCSE	Quantum Confined Stark Effect
QW	Quantum Well
QWIP	Quantum well infrared photodetector
RBS	Rutherford Backscattering Spectroscopy
RHEED	Reflection High Energy Electron Diffraction

RMS	Root Mean Square
RSF	Relative Sensitivity Factor
SWIR	Short-Wavelength Infrared
ToF-SIMS	Time of Flight- Secondary Ion Mass Spectroscopy
UHV	Ullta-High Vacuum
VLS	Vapour-liquid-solid
xD	(x=1,2,3) Dimension

Due to its novel properties nanowires have emerged as promising building blocks for various advanced device applications. This work focuses on Intersubband (ISB) engineering of nanowires where we custom design GaN/(Al,Ga)N heterostructures to be inserted in a GaN nanowire to render it optically active in the infrared (IR) spectral region. ISB transitions refer to energy transitions between quantum confined levels in the conduction band of the nanostructure. All the structures analyzed in this thesis were synthesized by plasma-assisted molecular beam epitaxy.

Precise control of high doping levels is crucial for ISB devices. Therefore, we explored Ge as an alternative dopant for GaN and AlGaN, to replace commonly-used Si. We grew Ge-doped GaN thin films with carrier concentrations of up to 6.7×10^{20} cm^{-3} at 300 K, well beyond the Mott density, and we obtained conductive Ge-doped $Al_xGa_{1-x}N$ thin films with an Al mole fraction up to x = 0.66. In the case of GaN, the presence of Ge does not affect the growth kinetics or structural properties of the samples. However, in Ge doped $Al_xGa_{1-x}N$ samples with x > 0.4 the formation of Ge rich clusters was observed, together with a drop in the carrier concentration.

Then, we performed a comparative study of Si vs. Ge doping in GaN/AlN heterostructures for ISB devices in the short-wavelength IR range. We considered both planar and nanowire architectures with identical doping levels and well dimensions. Based on this study, we concluded that both Si and Ge are suitable dopants for the fabrication of GaN/AlN heterostructures for the study of ISB optoelectronic phenomena, both in planar and nanowire heterostructures. Within this study, we reported the first observation of ISB absorption in Ge-doped GaN/AlN quantum wells and in Si-doped GaN/AlN nanowire heterostructures. In the case of nanowires, we obtained a record ISB absorption linewidth in the order of 200 meV. However, this value is still larger than that observed in planar structures, due to the inhomogeneities associated to the self-assembled growth process.

Trying to reduce the inhomogeneities while keeping the advantages of the nanowire geometry, we also presented a systematic analysis of ISB absorption in micro- and nanopillars resulting from top-down processing GaN/AlN planar heterostructures. We showed that, when the spacing of the pillar array is comparable to the probed wavelengths, photonic crystal resonances dominate the absorption spectra. However, when these resonances are at much shorter wavelengths than the ISB absorption, the absorption is clearly observed, without any degradation of its magnitude or linewidth.

We also explore the possibility to extend this nanowire technology towards longer wavelengths, to absorb in the mid-wavelength IR region. Using GaN/AlN nanowire heterostructures, we varied the GaN well width from 1.5 to 5.7 nm, which led to a red shift of the ISB absorption from 1.4 to 3.4 µm. Replacing the AlN barriers by $Al_{0.4}Ga_{0.6}N$, the reduction of polarization led to a further red shift of the ISB transitions to 4.5-6.4 µm.

The observation of ISB absorption in nanowire ensembles motivated us for the development of a nanowire-based quantum well infrared photodetector (NW-QWIP). The first demonstration of such a device, incorporating a GaN/AlN nanowire heterostructure that absorbs at 1.55 µm, is presented in this manuscript.

Keywords: GaN/AlGaN, nanowires, molecular beam epitaxy, n-doping, nanowire devices, intersubband.

Les propriétés innovantes des nanofils semi-conducteurs en font des candidats très prometteurs pour le développement de dispositifs avancés dans de multiples domaines d'application. Ce travail se concentre sur l'ingénierie Inter-sous-bande (ISB) des nanofils. Nous avons conçu des hétérostructures GaN/(Al,Ga)N à insérer dans un nanofil GaN pour le rendre optiquement actif dans la région spectrale infrarouge (IR). Les transitions ISB se réfèrent aux transitions d'énergie entre les niveaux confinés quantiques dans la bande de conduction de la nanostructure. Toutes les structures analysées dans cette thèse ont été synthétisées par épitaxie par jet moléculaire assisté par plasma.

Un contrôle précis des niveaux élevés de dopage est crucial pour les dispositifs ISB. Par conséquent, nous explorons Ge comme un dopant alternatif pour GaN et AlGaN, pour remplacer le Si couramment utilisé. Nous avons synthétisé des couches minces de GaN dopé Ge avec des concentrations de porteurs atteignant $6,7 \times 10^{20}$ cm^{-3} à 300 K, bien au-delà de la densité de Mott, et nous avons obtenu des couches minces conductrices d'$Al_xGa_{1-x}N$ dopées Ge avec une fraction molaire Al jusqu'à x = 0,66. Dans le cas du GaN, la présence de Ge n'affecte pas la cinétique de croissance ou les propriétés structurales des échantillons. Cependant, dans les échantillons $Al_xGa_{1-x}N$ dopés Ge avec x> 0,4, la formation de clusters riches en Ge a été observée, avec une baisse de la concentration des porteurs de charges.

Ensuite, nous avons réalisé une étude comparative du dopage Si et Ge dans des hétérostructures GaN/AlN pour des dispositifs ISB dans la gamme IR proche. Nous considérons les architectures planaire et nanofils avec des niveaux de dopage et des dimensions de puits identiques. Sur la base de cette étude, nous pouvons conclure que les deux Si et Ge sont des dopants appropriés pour la fabrication d'hétérostructures GaN/AlN pour l'étude des phénomènes ISB, à la fois dans les systèmes planaires et nanofils. Dans cette étude, nous rapportons la première observation de l'absorption ISB dans des puits quantiques GaN/AlN dopés au Ge et dans des hétérostructures de nanofils GaN/AlN dopés au Si. Dans le cas des nanofils, nous avons obtenu une largeur de ligne d'absorption ISB record de l'ordre de 200 meV. Cependant, cette valeur est encore plus grande que celle observée dans les structures planaires, en raison des inhomogénéités associées au processus de croissance auto-assemblé.

En essayant de réduire les inhomogénéités tout en gardant les avantages de la géométrie des nanofils, nous présentons également une analyse systématique de l'absorption ISB dans les micro- et nano-piliers résultant d'un traitement top-down des hétérostructures planaires GaN/AlN. Nous montrons que lorsque l'espacement du réseau de piliers est comparable aux longueurs d'onde sondées, les résonances des cristaux photoniques dominent les spectres d'absorption. Cependant, lorsque ces résonances sont à des longueurs d'onde beaucoup plus courtes que l'absorption ISB, l'absorption est clairement observée, sans aucune dégradation de son amplitude ou de sa largeur de bande d'absorption.

Nous explorons la possibilité d'étendre cette technologie de nanofils à des longueurs d'onde plus longues, pour les absorber dans l'IR moyen. En utilisant des nanofils incorporant des hétérostructures GaN/AlN, nous avons fait varier la largeur du puits GaN de 1,5 à 5,7 nm, ce qui a conduit à un décalage vers le rouge de l'absorption ISB de 1,4 à 3,4 µm. Remplaçant les barrières AlN par $Al_{0.4}Ga_{0.6}N$, la réduction de la polarisation conduit à un nouveau décalage vers le rouge des transitions ISB à 4,5-6,4 um.

L'observation de l'absorption ISB dans des ensembles de nanofils nous a motivé pour le développement d'un photodétecteur infrarouge à puits quantiques à base de nanofils (NW-QWIP). La première démonstration d'un tel dispositif, qui absorbe à 1,55 µm, est présentée dans ce manuscrit.

Mots clés : GaN/AlGaN, nanofils, Épitaxie par jet moléculaire dopage n, composants à base de nanofils, inter-sous-band.